

Study of Electrode Kinetics

A thesis submitted for the degree of

Doctor of Philosophy

in Physical and Theoretical Chemistry

Danlei Li

Exeter College

Trinity Term 2020

Contents

Abstract ..... **x**

Acknowledgements ..... **xi**

Glossary ..... **xii**

Chapter 1 ..... **1**

Introduction to Electrochemistry **1**

1.1 Electrochemical equilibrium 2

1.2 Electrode kinetics in aqueous solution 10

1.2.1 Electrochemical cells 10

1.2.2 Butler-Volmer (BV) kinetics for a simple one-electron transfer process 13

1.2.3 Tafel analysis 16

1.3 Mass transfer in electrochemical systems 18

1.3.1 Introduction of modes of mass transport 18

1.3.2 Diffusion of species in solution 20

1.4 Electrochemical techniques: cyclic voltammetry 26

1.4.1 Reversibility: mass transport versus electrode kinetics 27

1.4.2 Cyclic voltammetry at different electrode geometries 28

References: 38

Chapter 2 40

Experimental 40

2.1 Chemical reagents 40

2.2 Electrochemical instrumentation 41

2.3 Preparation and geometries of the working electrodes 43

2.3.1 Preparation of the working electrodes 43

2.3.2 Geometries of the working electrodes 44

2.4 Simulation programmes 45

References: 46

Chapter 3 47

Voltammetric Demonstration of Thermally Induced Natural Convection in Aqueous Solution 47

3.1 Introduction 48

3.2 Experimental 51

3.2.1 Chemical reagents 51

3.2.2 Instrumentation 51

3.2.3 Electrochemical cell designs for the study of convection effect on electrodes with different geometries 52

3.2.4 Electrochemical cell design for the study of convective effects on a macroelectrode with different orientations 55

3.2.5 Electrochemical measurements 56

3.3 Results and discussion 56

3.3.1 Chronoamperometric responses on a macrodisc electrode 57

3.3.2 Evaporation effects on the voltammetric behaviour of a microcylinder electrode 62

3.3.3 Vibration effects on the voltammetric behaviour of a microcylinder electrode 65

3.3.4 Effect of natural convection on different electrode geometries 70

3.4 Conclusions 75

References: 76

Chapter 4 78

Tafel Analysis under Different Electrode Geometries 78

4.1 Introduction 79

4.2 Background theory 82

4.2.1 Butler-Volmer kinetics 82

4.2.2 Tafel analysis 83

4.2.3 Mass-transport corrected Tafel analysis 86

4.3 Numerical simulation procedures 87

4.4 Results and discussion 91

4.4.1 Electrodes with linear diffusion 92

4.4.2 Microelectrodes under steady-state conditions 99

4.4.3 Electrodes under quasi-steady state conditions 107

4.5 Conclusions 119

References: 120

Chapter 5 122

Some Thoughts About Reporting the Electrocatalytic Performance of Nanomaterials 122

5.1 Standard, formal and equilibrium potentials 123

5.2 How should we quantify electrode-kinetics? 125

5.3 What is an overpotential? 129

5.4 What is an onset potential? 132

5.5 What is the appropriate Tafel region of the current-potential plot of a half-cell reaction in which to analyse a ‘Tafel slope’? 135

5.6 Units and electrochemical surface areas 138

5.7 Conclusions 141

References: 141

Chapter 6 143

Electrochemical Measurement of the Size of Microband Electrodes: A Theoretical Study 143

6.1 Introduction 144

6.1.1 Background overview 144

6.1.2 Fabrication methods 147

6.2 Background theory 152

6.2.1 General theory background on band electrodes 152

6.2.2 Numerical simulation procedures 159

6.3 Results and discussion 162

6.3.1 Fully reversible redox couple with equal diffusion coefficients 163

6.3.2 Fully irreversible redox couple with equal diffusion coefficients 165

6.3.3 Fully irreversible redox couple with unequal diffusion coefficients ... 173

6.3.4 Blind tests 180

6.4 Conclusions 187

References: 188

Chapter 7 190

Electrocatalysis via Intrinsic Surface Quinones Mediating Electron Transfer to and from Carbon Electrodes 190

7.1 Introduction 191

7.2 Experimental 193

7.2.1 Chemical reagents 193

7.2.2 Instrumentation 193

7.2.3 Electrochemical measurements 194

7.2.4 Simulation programmes 195

7.3 Tafel analysis on a microdisc electrode 195

7.3.1 Mass-transport corrected transfer coefficient plots 196

7.3.2 Non-uniformly mass-transport corrected transfer coefficient plots 197

7.4 Results and discussion 199

7.4.1 Determination of the diffusion coefficients and the formal potential of the Fe^{2+}/Fe^{3+} redox couple 199

7.4.2 Comparison of voltammetric responses on gold and carbon microdisc electrodes 202

7.4.3 Transfer coefficient plots measured at carbon electrodes 204

7.4.4 Adsorption of Fe^{2+}/Fe^{3+} on a carbon microdisc electrode 208

7.4.5 Proposed mechanistic model of the $Fe^{2+/3+}$ redox process 221

7.5 Conclusions 224

References: 225

Chapter 8 227

Mass Transport Corrected Transfer Coefficients from Microdisc Cyclic Voltammetry: 2D Simulation and Experiment 227

8.1 Introduction 228

8.2 Applications of the Koutecký-Levich method and the normal mass transport corrected method on a microdisc electrode 237

8.2.1 The Koutecký-Levich method on a microdisc electrode 237

8.2.2 The mass transport corrected method applied to a microdisc electrode 241

8.3 Experimental 246

8.3.1 Chemical reagents 246

8.3.2 Instrumentation 246

8.4 Theory 246

8.5 Numerical methods 251

8.6 Results and discussion 252

8.6.1 Data extraction process 252

8.6.2 Accuracy of the data extraction method 254

8.6.3 Experimental example using the extraction method 257

8.7 Conclusions 260

References: 261

Chapter 9 264

Overall Conclusions 264

Appendix A 268

Section A1: Derivation of the analytical expression for the mass-transport corrected transfer coefficient α' in Chapter 4 268

Section A2: Establishing the lower current limit on different electrodes in Chapter 4 271

Section A3: Determination for diffusion limit in Chapter 4..... 273

References: 274

Appendix B..... 275

Section B1: Convergence test for the home-written microband programme 275

Section B2: Blind tests 276

Section B2.1: Test 3 - Redox couple with low unequal diffusion coefficients (α_a = 0.3, α_c = 0.7) 276

Section B2.2: Test 4 - Redox couple with low unequal diffusion coefficients (α_a = 0.4, α_c = 0.6) 279

Study of Electrode Kinetics

Danlei Li

Exeter College, University of Oxford

A thesis submitted for the degree of D.Phil. in Physical and Theoretical Chemistry

Trinity Term, 2020

Abstract

This thesis reports the use of Tafel analysis in the study of electrode kinetics from both theoretical and experimental perspectives.

During electrochemical measurements, any changes in temperature cause changes in diffusion coefficient of the species, the electrochemical rate constant and the equilibrium potential. Concequently, the improtance of temperature control in electrochemical systems is first investigated. When and how thermally induced convective flows in bulk solution influence the votlammetric behaviour are presented in Chapter 3.

Chapters 4 and 5 theoretically discuss what fraction of a voltammetric wave is appropriate to use as the Tafel region for accurate analysis under linear, quasi-steady-state and steady-state mass-transport regimes for an irreversible one-electron transfer process. The measured transfer coefficient is found to deviate significantly from its true value as a function of potential due to the mass-transport limitation at high overpotentials. If and how a simple analytical mass-transport correction using a plot of $\ln\left|\frac{1}{I}-\frac{1}{I_{lim}}\right|$ against potential can be used to improve the measurement of transfer coefficient is investigated. The methodology of measuring transfer coefficient is further employed in the electrochemical characterisation of a single microband electrode with unknown dimensions (Chapter 6). Such Tafel analysis is applied to an experimental study where the intrinsic surface quinones on carbon substrates can catalyse $Fe^{2+/3+}$ redox reaction evidenced by a potential dependent transfer coefficient (Chapter 7).

Last but not least, a new simulation techinique is developed in Chapter 8 to extract the kinetic information from experimental voltammograms for electrodes under both radial and liner regimes on the basis of the prior knowledge of the physical parameters defining the system, most importantly the diffusion coefficient, analyte concentration and electrode radius.

Acknowledgements

First of all, I would like to express great thanks to my supervisor, Professor Richard Compton, for all the invaluable support and guidance throughout my D.Phil. study. Thank you for providing me lots of opportunities to develop my scientific skills as well as knowledge. Your meticulous attitude and passion about the research always inspired me during my D.Phil. I am now becoming more positive and thoughtful towards the difficulties.

Second, my deep appreciation goes to Dr Christopher Batchelor-McAuley for your generous help and constructive advice which have made a significant contribution towards my D.Phil. You are always so supportive and patient when I was in trouble. I could learn some new knowledge from every single discussion with you. My D.Phil. would not have been so productive without your help. I also would like to acknowledge Lifu who was such a helpful senior group member and friend. My D.Phil. would not have started smoothly without your help and guidance of the experiments when I was a totally 'fresher' to the group. Thanks to Dr Chuhong Lin for the home-written programme which has been employed throughout my projects.

To Jake, Ruochen and Haonan, it has been lucky for me to have you preparing and achieving milestones of the D.Phil. together. To Archana, Yuanyuan and Yifei, I would be more than happy if I have ever helped you in some ways during your research. To Yuanzhe, Haotian, Bertold, Xiuting and many other group members of the past and present, I have been truly enjoying working with you. I felt so lucky to have the chance to be a member of such a wonderful group full of warmth, kindness and experitise. I am also greatful to the funding from China Scholarship Council and University of Oxford.

Special thanks to my 'Oxford Family' -Xin and Yanjun- who were and are so considerate in many ways. It has been so nice to have you two as housemates. The tasty food I received from you, especially Xin, have given me lots of happiness and energy. Thank you for taking care of me and always being my side. Special thanks to my "Pigeon" friends for the uncountable joy and ease you brought to me during the pandemic.

Last but not least, I would like to express heartfelt thanks to my parents and other family members for your deepest love, strongest support and constant encouragement. I could be so brave and positive is because I know you are always there. Undertaking this D.Phil. has been a meaningful and valuable experience in my life. It would not be possible for me to complete D.Phil. without the help and support from all of you.

Glossary

Roman Symbols

Symbol	Meaning	Units
$\boldsymbol{A}$	(a) area	cm^2
	(b) frequency factor in a rate expression (1st order)	s^{-1}
	(c) oxidised form of the system $A + e^- \rightleftharpoons B$	none
$\boldsymbol{a_i}$	Activity of species i	none
$\boldsymbol{b}$	Tafel slope	$mV\ dec^{-1}$
$\boldsymbol{B}$	Reduced form of the system $A + e^- \rightleftharpoons B$	none
$\boldsymbol{C_{dl}}$	Capacitance of the double layer	$F\ cm^{-2}$
$\boldsymbol{c_{i,bulk}}$	Bulk concentration of species i	$mol\ dm^{-3}$
$\boldsymbol{c_{i,0}}$	Concentration of species i at the electrode surface	$mol\ dm^{-3}$
$\boldsymbol{c^{\ominus}}$	Standard concentration ($1\ mol\ dm^{-3}$)	$mol\ dm^{-3}$
$\boldsymbol{D_i}$	Diffusion coefficient of species i	$m^2\ s^{-1}$
$\boldsymbol{D_{\infty}}$	Diffusion coefficient of species i at infinite temperature	$m^2\ s^{-1}$
$\boldsymbol{E_a}$	Activation energy of a reaction	$kJ\ mol^{-1}$
$\boldsymbol{E}$	Applied potential at the electrode	V
$\boldsymbol{E_{pa}}$	Anodic peak potential	V
$\boldsymbol{E_{pc}}$	Cathodic peak potential	V
$\boldsymbol{E_{mid}}$	Mid-point potential	V
$\boldsymbol{E_g}$	Energy gap	V

ΔE_{p-p}	Peak to peak separation	V
$E_{eq,A/B}$	Equilibrium potential of the A/B redox couple	V
$E^{\ominus}_{A/B}$	Standard redox potential of the A/B redox couple	V
$E^{\ominus}_{f,A/B}$	Formal potential of the A/B redox couple	V
F	The Faraday cosntant	C mol^{-1}
$\Delta G^{\ddagger}_{0}$	Standard Gibbs energy of activation	kJ mol^{-1}
$\Delta G^{\ddagger}_{a}$	Standard Gibbs energy of activation of anodic process	kJ mol^{-1}
$\Delta G^{\ddagger}_{c}$	Standard Gibbs energy of activation of cathodic process	kJ mol^{-1}
I	Current	A
I_a	Anodic current	A
I_c	Cathodic current	A
I_{cap}	Capacitative current	A
I_{fara}	Faradaic current	A
I_p	Peak current	A
I_d	Diffusional current	A
$I_{s.s}$	Steady-state current	A
I_{qss}	Quasi-steady-state current	A
I_{lim}	Mass-transport limited current	A
I_0	Exchange current	A
j	Electrochemical flux	mol cm^{-2} s^{-1}
j_a	Electrochemical flux for anodic process	mol cm^{-2} s^{-1}

j_c	Electrochemical flux for cathodic process	mol cm^{-2} s^{-1}
k_a	Hetergeneous rate constant of anodic process	cm s^{-1}
k_c	Hetergeneous rate constant of cathodic process	cm s^{-1}
k_{red}	Hetergeneous rate constant of a reduction	cm s^{-1}
k^0	Standard hetergeneous electrochemical rate constant	cm s^{-1}
K	Dimensionless rate constant	none
m_0	Mass transfer coefficient	cm s^{-1}
n	Number of electrons transferred in an electrode reaction	none
n'	Total number of electrons transferred before the rate determining step	none
r	Electrode radius	m
R	Gas constant	J mol^{-1} K^{-1}
R_s	Solution resistance	Ω
R_f	Roughness factor	none
t	Time	s
T	Temperature	K
v	Scan rate	V s^{-1}
$v(x)$	Local velocity of fluid along the x-axis	cm s^{-1}
w	Band width	m
x	Distance, often from a planar electrode	cm
Z_i	Charge on species i	none

Greek Symbols

Symbol	Meaning	Units
α_a	Anodic transfer coefficient	none
α_c	Cathodic transfer coefficient	none
γ_i	Activity coefficient of species i	none
δ	Diffusion layer thickness	m
η	Overpotential	V
θ	Dimensionless potential	none
μ_i	Chemical potential of species i	kJ mol^{-1}
$\overline{\mu_i}$	Electrochemical potential of species i	kJ mol^{-1}
μ_i^0	Standard chemical potential of species i	kJ mol^{-1}
μ	Coordinate in the oblate spheroidal coordinate system	none
ν	(a) Kinematic viscosity	cm^2 s^{-1}
	(b) Coordinate in the oblate spheroidal coordinate system	none
σ	Dimensionless scan rate	none
ϕ_m	Electric potential of the metal electrode	V
ϕ_s	Electric potential of the solution	V

Abbreviations

Abbreviation	Meaning
ADI	Alternating direction implicit

BV	Bulter-Volmer
CNT	Carbon nanotube
CV	Cyclic voltammetry
ECSA	Electrochemical surface area
IFD	Implicit finite difference
IUPAC	International Union of Pure and Applied Chemistry
K-L	Koutecký-Levich
LOD	Limit of detection
ORR	Oxygen reductive reaction
PID	Proportional integral derivative
SCE	Saturated calomel electrode
SEM	Scanning Electron Microscopy
SECM	Scanning Electrochemical Microscopy
SHE	Standard hydrogen electrode
SPPE	Screen-printed platinum macroelectrode
TOF	Turnover frequency

Chapter 1

Introduction to Electrochemistry

Electrochemistry is the important branch of chemistry which studies reactions involving electron transfers, and which relates the flow of electrons to chemical changes. Such reactions are called redox (reduction-oxidation) reactions. Electrochemical measurements are powerful methods for studying the kinetics and thermodynamics of such processes. Electrochemical processes are widely involved in daily life for instance in metal corrosion and coating and the detection of breath alcohol in drivers through the redox reaction of ethanol with dichromate[1]. In addition food sensors including chilli sensors have been recently developed[2] along with the bio-electrochemical detection of bacteria[3] and viruses[4]. Energy-related applications such as fuel cells and batteries (e.g. lithium-ion batteries, all-vanadium redox flow batteries)[5] also provide significant benefits to the world. Such research requires solid knowledge of fundamental electrochemistry in order to have a better understanding of the science behind the redox reactions. In this chapter, we give an overview of the fundamental principles of electrode reactions as well as the electrochemical techniques used in this thesis, with the aim of providing a clear background knowledge for the following chapters.

1.1 Electrochemical equilibrium

Electrochemistry studies the chemical processes involving electrons transfer across the interface between an electronic conductor (an electrode) and an ionic conductor (an electrolyte). Here we consider an electrochemical system as shown in Figure 1.1[6] where a metallic electrode is immersed in an aqueous solution (aq) containing the redox couple A/B, leading to the following electrochemical equilibrium:

$$A(aq) + e^{-}(m) \rightleftharpoons B(aq) \qquad (1.1)$$

where (m) stands for the electrons in the metal electrode and species A and B are present in aqueous phase (aq).[7]

During the establishment of the equilibrium, species A obtains one electron from the electrode and becomes reduced to species B, while B releases one electron to the electrode and then is oxidised to A. A dynamic electrochemical equilibrium is then established at the electrode/electrolyte interface at which point the net number of electrons transferred is negligible and the concentrations of A and B are considered as constant. Similar to the chemical equilibrium, if reaction (1.1) lies to the left when the equilibrium is reached, the electrode will be negative and the solution will be positively charged and vice versa.[8]

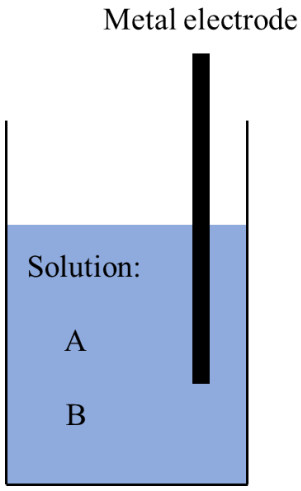


Figure 1.1 A metallic electrode immersed into an aqueous solution containing an A/B redox couple.

The charge transfer induces a charge separation between the electrolyte and the electrode, resulting in an electrical potential difference between them. An electrode potential is therefore established at the electrode relative to the bulk solution. The resulting electrode potential is associated with the energy levels of the species involved during the establishment of the equilibrium. Figure 1.2 shows the energy band diagram for an insulator, a semiconductor and a conductor where the upper (largely empty) band is called the conduction band which consists of orbitals with continuous higher energy orbitals and the lower (mostly filled) band is called the valence band which consists of continuous lower energy orbitals.[9] The Fermi level as shown by the dashed line in Figure 1.2 describes the top of the available electron energy levels at Absolute Zero of Temperature.[10] The ability of electrical conduction of a solid is crucially dependent on the position of the Fermi level relative to the conduction band (i.e. the presence of available electrons in the conduction band). The large energy gap between the conduction band and the valence band as shown in Figure 1.2 (a) inhibits the movement of electrons

from the valence band to the conduction band, resulting in an insulating characteristic without electrical conductivity. The relatively small energy gap in semiconductor (Figure 1.2 b) provides possibility of electron conduction; electrons in the valence band can be thermally excited to reach the conduction band and extra charge carriers can be added by doping.[9] According to the energy diagram of a hypothetical metal shown in Figure 1.2(c), the overlap of the conduction band and the valence band and existence of freely available electrons provide easy electron conduction.[9]

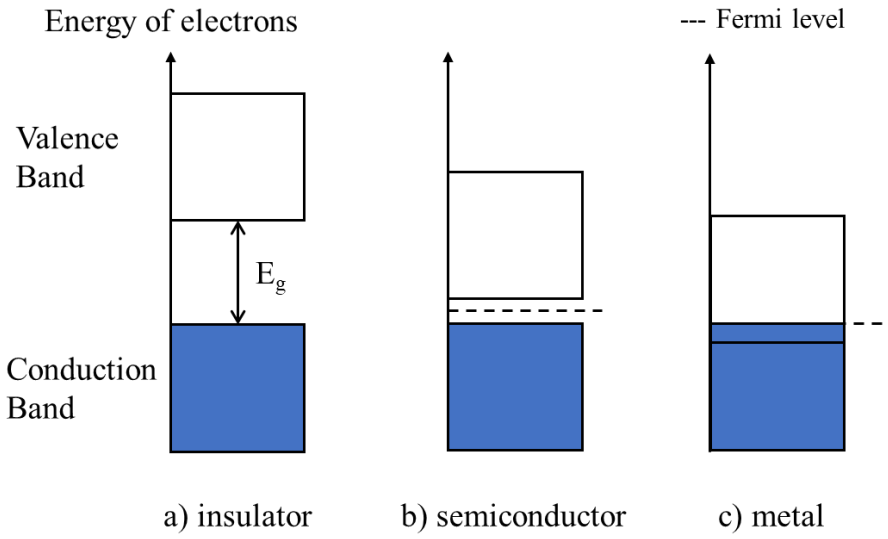


Figure 1.2 Possible energy band diagrams for (a) insulator, (b) semiconductor and (c) metal. E_g stands for the energy gap between the conduction band and the valence band. The dashed line represents the Fermi level.

Here we consider an electrochemical system using a metal electrode. The electron energy levels for the electrode and the solution phase are shown in Figure 1.3.[6] The electronic structure of the electrode has continuous energy levels whilst the electronic energy levels of species A and B in the solution phase are discrete. By way of example the solution

levels are assumed lower in energy than the Fermi Level of the electrode; in this case how the energy of electrons changes before (a) and after (b) electron transfer at the electrode/electrolyte interface is illustrated in Figure 1.3. The Fermi levels of the electrode and the solution are not usually equal when an initially uncharged metal electrode is immersed in an uncharged solution. In this example, before the electron transfers it is energetically favourable for the electrons flowing from the metal with a higher Fermi level to the vacant electronic states on species A in the solution phase and gets reduced to B. The metallic electrode consequently becomes positively charged after donating electrons to the ions which lowers the electronic energy presented as the lowered Fermi level in Figure 1.3(b). Meanwhile the solution phase becomes negatively charged and the electronic energy levels of the ions in the solution phase are progressively raised. The dynamic equilibrium will be finally attained once the rates of the oxidation of B and the reduction of A are the same (i.e. the rates of donating electrons to species A and gaining electrons from species B are matched). Note that it is shown in Figure 1.3(b), a charge separation due to the electron flowing exists between the metal electrode and the solution phase when the equilibrium is attained, which is the origin of the electrode potential established on the metal.[6] Of course if the Fermi level is below the solution energy levels then electrons move into the electrode before equilibrium is reached and in that case the electrode develops a negative charge.

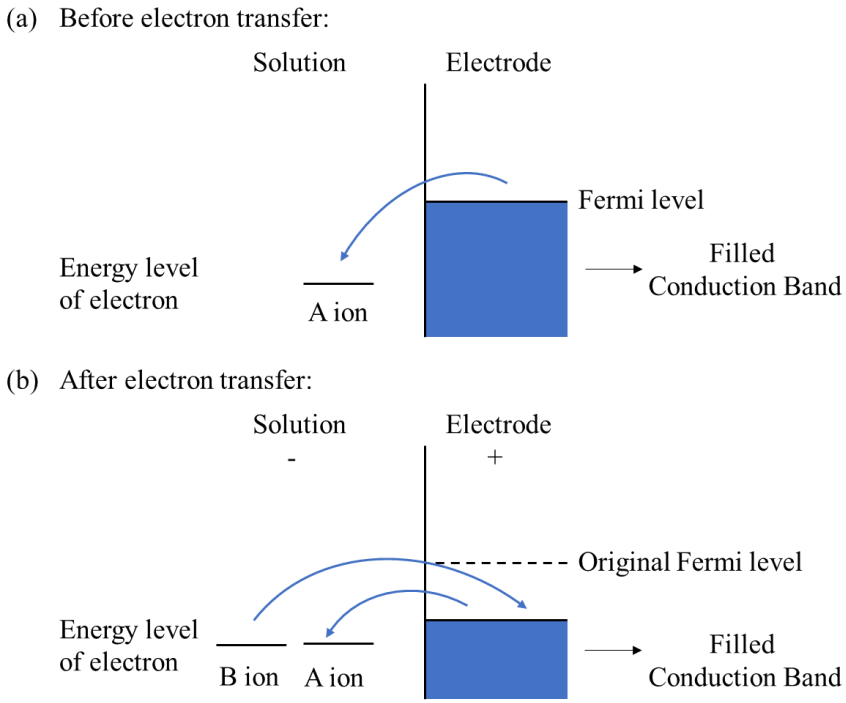


Figure 1.3 Representation of the electronic energy levels of the electrode and the electrolyte in aqueous solution before (a) and after (b) electron transfer.[6]

Unlike the case of a chemical equilibrium, which is controlled by the chemical potentials of the reactant and the product, the dynamic electrochemical equilibrium established for reaction (1.1) depends on not only the chemical potentials but electrical energies due to the electron transfer between the electrode and the solution phase. Here the electrochemical potential $\overline{\mu_i}$ of a species i is defined as:

$$\overline{\mu_i} = \mu_i + Z_i F \phi \qquad (1.2)$$

where μ_i is the chemical potential of species i, Z_i is the charge on species i, F is the Faraday constant (96485 C mol^{-1}) which corresponds to the charge on one mole of electrons and ϕ is the potential of the metal electrode (ϕ_m) or the solution containing species i (ϕ_s).

The chemical potential μ_i of species i is defined as:

$$\mu_i = \mu_i^0 + RTlna_i \tag{1.3}$$

where μ_i^0 is the standard chemical potential of species i, R is the universal gas constant (8.314 J K^{-1} mol^{-1}), T is the temperature in K and a_i is the activity of species i in the solution phase.

For reaction (1.1), the electrochemical potential at the equilibrium can be expressed as:

$$\overline{\mu_A} + \overline{\mu_{e^-}} = \overline{\mu_B} \tag{1.4}$$

Equation (1.4) can be converted to Equation (1.5) by applying Equation (1.2):

$$(\mu_A + Z_A F\phi_s) + (\mu_{e^-} + Z_{e^-}F\phi_m) = \mu_B + Z_B F\phi_s \tag{1.5}$$

Considering the charge on electron is -1, hence

$$(\mu_A + Z_A F\phi_s) + (\mu_{e^-} - F\phi_m) = \mu_B + (Z_A - 1)F\phi_s \tag{1.6}$$

Rearranging Equation (1.6), we can get:

$$F(\phi_m - \phi_s) = \mu_A + \mu_{e^-} - \mu_B \tag{1.7}$$

With the knowledge of the definition of chemical potential as shown in Equation (1.3), Equation (1.7) can be written as:

$$\phi_m - \phi_s = \frac{\Delta\mu^0}{F} + \frac{RT}{F} ln\left(\frac{a_A}{a_B}\right) \tag{1.8}$$

where $\Delta\mu^0 = \mu_A^0 + \mu_{e^-} + \mu_B^0$ which is a constant at a given temperature and pressure. Equation (1.8) is known as one form of the Nernst Equation describing a single electrode/solution interface in an electrochemical system as shown in Figure 1.1.

In reality the single boundary situation is extremely difficult to deal with as the potential differences cannot be realistically measured; hence an electrochemical cell which consists of two electrodes separated by at least one solution phase is necessarily employed. The introduced second electrode is called a *reference electrode* and this ideally has a fixed potential.[11] The internationally accepted primary reference electrode is the standard hydrogen electrode (SHE) where the standard conditions have protons at unit activity and hydrogen gas at one bar pressure. Other commonly used reference electrodes include the saturated calomel electrode (SCE) of which the potential is 0.242 V versus SHE and the silver-silver chloride electrode (Ag/AgCl) with a potential of 0.197 V in saturated KCl versus SHE at 25 ^{o}C.[11-12] With the use of a reference electrode the measured potential changes (ΔE) in the cell are all ascribable to the working electrode with respect to the reference electrode as shown as Equation (1.9).

$$\Delta E = (\phi_m - \phi_s)_{working} - (\phi_m - \phi_s)_{reference} \quad (1.9)$$

The Nernst equation for the electrode potential in such a two-electrode system is then expressed as:

$$E = E_{A/B}^{\ominus} + \frac{RT}{F} \ln \left(\frac{\alpha_A}{\alpha_B}\right) \quad (1.10)$$

where $E^{\ominus}_{A/B}$ is the standard redox potential of the A/B redox couple in the solution phase measured against a SHE. However, due to the non-ideality of the solution, the concentrations (c_i) of the electroactive species are usually not equal to their activity (a_i). The relationship between the activities and the concentrations of the electroactive species in solution phase has the expression $a_i = \gamma_i c_i / c^{\ominus}$, where γ_i is the activity coefficient of species i and $c^{\ominus}$ is the standard concentration (1 mol dm^{-3}) we can write:

$$E = E^{\ominus}_{A/B} - \frac{RT}{F} ln \frac{\gamma_B}{\gamma_A} - \frac{RT}{F} ln \frac{c_B}{c_A} \quad (1.11)$$

The formal potential ($E^{\ominus}_{f,A/B}$) of the A/B redox couple can then be expressed as:

$$E^{\ominus}_{f,A/B} = E^{\ominus}_{A/B} - \frac{RT}{F} ln \frac{\gamma_B}{\gamma_A} \quad (1.12)$$

For a simple one-electron transfer process (reaction 1.1), the Nernst equation describing the dynamic electrochemical equilibrium is consequently defined as:

$$E_{eq,A/B} = E^{\ominus}_{f,A/B} - \frac{RT}{F} ln \frac{c_B}{c_A} \quad (1.13)$$

Note that Equation (1.13) is sensitive to the ratio of the concentrations of species A and B. If a solution contains one order of magnitude higher concentration of the product as compared to the reactant the equilibrium potential will be ~59.1 mV negative of the formal potential of the system at 298K .[6] Classically the electrode potential is measured using a potentiometer which requires fast electrode kinetics in order to establish the dynamic electrochemical equilibrium as discussed in the next section.

1.2 Electrode kinetics in aqueous solution

1.2.1 Electrochemical cells

The two-electrode system mentioned above provides a feasible way to measure the *equilibrium* electrode potential at a working electrode (albeit relative to a reference electrode) which is expressed as Equation (1.9): $\Delta E = (\phi_m - \phi_s)_{working} - (\phi_m - \phi_s)_{reference}$ where $(\phi_m - \phi_s)_{reference}$ is assumed as a fixed value during the measurements. In practical measurements away from equilibrium, as shown in Figure 1.4 (a), if a two electrode system is used when a potential is applied to the working electrode, the generated current passes through both the working electrode and reference electrode, resulting in chemical changes inside the reference electrode (and hence a change in its potential). Moreover, a potential drop (iR_s), also known as 'ohmic drop', is gained due to the resistance of the solution (R_s) between the two electrodes. The potential, E, applied between the two electrodes is then given by:

$$E = (\phi_m - \phi_s)_{working} - (\phi_m - \phi_s)_{reference} + iR_s \quad (1.14)$$

The first term on the right-hand side of Equation (1.14) relates to the driving force for the electron transfer at the interface of interest and for a quantitative study changes in potential need to be reflected directly in this term. This requires the second term ($(\phi_m - \phi_s)_{reference}$) to be constant which in turn dictates that no current can pass through the reference electrode as discussed above. In addition, the third term, iR_s, needs to be

eliminated or minimised if changes in potential are to be reflected in changes in $(\phi_m - \phi_s)_{working}$.

To minimise the two, unwanted contributions a third electrode called a *counter electrode* (or *auxiliary electrode*) is consequently introduced to set up a three-electrode cell system as shown in Figures 1.4 (b) and (c). A device called *potentiostat* is used to control the electrochemical cell, which is able to impose a fixed potential between the working electrode and reference electrode, which drives the redox reaction of interest generating a current response. The current passes through the counter electrode but not the reference electrode. This allows the generation of current-voltage response at the working electrode/solution interface and the investigation of the redox reaction. To avoid the issue of potential change raised in a two-electrode system due to the current flowing across the reference electrode, the use of potentiostat which has a high impedance draws a negligible current flow through the reference electrode. The same amount of current as that flowing through the working electrode is then driven by the potentiostat to pass between the working electrode and the counter electrode to complete the electric circuit. The potential of the reference electrode ($(\phi_m - \phi_s)_{reference}$) can then be considered as a fixed value and also the unwanted contribution from the resistance between the working electrode and the reference electrode is minimised. In such a three-electrode cell, all the changes in the potential, E, appear in the term $(\phi_m - \phi_s)_{working}$ and the working electrode is regarded as being 'potentiostatted'. The counter electrode is chosen to have a good

electrical conductivity, a high surface area and not to produce any substances that affect the reactions of interest.[13]

The two-electrode cell can be employed when a microelectrode with dimensions of a few micrometres[14] is used as the working electrode. The current flowing through the working electrode is largely dependent on the size of the electrode; the use of such microelectrodes allows very low current flow in the order of nA which minimises the chemical changes in the reference electrode and the unwanted ohmic drop from iR_s is acceptable.[6, 10b]

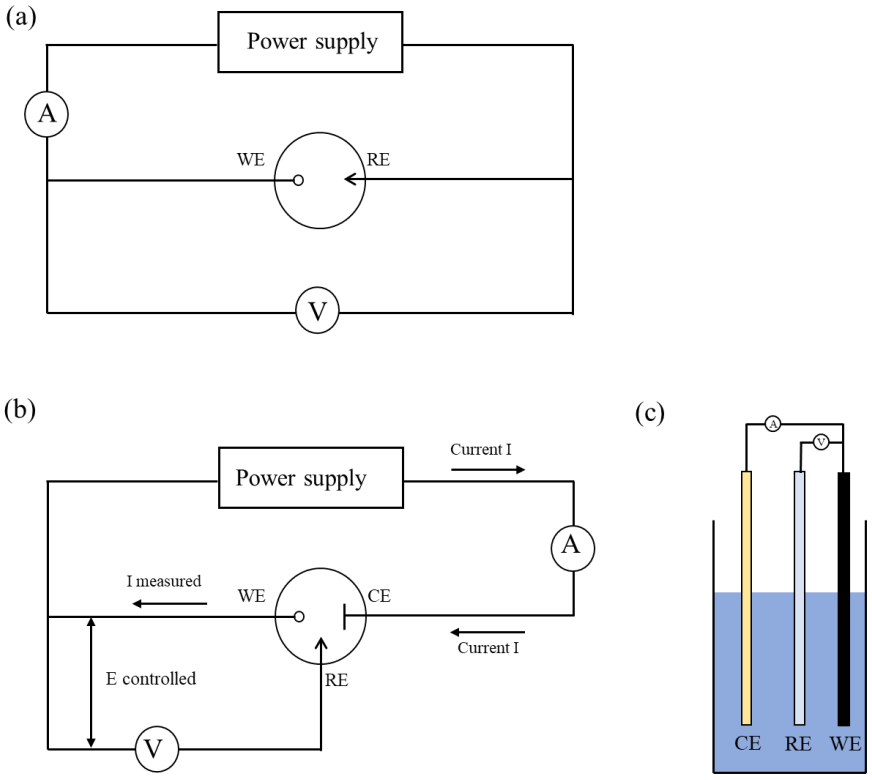


Figure 1.4 Schematic of a typical (a) two electrode cell and (b) (c) three electrode cell. WE, RE and CE represent the working electrode, reference electrode and counter electrode.

The passage of the electrical current I (amps) through the working electrode is related to the electrochemical flux j (mol cm^{-2} s^{-1}) of the reactant via the following equation:

$$I = -nFjA \tag{1.15}$$

where A the electrode area in cm^2 and n=1 throughout the thesis for a one electron transfer process. The electrochemical flux measures the rate of heterogeneous interfacial reaction, which if assumed to be first order can be written as:

$$j_{a/c} = k_{a/c}[reactant]_0 \tag{1.16}$$

where $j_{a/c}$ is the electrochemical flux for anodic (oxidative) or cathodic (reductive) reaction, $k_{a/c}$ is the heterogeneous rate constant for anodic or cathodic reaction (cm s^{-1}) and subscript '0' stands for the concentration of the reactant at the electrode surface. Note that the concentration at the electrode surface $[reactant]_0$ is generally different from that of the bulk solution $[reactant]_{bulk}$ due to the mass transport of the species from the bulk solution to the interface, which will be discussed later in this chapter.

1.2.2 Butler-Volmer (BV) kinetics for a simple one-electron transfer process

Here we consider a simple one-electron transfer process as discussed above in reaction (1.1):

$$A_{(aq)} + e^-_{(m)} \underset{k_a}{\overset{k_c}{\rightleftharpoons}} B_{(aq)} \tag{1.17}$$

The total (net) flux can be expressed using the rate law as shown in Equation (1.16):

$$j_{tot} = j_c - j_a = k_c[A]_0 - k_a[B]_0 \tag{1.18}$$

According to Equation (1.18), the cathodic reaction will become dominant at relatively negative overpotentials and the anodic reaction will dominate at relatively positive potentials. This can be clearly illustrated from the reaction profile as shown in Figure 1.5 where the ϕ_m and ϕ_s are assumed to be fixed.

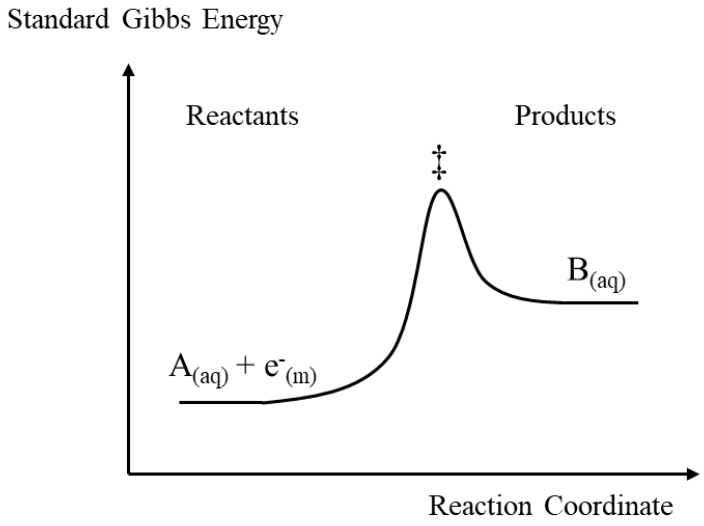


Figure 1.5 Simple representation of a reaction profile for the electrode process for reaction (1.17). ‡ stands for the transition state.

The reaction coordinates are changed from reactant to product through a transition state with a maximum energy as the reaction happens. This energy is defined as the Gibbs energy of activation which can be expressed as following:[15]

$$\Delta G_c^{\ddagger} = \Delta G_0^{\ddagger} + \alpha_c F(E - E_{f,A/B}^{\ominus}) \quad (1.19)$$

$$\Delta G_a^{\ddagger} = \Delta G_0^{\ddagger} - \alpha_a F(E - E_{f,A/B}^{\ominus}) \quad (1.20)$$

where $\Delta G_c^{\ddagger}$ and $\Delta G_a^{\ddagger}$ are the standard Gibbs energies of activation of the cathodic and anodic reactions, respectively and α_a and α_c are the anodic and cathodic transfer

coefficients of which the values are between 0 to 1. For a one-electrode transfer process normally $\alpha_a + \alpha_c = 1$.[16]

According to the Arrhenius Equation, the rate constants for cathodic and anodic processes are given by[10b]:

$$k_c = A_c e^{-\Delta G_c^{\ddagger}/RT} \tag{1.21}$$

$$k_a = A_a e^{-\Delta G_a^{\ddagger}/RT} \tag{1.22}$$

where $A_{a/c}$ is the exponential factor which is generally known as the frequency factor. The existence of the temperature T implies the importance of temperature control during electrochemical measurements.

Substituting $\Delta G_c^{\ddagger}$ and $\Delta G_a^{\ddagger}$ in Equations (1.21) and (1.22) using Equations (1.19) and (1.20):

$$k_c = A_c e^{-\Delta G_0^{\ddagger}/RT} \times e^{-\alpha_c F(E - E_{f,A/B}^{\ominus})/RT} \tag{1.23}$$

$$k_a = A_a e^{-\Delta G_0^{\ddagger}/RT} \times e^{\alpha_a F(E - E_{f,A/B}^{\ominus})/RT} \tag{1.24}$$

At the formal potential the anodic and cathodic rate constants become equal if the bulk concentrations and A and B are the same, and equal to the standard electrochemical rate constant:

$$k^0 = k_c = A_c e^{-\Delta G_c^{\ddagger}/RT} = k_a = A_a e^{-\Delta G_a^{\ddagger}/RT} \tag{1.25}$$

The rate constants at other potentials can then be expressed as:

$$k_c = k^0 \times e^{-\alpha_c F(E-E^{\ominus}_{f,A/B})/RT} \quad (1.26)$$

$$k_a = k^0 \times e^{\alpha_a F(E-E^{\ominus}_{f,A/B})/RT} \quad (1.27)$$

Now the total net flux measured at the working electrode can be expressed as Equation (1.28), which is known as the *Butler-Volmer Equation*.[17]

$$j_{tot} = -Fk^0_{A/B}\left(c_{A,0}\exp\left(\frac{-\alpha_c F}{RT}\left(E - E^{\ominus}_{f,A/B}\right)\right) - c_{B,0}\exp\left(\frac{\alpha_a F}{RT}\left(E - E^{\ominus}_{f,A/B}\right)\right)\right) \quad (1.28)$$

1.2.3 Tafel analysis

The transfer coefficient is a dimensionless parameter and describes how the rate of an interfacial oxidation or reduction reaction varies as a function of the applied potential, with the assumption that the concentration of the reactant at the electrode surface is unaltered from its value in bulk solution.[16, 18] According to the BV theory discussed above, the total flux of reaction is given as Equation (1.28). When the applied potential is sufficiently far from the equilibrium potential E_{eq}, it is possible to neglect the flux contribution from the reduction or oxidation. Hence, for an oxidative process, the electrochemical flux can be expressed as Equation (1.29) at extreme positive potentials whilst for a reductive process, the flux can be written as Equation (1.30) at extreme negative potentials.

$$j_a = k_a[B]_0 = k^0 exp\left[\frac{\alpha_a F(E-E_f)}{RT}\right][B]_0 \quad (1.29)$$

$$j_c = k_c[A]_0 = k^0 exp\left[\frac{-\alpha_c F(E-E_f)}{RT}\right][A]_0 \quad (1.30)$$

Recall that the flux is related to the measured current using Equation $I = FjA$. Equations (1.29) and (1.30) can be rearranged as:

$$\ln|I_a| = \frac{\alpha_a F(E-E_f^0)}{RT} + ln(FAk^0[A]_0) \quad (1.31)$$

$$\ln|I_c| = \frac{-\alpha_c F(E-E_f^0)}{RT} + ln(FAk^0[A]_0) \quad (1.32)$$

Hence, if the concentration at the electrode surface is assumed constant with respect to its bulk solution, a straight line with a gradient proportional to the transfer coefficient is obtained by plotting $\ln|I_{a/c}|$ versus E as shown in Figure 1.6. For a one-electron transfer process, $\alpha_a + \alpha_c = 1$ and the transfer coefficient is commonly qualitatively interpreted as a measure of the 'position' of the transition state[19], where a transfer coefficient close to zero implies the transition state is 'reactant-like' and similarly a value close to unity implies a 'product-like' transition state for an reductive process.

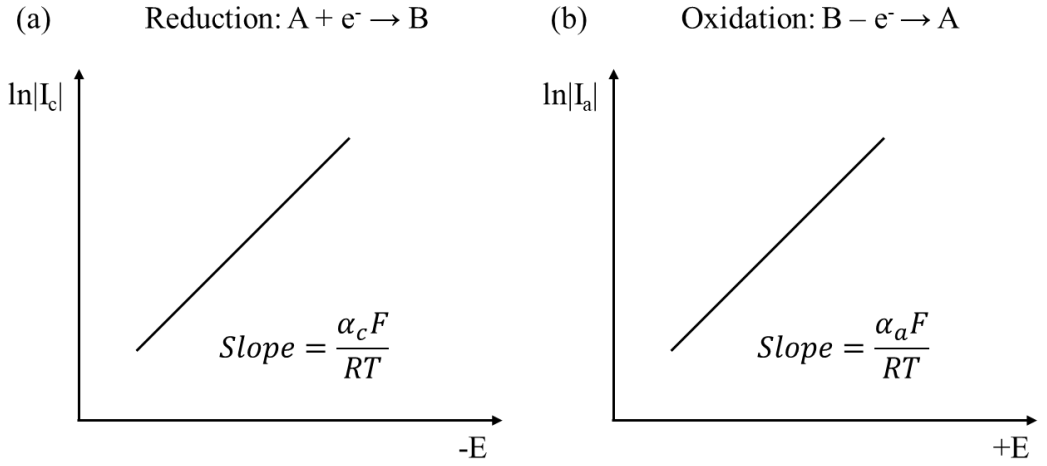


Figure 1.6 Tafel plots for (a) reductive and (b) oxidative processes.

1.3 Mass transfer in electrochemical systems

1.3.1 Introduction of modes of mass transport

Electrochemical mass transport is defined as the movement of the species in the bulk solution to the reaction interface (i.e. the electrode/solution interface) as illustrated in Figure 1.7. The reaction happens when the electroactive species is transferred to the interface, therefore how the species transported to the electrode surface plays an important role in studying the electrode kinetics. There are three modes of mass transport:[20]

a) Migration: this describes the movement of a charged molecule driven by the electrical potential gradient (i.e. under an electric field).

b) Diffusion: this describes the movement of species driven by the concentration gradient.

c) Convection: this describes the movement of species driven by the density gradient of the species themselves (natural convection) or external forces such as stirring or pumping (forced convection).

One-dimensional mass transport to an electrode along the x-axis is govern by the *Nernst-Planck equation*:[10b]

$$j_i(x) = -\frac{z_i F}{RT} D_i C_i \frac{\partial \phi(x)}{\partial x} - D_i \frac{\partial C_i(x)}{\partial x} + C_i \upsilon(x) \qquad (1.33)$$

where x is the distance from the electrode surface (cm), $j_i(x)$ is the flux of species i at distance x (mol cm^{-2} s^{-1}), D_i is the diffusion coefficient of species i (cm^2 s^{-1}), C_i is the concentration of species i (mol cm^{-3}), $\frac{\partial \phi(x)}{\partial x}$ is the potential gradient, $\frac{\partial C_i(x)}{\partial x}$ is the local concentration gradient at distance x, and $v(x)$ is the local velocity of fluid along the axis (cm s^{-1}). The three terms on the right stand for the flux contributions from migration, diffusion and convection, respectively. The negative sign in the equation implies the flux is down the gradient. The study of electrochemical systems with all the three modes of mass transport involved is mathematically complicated. The system is normally designed to eliminate one or two of the transport modes for the ease of investigation. The migration effect can be supressed to negligible by adding a supporting electrolyte (an inert electrolyte) with a much higher concentration (>100 times higher) than that of the electroactive species. The addition of such supporting electrolyte also decreases the solution resistance which improves the accuracy of the potential measured or controlled at the working electrode. The convection effect can be eliminated by avoiding the stirring and vibration of the solution and the possible density gradient introduced due to the temperature difference which will be investigated in detail later in Chapter 3. The diffusion of species in the solution is one of the key points in this thesis which will be discussed further in the following sections.

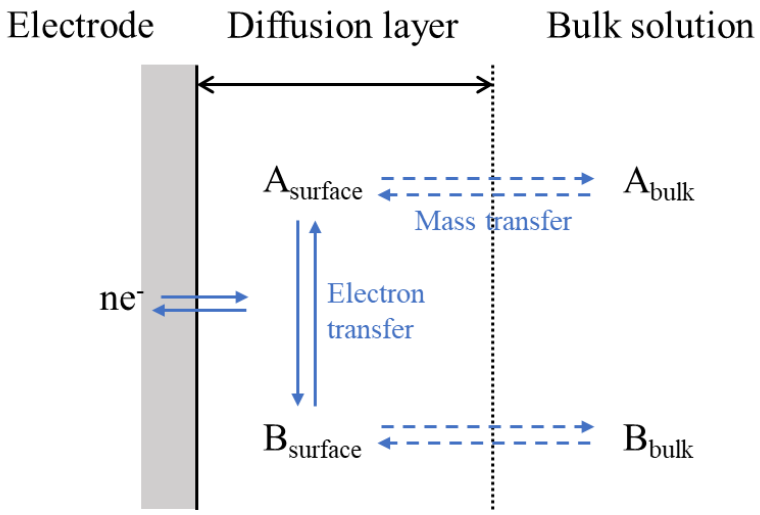


Figure 1.7 Schematic of the pathway of a diffusion-only process.

1.3.2 Diffusion of species in solution

1.3.2.1 Fick's Law of diffusion

As introduced in the previous section, the behaviour of species in the solution phase can be restricted to diffusion-only by supressing the migration (adding supporting electrolyte) and convection (using a quiescent solution). Here we first introduce the science behind the diffusion phenomenon before considering real experiments.

Diffusion of the species in solution is driven by the concentration gradient where the electroactive species tend to move from high concentration to low concentration. The flux contributed from a one-dimensional diffusion (j_d) to the electrode along x-axis can be quantified by *Fick's 1st Law* as shown below which is the same as the second term in Equation (1.33).[21]

$$j_d = -D_i \frac{\partial c_i(x)}{\partial x} \tag{1.34}$$

It is known that in the same way that a rate constant is dependent on the temperature, the diffusion coefficient of species i is also strongly dependent on the temperature following an Arrhenius type relationship:

$$D_i = D_\infty \exp\left(\frac{-E_a}{RT}\right) \tag{1.35}$$

where D_∞ is the diffusion coefficient of species i at infinite temperature and E_a is the activation energy for diffusion. This relationship further implies the requirement of a high quality thermostated system during electrochemical experiments.

Fick's 1st Law provides information on how the flux and concentration of the species i varies with the distance to the interface. The relationship between the flux and local concentration of the species i at the distance x and the time t is further given by *Fick's 2nd Law of diffusion*, which is derived from *Fick's 1st Law* by considering mass conservation.

Now we consider a one-dimensional system as shown in Figure 1.8(a), according to *Fick's 2nd Law*, the change in concentration of species i with time:

$$\frac{\partial C_i(x,t)}{\partial t} = D_i \frac{\partial C_i(x,t)}{\partial x^2} \tag{1.36}$$

The equation can be written as following in three-dimensions:

$$\frac{\partial C_i}{\partial t} = D_i \nabla^2 C_i \tag{1.37}$$

where ∇^2 is the Laplacian operator which has different forms for different electrode geometries as listed in Table 1.1.[6, 10b, 22] The variable electrode geometries will be discussed later in this chapter.

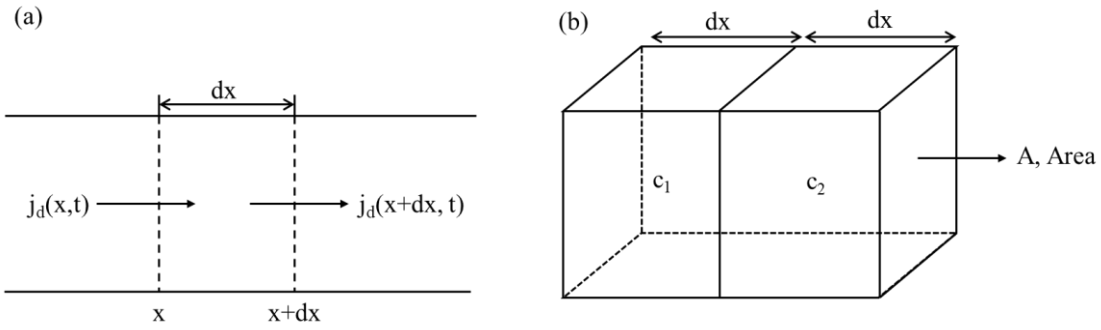


Figure 1.8 (a) Schematic of the flux of Fick's 2nd Law for a one-dimensional diffusion.[10b] (b) The molecular basis of Fick's Law.[6]

Table 1.1 Forms of Laplacian operator for different electrode geometries.[6, 10b, 22]

Type	**Variables**	∇^2	**Example**
Linear	x	$\frac{\partial^2}{\partial x^2}$	Macro-disc electrode
(Hemi)-spherical	r	$\frac{\partial^2}{\partial r^2}+\frac{2}{r}\frac{\partial}{\partial r}$	Mercury electrode
(Hemi)-cylindrical	r	$\frac{\partial^2}{\partial r^2}+\frac{1}{r}\frac{\partial}{\partial r}$	Wire electrode
Disk[1]	r, z	$\frac{\partial^2}{\partial r^2}+\frac{1}{r}\frac{\partial}{\partial r}+\frac{\partial^2}{\partial z^2}$	Ultra-microdisc electrode
Band[2]	x, z	$\frac{\partial^2}{\partial x^2}+\frac{\partial^2}{\partial z^2}$	Inlaid band electrode

[1]r and z are the radial and normal distances from the centre of electrode, respectively.

[2]x is the distance in the plane of band; z is the distance normal to the band surface.

Now if we consider *Fick's Laws* on a molecular basis as shown in Figure 1.8 (b) where two regions (half-box) have different concentrations c_1 and c_2. Assuming a particle moves dx during a given time dt, the number of moles of particle travelling from left to right in the left region is $\frac{c_1 A dx}{2}$ and similarly the number of moles of particles travelling from right to left is $\frac{c_2 A dx}{2}$. The net rate of mass transfer can then be expressed as a function of time:

$$rate = \frac{(c_1 - c_2) A dx}{2dt} \tag{1.38}$$

The local concentration gradient in the 'box' is $(c_1 - c_2) \sim -dx(\frac{\partial c}{\partial x})$. Hence the flux can be written as:

$$j = -\frac{(dx)^2}{2dt}\frac{\partial c}{\partial x} \tag{1.39}$$

Recall that from *Fick's 1st Law* $j = -D_i \frac{\partial C_i(x)}{\partial x}$, we can get:

$$D_i = \frac{(dx)^2}{2dt} \tag{1.40}$$

and

$$\sqrt{x^2} = \sqrt{2D_i t} \tag{1.41}$$

The above equation originally due to Einstein implies how far the molecule diffuses in the solution as a function of time, which provides a way in estimating the diffused distance of species in a certain time. The value of D_i normally lies in the range of 10^{-10} to 10^{-9} m^2 s^{-1}.

1.3.2.2 The Nernst diffusion layer

In an electrochemical experiment, the measured current results from two different processes: *Faradaic* and *non-Faradaic*. The former process involves the charge transfer which is govern by Faraday's law[23], resulting in a so-called *Faradaic current*. However, during the reaction processes the Faradaic current is often obscured by non-Faradaic current due to the non-Faradaic processes. Processes such as adsorption and desorption of species or the charge build-up (charging current or capacitative current) at the electrode/solution interface resulting from changes of potential and solution composition are categorised as non-Faradaic processes. As discussed in previous sections the concentration at the electrode surface is normally different from that in the bulk solution as shown in Figure 1.7 so that the species moves from the bulk solution to the interface across a "*diffusion layer*"[24] in which a concentration gradient exists. The existence of such processes contributes to a non-zero constant current even if there is no electrochemical reaction which is consistent with the model of the concentration profile in Figure 1.9. Such a simplified model is held with the assumption that beyond a distance of δ which is the thickness of *Nernst diffusion layer*, the bulk solution is well-mixed with a constant concentration C_{bulk}. According to *Fick's 1st Law*, the steady-state diffusional flux is:

$$j_d = D_i \frac{\partial C_i(x)}{\partial x} = \frac{D_i C_{bulk}}{\delta} \tag{1.42}$$

The corresponding steady-state current $I_{s.s}$ at the electrode with a Nernst diffusion layer of thickness is:

$$I_{s.s} = nFAj_d = \frac{nFAD_i C_{bulk}}{\delta} \tag{1.43}$$

Here a so-called mass transport diffusion coefficient is defined as:[6]

$$m_0 = \frac{D_i}{\delta} \tag{1.44}$$

where the unit of m_0 is cm s^{-1} which is the same as that of the electrochemical rate constant, allowing the direct comparison between the mass transfer of species and the electrode kinetics as will be discussed in section 1.4.

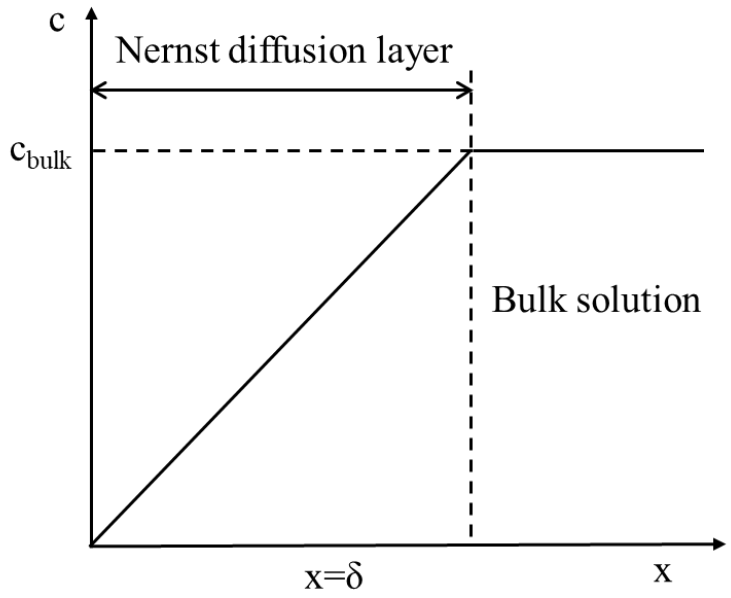


Figure 1.9 Nernst diffusion layer[24]. The y-axis is the concentration and x-axis is the distance from the electrode surface.

1.4 Electrochemical techniques: cyclic voltammetry

As is discussed above, the three-electrode cell in an electrochemical system is controlled by a potentiostat through which the current or the potential can be applied to the working electrode. Cyclic voltammetry (CV) is a simple but powerful method which is widely employed in the study of electrode kinetics in electrochemical systems.[25] In cyclic voltammetry the potential is applied at the working electrode as a function of time, resulting in a corresponding voltammetric current response as a function of applied potential.[26] CV is similar to linear sweep voltammetry but the potential in this case is reversed back to the starting potential. Here we consider a simple one electron transfer reductive process $A + e^- \rightleftharpoons B$ where A and B are in aqueous solution and initially only A exists. The potential is applied to the working electrode in a way illustrated in Figure 1.10 where the starting potential is labelled as E_1 at which point usually no electrochemical reaction happens so that the electroactive species of interest at first remains in its initial state. The potential is then swept linearly to E_2 with a fixed scan rate ν, at which point the direction of scan is reversed and swept back to E_1. The potential window (E_1-E_2) is chosen so that the electrochemical reaction under investigation occurs over such potential range. The resulting voltammetric current response as a function of the applied potential is known as a cyclic voltammogram.

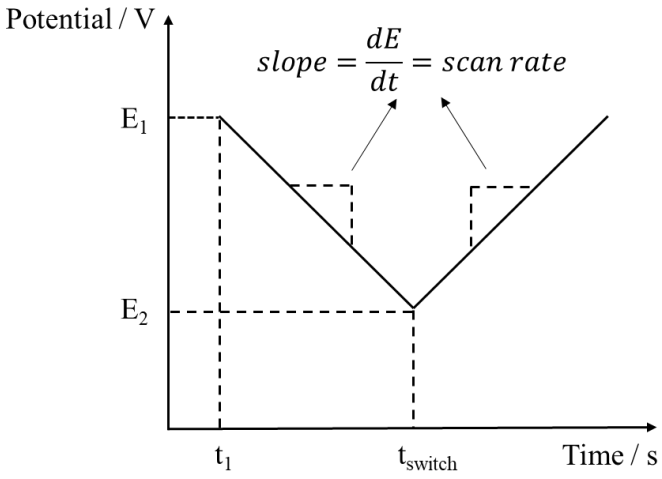


Figure 1.10 The potential-time profile for a cyclic voltammetry.

1.4.1 Reversibility: mass transport versus electrode kinetics

Here we still consider a one-electron transfer process (reaction 1.16) in aqueous solution.

$$A_{(aq)} + e^-_{(m)} \underset{k_a}{\overset{k_c}{\rightleftharpoons}} B_{(aq)} \qquad (1.16)$$

When a potential is applied to the working electrode at which point the potential is negative enough to reduce A to B or positive enough to oxidise B to A, there is a competition between how fast the species is transferred to the interface (mass transport) and the species is reduced or oxidised (electrode kinetics). The rate of mass transport is measured by the mass transport coefficient $m_0 = \frac{D_i}{\delta}$,[6] where δ is dependent on time t ($\delta \sim \sqrt{Dt}$).

According to $E \sim \frac{RT}{F}$, then the time $t \sim \frac{RT}{F\nu}$ where ν is the scan rate in V s^{-1}, consequently, the mass transport coefficient for a cyclic voltammetric experiment can be estimated by:

$$m_0 = \sqrt{\frac{D}{(RT/F\nu)}} \qquad (1.45)$$

The rate of electrode kinetics is measured using the standard electrochemical rate constant k^0, therefore the process is considered as *reversible* if $k^0 \gg m_0$ and *irreversible* if $k^0 \ll m_0$. The transition between the reversible and irreversible limit is considered as *quasi-reversible* or *quasi-irreversible* process. How the voltammetric behaviour varies with reversibility is discussed in the following sections.

1.4.2 Cyclic voltammetry at different electrode geometries

Working electrodes normally used in electrochemical measurements are categorised as either *macroelectrodes or microelectrodes* in terms of the size of the electrodes. Macroelectrodes are large electrodes with dimensions usually in the millimetre scale. A microelectrode has a definition by the International Union of Pure and Applied Chemistry (IUPAC) that a microelectrode has at least one dimension of tens of micrometers or less, down to the submicrometer range.[14] For electrodes with dimensions in less than micrometre scale, other terms, for example, ultramicroelectrodes[27] and nanoelectrodes[28], are sometimes used in the literature. The size difference among electrodes results in distinguishable diffusional profiles and hence different voltammetric behaviours. In the following, discussion is divided into three regimes in terms of their diffusion profile and mass-transport regime: linear diffusion, steady-state and quasi-steady state. Note that the reaction considered is reaction (1.16) throughout this chapter unless otherwise stated.

1.4.2.1 CV at macroelectrodes under linear regime

The most commonly used macroelectrode is a macrodisc electrode which is a large planar electrode embedded in an insulating material. As is shown in Figure 1.11, due to the large size of the electrode, the diffusion layer δ is far smaller compared to the radius of the electrode, the electrode is considered as *uniformly accessible* where the flux is constant across the whole electrode surface. In this case, the diffusion to the electrode surface is controlled by *linear diffusion*; the non-linear diffusion (diffusion to the edge of the electrode) is negligible at macroelectrodes. Such linear diffusion will give a peak-shaped voltammogram for a one electron transfer reductive process shown in Figure 1.12 (a). Assuming A and B are both in solution phase with only reactant A initially present in bulk solution, at relatively positive potentials the current approaches zero because the potential is not negative enough to drive the reduction of A. As the potential becomes more negative, the cathodic electrochemical rate constant k_c increases and the reactant transferred to the electrode surface starts being reduced to B, resulting in an increasing current. A maximum peak current is reached as the scan goes to more negative direction and then the current drops down giving a tail called *diffusional tail*. The peak current in cyclic voltammogram at a macroelectrode is due to the expanding diffusion layer as time goes by until the species at the electrode surface is completely consumed (i.e. $c_{A,0} \rightarrow 0$). The potential difference (ΔE_{p-p}) between the anodic and cathodic peak potential (E_{pa} and E_{pc}) is associated with the reversibility of the reaction.

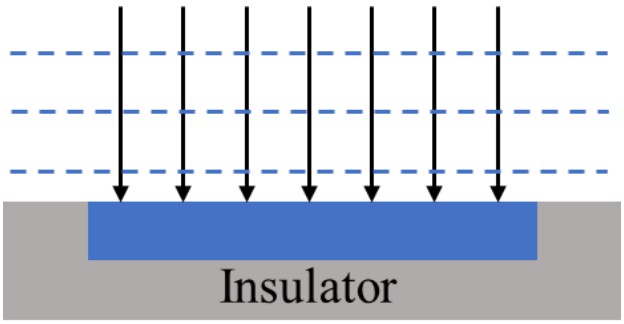


Figure 1.11 Diffusion profile at a macrodisc electrode.

Figure 1.12(b) shows the voltammograms on a macroelectrode with different electrochemical rate constants (red – reversible; blue – quasi-reversible; yellow – irreversible). As k^0 decreases, the peak-to-peak separation (ΔE_{p-p}) becomes larger which indicates the process is becoming more irreversible. For the fully irreversible process, ideally there is a potential region where the net current is zero, implying that a significant potential above the thermodynamically required potential need to be applied to drive the process of the reaction. However, in the reversible limit with fast electrode kinetics (relative to the mass transport), apparent current flow is observed at the potential near equilibrium potential at which point the *Nernst equilibrium* is attained. The concentration at the electrode surface for a fully reversible process then follows *Nernst equation*:

$$E = E^{\ominus}_{f,A/B} - \frac{RT}{F} ln \frac{c_{B,0}}{c_{A,0}} \quad (1.46)$$

where $c_{A,0}$ and $c_{B,0}$ are the concentrations of species A and B at the electrode surface.

Another important parameter obtained from the voltammogram is the *mid-point potential*:

$$E_{mid} = \frac{|E_{pa} - E_{pc}|}{2} \quad (1.47)$$

For a reversible process, E_{mid} is expressed as:

$$E_{mid} = E^{\ominus}_{f,A/B} - \frac{RT}{2F} ln \frac{D_B}{D_A} \quad (1.48)$$

For an irreversible process with the anodic and cathodic transfer coefficients of 0.5, E_{mid} is expressed as:

$$E_{mid} = E^{\ominus}_{f,A/B} - \frac{RT}{F} ln \frac{D_B}{D_A} \quad (1.49)$$

According to Equations (1.48) and (1.49), the formal potential of a redox couple A/B can be estimated from its mid-point potential with the known knowledge of the ratio of the diffusion coefficients of species A and B.

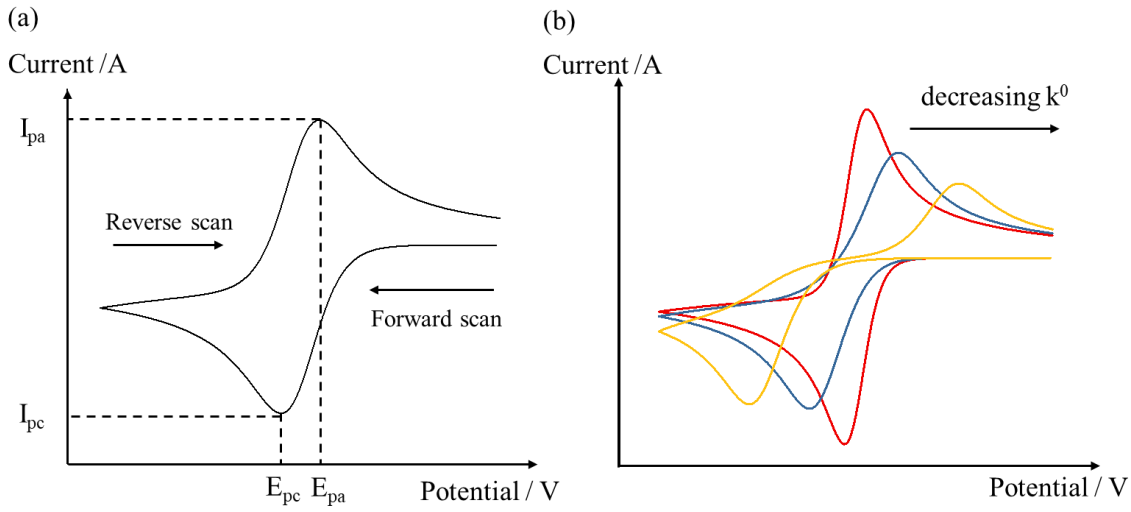


Figure 1.12 (a) Example of the cyclic voltammogram at a planar macrodisc electrode. (b) Voltammogram on a macrodisc electrode with different electrochemical rate constants k^0.

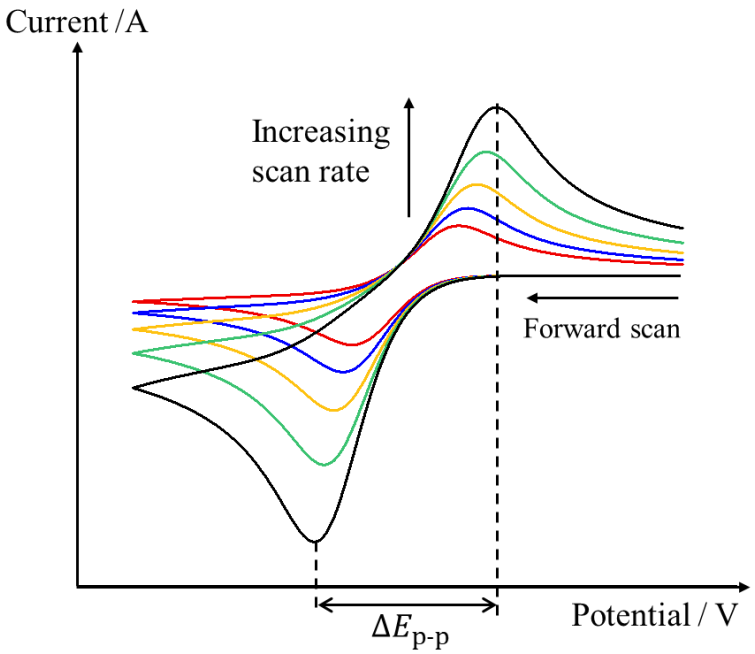


Figure 1.13 Example voltammograms for a quasi-reversible process at variable scan rates.

Figure 1.12 describes how the voltammetric behaviour changes with reversibility at a given scan rate. In a diffusion-controlled system, the peak current is proportional to the square root of scan rate for both the reversible and irreversible limiting cases. Such a relationship for a one-electron transfer process is mathematically shown by *Randles-Ševčík equation*:[6]

$$Reversible: I_p = 0.446FAc_{bulk}\sqrt{\frac{FD\nu}{RT}} \tag{1.50}$$

$$Irreversible: I_p = 0.496\sqrt{\alpha_{a/c}}FAc_{bulk}\sqrt{\frac{FD\nu}{RT}} \tag{1.51}$$

where $\alpha_{a/c}$ is the anodic or cathodic transfer coefficient. By plotting I_p versus the square root of scan rate, the diffusion coefficient of an unknown species can be measured from the slope of the resulting straight line.

Figure 1.13 shows an example of how the voltammogram changes at different scan rates for a quasi-reversible process. There are two changes to the voltammetric response as the scan rate increases: 1) the magnitude of current increases at higher scan rates; 2) the peak-to-peak separation increases at higher scan rates, indicating an increased irreversibility. Since the thickness of diffusion layer built up during the voltammogram increases with the time taken of the scan, for the same potential window, a higher scan rate requires shorter time to build up the diffusion layer around the electrode, resulting in a thinner diffusion layer which gives a large concentration gradient. According to *Fick's 1st Law*, a larger concentration gradient produces a higher current flux. In addition since the thickness of diffusion layer influences the rate of mass transfer as discussed in section 1.4.1, the ratio between the mass transport and the electrode kinetics becomes relatively large, which encourages electrochemical irreversibility at higher scan rates.

For processes involving more than one electron transfer, the current can be predicted by:

$$Reversible: I_p = 0.446nFAc_{bulk}\sqrt{\frac{nFD\nu}{RT}} \quad (1.52)$$

$$Irreversible: I_p = 0.496\sqrt{n' + \alpha_{n'+1}}nFAc_{bulk}\sqrt{\frac{FD\nu}{RT}} \quad (1.53)$$

where n is the number of electrons transferred, n' is the total number of electrons transferred before the rate determining step and $\alpha_{n'+1}$ is the transfer coefficient of the rate determining step.

1.4.2.2 CV at microelectrodes under a steady-state diffusion regime

Two types of electrode geometries are discussed in this section: the microdisc electrode and the micro-hemispherical electrode (a spherical electrode is similar but with the only difference of double the current magnitude). The diffusional profiles at the microelectrodes with both geometries are shown in Figure 1.14 where the electrode radius is much smaller than the steady-state diffusion layer thickness ($r \ll \sqrt{D\pi t}$). Unlike the peak-shaped voltammogram at macroelectrodes, a steady-state flux can be achieved without stirring of the solution as a consequence of radial diffusion. Such radial diffusion improves the efficiency of mass transport, resulting in a sigmoidal voltammogram with a steady-state current $I_{s.s}$ at sufficiently slow scan rates. When the potential is applied to the electrode, at very short time limit, the diffusion layer built-up is still much smaller compared to the radius of electrode ($r \gg \sqrt{D\pi t}$), which corresponds to the response obtained under linear diffusion as discussed in the previous sections. As time goes by, the diffusion layer becomes thicker and thicker until $r \ll \sqrt{D\pi t}$ at long-time limit.

Here the current on a uniformly accessible (hemi)spherical electrode is given as:

$$I_{s.s} = 2\pi r D F c_{bulk}\ (hemispherical\ electrode) \tag{1.54}$$

$$I_{s.s} = 4\pi r D F c_{bulk}\ (spherical\ electrode) \tag{1.55}$$

For the microdisc electrode of which the transient behaviour reflects a 2D diffusional problem. Under steady-state conditions, the current to the electrode is given by Equation (1.56) as originally described by Saito.[29]

$$I_{s.s} = 4nFDc_{bulk}r \quad (1.56)$$

From Equations (1.54), (1.55) and (1.56), the steady-state current on a microelectrode is independent of scan rate, which provides an easier way for the measurement of the diffusion coefficient of a species.

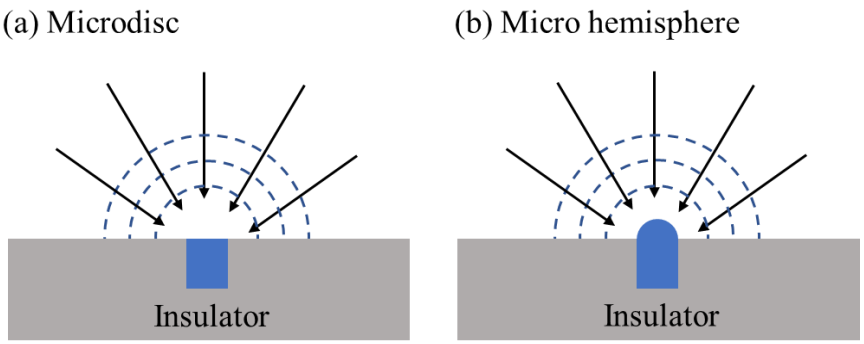


Figure 1.14 Diffusion profile for a (a) microdisc electrode and (b) micro hemispherical electrode.

Similar to the cases on macroelectrodes, the voltammetric behaviour is influenced by the reversibility of the processes. Figure 1.15 shows examples of the voltammograms at a micro-hemispherical electrode with variable electrochemical rate constants. In this case, the half-wave potential ($E_{1/2}$) at which point the current is half of the steady-state current is given by:

$$Reversible: E_{1/2} = E^{\ominus}_{f,A/B} + \frac{RT}{nF}\ln\left(\frac{D_B}{D_A}\right) \quad (1.57)$$

$$Irreversible: E_{1/2} = E^{\ominus}_{f,A/B} + \frac{RT}{\alpha F}\ln\left(\frac{rk^0}{D_A}\right) \quad (1.58)$$

From the above two equations, the formal potential can be estimated for a reversible process with the knowledge of the ratio of diffusion coefficients of reactant and product;

whereas for the irreversible process, k^0 also needs to be known for the estimation of the formal potential of redox couple A/B.

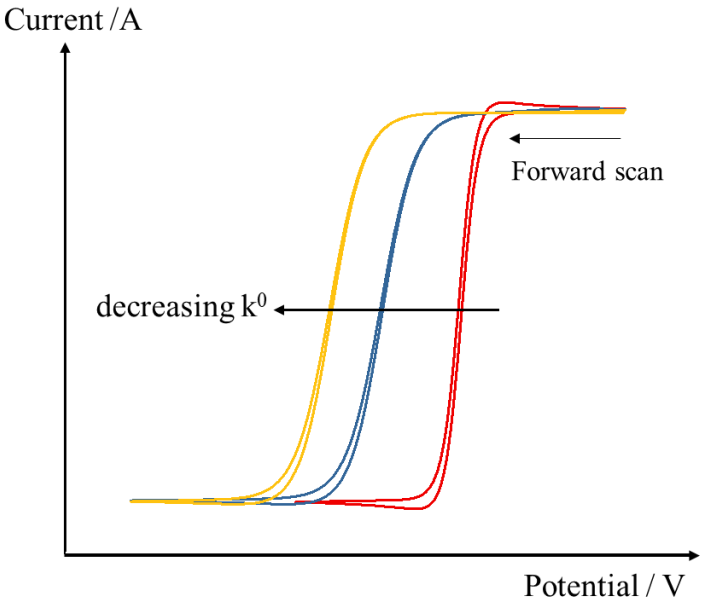


Figure 1.15 Steady-state voltammograms on micro-spherical electrode with variable electrochemical rate constants k^0.

1.4.2.3 CV at other microelectrodes under a quasi-steady-state diffusion regime

Microelectrodes discussed in this chapter are under a quasi-steady-state regime. These electrodes are characteristically microscopic in one dimension and macroscopic in another. (Hemi)-cylindrical electrodes and single microband electrodes are two examples of such electrodes.[30] As shown in Figure 1.16, the length of a microcylinder electrode is macroscopic and the radius is microscopic while the microband electrode is macroscopic in length and microscopic in width.[30b, 31] For both electrode geometries, the flux has contributions from both radial diffusion and linear diffusion. The voltammetric

waveshape on such electrodes is intermediate between peak-shaped and sigmoidal voltammogram and the voltammetric response has a scan rate dependency.

In the long-time limit, the current at a micro-cylindrical electrode can be predicted from:[10b]

$$I_{qss} = \frac{2nFADc_{bulk}}{rln\tau} \quad (1.59)$$

where I_{qss} is the quasi-steady-state current and $\tau = \frac{4Dt}{r^2}$. The measured current is proportional to the inverse logarithm of time, resulting in a rather slow decay of current in the long-time limit compared to that for the macroelectrodes.

For the single microband electrode which is a two-dimensional problem, the current at a microband electrode is often approximated to that of a hemi-cylinder of equivalent area ($r = w/\pi$).[19, 30a, 32] At long-time limit, the current at a single microband electrode can be expressed as:[10b]

$$I_{qss} = \frac{2\pi nFADc_{bulk}}{wln(\frac{64Dt}{w^2})} \quad (1.60)$$

Therefore, neither of the two electrode geometries is able to reach a true steady-state current at long times.

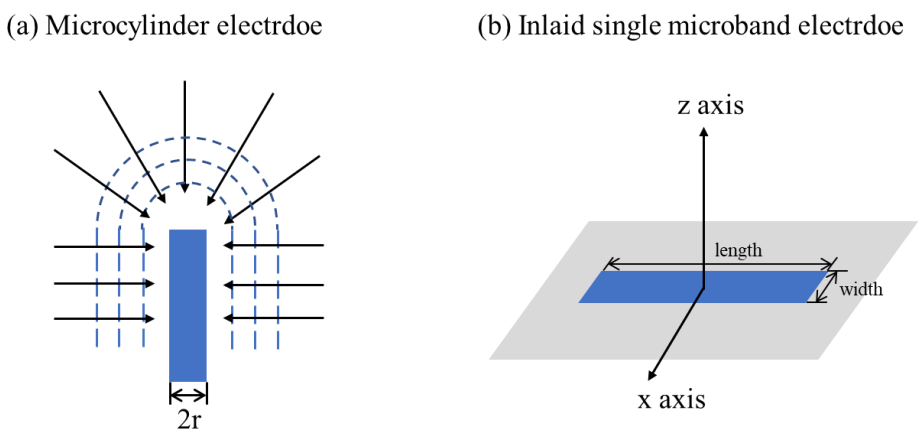


Figure 1.16 Schematic of (a) a micro-cylindrical electrode and (b) an inlaid single microband electrode.

References:

[1] Y. H. Caplan, B. A. Goldberger, *Garriott's Medicolegal Aspects of Alcohol*, Lawyers & Judges Publishing Company, Incorporated, **2015**.

[2] R. T. Kachoosangi, G. G. Wildgoose, R. G. Compton, *Analyst* **2008**, *133*, 888-895.

[3] S. Kuss, R. A. S. Couto, R. M. Evans, H. Lavender, C. C. Tang, R. G. Compton, *Analytical Chemistry* **2019**, *91*, 4317-4322.

[4] aA. D. Chowdhury, K. Takemura, T.-C. Li, T. Suzuki, E. Y. Park, *Nature Communications* **2019**, *10*, 3737; bL. Sepunaru, B. J. Plowman, S. V. Sokolov, N. P. Young, R. G. Compton, *Chemical Science* **2016**, *7*, 3892-3899.

[5] S. P. S. Badwal, S. S. Giddey, C. Munnings, A. I. Bhatt, A. F. Hollenkamp, *Front Chem* **2014**, *2*, 79-79.

[6] R. G. Compton, C. E. Banks, *Understanding Voltammetry*, thrid ed., World Scientific, **2018**.

[7] J. D. Cox, *Pure and Applied Chemistry* **1982**, *54*, 1239.

[8] J. O. M. Bockris, A. K. N. Reddy, *Modern Electrochemistry: Volume 1: An Introduction to an Interdisciplinary Area*, Springer US, **2012**.

[9] J. F. Cornwell, *Group Theory and Electronic Energy Bands in Solids*, American Elsevier Publishing Company, **1969**.

[10] aC. Kittel, *Introduction To Solid State Physics* 8th ed., New Jersey: John wiley & Sons, **2005**; bA. J. Bard, L. R. Faulkner, *Electrochemical Methods: Fundamentals and Applications, 2nd Edition*, Wiley Textbooks, **2000**.

[11] D. T. Sawyer, A. Sobkowiak, J. L. Roberts, *Electrochemistry for Chemists*, Wiley, **1995**.

[12] H. S. Harned, B. B. Owen, A. C. Society, *The Physical Chemistry of Electrolytic Solutions*, Reinhold Publishing Corporation, **1958**.

[13] H. Gamsjäger, J. W. Lorimer, P. Scharlin, D. G. Shaw, *Pure and Applied Chemistry* **2008**, *80*, 233.

[14] S. Karel, A. Christian, H. Karel, M. Vladimír, K. Wlodzimierz, *Pure and Applied Chemistry* **2000**, *72*, 1483-1492.

[15] D. G. Truhlar, W. L. Hase, J. T. Hynes, *The Journal of Physical Chemistry* **1983**, *87*, 2664-2682.
[16] R. Guidelli, R. G. Compton, J. M. Feliu, E. Gileadi, J. Lipkowski, W. Schmickler, S. Trasatti, *Pure and Applied Chemistry* **2014**, *86*, 259-262.
[17] T. Erdey-Grúz, M. Volmer, *Zeitschrift für physikalische Chemie* **1930**, *150*, 203-213.
[18] R. Guidelli, R. G. Compton, J. M. Feliu, E. Gileadi, J. Lipkowski, W. Schmickler, S. Trasatti, *Pure and Applied Chemistry* **2014**, *86*, 245-258.
[19] R. G. A. B. Compton, Craig E, *Understanding Voltammetry*, third ed., World Scientific, **2018**.
[20] J. Agar, *Discussions of the Faraday Society* **1947**, *1*, 26-37.
[21] aA. Fick, *Annalen der Physik* **1855**, *170*, 59; bA. Fick, *The London, Edinburgh, and Dublin Philosophical Magazine and Journal of Science* **1855**, *10*, 30-39.
[22] J. Crank, *The mathematics of diffusion* Clarendon Press, Oxford [England], **1975**.
[23] aM. Faraday, *Philosophical Transactions of the Royal Society of London* **1834**, *124*, 55-76; bM. Faraday, *Philosophical Transactions of the Royal Society of London* **1834**, *124*, 77-122.
[24] N. Ibl, *Pure and Applied Chemistry* **1981**, *53*, 1827.
[25] N. Elgrishi, K. J. Rountree, B. D. McCarthy, E. S. Rountree, T. T. Eisenhart, J. L. Dempsey, *Journal of Chemical Education* **2018**, *95*, 197-206.
[26] D. Pletcher, S. E. Group, R. Greff, R. Peat, L. M. Peter, J. Robinson, *Instrumental Methods in Electrochemistry*, Elsevier Science, **2001**.
[27] a*Electroanalysis* **2002**, *14*, 1041-1051; bJ. Heinze, *Angewandte Chemie International Edition in English* **1993**, *32*, 1268-1288.
[28] *Analyst* **2004**, *129*, 1157-1165.
[29] Y. Saito, *Review of Polarography* **1968**, *15*, 177-187.
[30] aC. A. Amatore, B. Fosset, M. R. Deakin, R. M. Wightman, *Journal of Electroanalytical Chemistry and Interfacial Electrochemistry* **1987**, *225*, 33-48; bM. P. Nagale, I. Fritsch, *Analytical Chemistry* **1998**, *70*, 2908-2913.
[31] M. P. Nagale, I. Fritsch, *Analytical Chemistry* **1998**, *70*, 2902-2907.
[32] A. Szabo, D. K. Cope, D. E. Tallman, P. M. Kovach, R. M. Wightman, *Journal of Electroanalytical Chemistry and Interfacial Electrochemistry* **1987**, *217*, 417-423.

Chapter 2

Experimental

This chapter presents first the generic details of experiments reported in this thesis including the chemical reagents, the instrumentation and the preparation and geometries of the electrodes. Second, the simulation programmes used in the thesis are outlined. More details regarding bespoke experiments, are separately described in the relevant Chapters 3-8.

2.1 Chemical reagents

All the chemical reagents used are listed in Table 2.1. Concentrations of each solution used in individual experiments are described in relevant chapters 3-8. All the solutions were prepared using deionised water (Milipore) with a resistivity of 18.2 MΩ cm at 25 ^{o}C.

Table 2.1 Chemical reagents used in the thesis.

Chemical Name	**Formula**	**Purity**	**Supplier**
Ammonium iron (II) sulfate hexahydrate	$(NH_4)_2Fe(SO_4)_2$	99.0%	Aldrich
Ammonium iron (III) sulfate dodecahydrate	$NH_4Fe(SO_4)_2$	99.0%	Aldrich
Ammonium sulfate	$(NH_4)_2SO_4$	≥ 99.0%	Aldrich

Ferrocenemethanol	$C_{11}H_{12}FeO$ ($FcCH_2OH$)	≥ 97%	ChemCruz
Perchloric acid	$HClO_4$	70%	Aldrich
Potassium chloride	KCl	≥ 99.0%	Sigma-Aldrich
Hexaammineruthenium (III) chloride	$[Ru(NH_3)_6]Cl_3$	≥ 98.3%	Alfa Aesar
Nitrogen gas	N_2	≥ 99.99%	BOC

2.2 Electrochemical instrumentation

All the experiments were performed with μAutolab Type III potentiostat using a standard three-electrode setup in a grounded Faraday cage. The electrochemical cell was thermostated at 25.0 (±0.1) ^oC unless otherwise stated through the use of either a conventional water bath or a home-made optimised thermostated system (Figure 2.1). This design of an optimised thermostated electrochemical cell was developed in previous work in the Compton Group where a Peltier-effect heat pump (type ETH-127-14-15-RS, R. S. Components Ltd, Corby, U.K.) was used to fabricate the thermostat system.[1] This pump was 40 mm × 40 mm in area and 3.9 mm thick with a maximum cooling capacity of 58.6 W and a maximum temperature difference of 65 K.[1] As shown in Figure 2.1, the glass vial containing the solution and electrodes was held tightly in an aluminium block with a cylindrical hole (23 mm in diameter; 40 mm in height) and the temperature control of the solution was achieved by immersing a temperature probe into the solution.[1] The Peltier element and the solution temperature were further monitored using a proportional-integral-derivative (PID) loop script written in Python 3.5.[1] A saturated calomel

electrode (SCE; BASi, Japan) was used as the reference electrode; a graphite rod or a platinum wire was used as the counter electrode. Various working electrodes were used depending on the purpose of study: a commercial glassy carbon macroelectrode (GC, 3 mm in diameter; BASi, Japan); a commercial screen printed platinum macroelectrode (SPPE); a commercial carbon microdisc electrode (7 μm or 33 μm in diameter; BASi, Japan); a commercial gold microdisc electrode (10 μm in diameter; BASi, Japan); a commercial carbon fibre micro tip electrode (7μm in diameter; Carbonstar-1, Kation Scientific); and a conventional home-fabricated carbon fibre micro-cylinder electrode (7μm in diameter, ca. 1 mm in length). Specific information on different working electrodes is presented in the relevant chapters.

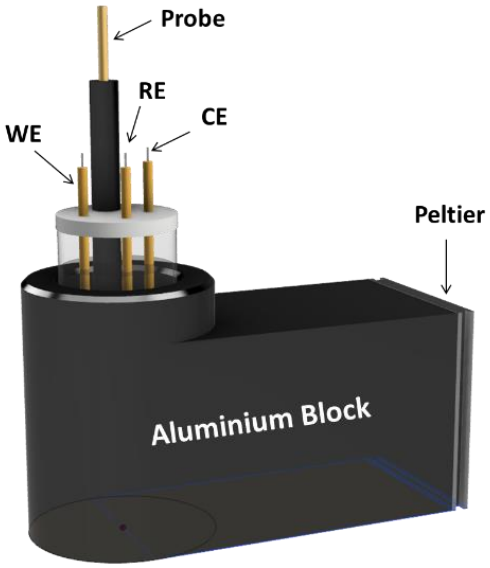


Figure 2.1 Schematic of the optimised thermostated electrochemical cell. The probe is used to sense the temperature of the electrochemical cell, which is controlled by a Peltier. WE, RE and CE represent the working electrode, reference electrode and counter electrode, respectively.

2.3 Preparation and geometries of the working electrodes

2.3.1 Preparation of the working electrodes

Macro- and microdisc electrode preparations All the commercial macro- or micro- disc electrodes were, before use, polished using alumina of decreasing size (1.0, 0.3 and 0.05 μm, Buehler, IL) on a polishing pad, washed with deionised water and then dried with nitrogen. The radii of macroelectrodes were determined using a travelling microscope from at least three independent measurements. The radii of microdisc electrodes were calibrated from the steady-state current obtained in a solution containing 1.0 mM ferrocenemethanol and 0.1 M KCl using a diffusion coefficient for $FcCH_2OH$ of 7.81×10^{-10} m^2 s^{-1} at 25 ^oC or a solution containing 1.0 mM hexaammineruthenium chloride and 0.1 M KCl using a diffusion coefficient for $[Ru(NH_3)_6]Cl_3$ of 8.43×10^{-10} m^2 s^{-1} at 25 ^oC.[2]

Carbon fibre micro-cylinder electrode fabrication Carbon fibre micro-cylinder electrodes were fabricated in-house using a method developed by Ellison *et al*.[3] A carbon fibre (7 μm in diameter, Goodfellow, Cambridge, U.K.) was connected to a metal wire using conductive silver epoxy adhesive (RS Components Ltd.) which was then cured in the oven for 15 minutes at ca. 60 ^oC. The dried connection wire was then threaded through a plastic pipette tip until only the carbon fire extended out of the pipette tip. A non-conducting cyanoacrylate adhesive was used to seal the wire and the tip. The resulting electrode was left overnight at room temperature to dry the glue. The desired wire

electrode was obtained by cutting the wire to approximately 1 mm length. The exact length of the wire electrode was calibrated from the peak current of the voltammograms obtained in a solution containing 1.0 mM ferrocenemethanol and 0.1 M KCl using a diffusion coefficient for $FcCH_2OH$ of 7.81×10^{-10} m^2 s^{-1} at 25 ^oC.[2] The electrode was rinsed with deionised water before and after experiments. The geometry of the electrode is shown in the following section.

2.3.2 Geometries of the working electrodes

The schematics of the electrode geometries used in this thesis are shown in Figure 2.2. The commercial macro- and micro-disc electrodes are shown in Figure 2.2(a) and (b), respectively. In both electrodes the electrode materials are embedded in an insulating sheath. For the glassy carbon macrodisc electrode (Figure 2.2(a)), the calibrated diameter was 2.984 (±0.005) mm and the total diameter of the electrode including the insulating sheath was 6 mm. In Figure 2.2(b), the total diameter of microdisc electrode (i.e. including the glass sheath) was 3.5 mm of which the diameter of the electrode material was only a few micrometres. The carbon fibre used in the home-fabricated micro-cylinder electrode (Figure 2.2(c)) was 7 μm in diameter of which the length was calibrated individually as mentioned above. The carbon fibre micro tip electrode is shown in Figure 2.2(d) where the diameter of the carbon fibre was 7 μm and the estimated length was ca. 15 μm.

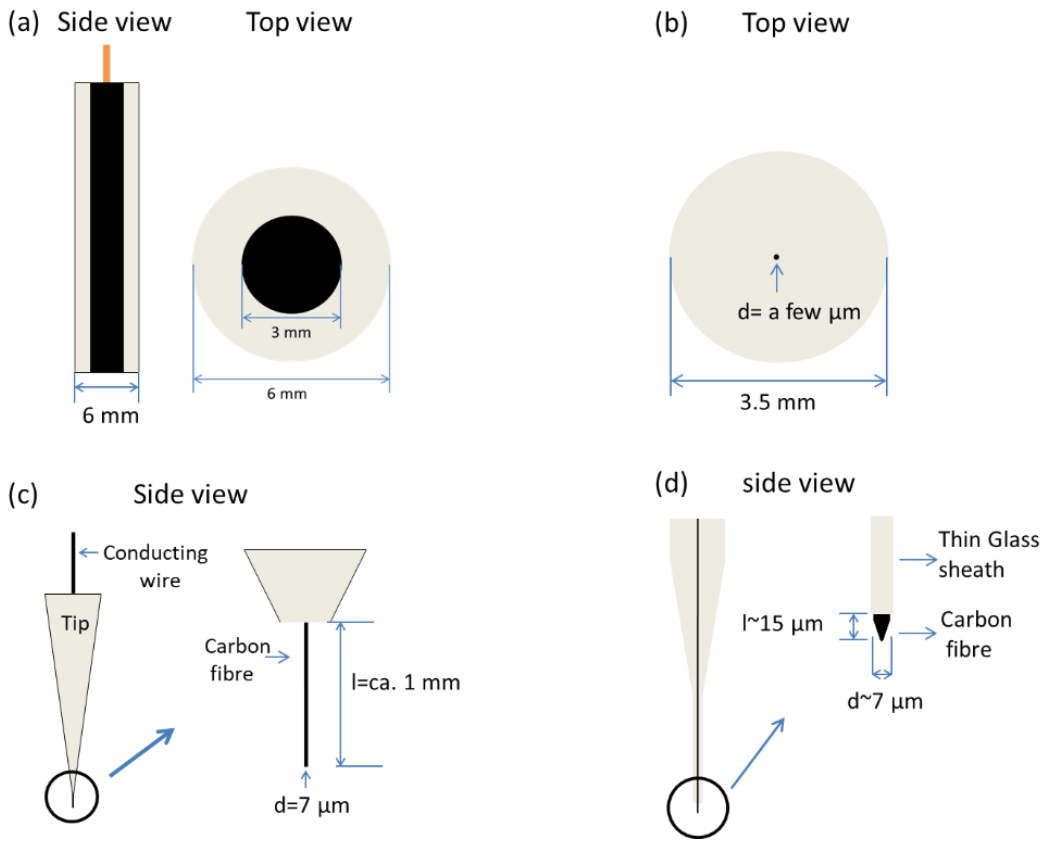


Figure 2.2 Schematic of the geometries of the electrodes: (a) commercial glassy carbon macrodisc electrode; (b) commercial microdisc electrode; (c) conventional carbon fibre micro-cylinder electrode; (d) commercial carbon fibre micro tip electrode.

2.4 Simulation programmes

The commercially available simulation software DigiSim® was used to simulate *one-dimensional (1D)* diffusion only models, notably planar, (hemi-) cylindrical, (hemi-) spherical geometries. This simulation package is based on a fully implicit finite difference (IFD) algorithm suggested by Manfred Rudolph[4] and it allows simulations for a wide range of mechanisms**.** The voltammetric response on a *2D diffusion* microdisc electrode was simulated using a home-written programme by Dr Oleksiy Klymenko which is based

on the conformal mapping of the spatial coordinates and uses an exponentially expanding time grid.[5]

The voltammogram on a microband electrode was simulated using a bespoke programme was written by Dr Chuhong Lin.[6] The numerical simulation procedures are introduced further in detail in Chapters 4 and 6.

A home-written programme for a rotating disc electrode was written by Dr Christopher Batchelor-McAuley. This simulation numerically calculates the voltammetric profile using a fully implicit finite difference method and makes use of the Hale transform[7] which is employed in Chapter 5.

References:

[1] X. Li, C. Batchelor-McAuley, J. K. Novev, R. G. Compton, *Phys. Chem. Chem. Phys.* **2018**, *20*, 11794-11804.

[2] K. Ngamchuea, C. Lin, C. Batchelor-McAuley, R. G. Compton, *Analytical Chemistry* **2017**, *89*, 3780-3786.

[3] J. Ellison, C. Batchelor-McAuley, K. Tschulik, R. G. Compton, *Sensors and Actuators B: Chemical* **2014**, *200*, 47-52.

[4] aM. Rudolph, *J. Electroanal. Chem. Interfacial Electrochem.* **1991**, *314*, 13-22; bM. Rudolph, *J. Electroanal. Chem.* **1992**, *338*, 85-98; cM. Rudolph, *J. Electroanal. Chem.* **1994**, *375*, 89-99.

[5] O. V. Klymenko, R. G. Evans, C. Hardacre, I. B. Svir, R. G. Compton, *Journal of Electroanalytical Chemistry* **2004**, *571*, 211-221.

[6] D. Li, C. Lin, C. Batchelor-McAuley, L. Chen, R. G. Compton, *Journal of Electroanalytical Chemistry* **2019**, *840*, 279-284.

[7] aR. G. Compton, E. Laborda, K. R. Ward, *Understanding Voltammetry: Simulation Of Electrode Processes*, World Scientific Publishing Company, **2013**; bJ. M. Hale, *Journal of Electroanalytical Chemistry (1959)* **1963**, *6*, 187-197.

Chapter 3

Voltammetric Demonstration of Thermally Induced Natural Convection in Aqueous Solution

Temperature control is normally used during electrochemical measurements since changes in temperature affect the equilibrium potentials, diffusion coefficients, rate constants (both homogeneous and heterogeneous), and hence the currents flowing. In addition imperfect thermostating inevitably leads to the presence of bulk convective flows. Whilst as recognised by Nernst[1] the damping of these bulk convective flows next to a solid surface, or at an electrode, leads to diffusional mass transport predominating locally, this chapter questions the exclusivity of diffusional transport and provides hitherto unexplored physical insights into how thermally induced flows in bulk solution can, on both macro- and microelectrodes, influence a voltammetric measurement. Imperfect thermostating results in flows in the bulk solution which are predicted and here experimentally shown to be as large as of the order of 100 μm s^{-1}. We show that even in the absence of natural convective flows induced by the electrochemical reaction itself, this thermally induced bulk convection can significantly affect the voltammetric response. First, we show that evaporative losses from an open electrochemical cell can be sufficient to produce convective flows that can alter the electrochemical response. Second, electrodes with various sizes and geometries have been investigated and experimental

results evidence that the sensitivity of an electrode to these flows in bulk solution is to a large extent controlled by the size of the surrounding non-conductive supporting substrate used to insulate parts of the electrode.

This work presented in this chapter has been published as a first author paper in *Physical Chemistry Chemical Physics*[2] and was carried out in collaboration with Dr. Christopher Batchelor-McAuley and Mr. Lifu Chen.

3.1 Introduction

Voltammetry lies at the very centre of the study of electrode reactions and, as well as being key to understanding catalysis and analysis, it offers a plethora of fundamental insights across a diversity of problems. Regardless of whether potential steps, sweeps[3] or pulses[4] are used, the current-voltage behaviour is generally interpreted on the basis of a signal in which the mass-transport is controlled exclusively by diffusion except when forced convection is introduced either by flowing the solution or rotating or vibrating the electrode. However, even in the absence of deliberately imposed convection, so-called natural convection can arise. As clarified by Levich[5] one mechanism by which this may arise originally from the heterogeneous reaction and relate to changes in solution density in the proximity of the reaction surface. Levich[5] identified two cases that can induce a density change, namely first, the intrinsic exo- or endothermicity of the electrode reactions locally altering the solution temperature and second, the local changes in chemical composition induced by the electrolysis causing altered local densities. Levich[5]

describes such density driven motion, arising from the occurrence of a heterogeneous reaction, as ‘spontaneous’ and implicit in these cases is the essential presence of a gravitational field.[5]

The effect of these reaction driven density changes have been quantified and in the cases of the former (reaction enthalpy induced convection)[6] shown to be negligible, fundamentally reflecting the order of magnitude faster transport of heat as compared to mass, a phenomenon which is restrictively limiting in the case of deliberately heated electrodes as pioneered separately by Wang, Flechsig, Grundler, Baranski and Marken[7] for electroanalysis. The situation in which the effects of changes in chemical composition cause density differences (reaction molar volume induced convection) and hence convective flows which augment transport by diffusion has been modelled, for example by Tschulik et al.[8] This latter case is shown to contribute noticeably as compared to so-called ‘edge effects’ arising from deviations from exclusively linear diffusion for macroelectrodes, positioned horizontally relative to the gravitational field acting vertically, at times greater than ca. 30 seconds in chronoamperometry when performed in aqueous solution. The magnitude of this effect reflects the change in the molar volume during the course of the reaction, the concentration of the electroactive species and the orientation of the electrode relative to the direction of the gravitational field.[9]

Beyond reaction enthalpy and reaction molar volume induced convective flow as described above, another important physical phenomena is that of electro-osmotic flow.[10]

Such flows may be induced by applying an electric field in a perpendicular direction to a double-layer. These flows have important technological applications in microfluidic devices; however, they are of less direct relevance to electro-analytical systems and hence will not be considered further in this work.

When theoretically analysing the influence of electrochemical reaction induced convection (i.e. enthalpy or molar volume induced convection) it is common in electrochemical simulations[8] to presume the presence of a stagnant bulk solution. Such a situation requires a uniform temperature throughout the cell. This assumption has recently been questioned and the simulation of typical electrochemical cells using finite element methods has shown the existence of significant flows in bulk solution.[11] These flows can arise from imperfect thermostating of a solution which is, at least to some extent, intrinsic to the concept of maintaining a cell at a fixed temperature within surroundings of different and variable temperatures. A common situation is that an electrochemical cell is immersed in a thermostated water bath but also exposed to the air which may produce a different temperature and/or allow evaporation from the water bath itself. Moreover if the thermal conductivity of the wall in contact with the electrolytic solution is spatially heterogeneous then local differential thermal conduction can lead to local solution phase flows near the glass/solution interface inside the electrochemical cell. Furthermore and in particular, evaporation of solvent from the surface of the liquid contained in the cell locally reduces the temperature and can cause significant flows. These flows are driven by the local temperature differences causing changes in the solution density. The

consequence of these effects is that even in the absence of other extrinsic forces (such as vibrations) the bulk solution contains natural convective flows; due to imperfect thermostating an aqueous solution will tend not towards a quiescent state but a convective stationary one with a non-zero flow velocity. The question arises as to the extent to which these density induced convective flows can influence voltammetry?

3.2 Experimental

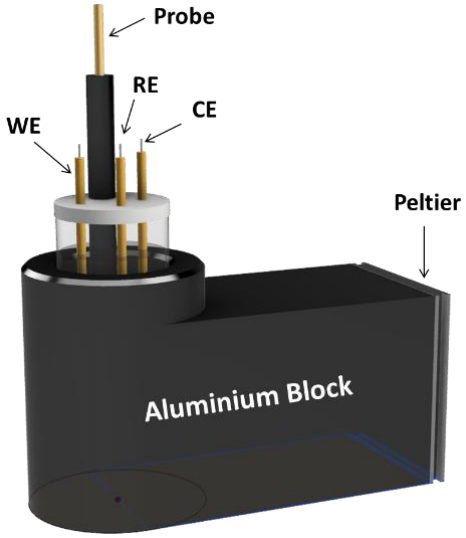
3.2.1 Chemical reagents

Ferrocenemethanol ($FcCH_2OH$; ChemCruz; >97%), Hexaammineruthenium (III) chloride ($[Ru(NH_3)_6]Cl_3$; Alfa Aesar; >98.3%) and potassium chloride (KCl; Sigma-Aldrich; ≥ 99.0%) were used as purchased without further purification. Solutions (1 mM $FcCH_2OH$ in 0.1 M KCl) were prepared using deionised water (Millipore) with a resistivity of 18.2 MΩ cm.

3.2.2 Instrumentation

Electrochemical measurements were performed with a μAutolab Type III potentiostat using a standard three electrode setup in an optimised thermostated electrochemical cell (Scheme 3.1). This design was developed in previous work[12] and has been described in Chapter 2. A saturated calomel electrode (SCE; BASi, Japan) and a platinum wire were used as the reference electrode and the counter electrode, respectively. Five different

electrodes were used as working electrodes depending on the purpose of study as mentioned below.

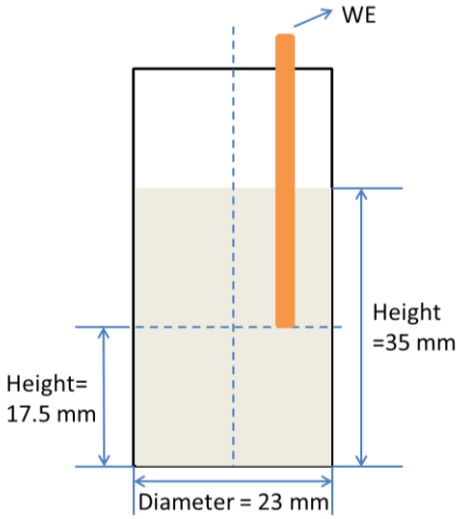


Scheme 3.1 Schematic of the optimised thermostated electrochemical cell. The probe is used to sense the temperature of the electrochemical cell, which is controlled by a Peltier. WE, RE and CE represent the working electrode, reference electrode and counter electrode, respectively.

3.2.3 Electrochemical cell designs for the study of convective effect on electrodes with different geometries

All experiments were conducted in a glass vial (Specimen tubes soda glass, 50 × 23 mm, SAMCO) containing 12 mL of solution (1 mM $FcCH_2OH$ in 0.1 M KCl) except where otherwise stated. The side view of the set-up of the vial is shown in Scheme 3.2, in this system the electrodes were positioned horizontally facing downward and at a height equal to half of the solution depth.

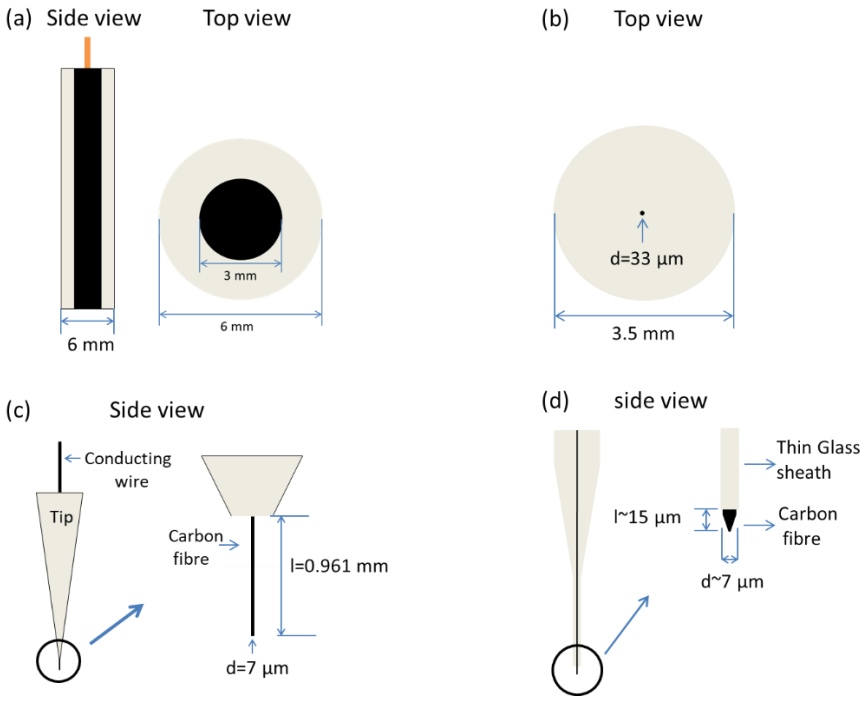
Four different electrodes were used as working electrodes: a conventional carbon fibre microcylinder electrode (7 μm in diameter), a commercial carbon fibre micro tip electrode (7μm in diameter; Carbonstar-1, Kation Scientific), a commercial carbon microdisc electrode (33 μm in diameter; BASi) and a commercial glassy carbon macroelectrode (3 mm in diameter; BASi). Prior to experiments, the latter two electrodes were polished using alumina of decreasing size (1.0, 0.3 and 0.05 μm, Buehler, IL), washed with deionised water and dried with nitrogen.



Scheme 3.2 Schematic of the side-view of the set-up within the glass vial. The surface of working electrode shown here is horizontal facing downward.

Geometries of the electrodes The schematics of the electrode geometries are shown in Scheme 3.3. For the commercial macrodisc electrode (Scheme 3.3(a)), the calibrated diameter of glassy carbon is 2.984 (±0.005) mm and the total diameter of the electrode (i.e. including the insulating sheath) is 6 mm; for the commercial microdisc electrode (Scheme 3.3(b)), the diameter of carbon fibre is 33 μm and the total diameter of the electrode (i.e. including the glass sheath) is 3.5 mm; for the conventional carbon fibre

microcylinder electrode (Scheme 3.3(c)), the diameter of carbon fibre is 7 μm and the measured length is 0.961 mm; for the commercial carbon fibre micro tip electrode (Scheme 3.3(d)), the diameter of the carbon fibre 7 μm and the estimated length is ca. 15 μm, of which the image using Scanning Electron Microscope (SEM) is provided in Figure 3.1.



Scheme 3.3 Schematic of the geometries of the electrodes: (a) commercial glassy carbon macrodisc electrode; (b) commercial carbon microdisc electrode; (c) conventional carbon fibre microcylinder electrode; (d) commercial carbon fibre micro tip electrode.

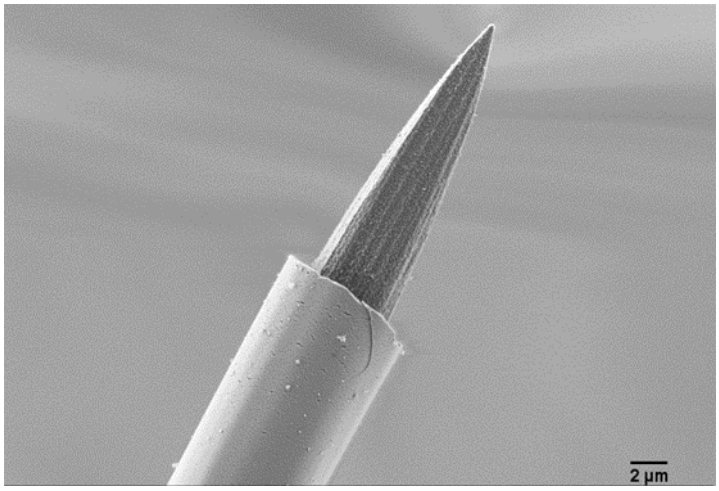
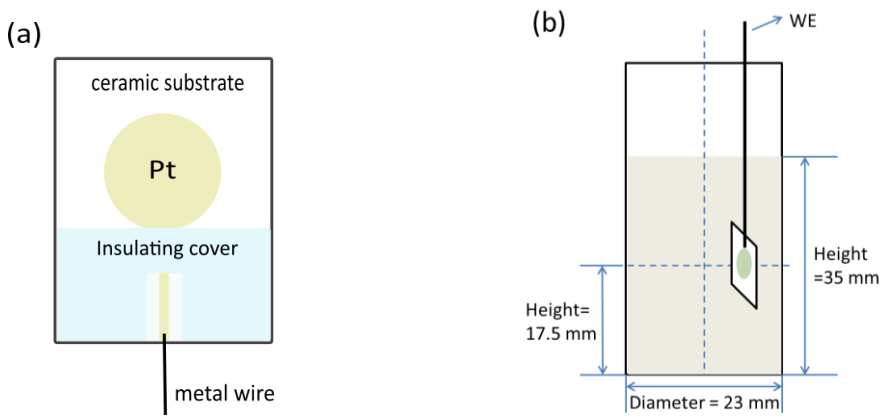


Figure 3.1 SEM image of a commercial carbon fibre tip electrode.

3.2.4 Electrochemical cell design for the study of convective effects on a macroelectrode with different orientations

Experiments performed with the electrode in different orientations relative to the gravitational field are detailed here. Scheme 3.4 show the schematic of working electrode (Scheme 3.4(a)) and the cell design (Scheme 3.4(b)) including the geometry and position of working electrode. A screen-printed platinum macroelectrode (SPPE) was used as the working electrode. Its own reference and counter electrodes were covered using insulating tape. The uncovered Pt working electrode was connected to a metal wire using silver epoxy. A saturated calomel electrode and a platinum wire were used as reference electrode and counter electrode, respectively.



Scheme 3.4 Schematic of vertical SPPE (a) and the cell design (b). WE represents for working electrode (SPPE).

3.2.5 Electrochemical measurements

Thermostating measurements All voltammetric measurements were carried out at 25.0 ^{o}C within both a closed cell and an open cell. The cyclic voltammetry was scanned from -0.1 V to 0.5 V at a scan rate of 25 mV s^{-1} except where otherwise stated. For the experiments in an open cell, the measurements were taken every 15 mins.

Simulation software The commercially available simulation software DigiSim® is used to simulate the one-dimensional (1D) diffusion only models, for example planar, (hemi-) cylindrical, (hemi-) spherical geometries.

3.3 Results and discussion

The design and application[12] of an optimised thermostated cell has recently been reported with minimised vibration and thermal effects which were well-characterised by means of both experiments and computational modelling to describe the extent to which

the full thermostating of a cell by a heated bath can be realised. The detailed design of this optimised thermostated cell is described in above Section 3.2.2. The modelling included heat transfer due to evaporation and radiative processes and, in agreement with experiments, indicated that the steady-state temperature of the cell could deviate from that of the thermostat by ~0.1 K. Such a spatial inhomogeneity of the temperature is predicted to drive convective flows of speed of the order of 100 μm s^{-1} in bulk solution.[12]

3.3.1 Chronoamperometric responses on a macrodisc electrode

First, the oxidation of a model redox probe under relatively quiescent conditions is studied in the electrochemical cell schematically shown in Scheme 3.1. Figure 3.2 shows the chronoamperometric response of a glassy carbon macro-electrode (3 mm in diameter) obtained by applying a constant positive potential of 0.35 V for 60 s for the oxidation of 1 mM ferrocenemethanol at 25 ºC. In this experiment the working electrode is facing downward, as would be most commonly done in an electroanalytical experiment. Overlaid is the theoretical time current transient as predicted using a) the Cottrell equation[3] and b) the Shoup-Szabo equation.[14] The Cottrell equation is given as Equation 3.1:

$$I = \frac{nFA\sqrt{D}c_{bulk}}{\sqrt{\pi t}} \qquad (3.1)$$

The Shoup-Szabo equation is given as Equation 3.2 which additionally accounts for the contribution of radial diffusion towards the macrodisc electrode.

$$\frac{I(t)}{n\pi FcDr} = 1 + \frac{r}{\sqrt{\pi Dt}} + \left(\frac{4}{\pi} - 1\right) \exp\left(\frac{-0.39115r}{\sqrt{Dt}}\right) \quad (3.2)$$

where n is the number of electrons transferred, F is the Faraday constant, c is the bulk concentration of the reactant, D is the diffusion coefficient of the reactant, r is the radius of the electrode, t is the time. In the present case of ferrocenemethanol a diffusion coefficient of 7.8×10^{-10} m^2 s^{-1} was chosen in the calculation.[15] Excluding the first 0.3 seconds of the experiment where capacitative charging is important, over the course of the rest of the experiment the measured current deviates from the theoretical results by an average of 1.4%, as shown in the inlay of Figure 3.2 where the error was calculated using Equation 3.3.

$$Error\ in\ percentage = \frac{I_{exp} - I_{Shoup-Szabo}}{I_{Shoup-Szabo}} \times 100\% \quad (3.3)$$

where I_{exp} is the experimentally measured current and $I_{Shoup-Szabo}$ is the predicted current which accounts for both linear and radial diffusional currents on the basis of Shoup-Szabo equation (i.e. Equation 3.2). In this system, with a downward orientation of the electrochemical interface and in which external causes of convection have been minimised the macro-electrode response can (within the uncertainty of the reported diffusion coefficient and electrode dimensions) be fully and accurately described by a diffusion only model.

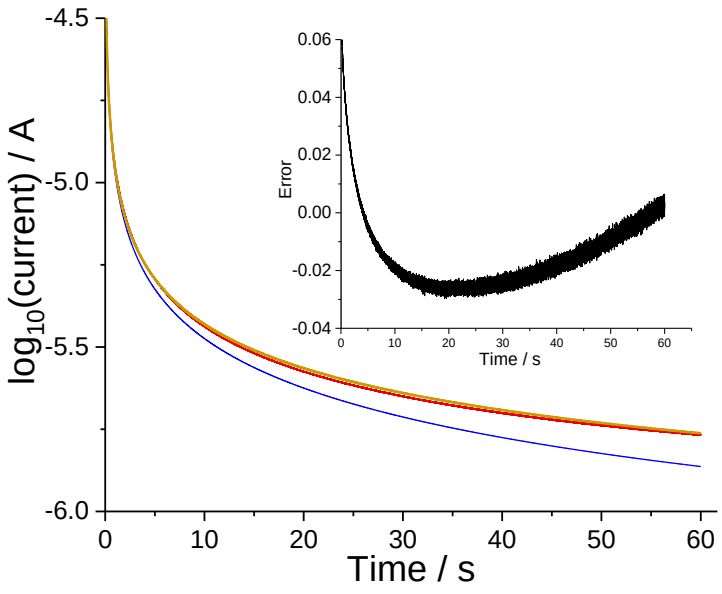


Figure 3.2 The experimentally recorded chronoamperometric response of a glassy carbon macrodisc electrode (red) (r = 0.15 cm) plotted against that predicted on the basis of the Cottrell (blue) and Shoup-Szabo equations (brown). Inlay in (a) depicts the error between the experimental (red) and simulated chronoamperometric response that predicted by the Shoup-Szabo (brown). The excellent agreement of the experimental data with the Shoup-Szabo equation highlights the importance of accounting for radial diffusion at this time scale even when using an electrode of millimetres in dimension. The experiment was run in a glass vial with 12 mL solution (1 mM $FcCH_2OH$ in 0.1 M KCl) at a constant applied potential of +0.35 V with the macroelectrode facing downwards.

It should be noted that the Shoup-Szabo equation is itself approximate being based on fitting to simulations and can be in error by up to 0.6%. Figure 3.3 below presents the plot of the normalised difference ($(I_{exp} - I_{sim})/I_{sim}$) of choronoamperometric response for the oxidation of 1 mM ferrocenemethanol at 25°C at a glassy carbon macroelectrode, where I_{exp} is the experimental measured current and I_{sim} is the simulated current response. The simulation was based on a two-dimensional microdisc model solved using the ADI method.[16] This result shows that with the consideration of radial diffusion, the

response on a macroelectrode can be predicted with an average error of 1.1%. Consequently, the inlay of Figure 3.2 marginally over-estimates the discrepancy between the experimental and theoretically predicted results.

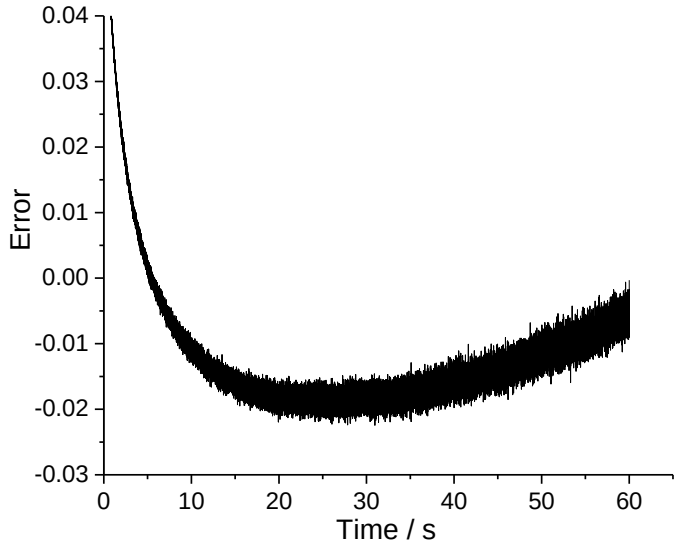


Figure 3.3 Error between the experimental and simulated chronoamperometric response in 1 mM ferrocenemethanol solution on a glassy carbon macroelectrode (3 mm in diameter). The error= $(I_{exp}-I_{sim})/I_{sim}$.

Convective effects on macroelectrode with different orientations An important question is to what extent may the orientation of the electrode affect this result? In order to study if and how the density driven natural convective flows influence the voltammetric response when the electrode changes its orientation, a screen-printed platinum electrode was used as the working electrode with its own reference and counter electrodes both covered with insulating tape. The detail of the cell design and the results for vertical electrodes are shown in Scheme 3.4. Figure 3.4 below presents the experimentally (red) recorded chronoamperometric response for the oxidation of 1 mM ferrocenemethanol at 25 ^{o}C at a vertical SPPE plotted against the predicted (brown) response on the basis of

Shoup-Szabo equation. The inlay shows the normalised difference (i.e. the error) of chronoamperometric response using Equation 3.2. The result shows that at long time scale (> 20 s), the current becomes larger compared to the predicted current, proving the existence of density driven convective flow. At 60 s, around 10% extra current was contributed from natural convection.

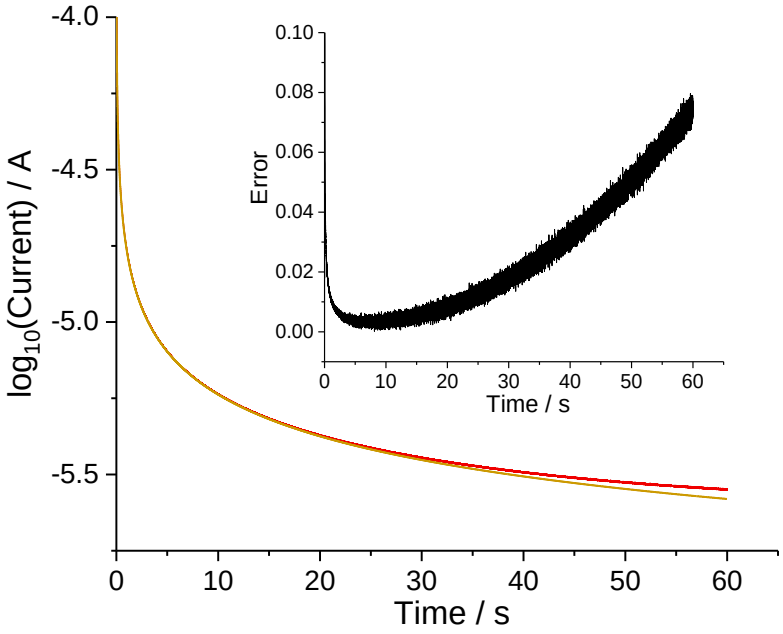


Figure 3.4 The experimentally recorded chronoamperometric response of a vertical SPPE (red) (r = 0.185 cm) plotted against that predicted on the basis of Shoup-Szabo equations (brown). Inlay in (a) depicts the error between the experimental (red) and simulated chronoamperometric response that predicted by the Shoup-Szabo equation (brown).

Briefly the results show that for the present experimental case (1mM ferrocene methanol aqueous solution with 0.1 M KCl) only in the situation in which the electrode is vertical (perpendicular to the gravitational field) is there an appreciable effect on the electrochemical response. As the electrochemical reaction proceeds it induces a change in density of the solution adjacent to the electrochemical interface causing convective

flows. In the case of a vertically orientated electrode this results in the mass-transport limited current being 10% greater than predicted current on the basis of Shoup-Szabo equation[14]. The influence of such electrochemical reaction induced convection will lessen as the size of the electrode decreases[9]. Consequently, the above 10% increase in current for a vertically orientated macroelectrode represents, in this work, a likely largest possible contribution for natural convection induced by the occurrence of the interfacial reaction. Hence, in the remainder of this work we continue by only considering the voltammetric contribution associated with bulk convection arising from thermal differences in the cell.

3.3.2 Evaporation effects on the voltammetric behaviour of a microcylinder electrode

We now turn to use a less 'conventional' electrode design; that of a micro-cylinder electrode. The reason for this choice will be evidenced below. Figure 3.5 presents the voltammetric response of carbon fibre microcylinder electrode (diameter = 7.0 μm and length 0.961 mm) towards the oxidation of ferrocenemethanol (1 mM) at a scan rate of 25 mV s^{-1} in both closed (Figure 3.5(a)) and open (Figure 3.5 (b)) cells. The microcylinder electrode is an interesting geometry for voltammetric experiments where, as is the case for band electrodes, due to the electrode being macroscopic in one dimension under diffusion only conditions the voltammogram does not reach a true steady state flux and in the mass-transport limit the current varies with the inverse of logarithmic time; this

leads to a peak shaped voltammogram.[17] Prior to recording the cyclic voltammograms presented in Figure 3.5 the cell was thermostated to 25 ^{o}C and allowed to equilibrate for a period of ca. 10 minutes. For a 'closed' voltammetric cell (one sealed to avoid evaporative losses) then the voltammetric response of the electrode was invariant with time (Figure3.5 (a)) and found to be within experimental error of that predicted for a diffusion only system (the simulated diffusion only response for this electrode is overlaid with the data in Figure 3.5 (b)). Conversely for the same electrode submerged in an 'open' cell (one in which the solution is free to evaporate), although the initial voltammetric scans are equivalent to that measured in a closed cell, at longer times ca. 45 minutes the voltammetric wave shape is altered and the current at high overpotentials (in the mass-transport limited region) increases. This increase in the current indicates that a process other than diffusion is contributing to the mass-transport limited flux of material to the electrode surface. By considering the magnitude of the increase in current to the micro-cylinder electrode shown in Figure 3.5(b), we can estimate that the solution phase velocity is of the order of 10 μm s^{-1} after 60 minutes. The velocity was estimated by measuring the current difference (I) between the blue and green curves and converted into the difference in the current density ($j = I/A$, where A is the electrode area) and dividing it by concentration (c) of the analyte (i.e. velocity = j/c). The rate of evaporation of water in an open cell was calculated to be in the order of 3×10^{-5} g s^{-1}; the corresponding percentage of concentration change of the bulk solution after one hour is estimated to be roughly 0.01% which is too small to show effect on the magnitude of the peak current.

Consequently the change in the voltammetric waveshape with time as shown in Figure 3.5 (b) is due to the increased mass transport of the materials resulting from convective flow.

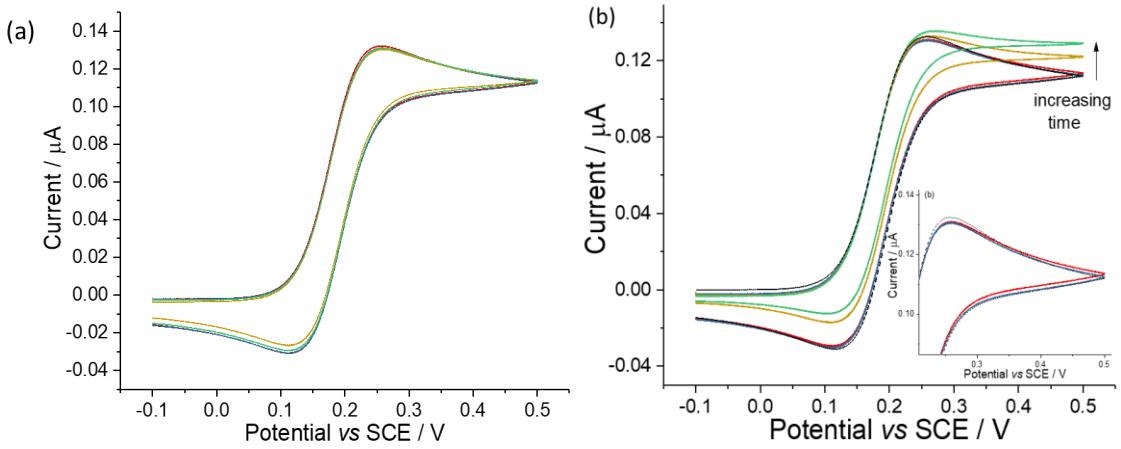


Figure 3.5 The oxidation of ferrocenemethanol (1 mM) at 25 °C at a carbon fibre micro-cylinder electrode (d= 7.0 µm, l = 0.92 mm) as a function of time in a cell (a) closed and (b) open to the environment at times after the cell has been brought to temperature, 25 minutes (blue), 45 minutes (brown), 60 minutes (green). The experimental voltammogram in a closed cell (red) and the simulated result (black dashed line) are also depicted for comparison. Inlay shows the zoom-in version of the comparison between the simulated voltammogram (black dashed line) and the experimental results. The experiment was run in a glass vial with 12 mL solution (1 mM $FcCH_2OH$ in 0.1 M KCl) at 25 mV s^{-1}.

Although a crude estimate this rate of flow is comparable to that previously predicted for bulk flows in this cell associated with thermal gradients induced by evaporative losses. Moreover, such evaporation of solvent in an open cell will not only induce convection in the bulk solution but drive convection in the air near the surface of the solution, which in turn will increase the evaporation. This conclusion that evaporation is leading to bulk convective flows and that it is these bulk flows that are altering the voltammetric response

is evidenced by the fact that the change in the voltammetric response is only observed when the cell is open to the environment. Consequently, we conclude that evaporative losses and the possible induced air movement above the surface of the solution from a cell can significantly influence the voltammetric response by changing the mass transport. A closed cell is suggested to be used in experiments to minimise such evaporation effect (but only once the vapour pressure above the solution reaches the saturated vapour pressure at 25^{o}C) and meanwhile to suppress any air movement above the solution.

3.3.3 Vibration effects on the voltammetric behaviour of a microcylinder electrode

The optimised thermostated electrochemical cell was used throughout the experiment to minimised the temperature difference between the normal water bath and the solution in the cell. In a conventional cell system the electrochemical cell is held in the water bath using a laboratory clamp held by a clamp stand in a Faraday cage; consequently the possible vibration of the clamp may be induced by putting the working electrode into the solution just before the measurement or the closure of the door of the Faraday cage, which may induce the external convection to the solution and further induce mechanical movement of the electrode during the measurement. Figure 3.6 shows how the voltammetric response varies with time in both cell conditions; the comparison between the experimental and simulated voltammograms is shown in Figure 3.7.

These results show that at short times in the conventional electrochemical system the microcylinder electrode exhibits a near steady state response (Figure 3.6 (a) red line),

over time (ca. minutes) the system stabilises towards a more peaked and hence more diffusional response. This behaviour is interpreted on the likely basis of the cell not being held fully rigidly in place despite being 'clamped' and as time goes on the vibration of the cell or the effect of vibration decreases minimising the magnitude of the convective contribution to the measured Faradaic current at high overpotentials. It is important to note that in this cell design where a water bath has been used to control the temperature the voltammetric response, even at long times, does not become purely diffusional as evidenced through comparison of the voltammetric waveshape with that predicted by numerical simulation (DigiSim; see experimental section) as shown in Figure 3.7.

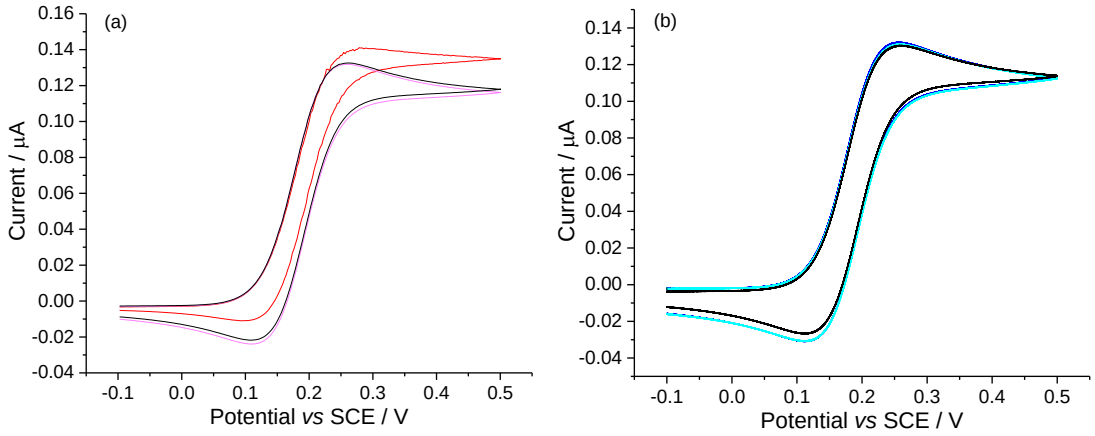


Figure 3.6 The oxidation of ferrocenemethanol (1 mM) at 25°C at a carbon fibre microcylinder electrode (r=3.5 µm, l=0.916 mm) as a function of time in a closed cell in (a) conventional water bath system (clamp stand) and (b) optimised thermostated electrochemical cell at 25 mV s^{-1}. In Figure (a), the red, magenta and gray curves represent the voltammograms at the time of 0 s, 600 s and 1200 s respectively. In figure (b), blue, cyan and black curves represent the voltammograms at the time of 0 s, 600 s and 1200 s respectively.

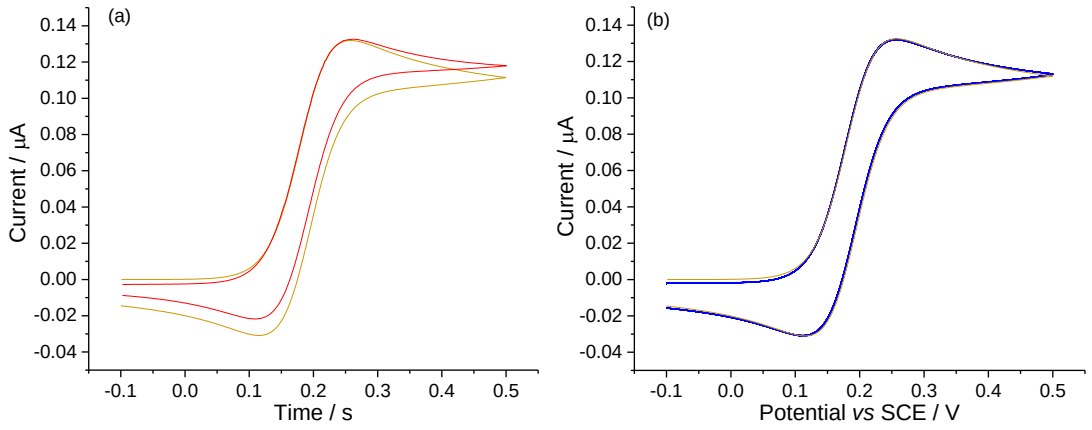


Figure 3.7 Comparison of experimental (red in (a), blue in (b)) and simulated (yellow) voltammograms for a carbon fibre microcylinder electrode in (a) water bath and (b) optimised thermostated electrochemical cell. The brown curves were obtained from simulation. Parameters in the simulation: ν=25 mV s^{-1}; temperature T=25 ^{o}C; formal potential E^{o}=0.1872 V; k^{0}=10 m s^{-1}; D=7.81×10^{-10} m^{2} s^{-1}; $\alpha_a=\alpha_c$=0.5; r=3.5µm, length of the electrode l=0.092 cm.

It is useful at this stage to consider some results previously presented in the literature. Amatore et al.[18] reported experiments conducted in a cell (a microscope petri dish) with no thermostating and which was 'open' to the environment allowing evaporative losses. In their work chronoamperometry was semi-empirically modelled using a distance dependent effective diffusion coefficient (which scaled with the 4th power of the normal distance from the electrode surface)[19]. First, the magnitude of the reported distance dependent diffusion coefficients allow the back calculation and estimation of the speed of the convective eddies; these estimates are consistent with the magnitude for the flow simulated as described above.[6, 20] Second, the work explicitly did not consider the influence of radial diffusion on the chronoamperometric response and at least 50% of their 'measured' discrepancy can be understood on the basis of a diffusion only mass-transport model which fully accounts for this additional flux. In Amatore et al's paper, an

elliptic Pt disk of 1.2 mm equivalent diameter obtained from the slant cross-section (45^{o}) of a 1 mm diameter platinum wire was used.[21] Here we use a 'elliptic disk' model adapted from Dudko et al's paper[22] to predict the chronoamperometric response. These results should be compared to Figure 4 in Amatore's paper[23], the difference between the theoretical (with radial diffusion) and Cottrellian chronoamperometric responses in Figure 3.8 (below) shows that the radial diffusion is likely important in their experimental setup and should have been considered. These results indicate that at least 50% of their measured current discrepancy can be understood in terms of the radial diffusion contribution. However, we speculate the remaining 'missing' current may be due to a) evaporative losses causing bulk fluid motion b) electrode vibrations or c) 'spontaneous' convection as defined by Levich i.e. convection arising due to density changes associated with the occurrence of the electrochemical reaction. We note that Amatore et al. do discuss the latter point but do not provide evidence that such convection is not operative.

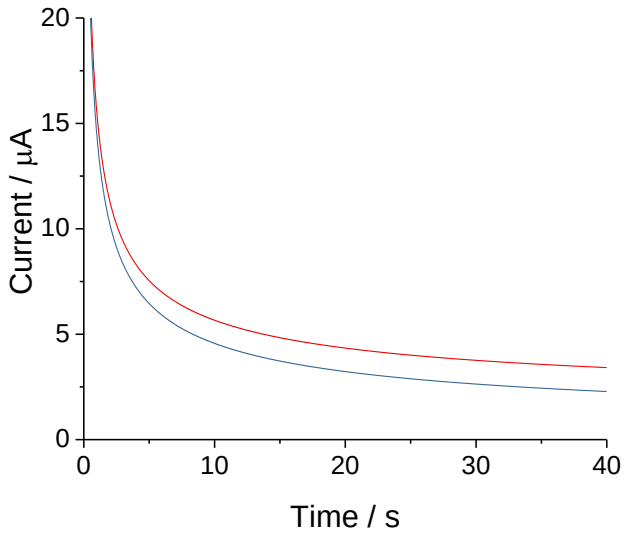


Figure 3.8 The comparison between the predicted chronoamperometric response from (blue) Cottrell equation and (red) the 'elliptic disk' equation taken from Dudko et al's paper[22]. All parameters used were the same as those in Amatore et al's paper: $D(Fe(CN)_6^{4-}) = (5.7 \pm 0.5) \times 10^{-10}$ m^2 s^{-1}, concentration c = 10 mM.

Further work in the literature[23] suggests that beyond forced and density (aka gravitationally) driven convection an additional microscopic convection model needs to be considered to understand natural convection in electrochemical systems. We note however that first, "a spontaneous excitation of internal convection cannot be generated from a state at rest in a system which is at thermodynamic equilibrium",[24] the 'spontaneous' natural convection discussed by Levich[5] arises due to the occurrence of an electrochemical reaction (i.e. it is induced by the system being in a non-equilibrium state). Moreover, the experimental results we present in Figure 3.2 clearly demonstrate that for the electrode orientation used relative to the gravitational field (downward), analyte identity and concentration and, where external influences such as vibrations and non-perfect thermostating have been minimised, then over a timeframe of 60 seconds at

a macro-electrode, no other mass-transport mechanism need be invoked to explain the results. Furthermore nor do distance dependence diffusion coefficients represent physical reality but merely attempt to parameterise the transition from stagnant to density driven convection zone. The results shown in Figure 3.5 demonstrate how convection can be induced to occur, due to the influence of the external environment on the cell causing evaporative losses.

It is on the basis of such literature experiments[18a, 23] into convection that a categorisation of electrodes as either being 'microelectrodes' or 'ultra-microelectrodes' has been previously proposed.[21] Zonal diagrams were produced to reportedly define the behaviour of an electrochemical system. Succinctly it was suggested that larger electrodes are more sensitive (in terms of their measured voltammetric response) towards natural convection than smaller ones. Here we ask, to what extent is this generally true?

3.3.4 Effect of natural convection on different electrode geometries

In order to reproducibly and controllably create a density gradient in the electrochemical cell the system was first thermostated and allowed to equilibrate. Having attained a near quiescent system the thermostat temperature was increased by one degree Celsius. In the present experimental system a Peltier heat pump is used to control the thermostat temperature. This temperature jump method will necessarily induce convective flows in the electrochemical cell which are likely of the order of 1 mm s^{-1}.[12] Figure 3.9 presents the recorded voltammetric response for four different electrode types towards the

oxidation of ferrocenemethanol prior to (red line) and immediately after (blue line) the onset of the temperature jump. Over the course of the voltammetric experiment the solution phase temperature, as recorded in-situ by a thermocouple, was raised by approximately one degree Celsius, note however, under these conditions the solution phase temperature in the cell is heterogeneous. Figure 3.9 a) and b) present the voltammetric responses for a macroscopic (d = 2.98 mm) and a microscopic (d = 33 μm) disc electrodes where both electrodes are inlaid in a non-conductive support (support diameters of 6.0 and 3.5 mm). The voltammetric response of neither electrode is particularly altered by the change in the systems thermostating or hence the induced convection. Conversely Figure 3.9 c) and d) depicts the voltammetric response of a carbon fibre microcylinder electrode and a carbon fibre micro tip electrode. Importantly the carbon fibre electrode (Figure 3.9 d) is only surrounded by a thin glass sheath (~0.4 μm). The various electrode geometries used are outlined schematically in Figure 3.9. The voltammetric responses of both electrodes (c and d) are markedly altered by the change in the thermostating conditions. Moreover, the increase in the mass-transport limited current cannot be rationalised in terms of the diffusion coefficient of ferrocenemethanol. For a one degree Celsius change in the solution temperature the diffusion coefficient of ferrocenemethanol is only anticipated to increase by ca. 2.5 %.[25]

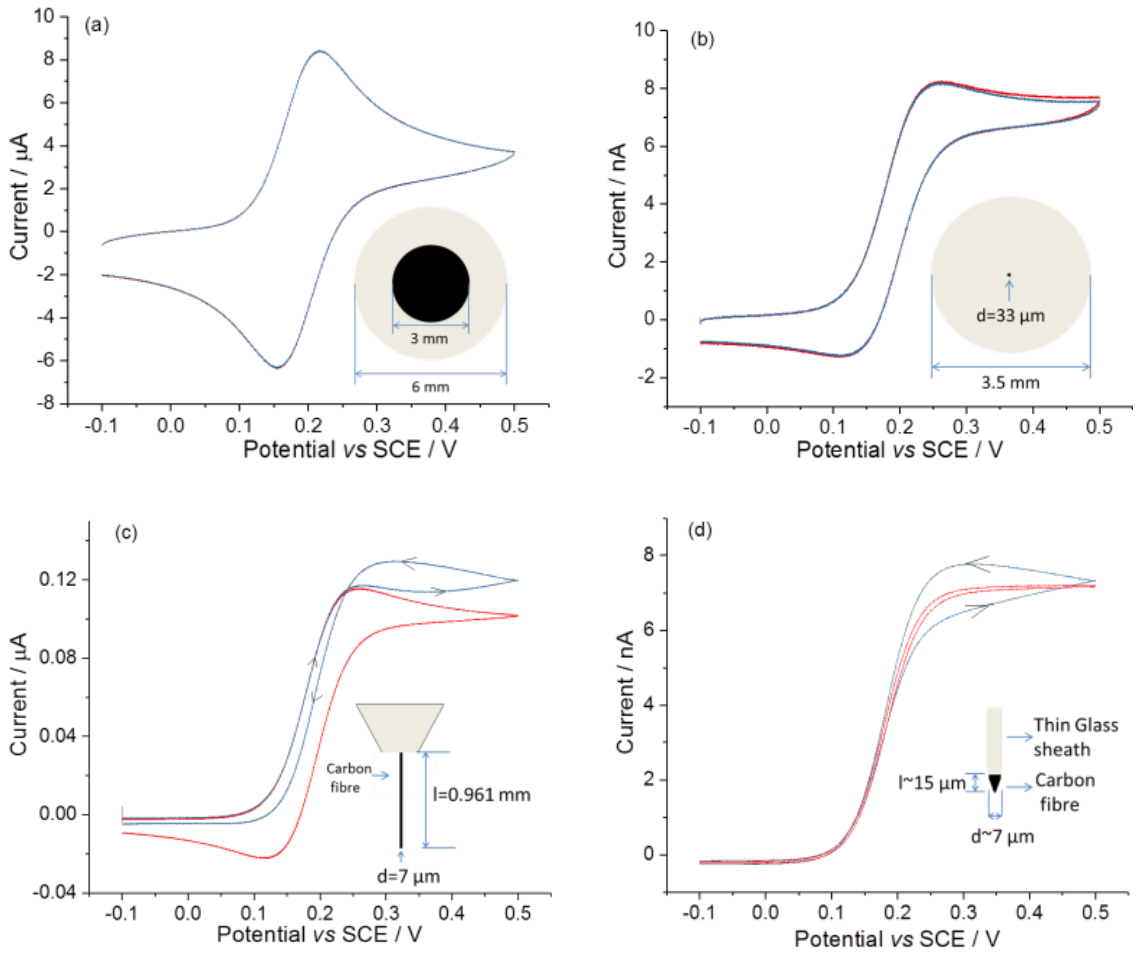


Figure 3.9 Effect of temperature change on the voltammograms for (a) macroelectrode, (b) commercial carbon microdisc electrode, (c) carbon fibre microcylinder electrode and (d) carbon fibre tip electrode. Macroelectrode used in (a) is glassy carbon electrode with a diameter of 3 mm. Commercial carbon microdisc electrode used in (b) is 33 µm in diameter. The carbon fibre used in (c) and (d) are 7 µm in diameter. The red curves represent for the voltammograms at a constant temperature (20 ^{o}C), and the blue curves represents for the voltammograms at each electrode with a temperature jump. Inlays in each figure represent the schematic of each electrode. The experiments were run in a glass vial with 12 mL solution (1 mM $FcCH_2OH$ in 0.1 M KCl) at 25 mV s^{-1}.

The above results directly point to the importance of the electrode surround in altering the convective profile near the electrode which influences the mass-transport environment local to the electrochemical interface. The solution phase velocity at a solid surface is

necessarily zero (no slip boundary) and a microelectrode inlaid in a relatively large glass sheath is essentially shielded from the bulk convective flows. Microelectrodes that are inlaid in non-conductive glass sheaths are less sensitive to bulk convective flows as compared to macroelectrodes (that are also inlaid in a non-conductive surface). This however does not mean that microelectrodes are inherently immune to such flows; it is the non-conducting support structure that creates a larger stagnant layer adjacent to the electrochemical interface. The notion of a bulk solution in which there is significant mixing, promoted by density differences, and which is separated from a surface by a stagnant diffusion layer is of course the physical basis for the simple Nernst diffusion layer model dating from 1904.[1] But the above results demonstrate more broadly that this stagnant layer thickness is sensitive to the local environment; the mass-transport to and from a point on a non-reactive surface will, in terms of the influence of convection, differ from that of an isolated point in solution.

It is important to recognise that microelectrodes that are not encased in large insulating surfaces are routinely used in electrochemical experiments. Such electrodes are often employed for example as probe electrodes in scanning electrochemical microscopy (SECM) and other analytical contexts. Consequently, if such ‘unsheathed’ microelectrodes are in bulk solution then depending on the local convective environment the measured steady-state current may differ significantly from that of a diffusion only model. This has two potential implications: first, the accurate calibration of such electrodes may be challenging; second, in experimental setups where the electrodes

distance from an interface is varied, such as an approach curve, the influence of convection on the measured electrochemical response will vary as a function of the electrode/surface separation. Therefore, the careful and rigorous[26] thermostating of electrochemical systems using such unsheathed microelectrodes is a likely necessary requisite.

In summary, convection in electrochemical systems can significantly influence the voltammetric response. Generally convection is classified as either forced or natural. Forced convection induced by deliberate flowing, vibrating or rotating of the electrode is a routinely used method to enhance the rate of mass-transport to an electrochemical interface. However, in the absence of deliberately induced convection it is common for an electrochemical system to be interpreted solely on the basis of a diffusion-only model. However, there are a number of mechanisms that may still lead to the convective movement of the solution in an electrochemical cell. First, there may be sources of external adventitious forced convection, a prime example being vibrations arising from the laboratory environment. Such unintentional sources of forced convection can be, as is done in this work, often easily and sufficiently minimised by firmly securing the cell and damping local vibration sources. More complex is the issue of so-called natural convection. Natural convection is a broad term encompassing a number of physical phenomena. Generally natural convection refers to gravitationally driven convection resulting from local density differences in the solution. As outlined by Levich[5] such density differences may be driven by the occurrence of the electrochemical reaction itself,

arising either due to the reaction enthalpy or molar volume change associated with the electrochemical reaction.

3.4 Conclusions

In this work we use low (millimolar) concentrations of the electroactive analyte and demonstrate experimentally that for the orientation (horizontally facing downward) of the electrode the influence of natural convection induced by the change in enthalpy or the reaction molar volume of the electrochemical reaction itself only contributes minimally to the observed voltammetry. Consequently, having minimised and controlled all other sources of forced and natural convection this allows us to investigate to what extent thermally induced natural convection can be important in such voltammetric measurements. We demonstrate how imperfect thermostating of an electrochemical cell can and does lead to significant density driven convective flows. These convective flows may influence an electrochemical response of a system by altering the mass-transport regime. This convection can be driven simply by the evaporative loss of solution from an electrochemical cell which is open to the environment. The use of distance dependent diffusion coefficients to model the effects of convection in an electrochemical cell, as employed in the literature, is cautioned against on conceptual, theoretical[24] and experimental bases.

Importantly, we show how the sensitivity of an electrode towards convective flows in the bulk solution is not just a function of the electrodes size but is also importantly influenced

by the size and geometry of the non-conductive support surrounding the electrode. The sensitivity of a microelectrode towards bulk convective flows is less if the electrode is inlaid into a large macroscopic surface. The surrounding substrate serves to shield the electrode and creates a larger stagnant layer near the reactive interface. This highlights a general insight that unsheathed microelectrodes i.e. ones that are not embedded in a large non-conductive support surface are generally more sensitive to solution phase convection. This has potential implications for a variety of experimental systems that used such unsheathed electrodes; highlighting a source of irreproducibility that is generally not considered.

References:

[1] W. Nernst, *Z. Phys. Chem.* **1904**, *47U*, 52.

[2] D. Li, C. Batchelor-McAuley, L. Chen, R. G. Compton, *Physical Chemistry Chemical Physics* **2019**, *21*, 9969-9974.

[3] R. G. Compton, C. E. Banks, *Understanding Voltammetry*, 3rd ed., World Scientific Publishing Company Pte Limited, **2018**.

[4] Á. Molina, J. González, *Pulse Voltammetry in Physical Electrochemistry and Electroanalysis: Theory and Applications*, Springer International Publishing, **2015**.

[5] V. G. Levich, *Physicochemical Hydrodynamics: (by) Veniamin G. Levich. Transl. by Scripta Technica, Inc*, Prentice-Hall, **1962**.

[6] J. K. Novev, S. Eloul, R. G. Compton, *J. Phys. Chem. C* **2016**, *120*, 13549-13562.

[7] aG.-U. Flechsig, *Curr. Opin. in Electrochem.* **2018**, *10*, 54-60; bP. Gründler, *In-situ Thermoelectrochemistry: Working with Heated Electrodes*, Springer Berlin Heidelberg, **2015**; cP. Gründler, D. Degenring, *J. Electroanal. Chem.* **2001**, *512*, 74-82; dP. Gründler, G.-U. Flechsig, *Microchimica Acta* **2006**, *154*, 175-189; eP. Gründler, T. Zerihun, A. Möller, A. Kirbs, *J. Electroanal. Chem.* **1993**, *360*, 309-314; fA. S. Baranski, *Anal. Chem.* **2002**, *74*, 1294-1301; gF. Marken, Y.-C. Tsai, B. A. Coles, S. L. Matthews, R. G. Compton, *New J. Chem.* **2000**, *24*, 653-658; hA. Boika, A. S. Baranski, *Anal. Chem.* **2008**, *80*, 7392-7400; iJ. Wang, P. Gründler, G.-U. Flechsig, M. Jasinski, G. Rivas, E. Sahlin, J. L. Lopez Paz, *Anal. Chem.* **2000**, *72*, 3752-3756.

[8] K. Ngamchuea, S. Eloul, K. Tschulik, R. G. Compton, *Anal. Chem.* **2015**, *87*, 7226-7234.

[9] X. Gao, J. Lee, H. S. White, *Anal. Chem.* **1995**, *67*, 1541-1545.

[10] T. M. Squires, M. Z. Bazant, *J. Fluid Mech.* **2004**, *509*, 217-252.

[11] aJ. K. Novev, R. G. Compton, *Phys. Chem. Chem. Phys.* **2017**, *19*, 12759-12775; bJ. K. Novev, R. G. Compton, *Phys. Chem. Chem. Phys.* **2016**, *18*, 29836-29846.

[12] X. Li, C. Batchelor-McAuley, J. K. Novev, R. G. Compton, *Phys. Chem. Chem. Phys.* **2018**, *20*, 11794-11804.

[13] aM. Rudolph, *J. Electroanal. Chem. Interfacial Electrochem.* **1991**, *314*, 13-22; bM. Rudolph, *J. Electroanal. Chem.* **1992**, *338*, 85-98; cM. Rudolph, *J. Electroanal. Chem.* **1994**, *375*, 89-99.

[14] D. Shoup, A. Szabo, *J. Electroanal. Chem. Interfacial Electrochem.* **1982**, *140*, 237-245.

[15] K. Ngamchuea, C. Lin, C. Batchelor-McAuley, R. G. Compton, *Anal. Chem.* **2017**, *89*, 3780-3786.

[16] R. G. Compton, E. L. Laborda, K. R. Ward, *Understanding Voltammetry: Simulation Of Electrode Processes*, World Scientific Publishing Company, **2013**.

[17] A. J. Bard, L. R. Faulkner, *Electrochemical Methods: Fundamentals and Applications, 2nd Edition*, John Wiley & Sons, **2000**.

[18] aC. Amatore, S. Szunerits, L. Thouin, J. S. Warkocz, *Electroanalysis: An International Journal Devoted to Fundamental and Practical Aspects of Electroanalysis* **2001**, *13*, 646-652; bN. Baltes, L. Thouin, C. Amatore, J. Heinze, *Angewandte Chemie International Edition* **2004**, *43*, 1431-1435.

[19] A questionable consequence of this approach is that diffusion coefficients measured electrochemically may not quantitatively agree with those made by other 'bulk' measurement techniques such as conductance.

[20] J. K. Novev, R. G. Compton, *Curr. Opin. in Electrochem.* **2018**, *7*, 118-129.

[21] C. Amatore, C. c. Pebay, L. Thouin, A. Wang, J. S. Warkocz, *Analytical chemistry* **2010**, *82*, 6933-6939.

[22] O. K. Dudko, A. Szabo, J. Ketter, R. M. Wightman, *Journal of Electroanalytical Chemistry* **2006**, *586*, 18-22.

[23] C. Amatore, S. Szunerits, L. Thouin, J.-S. Warkocz, *J. Electroanal. Chem.* **2001**, *500*, 62-70.

[24] P. Glansdorff, I. Prigogine, *Thermodynamic Theory of Structure, Stability and Fluctuations*, Wiley, **1971**.

[25] The diffusion coefficient is inversely proportional to the dynamic viscosity of the liquid. The percentage difference in diffusion coefficient was calculated using the inverse ratio of viscosity of water at 20 degree Celsius to viscosity at 21 degree Celsius.

[26] D. Schäfer, A. Puschhof, W. Schuhmann, *Phys. Chem. Chem. Phys.* **2013**, *15*, 5215-5223.

Chapter 4

Tafel Analysis under Different Electrode Geometries

Tafel analysis is a basic and powerful tool to extract kinetic information from measured voltammograms. In this chapter voltammetric waves under five different mass-transport regimes (macroelectrode, microdisc, micro-hemisphere, micro-hemicylinder and single microband) for an irreversible one electron transfer process were simulated and analysed to find the appropriate Tafel region for accurate analysis. The transfer coefficient was found to deviate significantly from its true value as a function of potential in all cases due to the influence of mass-transport. If and how a simple analytical mass-transport correction in which the current is corrected for the change in the reactant concentration at the surface can be used to improve the measurement of transfer coefficient were investigated. It is shown that this correction is only rigorously valid for a uniformly accessible microelectrode under a true steady-state condition. This translates to hemispherical electrodes only of the set of five considered. The fraction of the current used in Tafel analysis (Tafel region) can be increased to around 50% for quasi-steady state regimes (hemi-cylindrical and single band electrodes) with this analytical correction but it completely failed in linear diffusion regimes (macroelectrodes). In the latter case an improved empirical correction is suggested.

This work presented in this chapter has been published as a first author paper in *Journal of Electroanalytical Chemistry*[1] and was carried out in collaboration with Dr. Chuhong Lin, Dr. Christopher Batchelor-McAuley and Mr. Lifu Chen.

4.1 Introduction

Voltammetric experiments can yield significant thermodynamic and kinetic information.[2] However, due to the convolution of the time and energy domains extraction of this data is often non-facile. In many cases measurement of the related physico-chemical parameters may only be fully achieved through simulation of the system. Notwithstanding this, due in part for ease and expediency, it is very common for voltammetric experiments to be analysed using mathematically analytical procedures. Of these analytical methods, Tafel analysis is a cornerstone of the electrochemist's tool box. Tafel analysis of a voltammogram yields a measure of the electrochemical system's transfer coefficient[3]. First, under appropriate conditions, the transfer coefficient can provide information regarding the electrochemical mechanism[4]. Classically, Tafel analysis has been used to great effect in the analysis and elucidation of the catalytic activity of various metal surfaces towards the hydrogen evolution reaction[5]. Second, for irreversible voltammetry at a macroelectrode (linear diffusion regime) the transfer coefficient needs to be known in order for the species diffusion coefficient to be accurately determined[6].

The transfer coefficient is a dimensionless parameter and describes how the rate of an interfacial oxidation or reduction reaction varies as a function of the applied potential, under the caveat that the concentration of the reactant at the electrode surface is unaltered from its value in bulk solution. The physical interpretation of the transfer coefficient is often dependent upon the assumption of an underlying electrochemical mechanism. Moreover, for electrochemical processes involving the transfer of multiple electrons and/or the formation and breaking of chemical bonds (i.e. processes comprised of multiple sequential elementary steps) the interpretation of the transfer coefficient is not straightforward[7]. However, for a simple and single electron transfer process the transfer coefficient is commonly qualitatively interpreted being a measure of the 'position' of the transition state[6], where a transfer coefficient close to unity implies the transition state is 'reactant-like' and similarly a value close to zero implies a 'product-like' transition state for an oxidative process.

The Butler-Volmer equation is a phenomenological description of the rate of an interfacial redox reaction where the reaction rate increases exponentially as a function of the applied potential. In this framework it is commonly assumed that the transfer coefficient is a constant and independent of the applied potential. In contrast Marcus-Hush theory[8] provides a microscopic model of an interfacial electron transfer process, here the rate of the reaction is rationalised in terms of the reaction Gibbs energy and a reorganisation energy[9]. The reorganisation energy is related to the energy required to distort the reactant molecule and its solvation shell to those of the product. Commonly,

the force constants for the reduced and oxidised species are assumed to be equal (symmetric): this is equivalent to assuming that at low overpotentials that the transfer coefficient has a value of 0.5. However, even for many apparently outer-sphere redox processes the transfer coefficient is found to deviate from 0.5[10]. Relaxation of the assumption of equal force constants, allows (asymmetric) Marcus-Hush theory to be reconciled with the Butler-Volmer equation[11]. The latter can be viewed as a good approximation of the former at low overpotentials and the transfer coefficient can be quantitatively interpreted as reflecting the asymmetry in the force constants for the reduced and oxidised species.

For both the symmetric and asymmetric forms of Marcus-Hush theory, these microscopic theories predict a deviation of the reaction rate from exponentially increase at high overpotentials; ultimately the rate becomes independent of the applied potential, becoming mass-transport controlled. The predicted deviation away from exponentially increasing reaction rate may be expressed as a potential dependent transfer coefficient (or equivalently as a 'curved' Tafel slope). The experimental reporting of such curved Tafel slopes and potential dependent transfer coefficients have historically[12] played an important role in validating and advancing our physical insight into this class of heterogeneous reactions. However, during the course of a voltammogram the reactant rapidly becomes depleted at the electrode surface and the rate determining step becomes the mass-transport of material to the electrode surface. Consequently, before interpreting an experimental Tafel plot and the associated transfer coefficient it is important to

quantify over what range of voltammetric currents can the voltammogram be directly analysed within the Butler-Volmer approach to yield an accurate measure of the transfer coefficient? A further issue is to what extent can the depletion of the reactant be corrected for using analytical approximations? The present work in this chapter addresses and answers these two questions.

4.2 Background theory

4.2.1 Butler-Volmer kinetics

We consider the following one electron transfer oxidative process under different mass-transport geometries:

$$A \rightleftarrows B + e^- \tag{4.1}$$

where the reactant and product in the process are assumed to have equal diffusion coefficients with only reactant present in bulk solution.

Butler-Volmer (BV) theory is experimentally the most commonly used kinetic model.[13] According to BV theory, the oxidative and reductive rate constants ($k_a,\ k_c$) are functions of the transfer coefficients, the standard rate constant k^0 and the formal potential E_f^0[6]:

$$k_a = k^0 exp\left[\alpha_{a,BV}\theta\right] \tag{4.2}$$

$$k_c = k^0 exp\left[-\alpha_{c,BV}\theta\right] \tag{4.3}$$

where the anodic transfer coefficient $\alpha_{a,BV}$ and the cathodic transfer coefficient $\alpha_{c,BV}$ are between 0 and 1, $\alpha_{a,BV} + \alpha_{c,BV} = 1$, and θ is the dimensionless potential given by:

$$\theta = \frac{F}{RT}\left(E - E_f^0\right) \tag{4.4}$$

where E is the potential of the working electrode, F is the Faraday constant (96485 C mol^{-1}), R is the gas constant (8.314 J mol^{-1} K^{-1}) and T is the temperature in K. $\alpha_{a,BV}$ and $\alpha_{c,BV}$ are commonly assumed to be independent of potential.

4.2.2 Tafel analysis

The International Union of Pure and Applied Chemistry (IUPAC) formally defines the anodic and cathodic transfer coefficients as being experimentally determined values and given by[3]:

$$\alpha_a = \frac{RT}{F}\left(\frac{dln j_{a,corr}}{dE}\right) \tag{4.5}$$

$$\alpha_c = -\frac{RT}{F}\left(\frac{dln|j_{c,corr}|}{dE}\right) \tag{4.6}$$

where $j_{a,corr}$ and $j_{c,corr}$ are the anodic and cathodic current densities corrected for any changes in the reactant concentration at the electrode surface with respect to its bulk value. The definitions avoid the need for any knowledge of the overall number of electrons transferred.

If a process is considered to be fully irreversible, for an oxidative process, when the applied potential is sufficiently far from the equilibrium potential E_{eq}, it is possible to

neglect the flux contribution from the reduction. Hence, the electrochemical flux can be expressed as:

$$j_a = k_a[A]_0 = k^0 exp\left[\frac{\alpha_a F(E-E_f)}{RT}\right][A]_0 \quad (4.7)$$

where j_a is the experimentally measured anodic flux density and $[A]_0$ is the concentration of the reactant at the electrode surface, which is typically different from that in bulk solution except close to the 'foot' of the voltammetric wave. Due to the sensitivity of j_a to $[A]_0$, surface depletion of the reactant inherently leads to a mass-transport limitation of the measured current.

This anodic electrochemical flux I_a can be directly related to the measured current by:

$$I_a = \int F j_a dA \quad (4.8)$$

By combining Equations 4.7 and 4.8, rearranging and assuming the flux is uniform across the electrode surface, we get the expression:

$$\ln|I_a| = \frac{\alpha_a F(E-E_f^0)}{RT} + ln(FAk^0[A]_0) \quad (4.9)$$

Consequently, if $[A]_0$ does not deviate significantly from its bulk value, a plot of $\ln|I_a|$ versus E yields a straight line with a gradient proportional to α_a. Hence plots of $\ln|I|$ versus E are commonly used to extract the transfer coefficient from voltammetric data and are referred to as '*Tafel plots*'. The resulting line of best fit will yield a measure of the transfer coefficient averaged over a range of potentials. However, mirroring the

IUPAC recommendations, if the plot is curved, the transfer coefficient can be defined as a function of potential.

Problematically, implementation of Equations 4.5 and 4.6 requires precise knowledge of the mass-transport regime to allow the flux to be suitably corrected for deviations in the surface concentration of the reactant. Consequently, for expediency and/or due to the lack of knowledge regarding the nature of the mass-transport regime (in contrast to Equations 4.5 and 4.6), the experimentally accessible parameters are:

$$\frac{RT}{F}\frac{dlnI_a}{dE} = \alpha_{a,nc} \tag{4.10}$$

$$-\frac{RT}{F}\frac{dln|I_c|}{dE} = \alpha_{c,nc} \tag{4.11}$$

where I_c is the experimentally measured cathodic current, $\alpha_{a,nc}$ and $\alpha_{c,nc}$ are the non-mass-transport corrected or 'apparent' transfer coefficients. The transfer coefficient α_{nc} may deviate from its true value α_a due to the local depletion of reagents at the electrochemical interface. However, at low current densities (i.e. $I \to 0$), $\alpha_{nc} \to \alpha$.

It is useful to comment that Tafel plots ($\ln|I|$ versus E) as used in this work differ from its historical form (overpotential η versus $log_{10}I$) as measured from galvanostatic experiments. The classically defined Tafel slope with the unit as mV per decade of current is directly related to the transfer coefficient ($Tafel\ slope = 2.3RT/\alpha_a F$). For example, α_a = 0.5 is equivalent to the Tafel slope of ca. 118 mV per decade. In this work, potentiostatic control is assumed, and consequently it is appropriate to define the Tafel plot as $\ln|I|$ versus E, the slope of which is proportional to the transfer coefficient.

4.2.3 Mass-transport corrected Tafel analysis

Correction of the current or flux to account for the change in the reactant concentration at the surface requires knowledge of the mass-transport regime. Such corrections may be achieved through numerical simulation using the experimentally measured current as a boundary condition[2b]. However, it is far more common to use an analytical expression to provide an approximate mass-transport correction[6, 14].

The analytical expression is based on the assumption of a uniformly accessible microelectrode, where a true steady state can be attained after sufficient long time. Under these conditions, for a fully irreversible electrode process, the flux can be expressed via the Nernst diffusion layer approximation, where the diffusion layer thickness δ is often taken as invariant with time[6, 15] and is:

$$j_a = D\left(\frac{[A]_0 - [A]_{bulk}}{\delta}\right) \tag{4.12}$$

Under BV theory, the analytical expressions describing mass-transport corrected transfer coefficients α' are:

$$-\frac{RT}{F}\frac{dln\left(\frac{1}{I_a}-\frac{1}{I_{lim}}\right)}{dE} = \alpha_a{}' \tag{4.13}$$

$$\frac{RT}{F}\frac{dln\left|\frac{1}{I_c}-\frac{1}{I_{lim}}\right|}{dE} = \alpha_c{}' \tag{4.14}$$

where I_{lim} is the mass-transport limiting current and $\alpha_a{}'$ and $\alpha_c{}'$ are the measured analytically mass-transport corrected anodic and cathodic transfer coefficients,

respectively. The full deviation of these expressions is presented in the Appendix A Section A1.

Ideally, α' should have the same value as α after mass-transport correction. However, this analytical mass-transport correction as a result of the breakdown of the assumptions made in its derivation is not applicable in all cases. Therefore, α' is considered as an analytical *approximation* to the mass-transport corrected transfer coefficient. A linear relationship of $\ln\left|\frac{1}{I}-\frac{1}{I_{lim}}\right|$ with the dimensionless potential θ is expected when the assumptions are met.[16] In this work, the extent to which how accurate the analytically mass-transport corrected Tafel analysis is under different diffusion geometries is studied.

4.3 Numerical simulation procedures

The commercially available simulation software DigiSim® is used to simulate the one-dimensional (1D) diffusion models. It is based on a fully implicit finite difference (IFD) algorithm suggested by Manfred Rudolph[17] and it allows simulations for a wide range of mechanisms.

The voltammetric response on a 2D diffusion microdisc electrode is simulated using a home-written programme which is based on the conformal mapping of the spatial coordinates and uses an exponentially expanding time grid.[18]

Although the current at a microband electrode is often approximated by a hemicylinder of equivalent area ($r = w/\pi$, where r is the radius of the hemicylinder and w is the

width of the band), there is no true equivalence between these two geometries[19]. Consequently, a bespoke programme for single microband simulation was written by Dr Chuhong Lin. The geometry of the microband electrode is shown in Figure 4.1 (a). As the length of the microband is assumed to be macroscale, the diffusion in the y dimension can be regarded constant and only the coordinates *x* and *z* are considered in the simulation. The two-dimensional simulation model is shown in Figure 4.1 (b). The concentration distribution of the reactant as a function of time and space is calculated via solving the diffusion equation coupled with boundary conditions as shown in Figure 4.1 (b). In this work, dimensionless parameters are applied. The transformation between the dimensional and dimensionless parameters is listed in Table 4.1. The diffusion coefficients of the redox couples are assumed to be the same and initially there is only the reactant in bulk solution. The boundary condition at the microband electrode is the BV equation and can be written as:

$$\frac{\partial C}{\partial Z} = K^0 exp(\alpha_a \theta) C - K^0 exp(-\alpha_c \theta)(1 - C) \tag{4.15}$$

where $\alpha_a + \alpha_c = 1$[3]. K^0 is the dimensionless format of the standard electrochemical rate constant. The dimensionless overpotential θ is the difference between the applied potential on the electrode and the formal potential of the redox reaction. To simulate the cyclic voltammetry, the applied potential is defined as a function of the scan rate as:

$$\theta = \begin{cases} \theta_i + \sigma\tau & \tau \leq \frac{\theta_f - \theta_i}{\sigma} \\ \theta_f - \sigma\left(\tau - \frac{\theta_f - \theta_i}{\sigma}\right) & \tau > \frac{\theta_f - \theta_i}{\sigma} \end{cases} \tag{4.16}$$

$[\theta_i, \theta_f]$ is the potential window in the cyclic voltammetry. For the oxidative reaction discussed in this work, $\theta_i < \theta_f$. The current J measured on the microband electrode is calculated from the concentration gradient on the electrode surface:

$$J = 2\int_0^1 \frac{\partial C}{\partial Z} dX \tag{4.17}$$

The theoretical model is numerically solved by the finite difference method and the alternating direction implicit (ADI) method[20]. The simulation program is written in Matlab R2017a and run on an Intel(R) Xeon(R) 3.60G CPU.

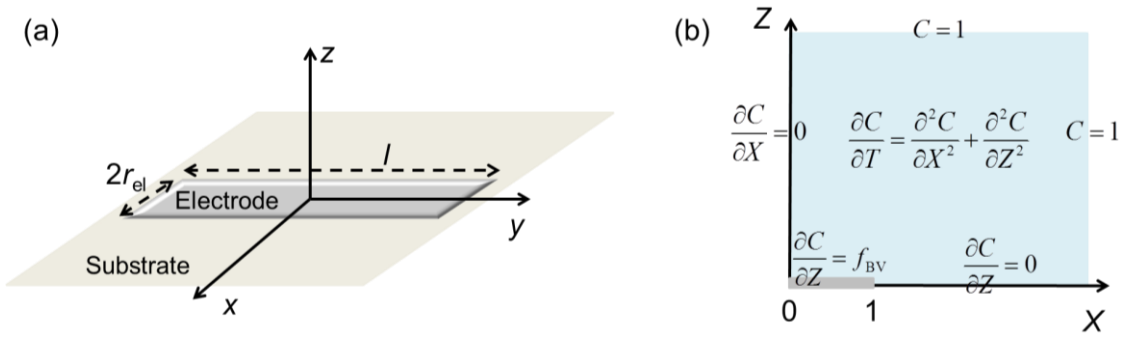


Figure 4.1 (a) A microband electrode in the Cartesian coordinate. (b) The simulation model for the redox reaction on the microband electrode. f_{BV} is the Butler-Volmer equation as written in Equation 4.15.

Table 4.1 Interpretation and transformation of dimensionless parameters.

SI unit parameters	**Interpretation**	**Dimensionless parameters**
r_{el} (m)	Half of the electrode width (microband); Radius of the electrode (disc, sphere, cylinder)	$R_{el} = r_{el}/r_{el} = 1$

l_{el} (m)	Length of the microband	
x (m)	Space coordinate, parallel to the electrode surface	$X = x/r_{el}$
z (m)	Space coordinate, perpendicular to the electrode surface	$Z = z/r_{el}$
c_{bulk} (mM)	Concentration in the bulk solution	$C_{bulk} = c_{bulk}/c_{bulk} = 1$
c (mM)	Concentration	$C = c/c_{bulk}$
D ($m^2\ s^{-1}$)	Diffusion coefficient	$d = D/D = 1$
t (s)	Reaction time	$\tau = t*D/r_{el}^2$
F ($C\ mol^{-1}$)	Faraday constant (96485 $C\ mol^{-1}$)	
R ($J \cdot mol^{-1} \cdot K^{-1}$)	Gas constant (8.314 $J \cdot mol^{-1} \cdot K^{-1}$)	
T (K)	Experiment temperature (298.2 K)	
E_f (V)	Formal potential	
E (V)	Applied electrode potential	$\theta = (E - E_f)F/(RT)$
k^0 ($m\ s^{-1}$)	Standard electrochemical rate constant	$K = k^0 r_{el}/D$
v ($V\ s^{-1}$)	Scan rate	$\sigma = vFr_{el}^2/(RTD)$
I (A)	Current	$J = I/(FDc_{bulk}l_{el})$

4.4 Results and discussion

Oxidative voltammograms on different electrode geometries were simulated. The waveshapes and the non-mass-transport corrected ('apparent') transfer coefficient α_{nc} as a function of potential were analysed. We first aim to assess over which range of voltammetric current without mass-transport correction α_{nc} closely reflects the true transfer coefficient α. Second, the accuracy or otherwise of using the analytical defined mass-transport correction (Equations 4.13 and 4.14) is investigated.

The process studied in this work is a fully irreversible, one-electron transfer reaction (Equation 4.1). Five different diffusion geometries, macrodisc, micro-hemispherical, micro-disc, micro-hemicylindrical and single microband electrodes, are investigated in this work. Voltammograms on different geometries were simulated using either DigiSim® or a home-written programme as described above. The analysis presented here focuses on oxidative processes only, but the results are also equally applicable to the irreversible reductive processes. The anodic and cathodic transfer coefficients as used in the BV equation are added to unity except where otherwise stated. All the Tafel analysis was undertaken in the current range from 1% to 99% of the peak current I_p or steady-state current $I_{s.s}$. Experimentally, the lower limit percentage of current should be chosen based on the ratio of faradaic current to background current, this lower limit will vary between different electrode systems, further details on which are outlined in the

discussion presented in Appendix A Section A2. Three mass-transport regimes will be discussed in the sequence: linear diffusion, steady-state and quasi-steady state.

4.4.1 Electrodes with linear diffusion

4.4.1.1 Tafel analysis under linear diffusion

For a planar disc electrode, both linear and radial (near the electrode edge) diffusion contribute to the total mass-transport limited flux. However, at sufficiently short times or for larger electrodes, when the diffusion layer thickness is small as compared to the electrode radius, only the linear diffusion contribution needs to be considered. The limits of this linear diffusion regime can be described via the dimensionless scan rate σ (defined in Table 4.1). When σ is in excess of ca 3350[21] − as is commonly encountered when using a macroelectrode − the diffusion to the electrode can be assumed to be linear. Under these conditions the resulting maximum current is expected to be within experimental error (no more than 3% greater compared to that predicted for a linear diffusion regime from Randles-Ševčík equation)[21]. The flux is then considered as uniform over the electrode surface and results in a peak-shaped cyclic voltammogram.

The simulations were done at the same dimensionless scan rate and dimensionless rate constant for easy comparison. Here voltammograms on linear diffusion electrodes at different dimensionless scan rates were simulated using DigiSim®, with the transfer coefficients α_a and α_c equal to 0.5 and a dimensionless rate constant K of 1.5×10^{-3}. The

normalised voltammograms at different dimensionless scan rates ($\sigma = 2.19\times10^{3}$, 2.19×10^{4} and 2.19×10^{5}) were superimposed in Figure 4.2 where the y-axis is the dimensionless current which was normalised to the peak current and the x-axis is the dimensionless potential. The results show that in the fully irreversible limit, although the magnitude of the peak current is proportional to the square root of the scan rate and its position on the potential scale shifts with the scan rate, the dimensionless voltammetric *waveshape* is independent of the dimensionless scan rate. This fully irreversible case is further shown in Figure 4.3 (a) in the following section.

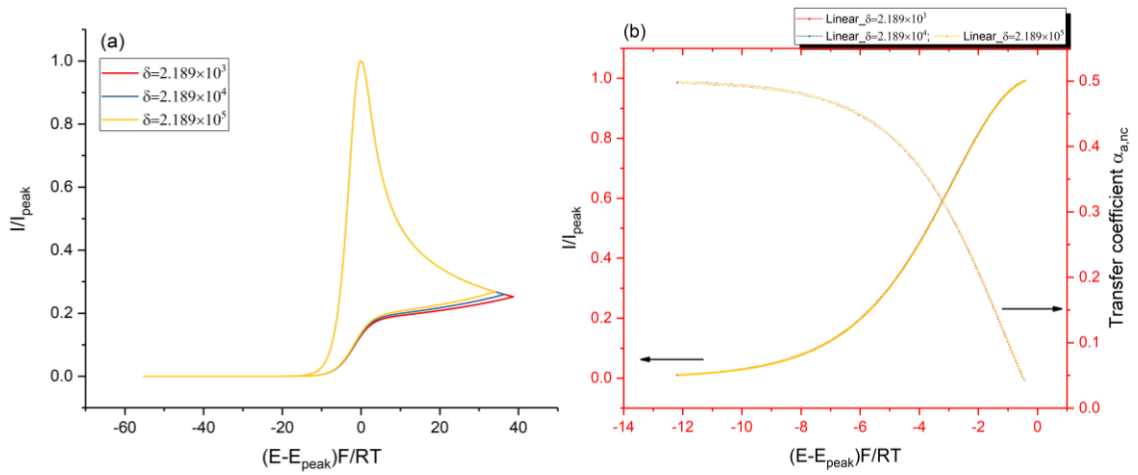


Figure 4.2 (a) Effect of various dimensionless scan rates on the waveshape under linear diffusion. (b) Anodic transfer coefficient plot for linear diffusion at different dimensionless scan rates. Red: $\sigma = 2.19\times10^{3}$; Blue: $\sigma = 2.19\times10^{4}$; Brown: $\sigma = 2.19 \times 10^{5}$. The dimensionless rate constant $K = 1.5 \times 10^{-3}$**.** Transfer coefficients $\alpha_a = \alpha_c = 0.5$.

Non-mass transport corrected transfer coeffiscient plot The voltammogram simulated for a dimensionless scan rate of 2.19×10^{4} were selected for Tafel analysis with a dimensionless rate constant K of 1.5×10^{-3}. The results where both the anodic and cathodic transfer coefficients α_a and α_c are 0.5 were first presented. Cases where the transfer

coefficient does not equal to 0.5 will be later discussed. Figure 4.3(a) shows the voltammogram normalised relative to the voltammetric peak current. The Tafel plot ($\ln|I_a|$ versus θ) was then calculated over the current range of 1% to 99% of the peak current and is shown in the inlay of Figure 4.3(a). The slope of the Tafel plot corresponds to the anodic transfer coefficient $\alpha_{a,nc}$. It can be seen that the Tafel plot is not a straight line over the potential range; the value of $\alpha_{a,nc}$ is not a constant.

In order to more clearly visualise how the non-mass-transport-corrected anodic transfer coefficient changes with dimensionless potential θ, the first derivative of the Tafel plot (Equation 4.10) is presented as the blue curve in Figure 4.3(b). It shows that at very low current, the measured anodic transfer coefficient $\alpha_{a,nc}$ approaches the true value of 0.5, but deviates from this value at high currents. This deviation occurs due to the depletion of the reactant at the electrode surface. Upon reaching the peak current the 'apparent' or non-mass-transport corrected transfer coefficient ($\alpha_{a,nc}$) tends to zero. Moreover, in order to numerically express how far the measured $\alpha_{a,nc}$ deviates from the true value as a function of potential, the fraction of the oxidative wave that can be used in the Tafel analysis for a given error has been calculated using Equation 4.18.

$$Error\ in\ \alpha_a = \frac{|\alpha_{a,nc} - \alpha_a|}{\alpha_a} \times 100\% \quad (4.18)$$

Frequently, up to 50% of the rising part of the voltammogram is taken for Tafel analysis in order to get rid of the influence from background current and diffusion effect[6, 22]. However, from the results presented in Table 4.2 it can be seen that at 50% of the way up

the voltammetric wave the value of the measured transfer coefficient is significantly below its actual value.

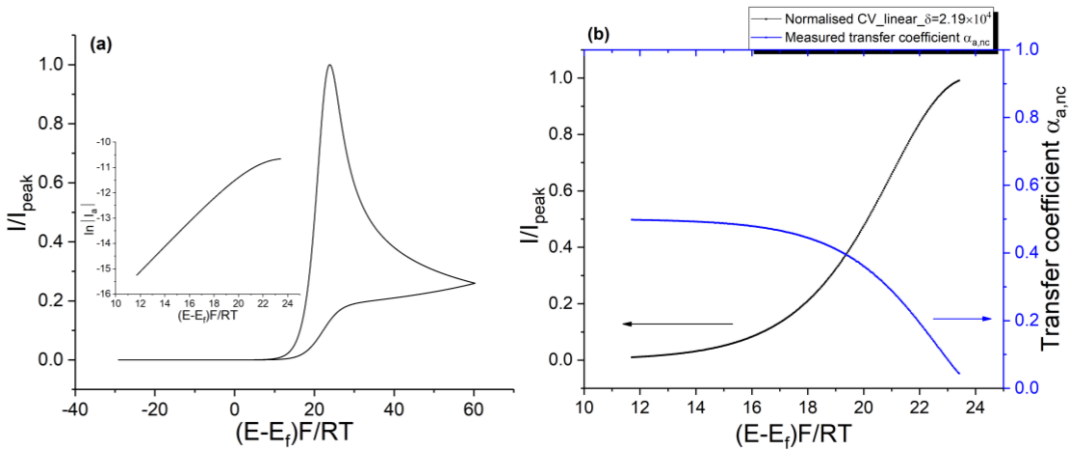


Figure 4.3 (a) Effect of various dimensionless scan rates on the wave-shape of linear diffusion at a dimensionless scan rate of 2.19×10^{4}. The inlayer is the Tafel plot in the current of 1% to 99% of the peak current. (b) Measured anodic transfer coefficient plot for linear diffusion in the current of 1% to 99% of the peak current (Black: oxidative wave; blue: measured transfer coefficient). The dimensionless rate constant $K=1.5\times10^{-3}$. Transfer coefficients assumed in the simulation: $\alpha_a= \alpha_c=0.5$.

Effect of the mass-transport correction on the measured transfer coefficient As discussed in Section 4.2, the voltammetric current becomes mass-transport limited at higher overpotentials. This leads to an underestimation of the transfer coefficient as $\alpha_{a,nc} < \alpha_a$. The analytically defined mass-transport corrected Tafel analysis was therefore calculated to attempt to minimise this mass-transport effect. As is shown in Figure 4.4, the black curve is the oxidative wave normalised to the peak current in the current range of 1% to 99% of I_{peak} and the blue and red curves are the transfer coefficient plots with and without mass-transport correction, respectively. The

analytically mass-transport corrected $\alpha_a{}'$ was calculated using Equation 4.13, replacing I_{lim} with I_{peak}. The equation then becomes:

$$-\frac{dln\left(\frac{1}{I_a}-\frac{1}{I_{peak}}\right)}{d\theta} = \alpha_a{}' \tag{4.19}$$

However, Equation 4.13 has been derived assuming a *steady-state* mass-transport regime; consequently, as can be seen from Figure 4.4, direct application of this equation does not satisfactorily apply to this mass-transport regime, such that the value of the analytically mass-transport corrected $\alpha_a{}'$ (blue curve) significantly *overestimates* the transfer coefficient. Although the electrode is uniformly accessible, the accuracy of this analytically defined mass-transport correction is poor under linear diffusion.

One interesting observation is that the variations of measured and mass-transport corrected transfer coefficient plots as a function of potential are in opposite directions and their behaviours are nearly symmetric in the low overpotential range. Hence on an *empirical* basis, the average value of the measured and mass-transport corrected transfer coefficients calculated using Equation 4.20 (brown curve in Figure 4.4) gives a significantly improved mass-transport correction for application to macro-electrode voltammetry. Equation 4.20 can be equivalently expressed as Equation 4.21. Hence, a mass-transport corrected Tafel plot obtained by plotting the first derivative of $ln\frac{I^2 I_{peak}}{I_{peak}-I}$ versus θ may lead to an improved estimate of the transfer coefficient.

$$Average\ \alpha_{a,aver} = \frac{\alpha_{a,nc}+\alpha_a'}{2} \tag{4.20}$$

$$Average\ \alpha_{a,aver} = \frac{1}{2} \times \frac{dln\frac{I^2 I_{peak}}{I_{peak}-I}}{d\theta} \tag{4.21}$$

when I<<I_{peak}, $average\ \alpha_{a,aver} = \frac{dlnI}{d\theta} = \alpha_a$.

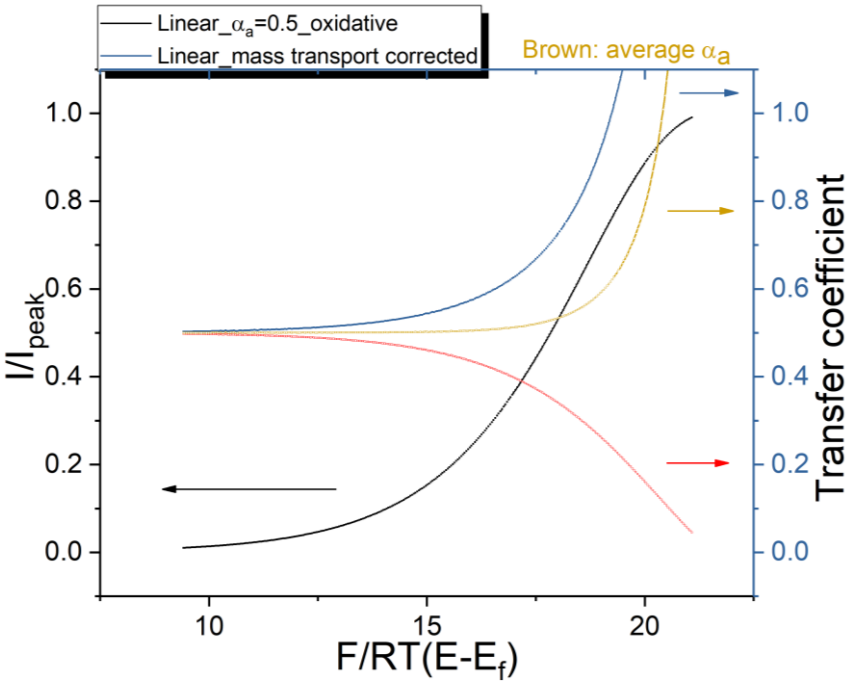


Figure 4.4 Effect of analytical mass-transport correction on the anodic transfer coefficient α_a. Black: oxidative wave; Red: measured transfer coefficient; Blue: mass-transport corrected transfer coefficient; Brown: average transfer coefficient. The true transfer coefficient α_a is 0.5 in the simulation. The current range is 1%-99% of the peak current.

Table 4.2 Fractions of the oxidative wave at a given error in transfer coefficient. The dimensionless rate constant $K=1.5\times10^{-3}$. Transfer coefficients $\alpha_a = \alpha_c = 0.5$ in the simulation. The dimensionless scan rate $\sigma=2.19\times10^{4}$.

	1% error in α_a	**5% error in α_a**	**10% error in α_a**	**20% error in α_a**
$\alpha_{a,nc}$	2.1% of $I_{s.s}$	10%	19%	36%
α_a'	1.7%	9.2%	17%	31%
$\alpha_{a,aver}$	25%	48%	61%	73%

The error in the measured transfer coefficient is calculated in Table 4.2. In the case of the average transfer coefficient, the fraction of the peak current that can be used in Tafel analysis is improved from 10% to 48% for a measured transfer coefficient that is expected to be within 5% error of its actual value across the full range of potentials.

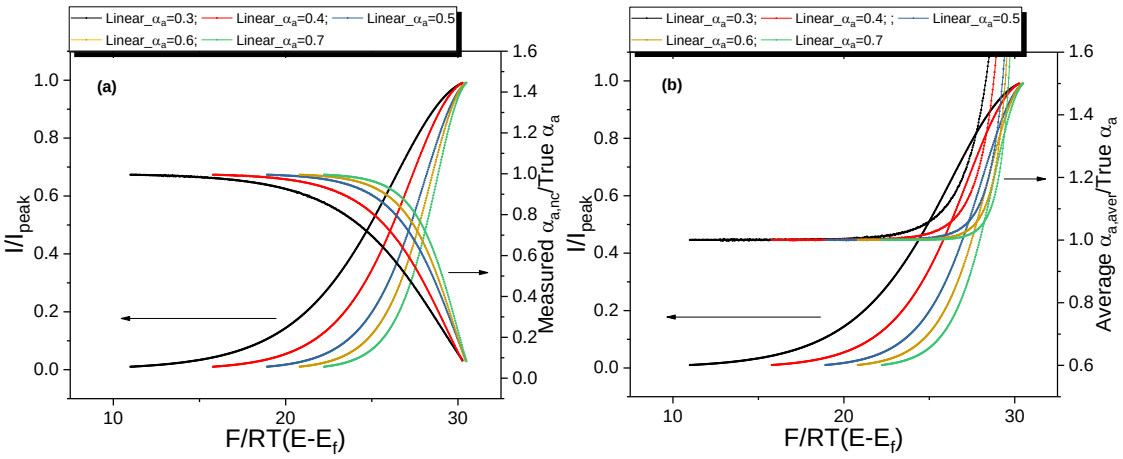


Figure 4.5 (a) Normalised measured α_a plot with different true transfer coefficients on linear diffusion electrode. (b) Averaged normalised$\alpha_{a,aver}$ plot with different true transfer coefficients on linear diffusion electrode. Black: $\alpha_a = 0.3$, red: $\alpha_a = 0.4$, blue: $\alpha_a = 0.5$, brown: $\alpha_a = 0.6$, green: $\alpha_a = 0.7$. The current range: 1% - 99% of peak current, $\alpha_c + \alpha_a = 1$.

Table 4.3 Fractions of the oxidative wave at a given error in transfer coefficient without analytical mass-transport correction.

True α_a	**-1% error**	**-5% error**	**-10% error**	**-20% error**
0.3	1.8% of I_{peak}	10%	19%	36%
0.4	2.1%	10%	19%	36%
0.5	2.1%	10%	19%	36%
0.6	1.9%	10%	19%	36%
0.7	2.1%	10%	19%	36%

Table 4.4 Fractions of the oxidative wave at a given error in transfer coefficient with the averaged analytical mass-transport correction.

True α_a	**+1% error**	**+5% error**	**+10% error**	**+20% error**
0.3	25%	49%	61%	73%
0.4	24%	48%	61%	73%
0.5	25%	48%	61%	73%
0.6	25%	48%	61%	73%
0.7	24%	48%	61%	73%

The above results are further valid in cases where the transfer coefficient does not equal 0.5. Voltammograms for different transfer coefficients (α_a = 0.3, 0.4, 0.6 and 0.7) were simulated and analysed via the same method, the dimensionless rate constant K was 1.5×10^{-3} and the dimensionless scan rate σ was 2.19×10^{4}. The measured and analytically mass-transport corrected transfer coefficient plots are shown in Figure 4.5. The percentage error in transfer coefficient is the same in all cases; consequently the anodic transfer coefficient at different fractions of the wave is insensitive to the true α_a value for linear diffusion, as tabulated in Tables 4.3 and 4.4.

4.4.2 Microelectrodes under steady-state conditions

For a microelectrode with a radius of the order of microns, a steady-state flux can be achieved without stirring of the solution as a consequence of radial diffusion. As a result, the voltammogram has a sigmoidal (Figure 4.6(a) and Figure 4.7(a)) waveshape rather than a peaked-shape voltammogram[6].

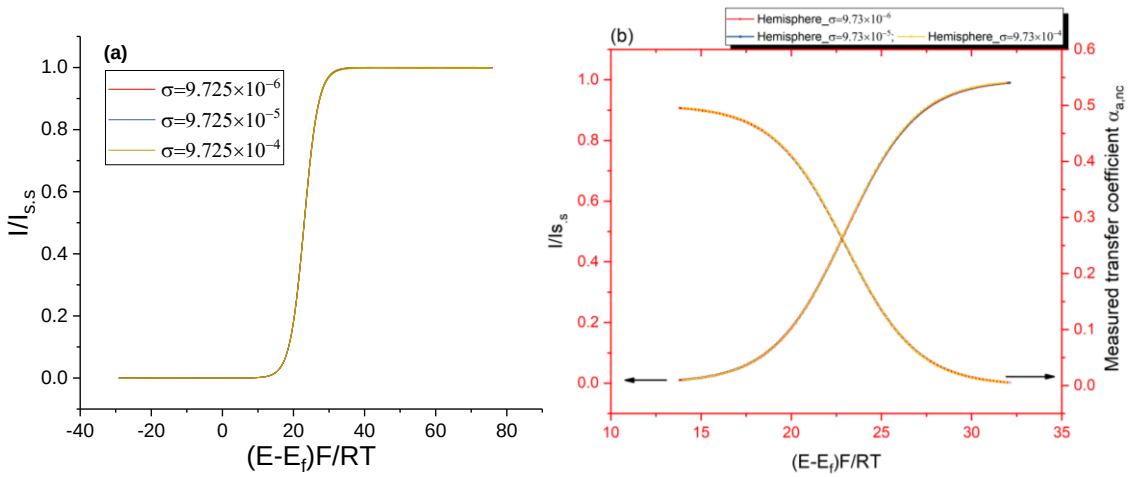


Figure 4.6 (a) Voltammograms on a micro-hemispherical electrode at different dimensionless scan rates. (b) Measured transfer coefficient plots. Red: $\sigma = 9.73 \times 10^{-6}$; Blue: $\sigma = 9.73 \times 10^{-5}$; Brown: $\sigma = 9.73 \times 10^{-4}$. Dimensionless rate constant $K = 1 \times 10^{-5}$, $\alpha_c = \alpha_a = 0.5$. The current range in (b) is 1% - 99% of steady-state current.

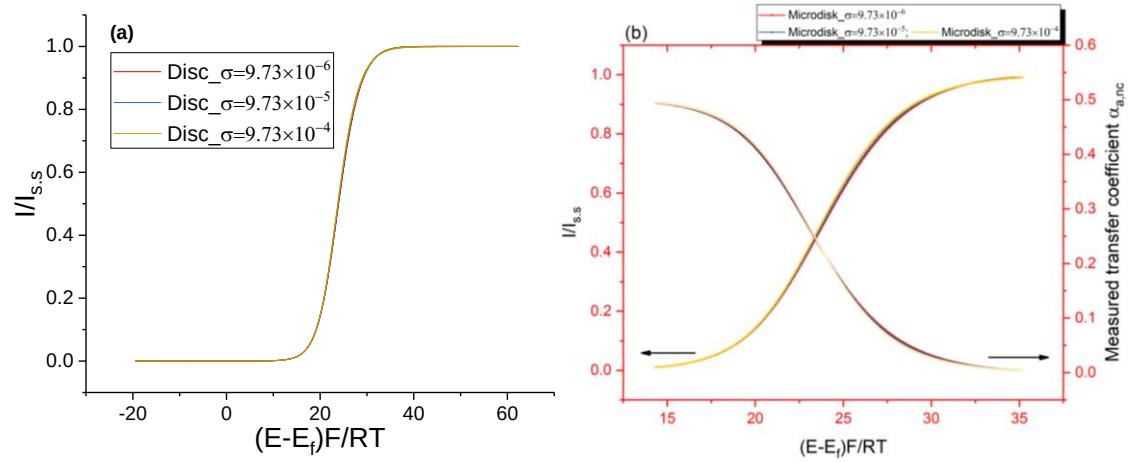


Figure 4.7 (a) Voltammograms on a microdisc electrode at different dimensionless scan rates. (b) Measured transfer coefficient plots on a microdisc electrode. Red: $\sigma = 9.73 \times 10^{-6}$; Blue: $\sigma = 9.73 \times 10^{-5}$; Brown: $\sigma = 9.73 \times 10^{-4}$. Dimensionless rate constant $K = 1 \times 10^{-5}$, $\alpha_c = \alpha_a = 0.5$. The current range in (b) is 1% - 99% of steady-state current.

Convergent diffusion dominates only when the diffusion layer thickness is large compared to the radius of the electrode. This limit can also be described by the dimensionless scan rate σ. When $\sigma < 4.30 \times 10^{-2}$ on a planar microelectrode, the diffusion

to the electrode is considered as almost convergent with a maximum peak current no more than 3% greater than that predicted for the steady-state flux (presented in Appendix A SectionA3). In this section, voltammograms at different dimensionless scan rates were simulated on micro-hemispherical and micro-disc electrodes using DigiSim® and a home-written programme, respectively, assuming the transfer coefficients α_a and α_c were equal to 0.5 and the dimensionless rate constant K was 1×10^{-5}. The effect of the dimensionless scan rate on the waveshape and the measured transfer coefficient on a micro-hemispherical electrode (Figure 4.6) and a micro-disc electrode (Figure 4.7) were also investigated. It is found that the voltammetric waveshape was found to be independent of the dimensionless scan rate when $\sigma<4.30\times10^{-2}$, where convergent diffusion dominates. The voltammetric responses of both geometries at a dimensionless scan rate σ of 9.73×10^{-6} are now further analysed in the region from 1% to 99% of $I_{s.s}$.

Micro-hemispherical electrode Figure 4.8(b) presents the oxidative wave (black curve) normalised to the steady-state current $I_{s.s}$ in the current range of 1% to 99% of $I_{s.s}$ for a hemispherical microelectrode.

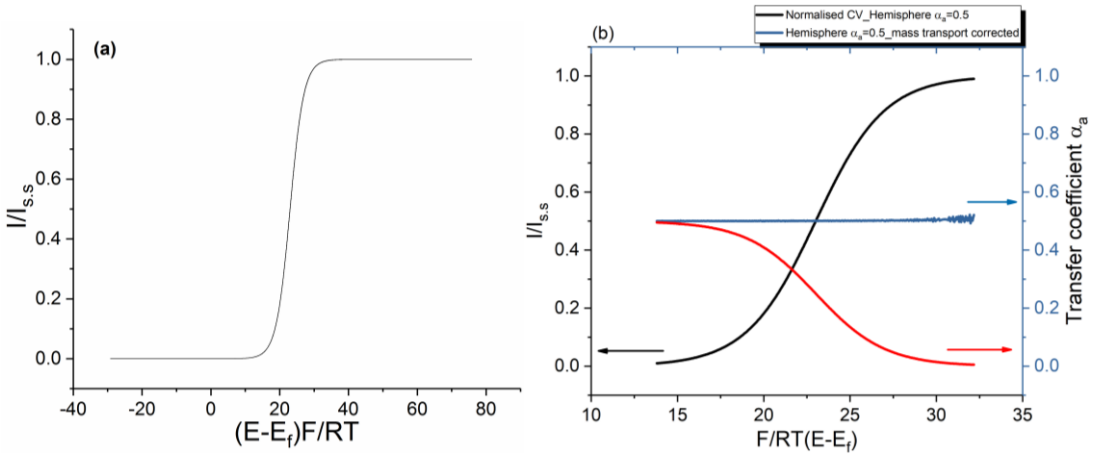


Figure 4.8 (a) Voltammogram on a hemispherical electrode. (b) Effect of analytical mass-transport correction on the α_a plots (Black: oxidative wave; Red: measured transfer coefficient; Blue: mass-transport corrected transfer coefficient). In the simulation, $\alpha_a = 0.5$, the dimensionless scan rate $\sigma = d\theta/d\tau = 9.73 \times 10^{-6}$ and dimensionless rate constant $K = 1 \times 10^{-5}$. The current range in (b) is 1% - 99% of steady-state current.

The red curve in Figure 4.8(b) depicts the variation of the measured transfer coefficient $\alpha_{a,nc}$ as a function of dimensionless potential. Similar to the case of linear diffusion, at higher overpotential the measured non-mass-transport corrected transfer coefficient deviates away from the value of 0.5. This again occurs due to the change in surface concentration of reactant as the current approaches steady state. Subsequently the influence of mass-transport was 'corrected' for by use of Equation 4.13. As can be seen from the blue curve in Figure 4.8(b), for this electrode geometry, the analytically corrected transfer coefficient α_a' accurately reflects the transfer coefficient across the full potential range. The percentage error of transfer coefficient with and without analytical mass-transport correction is also calculated in Table 4.5. Hence the analytical mass-transport correction as defined by Equation 4.13 is valid for a uniformly accessible

hemispherical microelectrode under a steady-state condition, which is consistent with the conclusions from literature[23].

Microdisc electrode A planar microdisc electrode is non-uniformly accessible. Consequently the transient behaviour of such systems reflects a 2D diffusional problem. Under steady-state conditions, the current to the electrode is given by $I_{s.s} = 4nFD[A]_{bulk}r_{el}$ as originally described by Saito, where n is the electron transferred in the process and r_{el} is the radius of the disc[24]. The normalised voltammogram is shown in Figure 4.9(a) and its corresponding non mass-transport corrected transfer coefficient is plotted as the red curve in Figure 4.9(b).

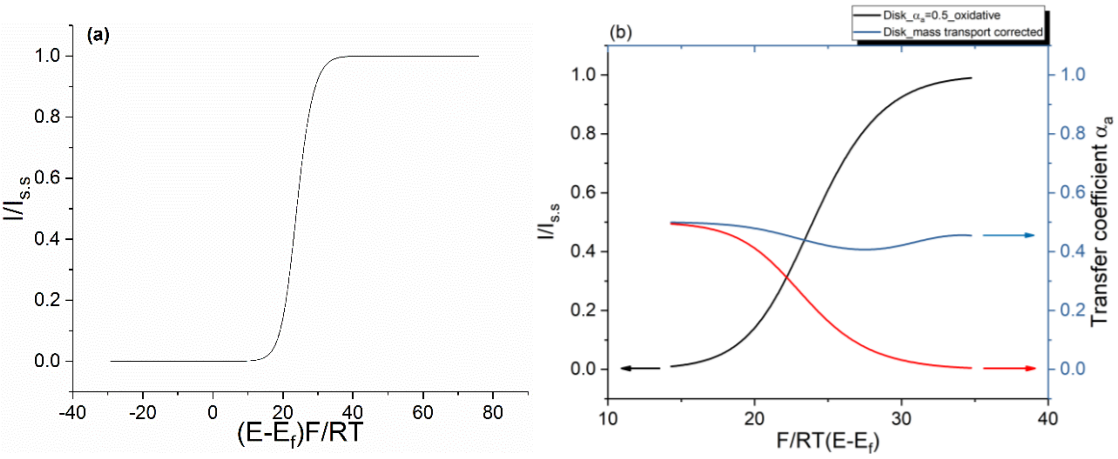


Figure 4.9 (a) Voltammogram on a microdisc electrode. (b) Effect of analytical mass-transport correction on the α_a plots of a microdisc electrode (Black: oxidative wave; Red: measured transfer coefficient; Blue: mass-transport corrected transfer coefficient). The current range in (b) is 1% - 99% of steady-state current. The dimensionless scan rate is 9.73×10^{-6}. The dimensionless rate constant $K=1\times10^{-5}$. Transfer coefficient $\alpha_a = \alpha_c = 0.5$ in the simulation.

As anticipated the measured transfer coefficient deviates from the true value and approaches zero at high overpotentials due to the mass-transport limitation. Surprisingly

however, the analytically mass-transport corrected Tafel analysis as shown in Figure 4.9(b) (blue line), although it gives a notably improved measured of the transfer coefficient, but shows significant fluctuation at higher fractions of the wave. The value of α_a' deviates from the true value of the transfer coefficient by up to 19%. Consequently, for precise work the analytically defined mass-transport corrected Tafel analysis is not suitable for use with microdisc voltammetry. The error in the transfer coefficient with and without mass-transport correction at different fractions of the wave is presented in Table 4.5.

Table 4.5 Fractions of the oxidative wave at a given error in transfer coefficient with and without mass-transport correction on micro-hemispherical and microdisc electrodes. The dimensionless scan rate is 9.73×10^{-6}. The dimensionless rate constant $K=1\times10^{-5}$. Transfer coefficient $\alpha_a= \alpha_c=0.5$ in the simulation.

Electrode geometry		1% error in α_a	5% error in α_a	10% error in α_a	15% error in α_a	20% error in α_a
Micro-hemisphere	$\alpha_{a,nc}$	1.0% of $I_{s.s}$	5.0%	10%	15%	20%
	α_a'	/	/	/	/	/
Microdisc	$\alpha_{a,nc}$	<1.0%	3.9%	7.9%	12%	16%
	α_a'	3.6%	17%	35%	57%	/

The trend of the anodic transfer coefficient plots at various fractions of wave is again independent of the true transfer coefficient for both micro-hemispherical and micro-disc electrodes. The voltammograms simulated with various α_a values and the corresponding

transfer coefficient plots are presented in Figure 4.10 (micro-hemispherical electrode) and Section 4.11 (micro-disc electrodes). The fraction of the wave at a given error in transfer coefficient for both electrode geometries are tabulated in Table 4.6 (micro-hemispherical electrode) and Tables 4.7 and 4.8 (micro-disc electrodes). The slight difference in percentage is considered to be from the numerical errors.

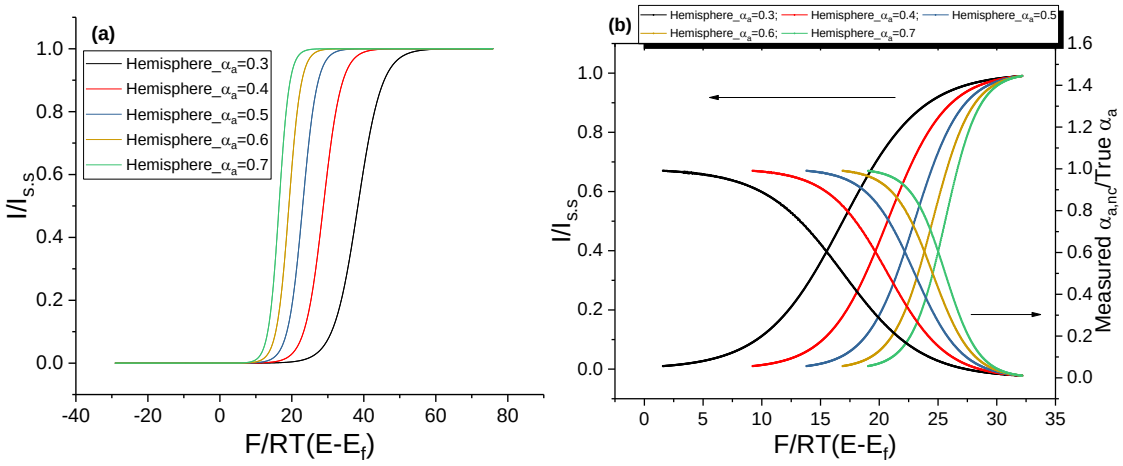


Figure 4.10 (a) CVs of micro-hemisphere with various true transfer coefficients. (b) The normalised α_a plots of micro-hemisphere with various true transfer coefficients. Black: $\alpha_a = 0.3$, red: $\alpha_a = 0.4$, blue: $\alpha_a = 0.5$, brown: $\alpha_a = 0.6$, green: $\alpha_a = 0.7$. The current range in (b) is 1% - 99% of steady-state current. Dimensionless rate constant $K = 1 \times 10^{-5}$, the dimensionless scan rate $\sigma = 9.73 \times 10^{-6}$, $\alpha_c + \alpha_a = 1$.

Table 4.6 Fractions of the oxidative wave at a given error in transfer coefficient without analytical mass-transport correction on a hemispherical electrode.

True α_a	**-1% error in α_a**	**-5% error in α_a**	**-10% error in α_a**	**-20% error in α_a**
0.3	1.0%	5.0%	10%	20%
0.4	1.0%	5.0%	10%	20%
0.5	1.0%	5.1%	10%	20%

0.6	1.0%	5.0%	10%	20%
0.7	1.0%	5.0%	10%	20%

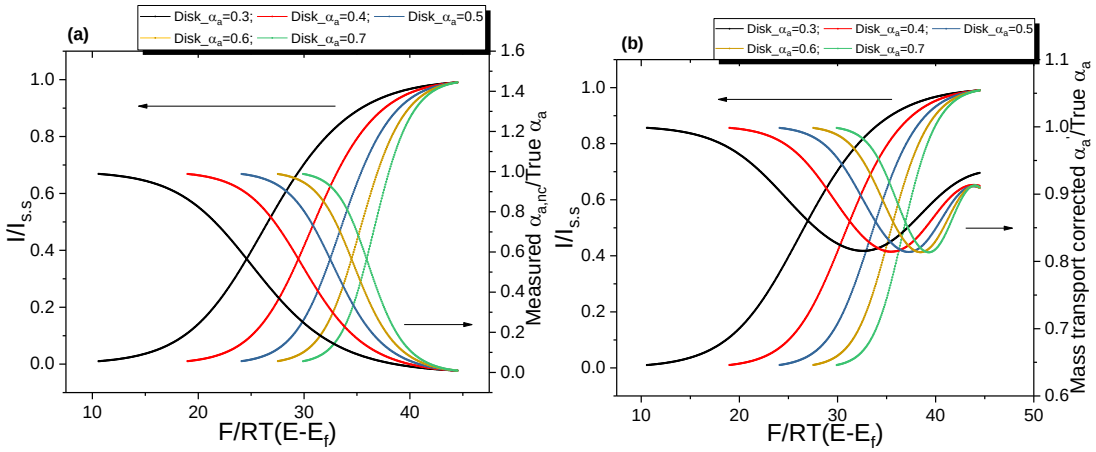


Figure 4.11 (a) Voltammograms and measured transfer coefficient plots on a microdisc with various true transfer coefficients. (b) The normalised α_a plots of microdisc with various true transfer coefficients. Black: $\alpha_a = 0.3$, red: $\alpha_a = 0.4$, blue: $\alpha_a = 0.5$, brown: $\alpha_a = 0.6$, green: $\alpha_a = 0.7$. The current range is 1% - 99% of steady-state current. The dimensionless rate constant $K = 1 \times 10^{-5}$, the dimensionless scan rate $\sigma = 9.73 \times 10^{-6}$. $\alpha_c + \alpha_a = 1$.

Table 4.7 Fractions of the oxidative wave at a given error in transfer coefficient without analytical mass-transport correction on a microdisc electrode.

True α_a	**-1% error**	**-5% error**	**-10% error**	**-15% error**	**-20% error**
0.3	<1.0%	3.9%	7.8%	12%	16%
0.4	<1.0%	3.9%	7.8%	12%	16%
0.5	<1.0%	3.9%	7.9%	12%	16%
0.6	<1.0%	4.0%	7.8%	12%	16%
0.7	<1.0%	3.9%	7.7%	12%	16%

Table 4.8 Fractions of the oxidative wave at a given error in transfer coefficient with analytical mass-transport correction.

True α_a	**-1% error**	**-5% error**	**-10% error**	**-15% error**
0.3	3.7%	17%	36%	57%
0.4	3.6%	17%	36%	57%
0.5	3.6%	17%	35%	57%
0.6	3.7%	17%	35%	56%
0.7	3.6%	17%	35%	56%

4.4.3 Electrodes under quasi-steady state conditions

Hemicylindrical and single band electrodes are two examples of quasi-steady state diffusion geometries. These electrodes are characteristically microscopic in one dimension and macroscopic in another. At sufficiently short time, linear diffusion dominates, while radial diffusion becomes important at longer times. However, true steady state behaviour is not attained under these geometries.[19, 25] Due to the macroscopic length, the radial diffusion is not as efficient as that on a micro-spherical electrode. Therefore voltammograms obtained on hemicylindrical (Figure 4.12(a)) or single band microelectrodes (Figure 4.13(a)) are intermediate between peak-shaped (linear diffusion) and sigmoidal characteristic ('true' steady state), resulting in a quasi-steady state diffusional flux to the surface. The magnitude of the current scales with the length of the electrode. Unlike electrodes under linear diffusion or steady-state condition,

the voltammetric waveshape on micro-hemicylinder and single microband is sensitive to the dimensionless scan rate. As can be seen from the Figure 4.12 (a) (micro-hemicylindrical electrode) and Figure 4.13 (a) (single microband), the voltammogram becomes more peak-shaped at higher dimensionless scan rates as a result of larger contribution from linear diffusion and more sigmoidal-like at sufficiently small dimensionless scan rates due to enhanced mass transport from non-linear diffusion. It is also found that this improvement in the estimation of transfer coefficient using analytical mass-transport correction becomes smaller at higher dimensionless scan rates where the linear diffusion contribution is larger, which further proves the assumption of the analytical mass-transport correction, as shown in Table 4.9 (micro-hemicylindrical electrode) and Table 4.10 (single microband electrode).

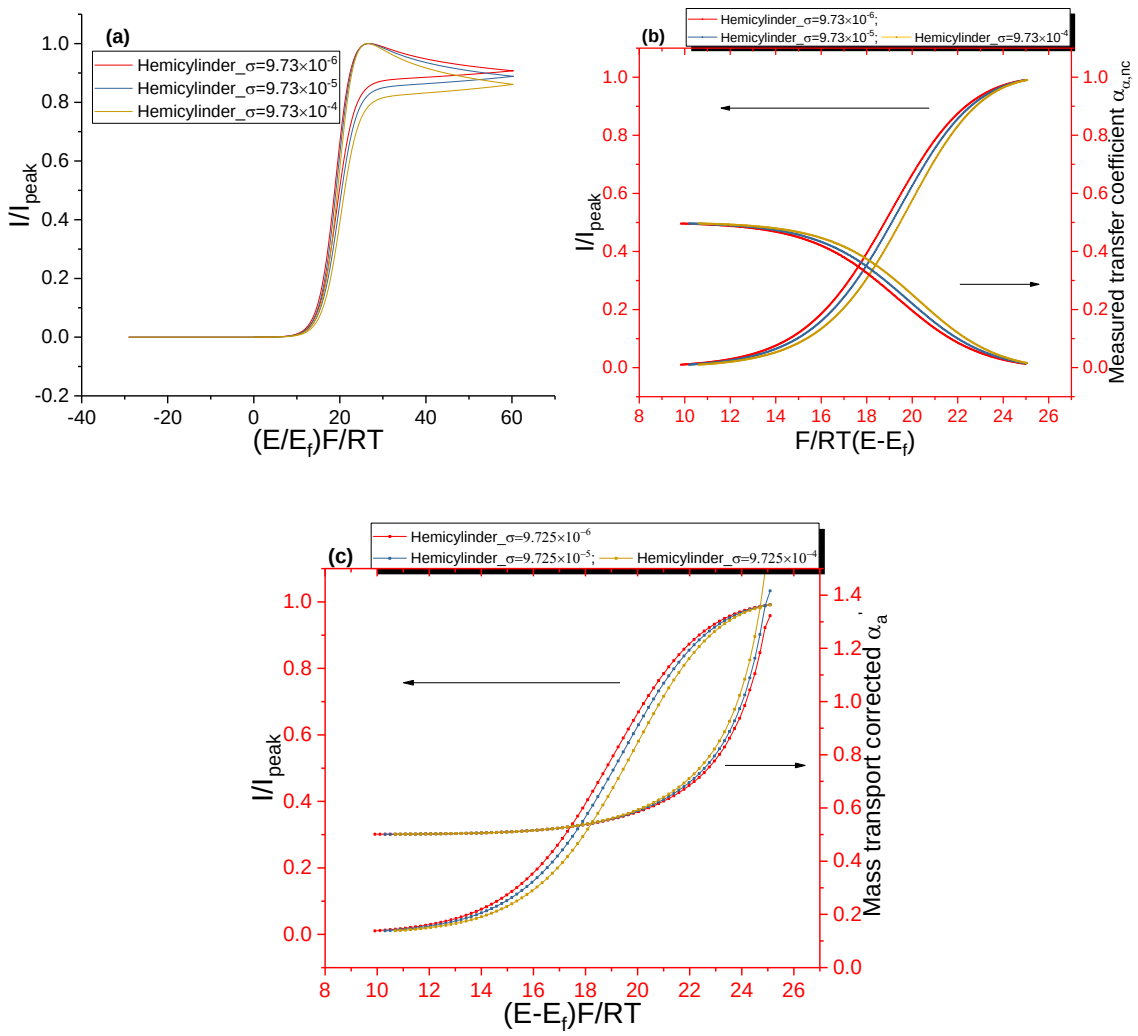


Figure 4.12 (a) Effect of various dimensionless scan rates on the waveshape of hemicylindrical electrodes. (b) Measured transfer coefficient plots for hemicylinder. c) Analytical mass-transport corrected transfer coefficient plots for hemicylinder. Red: $\sigma = 9.725 \times 10^{-6}$; Blue: $\sigma = 9.725 \times 10^{-5}$; Brown: $\sigma = 9.725 \times 10^{-4}$. The dimensionless rate constant $K = 1 \times 10^{-5}$; $\alpha_c = \alpha_a = 0.5$. The current range in (b) and (c) is 1% - 99% of steady-state current.

Table 4.9 Fractions of the oxidative wave at a given error in transfer coefficient with and without analytical mass-transport correction at different dimensionless scan rates with fixed dimensionless rate constant $K=1\times10^{-5}$, $\alpha_c = \alpha_a = 0.5$ at a micro-hemicylindrical electrode.

Dimensionless scan rate		**-1% error**	**-5% error**	**-10% error**	**-20% error**
9.73×10^{-6}	$\alpha_{a,nc}$	1.2%	5.9%	11.7%	23.0%
	α_a'	6.3%	28.8%	48.3%	71.8%
9.73×10^{-5}	$\alpha_{a,nc}$	1.3%	6.0%	12.0%	23.7%
	α_a'	5.4%	25.4%	43.9%	68.3%
9.73×10^{-4}	$\alpha_{a,nc}$	1.3%	6.3%	12.5%	24.5%
	α_a'	4.4%	21.6%	37.6%	59.5%

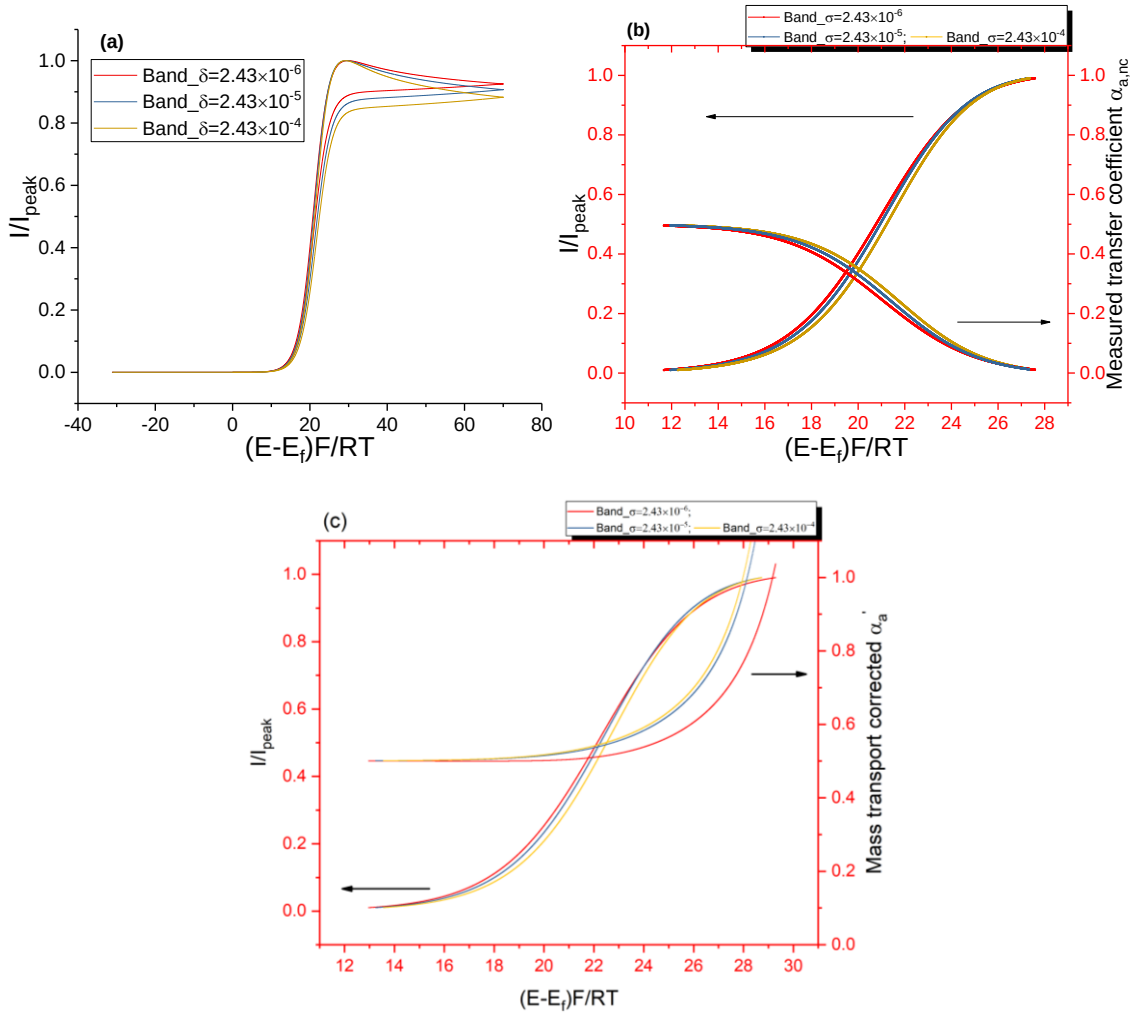


Figure 4.13 (a) Effect of various dimensionless scan rates on the wave-shape of single band. (b) Measured transfer coefficient plots on single band at different dimensionless scan rates. c) Analytical mass-transport corrected transfer coefficient plots for single band. Red: $\sigma = 2.43 \times 10^{-6}$; Blue: $\sigma = 2.43 \times 10^{-5}$; Brown: $\sigma = 2.43 \times 10^{-4}$. The dimensionless rate constant $K = 5 \times 10^{-6}$; $\alpha_c = \alpha_a = 0.5$. The current range in (b) is 1% - 99% of steady-state current.

Table 4.10 Fractions of the oxidative wave at a given error in transfer coefficient with and without analytical mass-transport correction at different dimensionless scan rates with fixed dimensionless rate constant K = 5×10^{-6}, $\alpha_c = \alpha_a = 0.5$ at a single microband electrode.

Dimensionless scan rate		**-1% error**	**-5% error**	**-10% error**	**-20% error**
2.43×10^{-6}	$\alpha_{a,nc}$	1.0% of I_{peak}	5.2%	10.4%	20.9%
	α_a'	38.4%	64.6%	77.6%	88.5%
2.43×10^{-5}	$\alpha_{a,nc}$	1.1%	5.7%	11.3%	22.4%
	α_a'	8.6%	35.8%	56.7%	77.8%
2.43×10^{-4}	$\alpha_{a,nc}$	1.2%	5.9%	11.7%	23.1%
	α_a'	6.4%	29.1%	49.5%	72.8%

Hemicylindrical microelectrodes Voltammograms on hemicylindrical microelectrodes at different dimensionless scan rates were simulated using DigiSim®, assuming the transfer coefficients α_a and α_c were equal to 0.5 and the dimensionless rate constant K was 1×10^{-5}. Although the waveshape for a hemicylindrical electrode is slightly sensitive to the scan rate, it shows that the difference in the fractions of the wave can be used in Tafel analysis with a given error at different σ is less than 2% (Table 4.9). Tafel plot was then calculated for the micro-hemicylindrical electrode at a dimensionless scan rate of 9.73×10^{-6} in the current range of 1% to 99% of I_{peak} (Figure 4.14(a)). The oxidative wave simulated is

normalised relative to its peak current as shown as the black curve in Figure 4.14(b). The measured non mass-transport corrected transfer coefficient $\alpha_{a,nc}$ (red curve) again deviates from its true value at higher potentials, as is seen under other geometries. The removal of mass-transport effect was attempted using the analytical approximation to get a better correction for the measure of the transfer coefficient as shown as the blue curve in Figure 4.14(b).

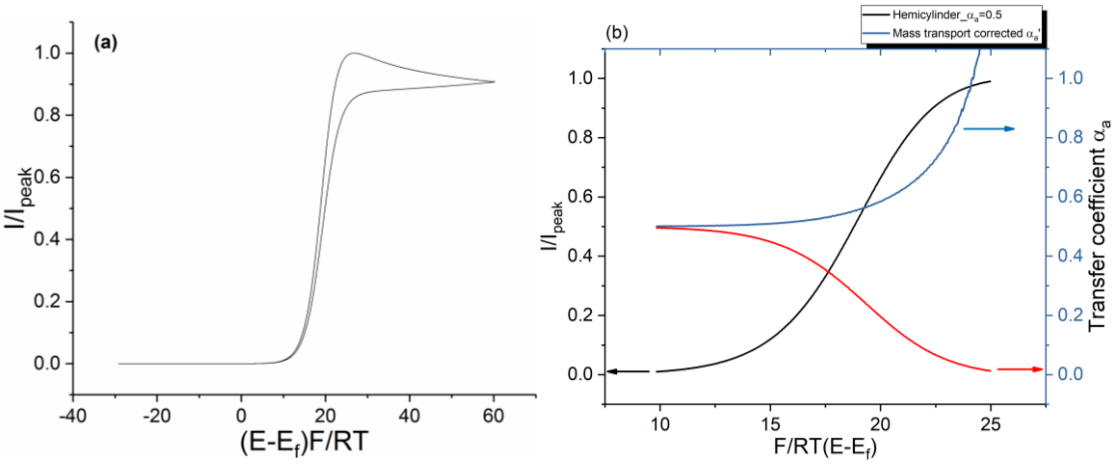


Figure 4.14 (a) Voltammogram on a micro-hemicylindrical electrode. (b) Effect of analytical mass-transport correction on the transfer coefficient plots of hemicylinder (Black: oxidative wave; Red: measured transfer coefficient; Blue: mass-transport corrected transfer coefficient). The current range in (b) is 1% - 99% of steady-state current. The dimensionless scan rate is 9.73×10^{-6}. The dimensionless rate constant $K=1\times10^{-5}$. Transfer coefficients $\alpha_a= \alpha_c=0.5$ in the simulation.

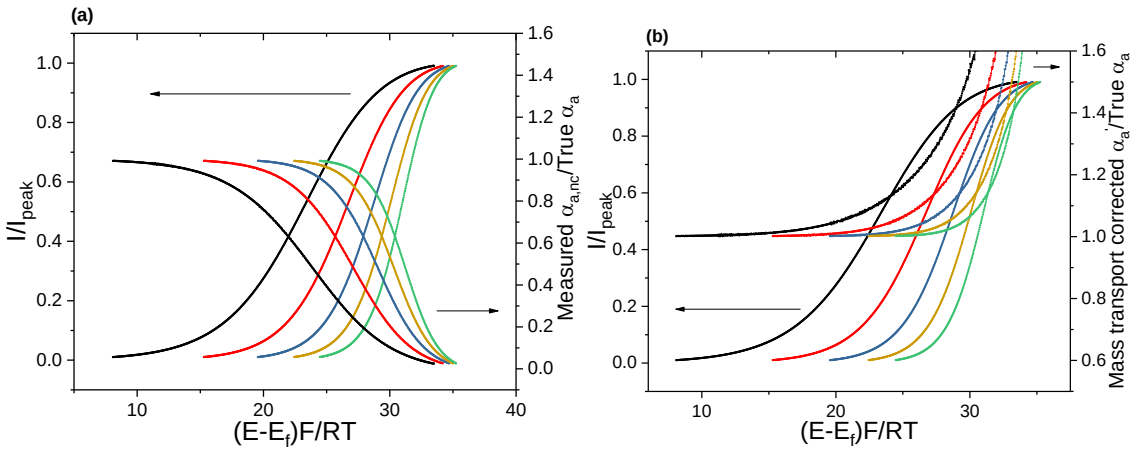


Figure 4.15 (a) The normalised measured transfer coefficient plots on hemicylinder with various true transfer coefficients. (b) The normalised mass-transport corrected transfer coefficient plots of hemicylinder with various true transfer coefficients Black: $\alpha_a = 0.3$, red: $\alpha_a = 0.4$, blue: $\alpha_a = 0.5$, brown: $\alpha_a = 0.6$, green: $\alpha_a = 0.7$. The current range: 1% - 99% of peak current. The dimensionless rate constant $K = 1 \times 10^{-5}$; $\alpha_c + \alpha_a = 1$.

The behaviour of this analytically mass-transport corrected transfer coefficient is between that of the macroelectrode and micro-hemispherical electrodes. The accuracy of this analytical correction on hemicylindrical microelectrodes is better than that for the macroelectrodes but worse than that for the micro-hemispherical electrodes. The lower accuracy is considered as a result of the breakdown of the true steady state. The fraction of the oxidative current for a given error of transfer coefficient is tabulated in Table 4.11 and Table 4.12. Accordingly, with mass-transport correction, the fraction of wave that is analysable can be improved from 11.6% to 48.3% of the peak current in Tafel analysis with less than 10% error in transfer coefficient at the smallest scan rate. Similar results were attained on hemicylindrical microelectrodes with different true transfer coefficients with a given dimensionless scan rate of 9.73×10^{-6} and a given dimensionless rate constant

of 1×10^{-5}. The corresponding transfer coefficient plots with and without analytical mass-transport correction are presented in Figure 4.15. The fraction of the voltammetric wave at a given error in transfer coefficient is tabulated in Table 4.11 and 4.12.

Table 4.11 Fractions of the oxidative wave at a given error in transfer coefficient without analytical mass-transport correction at a micro-hemicylindrical electrode.

True α_a	**-1% error**	**-5% error**	**-10% error**	**-20% error**
0.3	1.3%	5.9%	11.5%	22.9%
0.4	1.2%	5.9%	11.7%	22.9%
0.5	1.2%	5.9%	11.6%	23.0%
0.6	1.2%	5.9%	11.7%	22.9%
0.7	1.2%	5.9%	11.6%	23.0%

Table 4.12 Fractions of the oxidative wave at a given error in transfer coefficient with analytical mass-transport correction at a micro-hemicylindrical electrode.

True α_a	**+1% error**	**+5% error**	**+10% error**	**+20% error**
0.3	6.2%	30.8%	49.2%	72.5%
0.4	6.1%	28.9%	49.1%	72.0%
0.5	6.4%	28.4%	48.3%	71.8%
0.6	6.0%	27.7%	48.6%	71.8%
0.7	6.2%	27.6%	47.8%	71.3%

Single band electrodes Voltammograms on single microband electrodes at different dimensionless scan rates were simulated using the home written programme as described in Section 4.3, assuming the transfer coefficients α_a and α_c were equal to 0.5 and the dimensionless rate constant K was 5×10^{-6}. Tafel analysis on a single microband was undertaken at a dimensionless scan rate of 2.43×10^{-6} in the current range of 1% to 99% of I_{peak}.

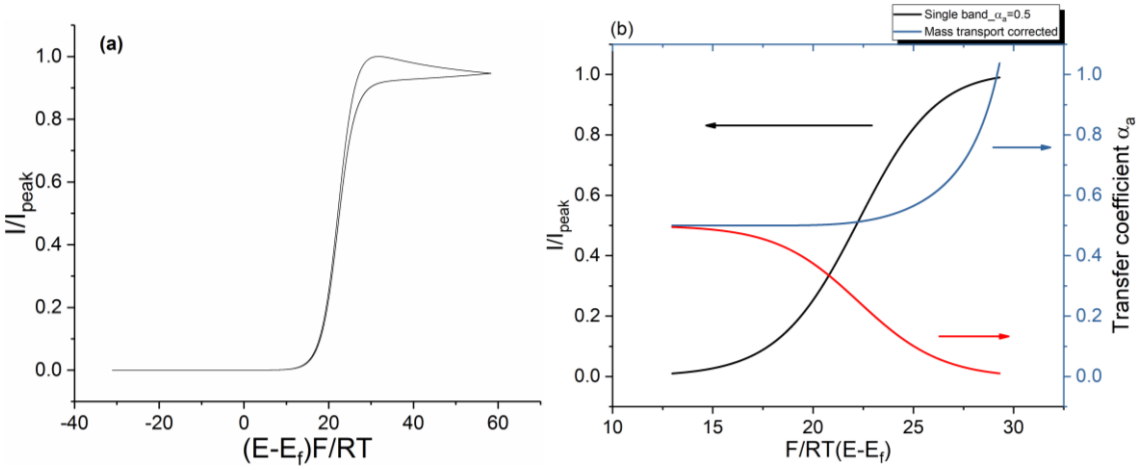


Figure 4.16 (a) Voltammogram on a microband electrode. (b) Effect of analytical mass-transport correction on the measured transfer coefficient (Black: oxidative wave; Red: measured transfer coefficient; Blue: mass-transport corrected transfer coefficient). The current range in (b) is 1% - 99% of steady-state current. The dimensionless scan rate $\sigma = 2.43 \times 10^{-6}$. The dimensionless rate constant $K = 5 \times 10^{-6}$. Transfer coefficients $\alpha_a = \alpha_c = 0.5$ in the simulation.

Figure 4.16(b) presents the oxidative wave normalised relative to its peak current (black curve) and the variation of measured non-mass-transport corrected transfer coefficient $\alpha_{a,nc}$ as a function of dimensionless potential (red curve). The effect of analytical mass-transport correction on the transfer coefficient on a single microband electrode (blue curve in Figure 4.16(b)) is similar to that on a hemicylindrical microelectrode. This is due

to both the quasi-steady state condition rather than a true steady state and the non-uniformly accessibility of the single microband. According to the results of the calculated fraction of the oxidative wave at given errors in transfer coefficient, with analytical mass-transport correction, the fraction of the peak current can be improved from 4.9% to 64.5% in Tafel analysis with less than 5% error in transfer coefficient. Similar to hemicylindrical electrodes, the analytical correction works better at lower dimensionless scan rates due to the increased radial diffusion to the electrode.

Voltammograms with other different transfer coefficients (α_a=0.3, 0.4, 0.6 and 0.7) with a given dimensionless scan rate of 2.43×10^{-6} and a given dimensionless rate constant of 5×10^{-6} were also simulated and analysed via the same method. A similar trend was observed in the case of the measured non mass-transport corrected transfer coefficient as shown in Figure 4.17. However, unlike the results for other geometries, the fraction of the oxidative wave which can be used in Tafel analysis at given errors increases with a larger transfer coefficient after analytical mass-transport correction. For example, from the data shown in Table 4.13 and 4.14, up to 82% of the oxidative current can be used in Tafel analysis with a 10% error in transfer coefficient when α_a equals to 0.7.

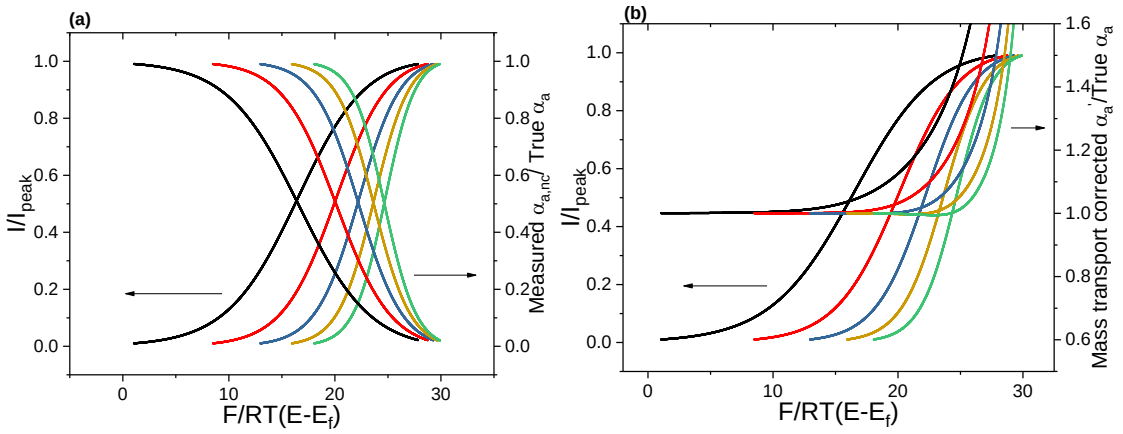


Figure 4.17 (a) The normalised measured transfer coefficient plots of single band with various true transfer coefficients. (b) The normalised mass-transport corrected transfer coefficient plots of single band with various true transfer coefficients Black: $\alpha_a = 0.3$, red: $\alpha_a = 0.4$, blue: $\alpha_a = 0.5$, brown: $\alpha_a = 0.6$, green: $\alpha_a = 0.7$. The current range: 1% - 99% of peak current. The dimensionless rate constant $K = 5 \times 10^{-6}$; the dimensionless scan rate $\sigma = 2.43 \times 10^{-6}$; $\alpha_c + \alpha_a = 1$.

Table 4.13 Fractions of the oxidative wave at a given error in transfer coefficient without analytical mass-transport correction.

True α_a	**-1% error**	**-5% error**	**-10% error**	**-20% error**
0.3	1.0%	5.1%	10.3%	20.7%
0.4	1.0%	5.0%	10.1%	20.3%
0.5	<1.0%	4.9%	10.0%	20.0%
0.6	<1.0%	4.9%	9.8%	19.8%
0.7	<1.0%	4.8%	9.6%	19.5%

Table 4.14 Fractions of the oxidative wave at a given error in transfer coefficient with analytical mass-transport correction.

True α_a	+1% error	+5% error	+10% error	+20% error
0.3	22.4%	55.4%	72.0%	85.9%
0.4	30.1%	60.1%	74.9%	87.3%
0.5	38.4%	64.5%	77.6%	88.5%
0.6	46.2%	68.5%	79.9%	89.6%
0.7	53.2%	72.0%	82.0%	90.6%

4.5 Conclusions

For all electrode geometries, and in the absence of mass-transport correction to the resulting flux, the measured non mass-transport corrected transfer coefficient deviates significantly from its true value even when only currents less than 10% of the steady-state or peak current are analysed in Tafel analysis. The exact fraction of the voltammetric wave that can be used in Tafel analysis is sensitive to the electrode geometry and the prevailing mass-transport regime. Due to the variation of $\alpha_{a,nc}$ as a function of potential as a result of the influence of mass transport, care must be taken in analysing such data so as to not wrongly conclude that curvature in such Tafel plots reflects a sensitivity of the underlying transfer coefficient to the electrode potential.

The use of a plot of $ln\left|\frac{1}{I}-\frac{1}{I_{lim}}\right|$ against θ to provide a mass-transport corrected Tafel plot is strictly only applicable to cases where the electrode is uniformly accessible and is

under a true steady-state diffusion regime. The use of such a mass-transport corrected Tafel plot even for micro-disc electrodes is found to potentially result in significant errors in the measured transfer coefficient (up to 19%). For the quasi-steady-state regimes with specific dimensionless constants, the fraction of the voltammetric wave can be improved to 48.3% (micro-hemicylinder) and 77.6% (single microband) with less than 10% error in transfer coefficient after this analytical correction. Moreover, such an analytical mass-transport correction completely fails when applied to voltammetry measured under a linear diffusion regime (macroelectrode). The new empirical mass-transport correction presented allows an improved estimation of the transfer coefficient for macroelectrode geometry.

References:

[1] D. Li, C. Lin, C. Batchelor-McAuley, L. Chen, R. G. Compton, *Journal of Electroanalytical Chemistry* **2018**, *826*, 117-124.

[2] aF. Scholz, *Electroanalytical Methods: Guide to Experiments and Applications*, Springer Berlin Heidelberg, **2009**; bM. C. Henstridge, R. G. Compton, *Journal of Electroanalytical Chemistry* **2012**, *681*, 109-112.

[3] aR. Guidelli, R. G. Compton, J. M. Feliu, E. Gileadi, J. Lipkowski, W. Schmickler, S. Trasatti, *Pure and Applied Chemistry* **2014**, *86*, 245-258; bR. Guidelli, R. G. Compton, J. M. Feliu, E. Gileadi, J. Lipkowski, W. Schmickler, S. Trasatti, *Pure and Applied Chemistry* **2014**, *86*, 259-262.

[4] S. Fletcher, *Journal of Solid State Electrochemistry* **2008**, *13*, 537-549.

[5] aW. Sheng, H. A. Gasteiger, Y. Shao-Horn, *Journal of The Electrochemical Society* **2010**, *157*, B1529; bD. V. Esposito, S. T. Hunt, A. L. Stottlemyer, K. D. Dobson, B. E. McCandless, R. W. Birkmire, J. G. Chen, *Angew Chem Int Ed Engl* **2010**, *49*, 9859-9862.

[6] R. G. A. B. Compton, Craig E, *Understanding Voltammetry*, third ed., World Scientific, **2018**.

[7] C. Batchelor-McAuley, R. G. Compton, *Journal of Electroanalytical Chemistry* **2012**, *669*, 73-81.

[8] aR. A. Marcus, *The Journal of Chemical Physics* **1965**, *43*, 679-701; bR. A. Marcus, N. Sutin, *Biochimica et Biophysica Acta (BBA) - Reviews on Bioenergetics* **1985**, *811*, 265-322; cN. S. Hush, *The Journal of Chemical Physics* **1958**, *28*, 962-972.

[9] E. Laborda, M. C. Henstridge, C. Batchelor-McAuley, R. G. Compton, *Chemical Society Reviews* **2013**, *42*, 4894-4905.

[10] V. Mirceski, E. Laborda, D. Guziejewski, R. G. Compton, *Analytical Chemistry* **2013**, *85*, 5586-5594.

[11] aM. C. Henstridge, E. Laborda, Y. Wang, D. Suwatchara, N. Rees, Á. Molina, F. Martínez-Ortiz, R. G. Compton, *Journal of Electroanalytical Chemistry* **2012**, *672*, 45-52; bE. Laborda, M. C. Henstridge, R. G. Compton, *Journal of Electroanalytical Chemistry* **2012**, *681*, 96-102.

[12] aJ. M. Savéant, D. Tessier, *Journal of Electroanalytical Chemistry and Interfacial Electrochemistry* **1975**, *65*, 57-66; bC. E. D. Chidsey, *Science* **1991**, *251*, 919-922.

[13] aT. Erdey-Grúz, M. Volmer, **1930**, *150A*, 203; bJ. Butler, *Transactions of the Faraday Society* **1924**, *19*, 729-733.

[14] aO. V. Klymenko, R. G. Compton, *Journal of Electroanalytical Chemistry* **2004**, *571*, 207-210; bN. V. Rees, J. A. Alden, R. A. W. Dryfe, B. A. Coles, R. G. Compton, *The Journal of Physical Chemistry* **1995**, *99*, 14813-14818.

[15] A. D. McNaught, A. Wilkinson, *Compendium of chemical terminology, Vol. 1669*, Blackwell Science Oxford, **1997**.

[16] W. J. Albery, *Philosophical Transactions of the Royal Society of London. Series A, Mathematical and Physical Sciences* **1981**, *302*, 221-235.

[17] aM. Rudolph, *Journal of electroanalytical chemistry and interfacial electrochemistry* **1991**, *314*, 13-22; bM. Rudolph, *Journal of Electroanalytical Chemistry* **1992**, *338*, 85-98; cM. Rudolph, *Journal of Electroanalytical Chemistry* **1994**, *375*, 89-99.

[18] O. V. Klymenko, R. G. Evans, C. Hardacre, I. B. Svir, R. G. Compton, *Journal of Electroanalytical Chemistry* **2004**, *571*, 211-221.

[19] C. Amatore, B. Fosset, *Analytical Chemistry* **1996**, *68*, 4377-4388.

[20] R. G. Compton, E. A Laborda, K. R. A Ward, *Understanding Voltammetry: Simulation of Eelctrode Processes*, Imperial College Press, **2013**.

[21] C. Batchelor-McAuley, M. Yang, E. M. Hall, R. G. Compton, *Journal of Electroanalytical Chemistry* **2015**, *758*, 1-6.

[22] N. Eliaz, E. Gileadi, *Physical Electrochemistry: Fundamentals, Techniques, and Applications*, Wiley, **2019**.

[23] I. Streeter, R. G. Compton, *Electrochimica acta* **2007**, *52*, 4305-4311.

[24] Y. Saito, *Review of Polarography* **1968**, *15*, 177-187.

[25] aJ. D. Seibold, E. R. Scott, H. S. White, *Journal of Electroanalytical Chemistry and Interfacial Electrochemistry* **1989**, *264*, 281-289; bC. A. Amatore, B. Fosset, M. R. Deakin, R. M. Wightman, *Journal of Electroanalytical Chemistry and Interfacial Electrochemistry* **1987**, *225*, 33-48.

Chapter 5

Some Thoughts about Reporting the Electrocatalytic Performance of Nanomaterials

Chapter 4 explored the use of Tafel analysis which is widely used for evaluating electro-catalysts. In this chapter, we further develop, more generally, some thoughts on reporting electrocatalytic activity of electrocatalysts, at least, from an electrochemical perspective, which are (surprisingly) often presented incorrectly in the ever expanding literature on electrocatalysts. In particular, we have been stimulated to consider the topic of this work by an Editorial[1] in ACS Nano which recently provided 'guidance' on the 'best practices' for the measuring and reporting the activity of new electrocatalytic materials. In the following we do not seek to provide an alternative set of 'best practice guidelines' nor a 'set of materials characterisation requisites' – this is likely ultimately an appropriate activity for an IUPAC committee – but rather correct, amplify and develop the discussion provided by the Editors of ACS Nano highlighting areas where we believe additional input is desirable and helpful. We focus on six topics that relate to recommendations made in the Editorial. In each section we start by making a brief statement that we believe is correct but different to that made by D. Voiry *et al* [1]. This statement is then followed by a more in-depth discussion and exploration of the issue at hand.

This work presented in this chapter has been published as a first author paper in *Applied Materials Today*[2] and was carried out in collaboration with Dr. Christopher Batchelor-McAuley.

5.1 Standard, formal and equilibrium potentials

The standard redox potential is <u>not</u> under most conditions equivalent to the equilibrium potential. The standard potential is the equilibrium electrode potential defined at standard conditions (STP) with all the electroactive species at unit activity and gases at standard pressure (assuming ideal behaviour of the gas).

The following definitions are vital to aspects discussed later. To maintain a level of clarity we focus on the example of a simple one electron transfer process as given by:

$$A(aq) + e^- = B(aq) \tag{5.1}$$

For this reaction the Nernst equation for the electrode potential (E) is:

$$E = E^{\ominus}_{A/B} - \frac{RT}{F} ln \frac{a_B}{a_A} \tag{5.2}$$

where a_i is the activity for the i^{th} species and $E^{\ominus}_{A/B}$ is the standard redox potential of the A/B redox couple. This latter value is directly related to the standard Gibbs energy of the reaction. If we express the solution phase activities of these electroactive solutes in terms of their activity coefficients on a concentration basis then using the expression $a_i = \gamma_i c_i / c^{\ominus}$, where $c^{\ominus}$ is the standard concentration (1 mol dm^{-3}) we can write:

$$E = E^{\ominus}_{A/B} - \frac{RT}{F} ln \frac{\gamma_B}{\gamma_A} - \frac{RT}{F} ln \frac{c_B}{c_A} \quad (5.3)$$

where γ_i is the activity coefficient and noting that the standard concentration terms have cancelled out, in cases where the stoichiometry of the reaction is not unity this is not the case. The formal (aka conditional) potential ($E^{\ominus}_{f,A/B}$) of the A/B couple is then:

$$E^{\ominus}_{f,A/B} = E^{\ominus}_{A/B} - \frac{RT}{F} ln \frac{\gamma_B}{\gamma_A} \quad (5.4)$$

First, the formal potential is not a fixed value solely dependent on the A/B couple but is specific to a given set of experimental conditions. If the activity coefficients of the electroactive species change, the formal potential is correspondingly altered. For this one-electron case only if $\frac{\gamma_B}{\gamma_A} = 1$ does the standard potential equal the formal potential. Second, in contrast to the above case where both the reactant and product are solutes, if the reaction involves a gas then the standard and formal potentials often differ markedly.[3] This arises due to the fact that most non-polar gases (such as hydrogen or oxygen) have a low solubility in aqueous solution.[4] Hence, at one bar pressure the gas is commonly only present in solution at millimolar concentrations; in contrast, the formal potential is defined at (a possibly hypothetical)[5] unit concentration. As such the solution phase dissolved gas concentration is often three orders of magnitude different between these two definitions.

For a simple one-electron transfer process we can define the equilibrium potential as:[6]

$$E_{eq,A/B} = E^{\ominus}_{f,A/B} - \frac{RT}{F} ln \frac{c_B}{c_A} \quad (5.5)$$

Even for this simple one electron transfer reaction, Equation 5.5 is explicitly sensitive to the ratio of the oxidized (A) and reduced (B) species. If a solution contains one order of magnitude higher concentration of the product as compared to the reactant the equilibrium potential will be ~59.1 mV negative of the formal potential of the system. This may seem a moot point but the differences between these definitions become even more pronounced if an electrode reaction involves multiple steps. For example if the reaction involves the transfer of one proton per electron then the equilibrium potential varies with 59.1 mV per pH. Electrocatalytic experiments performed at near neutral pH are often far from being under standard conditions!

5.2 How should we quantify electrode-kinetics?

For a half-cell reaction the idea of the exchange current (i_0) is only directly relevant in practical situations where both the electroactive product and reactant are present in the bulk solution phase and the reaction is to some extent reversible. Consequently, we cannot use i_0 as parameter for <u>generally</u> defining electrocatalytic activity.

In electrochemistry there are two common formulations of the Butler-Volmer equation. First the more general form used by physical electrochemists which is close to that first derived by Erdey-Gruz and Volmer:[7]

$$I = -FAk^0_{A/B}\left(\mathrm{c}_{A,0}\exp\left(\frac{-\alpha_c F}{RT}\left(E - E^{\ominus}_{f,A/B}\right)\right) - c_{B,0}\exp\left(\frac{\alpha_a F}{RT}\left(E - E^{\ominus}_{f,A/B}\right)\right)\right) \qquad (5.6)$$

I is the current (A), k^0 is the standard (strictly "formal" [8]) electrochemical rate constant (m s^{-1}) and the $c_{i,0}$ is the concentration of the i^{th} species at the electrode surface. The second form, originating from work by Laidler *et al.*,[9] is regularly employed in the materials and engineering literature and is given by the expression:

$$I = -I_{0,A/B}\left(\exp\left(\frac{-\alpha_c F}{RT}\left(E - E_{eq,A/B}\right)\right) - \exp\left(\frac{\alpha_a F}{RT}\left(E - E_{eq,A/B}\right)\right)\right) \quad (5.7)$$

where $I_{0,A/B}$ is the exchange current (A) for the A/B couple. Both expressions assume that $\alpha_c + \alpha_a = 1$. The first major difference between these two equations (5.6 and 5.7) is the potential against which they are referenced; in the first the potential is measured relative to the formal potential (Equation 5.4) but the second uses the equilibrium potential (Equation 5.5). Equation 5.7 can be derived from Equation 5.6 by rearranging the definition of the equilibrium potential (Equation 5.5) to give a definition of the formal potential in terms of the equilibrium potential and by substituting this definition into Equation 5.6. Further for Equation 5.7 the surface concentration terms ($c_{i,0}$) are assumed equal to their value in bulk. At the equilibrium potential the anodic and cathodic currents are equal in size but of opposite direction summing to zero current. At this potential the current in either the anodic or cathodic direction is given by:

$$I_{0,A/B} = FAk^0_{A/B}c_A^{1-\alpha}c_B^{\alpha} \quad (5.8)$$

This so called "exchange current" has little physical significance; the rate of the reaction is controlled by both $k^0_{A/B}$ and α as expressed by Equation 5.6.

Implicit in the use of Equation 5.7 is the assumption that both the reduced and oxidized species are present in the bulk solution phase; as is the case for classical work[10] on the proton/hydrogen redox couple where both acid and dissolved hydrogen gas are present: $H^+ + e^- \rightleftarrows \frac{1}{2}H_2$. D. Voiry *et al.* emphasize the importance of estimating/measuring the exchange current (I_0), as was undertaken classically, to quantify the activity of catalysts.[11] For the H^+/H_2 reaction we can usefully define and measure the associated exchange current (I_0). But, we can see even for the one-electron example given above, if the concentration of product (c_B) is zero then neither the equilibrium potential (Equation 5.5) nor the exchange current (Equation 5.8) are defined!

If only the reactant is present in bulk solution we face the question, how do we measure I_0? This is a very commonly encountered situation, for instance when studying the hydrogen evolution reaction or the reduction of carbon dioxide where often neither hydrogen nor the products (formate, oxalate, carbon monoxide etc.) of the carbon dioxide reduction process are initially present in the bulk solution phase. Hence, any attempts to provide general guidelines for quantifying the properties of electrocatalytic materials, which are predicated on the measurement of a quantity (I_0) that is only relevant to a special situation, is not helpful. Rather for individual half reactions, $A + e^- \rightarrow B$ or $A - e^- \rightarrow B$, the measurement of k^0 and α (or equally [1-α]) is preferred.

We note that at any given potential the Principle of Microscopic Reversibility[12] requires that the anodic and cathodic reactions have the same transition state; consequently, for a

one electron transfer process $\alpha_c + \alpha_a = 1$ *when measured at the same potential*. However, for couples with significant irreversibility the values of α_c and α_a are commonly evaluated at *different* potentials for the cathodic and anodic processes respectively. Since the Principle of Microscopic Reversibility only rigorously holds at the same potential, when α_c and α_a are measured at different potentials they need not add to unity. At other potentials the relative magnitudes of α_c and α_a may vary as the character of the transition state changes, for example as solvation/adsorption or the double layer structure alters with the applied potential. Thus generally for *experimentally measured* transfer coefficients $\alpha_c + \alpha_a \neq 1$. Hence, linear extrapolation of the cathodic and anodic branches of a voltammograms to give E_{eq} and I_0 will be in error.

Finally, for multi-step reactions the mechanism and hence the associated reaction product is often potential dependent. Consider two electrode reactions that occur in parallel, a hypothetical example might be the reduction of CO_2 to either CO or formate. If the formation of say, for example, CO on some new catalysts has a (comparatively) low standard electrochemical rate constant but a high transfer coefficient and the other reaction, in this case leading to the formation of formate, has a high standard electrochemical rate constant but a low transfer coefficient then the electrochemical reaction product will be potential dependent. At low potentials the reaction with the higher standard electrochemical rate constant will dominate and in this example we will yield formate as a product. Conversely at high overpotentials the relative rates of these two processes will have switched and the dominant reaction product will be the formation

of CO. For multi-step processes the nature of the electrode reaction mechanism will often change as a function of the applied potential!

5.3 What is an overpotential?

In the case where only the electroactive reagent is present in solution and under a steady-state mass-transport regime we can use the shift in the voltammetric half-wave potential from that expected for a reversible process as a measure of the applied overpotential. However, precise calculation of this expected reversible half-wave potential for a given set of experimental conditions is not necessarily facile; this is especially true for multistep reactions.[3]

The problems outlined in the previous section relating to the exchange current also underlie an issue in the IUPAC definition of overpotential. IUPAC rigidly define the overpotential in relation to the equilibrium potential ($\eta_e = E - E_{eq}$)[6] but from Equation 5.5 if either c_A or c_B is zero then the overpotential by this definition cannot be defined! This does not however imply that the thermodynamics of such a system are also ill-defined, we just need a different definition. Generally, if an electrochemical process is described as 'reversible' under a given mass-transport regime this implies that the electrode surface concentrations of the reduced and oxidized species are well described via the Nernst equation (i.e. they are locally at equilibrium).

In the literature it is common in cases where only the reactant is present in the bulk solution to define the overpotential relative to that of the formal potential ($\eta_f = E - E_f^{\ominus}$) or even in some cases the standard potential ($\eta_s = E - E^{\ominus}$). For a simple one-electron transfer process this definition of overpotential is clear and rational with Equation 5.6 as the inspiration. For example if we consider the reversible one-electron oxidation of ferrocene methanol: $\mathrm{Fc} - \mathrm{e}^- \rightleftarrows \mathrm{Fc}^+$. Under steady-state mass-transport conditions then the voltammetric half-wave[13] potential is approximately equal to the formal potential. In cases where the diffusion coefficients of the reduced and oxidized species are equal then the reversible half-wave potential ($E_{1/2}$) is exactly equal to the formal potential of the system. For the hydrogen evolution reaction ($\mathrm{H}^+ + \mathrm{e}^- \rightleftarrows \frac{1}{2}\mathrm{H}_2$) due to the process involving the formation and breaking of chemical bonds the situation is slightly different. Here we briefly consider the case of the hydrogen evolution reaction from an aqueous strong acid solution in the absence of dissolved hydrogen in the bulk phase. The Nernst equation describing the electrode potential can be expressed as:

$$E = E_{f,H^+/H_2}^{\ominus} + \frac{RT}{F} ln \frac{c_{H^+,0}}{{c_{H_{2,0}}}^{0.5} c^{\ominus 0.5}} \tag{5.9}$$

where the square-root associated with the concentration of hydrogen reflects the stoichiometry of the reaction. Under steady-state conditions, for example as obtained using a rotating disc electrode, at the voltammetric half-wave potential i.e. where 50% of the available protons are converted to hydrogen – and again assuming equal diffusion

coefficients for the electroactive species – then the surface concentrations of the reduced (hydrogen) and oxidized (protons) species will be equal to:

$$c_{H^+,bulk} \approx 2c_{H^+,0} \approx 4c_{H_2,0} \qquad \text{at} \quad E = E_{1/2} \tag{5.10}$$

where the subscript zero refers to the surface concentrations of the species. Equation 5.10 expresses that at the voltammetric half-wave potential the surface concentration of the protons $(c_{H^+,0})$ will be half of that in the bulk media $(c_{H^+,bulk})$. Moreover, on the basis of the reaction stoichiometry the reduction of half of the protons to hydrogen at the electrode surface implies that the surface concentration of hydrogen $(c_{H_2,0})$ is equal to a quarter of the bulk proton concentration. Substitution of equality 5.10 into Equation 5.9 yields an expression for the voltammetric half wave potential $(E_{1/2})$ as equal to:

$$E_{1/2} \approx E^{\ominus}_{f,H^+/H_2} + \frac{RT}{F} ln \frac{{c_{H^+,bulk}}^{0.5}}{c^{\ominus 0.5}} \tag{5.11}$$

Equation 5.11 is only exactly correct in the case that the diffusion coefficients of the reduced and oxidized species are equal. However, the salient point is that, as a result of conservation of mass at the electrode surface and due to the reactions stoichiometry, the position of the reversible voltammetric wave is, as measured by the voltammetric half-wave potential, related to the formal potential for the reaction but varies as a function of bulk acid concentration! It is important to recognise that this sensitivity to the bulk acid concentration is not the same as that of the so-called 'Reversible Hydrogen Electrode'. To this end we highlight the square-root present in the natural log term in Equation 5.11.

5.4 What is an onset potential?

The onset potential is neither a thermodynamically nor kinetically well-defined parameter; consequently, it is unhelpful when comparing activity of electrocatalysts between laboratories and hence across different experimental setups. A likely more appropriate method is, as is done with ORR catalysts, to report the Faradaic current density at a given and agreed potential.[15]

Although the "onset potential" is a widely reported parameter and at first sight appears to have an obvious definition[16] as something akin to the 'lowest overpotential at which a reaction product is formed at a given electrode under defined conditions' or 'the lowest overpotential at which the Faradaic current is observed to be over and above the measured background' these statements belie the true complexity of the issue as the following explains. First, consider an irreversible one-electron reduction process for which:

$$I = FAk^0_{A/B} \exp\left(\frac{-\alpha F\left(E-E^{\theta}_{f,A/B}\right)}{RT}\right) c_{A,0} \tag{5.12}$$

The cathodic current is predicted to asymptotically approach zero as $E \to +\infty$ and to increase exponentially as $E \to -\infty$. Defining where such an exponential rise 'starts' necessarily requires some additional *arbitrary* definitions. Second, the general interpretation of the onset potential is the potential at which a reductive or oxidative faradaic reaction becomes *measurable*. Immediately it becomes clear that such a parameter is essentially a measure of the signal-to-noise or signal-to-background ratio of the system and hence does not solely reflect the electrocatalytic properties of the material

under study but is also influenced by the measurement conditions. To exemplify this point Figure 5.1 shows a simulated one-electron irreversible reduction at a rotating disc electrode. The employed simulation numerically calculates the voltammetric profile using a fully implicit finite difference method and makes use of the Hale transform.[17] The theoretically predicted Faradaic current is plotted in black. Also plotted are some realistic values for the capacitative current of the electrode. In particular we have approximated the electrodes capacitance as constant with respect to the applied electrode potential and supposed that the specific capacitance has value that is representative for metals in aqueous solutions (20 μF cm^{-2}).[18]

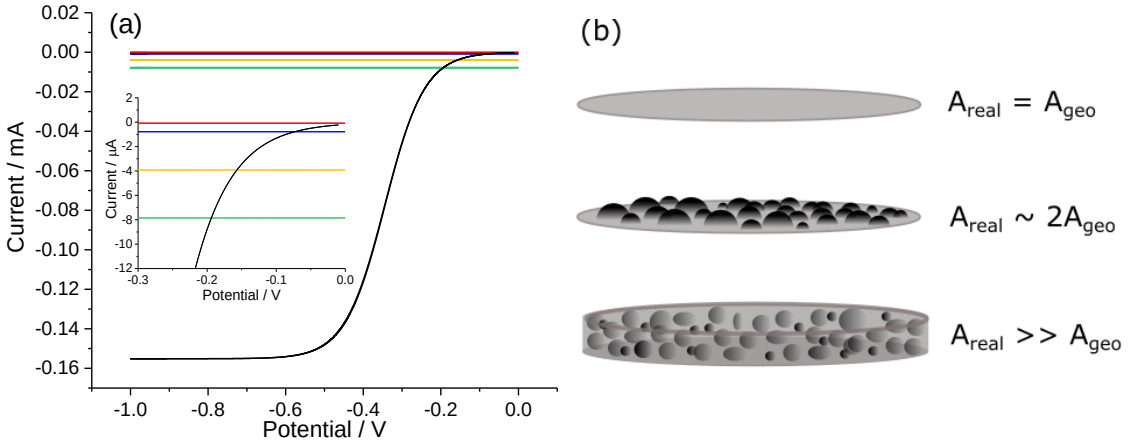


Figure 5.1: (a) Comparison of the simulated Faradaic current (black) and capacitative current at a rotating disc electrode (5 mm in diameter) with variable roughness factors (R_f), $R_f = 1$ (red), $R_f = 10$ (blue), $R_f = 50$ (yellow) and $R_f = 100$ (green). Inlay is the zoom-in version with a potential range from -0.3 V to 0 V. Parameters in the simulation: scan rate $\nu = 0.02$ V s^{-1}, rotation rate $\omega = 1600$ rpm, concentration $c = 1$ mM, diffusion coefficient $D = 1 \times 10^{-9}$ m^2 s^{-1}, formal electron transfer rate constant $k^0 = 1 \times 10^{-7}$ m s^{-1}, formal potential $E_f = 0$ V, viscosity = 8.9×10^{-7} m^2 s^{-1}, transfer coefficients $\alpha_a = \alpha_c = 0.5$. The capacitative current

$I_{cap} = C_{dl}$ (20 μF cm^{-2}) × R_f × A_{geo} × ν. (b) Schematic of electrode surface with different roughness factors. The roughness factor R_f = the real electrode area (A_{real}) / the geometric area (A_{geo}).

To calculate the total electrode area we have multiplied the simulated geometric electrode (A_{geo} / m^2) area by a roughness factor, R_f, so that $A_{real} = A_{geo} \times R_f$. As discussed later, for heterogeneous electrode surfaces another important quantity is the roughness factor which accounts only for the real area of the catalyst ($R_{f,catalyst}$). As outlined schematically in Figure 5.1 b) in the present example a perfectly atomically flat electrode would have a roughness factor of unity; a very well prepared polycrystalline electrode may be expected to have a roughness factor of ~1.5[15] and a thin-film modified RDE will have a widely variable roughness factor in the range of 10-1000. Thin-film modified electrodes find routine use in electrocatalyst experiments,[15] where a catalyst is mixed with a non-catalytic conductive support such as a form of nano-carbon and added as a thin-layer across the surface of the electrode. The capacitative charging of the carbon support and the catalyst will both contribute to the total background charging currents. As can be seen in the guidelines provided by Kocha *et al.*[15] in their experiments for a thin-film modified RDE of diameter 5 mm the total background currents are of the order of 15 μA, this corresponds to an effective roughness factor of approximately 190.

From Figure 5.1 a) we can see that if we define the onset potential in this model case as when the Faradaic current is expected to be equal in magnitude to the capacitative contribution then the potential at which this cross over occurs is *extremely* sensitive to the capacitance of the electrode. Even in this idealized case the value of the onset potential

varies by more than 200 mV for these realistic electrode capacitances. We further comment that the definition of the capacitance as being a constant, as is implied in the original editorial text, and as is used above is an over-simplification.[19]

5.5 What is the appropriate Tafel region of the current-potential plot of a half-cell reaction in which to analyse a 'Tafel slope'?

It is preferable to define a current range relative to the limiting steady state value as opposed to defining a suitable potential range for meaningful Tafel analysis giving either a transfer coefficient or, equivalently, a 'Tafel slope'. The analysis provided here indicates that provided a suitable background subtraction to remove the capacitative current contribution is first performed then the current in the range between 10-80% of the limiting current is suitable for kinetic analysis once a mass-transport correction has been made. If the latter correction is neglected only currents below ~20% of the steady-state current are suitable for use.

As described in Chapter 4, in a Tafel plot, the log of the current, $\log_{10}|i|$, is plotted against the applied potential, E. If we assume the reaction is fully irreversible and well described by the Tafel equation (Equation 5.12) then we can see for a one-electron transfer process that such a semi-log plot will have a slope that is equal to $-\alpha F/(RT \times ln10)$ and an intercept (at zero overpotential, η_f) equal to $log_{10}(FAk^0c_A)$. Originally electrocatalysis experiments were performed using a form of current-interrupt technique known as the commutator method.[20] Here a desired current density was driven to occur on a working

electrode, the cell was subsequently disconnected and the rapidly changing cell potential measured against a reference cell. Measurement of the potential of the disconnected cell as a function of the disconnection time allowed the original cell potential to be inferred by extrapolation. Hence in reporting data in terms of current/potential graphs on the y-axis the potential (the measured variable) was plotted against the current (the controlled variable).[20b] Modern experiments tend to be performed potentiometrically and hence one might expect the axes of the Tafel plot to be swapped, this is virtually never the case; old habits die hard.

A linear Tafel plot of $\log_{10}|i|$ vs E requires that, on the basis of Equation 5.6, the process is fully irreversible and that the surface concentrations of the electroactive species remain constant throughout the potential range of analysis. In practice the replenishment of the active species via diffusion is slow and distortions arise from mass-transport limitations. Consequently, it is necessary to 'correct' for these changes in the redox active species at the electrode surface. The rotating disc electrode is to a reasonable approximation[22] uniformly accessible. Consequently a plot of $\log_{10}(1/I - 1/I_{lim})$ against the applied potential allows for these changes in the surface concentration of the redox active species during the course of the scan to be suitably accounted for. The need to make a mass-transport correction has long been advocated.[23]

Figure 5.2 plots an example mass-transport corrected Tafel plot for a simulated RDE experiment. In this simulation we have assumed that the total current can be expressed

simply as the sum of both the Faradaic and non-Faradaic contributions ($I_{tot} = I_{farad} + I_{cap}$). For the solid lines in Figure 5.2 the contribution of the capacitance is assumed to be a constant ($I_{cap} = C_{dl} \times R_f \times A_{geo} \times \nu$), alternatively the dotted line assumes that the capacitance of the electrode varies linearly as a function of the applied potential, $i_{cap} = C_{dl} \times R_f \times A_{geo} \times \nu \times f(E)$, where the function f(E) is a dimensionless scalar that varies linearly between 1 and 2 across the simulated voltammetric potential range. In the absence of a background correction to removes the capacitative current Figure 5.2 shows how the mass-transport corrected Tafel plot is distorted by the presence of a capacitative "background" current.

Capacitative currents are symptomatic of the used voltammetric technique. This result first highlights the importance of background correction to remove the non-Faradaic contribution from the voltammetric data. It also gives a clear indication as to how sensitive the data will be to the quality of this correction. It is on this basis that Mayrhofer *et al.* previously proposed that the kinetically useful part of an RDE voltammogram is the mass-transport corrected current between 10-80% of the steady-state value[23b] Kocha *et al.*[24] were more cautious and on the basis of work by Vidal-Iglesias *et al.*[25], advised that only the 10-50% current regime is useable.

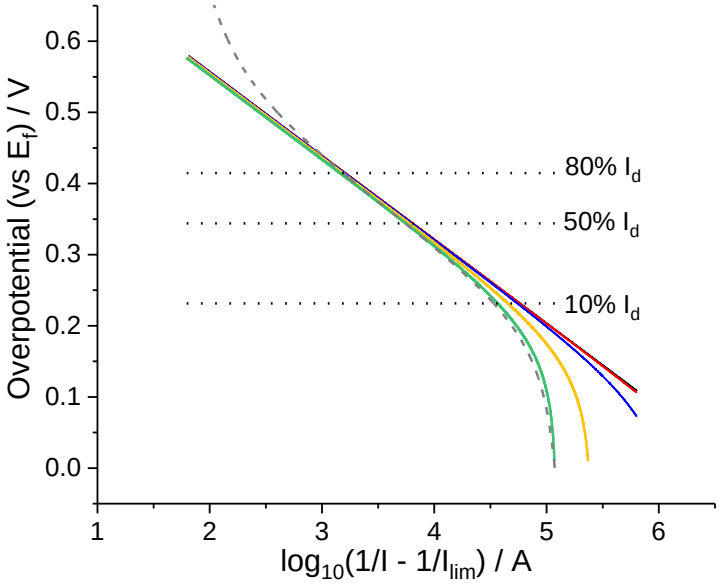


Figure 5.2 Simulated mass-transport corrected Tafel plots for a rotating disc electrode. Solid lines represent the electrode with constant capacitances with variable roughness factors R_f: $R_f = 0$ (black), $R_f = 1$ (red), $R_f = 10$ (blue), $R_f = 50$ (yellow) and $R_f = 100$ (green). The capacitative current $I_{cap} = C_{dl}$ (20 μF cm^{-2}) × R_f × A_{geo} × ν. Dashed line stands for the electrode with a variable capacitative current (grey dashed) where the variable capacitative current was calculated from $I_{cap} = C_{dl}$ (20 μF cm^{-2}) × R_f × A_{geo} × ν × f(E), where E is the electrode potential. Simulation parameters: scan rate ν = 0.02 V s^{-1}, rotation rate ω = 1600 rpm, concentration c = 1 mM, diffusion coefficient D = 1 × 10^{-9} m^2 s^{-1}, formal electron transfer rate constant k^0 = 1 × 10^{-7} m s^{-1}, formal potential $E_f = 0$ V, viscosity = 8.9 × 10^{-7} m^2 s^{-1}, transfer coefficient α = β = 0.5. $I_{tot} = I_{farad} + I_{cap}$.

5.6 Units and electrochemical surface areas

The size of the electrochemically available surface area of the catalyst is an important factor in determining meaningful information regarding its catalytic abilities if electron transfer (not mass-transport) is rate determining. Two chemically relevant quantities are the roughness factor (a dimensionless measure of the surface area of the catalyst per geometric area of the electrode) and the electrochemical surface area (the surface area

of the catalyst per gram of catalyst). Measurement of the real surface area of the catalyst is often experimentally challenging and is in some cases sensitive to how the measurement is made.

D. Voiry *et al.*[1] present both the electrochemical surface area (ECSA) and the turnover frequency (TOF) as dimensionless parameters! In the guidelines the ECSA is given as the dimensionless ratio of the specific double layer capacitance (C_{dl}) relative to a given reference surface specific capacitance, this definition seems to follow a previous article in ACS Catalysis.[26] Similarly the TOF is given as "$n_{product}$ / n_{site}";[1] how these two terms ($n_{product}$ and n_{site}) should be defined and measured is left to the reader. We note as follows, first, D. Voiry *et al.* have interpreted the ECSA as a roughness factor with a subsequent confusing conflation of terminology in the text. Second, we comment that it is essential for a surface area to contain the unit of length squared; similarly a quantity labelled as a "frequency" has units of reciprocal time. As a consequence of these non-conventional definitions some of the derived expressions provided D. Voiry *et al.* may also be usefully reconsidered.

In the literature the definition of the ECSA may vary depending on the context in which it is being used; however, following the ORR field the ECSA is probably most usefully defined as the area of the catalyst per gram of material ($m^2\ g_{catalyst}^{-1}$).[23b] This value in combination with the specific activity of the catalyst (A $m_{catalyst}^{-2}$, the catalytic Faradaic *current* in Ampere per catalyst area), yields the mass activity for the material (A $g_{catalyst}^{-1}$).

These latter two values vary as a function of potential. Consequently to get a relative measure of activity these values are often reported at a given potential. It is the value for the mass activity that most directly translates to the cost of a platinum based fuel cell device.[27] But in terms of physico-chemical insight the important factor is arguably the specific activity of the catalyst. This value of the catalysts specific activity gives a measure of the rate of reaction per unit area of the catalyst, accurate determination of the magnitude of this value is not necessarily as facile as it may seem; this is especially true if the catalytic surface is not uniformly accessible as is the case for porous electrode surfaces. Related to these values is the (dimensionless) *catalyst* roughness factor, this value is the surface area of the catalyst per geometric area of the electrode. In some contexts the roughness factor may also, *vide supra*, refer to the total surface area of the electrode relative to its geometric area.

The measurement of the surface area of the catalysts is not necessarily straightforward. Note that "best practice" documents in the field of ORR tend to only very briefly[15], if at all[23b], mention that such electrode capacitance measurements (or the measurement of other surface processes such as the under-potential deposition of hydrogen) need to be made using an analog[28] potentiostat. In the case of measuring platinum electrochemical surface areas, major errors can be made if staircase voltammetry is used and, of course, almost all modern commercial potentiostats provide staircase voltammetry as the default technique, so this can lead to the underestimation of the platinum surface area and will hence cause an overestimation regarding the material's specific activity. As an aside

similar issues arise with protein film voltammetry.[29] This issue with staircase voltammetry is often covered in potentiostat manuals;[30] but who reads a manual?[31]

5.7 Conclusions

Six topics have been discussed from electrochemical perspective. Some of the above is opinion and others in the field may dispute aspects of it. Many comments will be obvious to those in the electrochemical field but it is hoped that this chapter has clarified some of the important points.

References:

[1] D. Voiry, M. Chhowalla, Y. Gogotsi, N. A. Kotov, Y. Li, R. M. Penner, R. E. Schaak, P. S. Weiss, *ACS Nano* **2018**, *12*, 9635-9638.

[2] D. Li, C. Batchelor-McAuley, R. G. Compton, *Applied Materials Today* **2020**, *18*.

[3] X. Jiao, C. Batchelor-McAuley, E. Kätelhön, J. Ellison, K. Tschulik, R. G. Compton, *The Journal of Physical Chemistry C* **2015**, *119*, 9402-9410.

[4] E. Wilhelm, R. Battino, R. J. Wilcock, *Chemical reviews* **1977**, *77*, 219-262.

[5] Note the formal potential is still relevant for understanding the thermodynamics of electrochemical processes involving dissolved gases.

[6] E. R. Cohen, I. Mills, C. Royal Society of, T. Cvitas, P. International Union of, P. Applied Chemistry, D. Biophysical Chemistry, J. G. Frey, M. Quack, B. Holström, K. Kuchitsu, R. Marquardt, *Quantities, Units and Symbols in Physical Chemistry*, Royal Society of Chemistry, **2007**.

[7] T. Erdey-Grúz, M. Volmer, *Zeitschrift für physikalische Chemie* **1930**, *150*, 203-213.

[8] In strict accordance with IUPAC k^0 as defined here is the formal electrochemical rate constant as the used reference potential is the formal not the standard potential see ref 6.

[9] H. Eyring, S. Glasstone, K. J. Laidler, *The Journal of Chemical Physics* **1939**, *7*, 1053-1065.

[10] N. Pentland, J. M. Bockris, E. Sheldon, *Journal of The Electrochemical Society* **1957**, *104*, 182-194.

[11] S. Trasatti, *Journal of Electroanalytical Chemistry and Interfacial Electrochemistry* **1972**, *39*, 163-184.

[12] W. Thomson, *Transactions of the Royal Society of Edinburgh* **1853-1857**, *21*, 123-171.

[13] L. Meites, P. Zuman, H. W. Nurnberg, in *Pure and Applied Chemistry*, *Vol. 57*, **1985**, p. 1491.

[14] For more information on this additonal mass-transport correction to the predicted half-wave potential, the reader is directed towards ref 3. In the SI of this reference the additionally required correction for the half-wave potential is derived (Equation 12 of SI in ref.3), simply requiring the definition for the hydrodynamic layer thickness to be substituted into this expression.

[15] S. S. Kocha, K. Shinozaki, J. W. Zack, D. J. Myers, N. N. Kariuki, T. Nowicki, V. Stamenkovic, Y. Kang, D. Li, D. Papageorgopoulos, *Electrocatalysis* **2017**, *8*, 366-374.

[16] A. Maljusch, E. Ventosa, R. A. Rincón, A. S. Bandarenka, W. Schuhmann, *Electrochemistry Communications* **2014**, *38*, 142-145.

[17] aR. G. Compton, E. Laborda, K. R. Ward, *Understanding Voltammetry: Simulation Of Electrode Processes*, World Scientific Publishing Company, **2013**; bJ. M. Hale, *Journal of Electroanalytical Chemistry (1959)* **1963**, *6*, 187-197.

[18] B. B. Damaskin, A. N. Frumkin, *Electrochimica Acta* **1974**, *19*, 173-176.

[19] H. Gerischer, R. McIntyre, D. Scherson, W. Storck, *Journal of Physical Chemistry* **1987**, *91*, 1930-1935.

[20] aE. Newbery, *Journal of the Chemical Society, Transactions* **1914**, *105*, 2419-2435; bF. P. Bowden, a. E. K. Rideal, *Proceedings of the Royal Society* **1928**, *120*, 59.

[21] D. Li, C. Lin, C. Batchelor-McAuley, L. Chen, R. G. Compton, *Journal of Electroanalytical Chemistry* **2018**, *826*, 117-124.

[22] aJ. Newman, *Journal of the Electrochemical Society* **1966**, *113*, 1235-1241; bW. H. Smyrl, J. Newman, *Journal of The Electrochemical Society* **1971**, *118*, 1079-1081.

[23] aW. J. Albery, *Electrode kinetics*, Clarendon Press, **1975**; bK. J. J. Mayrhofer, D. Strmcnik, B. B. Blizanac, V. Stamenkovic, M. Arenz, N. M. Markovic, *Electrochimica Acta* **2008**, *53*, 3181-3188.

[24] K. Shinozaki, J. W. Zack, R. M. Richards, B. S. Pivovar, S. S. Kocha, *Journal of the Electrochemical Society* **2015**, *162*, F1144-F1158.

[25] F. J. Vidal-Iglesias, J. Solla-Gullón, V. Montiel, A. Aldaz, *Electrochemistry Communications* **2012**, *15*, 42-45.

[26] E. L. Clark, J. Resasco, A. Landers, J. Lin, L.-T. Chung, A. Walton, C. Hahn, T. F. Jaramillo, A. T. Bell, *ACS Catalysis* **2018**, *8*, 6560-6570.

[27] A. Kongkanand, M. F. Mathias, *The journal of physical chemistry letters* **2016**, *7*, 1127-1137.

[28] C. Batchelor-McAuley, M. Yang, E. M. Hall, R. G. Compton, *Journal of Electroanalytical Chemistry* **2015**, *758*, 1-6.

[29] H. A. Heering, M. S. Mondal, F. A. Armstrong, *Analytical chemistry* **1999**, *71*, 174-182.

[30] M.-. Autolab, pp. https://www.metrohm.com/en-gb/applications/AN-EC-007.

[31] R. G. Alethea L. Blackler, Vesna Popovic and M. Helen Thompson, **2018**.

Chapter 6

Electrochemical Measurement of the Size of Microband Electrodes: A Theoretical Study

Microband electrodes are popular in various applications, especially in sensors, since they have some of the advantages of both macro- and micro-electrodes. This work first briefly introduces the fabrication methods reported for both single microband electrodes and arrays and their uses in sensing applications. A theoretical section on band electrodes provides background information on the structure of band electrodes, their diffusional profiles and the types of voltammetric behaviour observed. Furthermore, due to the difficulties in measuring the dimensions of band electrodes, a theoretical proof-of-concept study demonstrating the use of an electrochemical method to measure the width and length of a band electrode of unknown dimensions is presented. It is found that by using a fully irreversible redox couple it is possible to characterise a band electrode without prior knowledge of the electron transfer rate constant or the formal potential. By using the peak-to-peak separation (E_{p-p}) and the magnitude of the ratio of backward peak current to forward peak current ($|I_{backward}/I_{forward}|$) as diagnostic parameters, the band width can be estimated with an error of less than 4% compared to its true value and with an error in length of less than 1%.

This work presented in this chapter consists of two first author papers which have been published in *Journal of Electroanalytical Chemistry*[1] and *ACS Sensors*[2], respectively.

6.1 Introduction

6.1.1 Background overview

Microelectrodes have, since the 1980s, attracted a lot of attention, providing new possibilities in both fundamental studies and applications, but most notably in sensors. The International Union of Pure and Applied Chemistry (IUPAC) has defined that a microelectrode has dimensions of tens of micrometres or less, down to the submicrometre range[3] whereas other terms, for example, ultramicroelectrodes and nanoelectrodes, are sometimes used in the literature to describe electrodes with dimensions less than micrometre scale. Decreasing the size of an electrode to the micron or sub-micron scale alters the voltammetric behaviour offering a number of advantageous properties over conventional macroelectrodes.[3-4] First, higher current densities are obtained due to the enhanced mass transport.[4a, 4c] Second, ohmic resistance effects decrease due to the smaller electrode size.[4a, 5] Third, microelectrodes have smaller capacitances which increases the signal-to-background ratio and improves the response time of the system. Furthermore, due to their sizes they can be applied in the measurements with samples with small volumes in, for example, medical and biological research.[6] Although the advantages of microelectrodes are clearly apparent, one drawback of the use of a single micro- or nano-disc electrode is the low absolute current output; the measured currents

are often in the nano to sub-nanoampere range. Consequently, the current measurement is sensitive to issues of electrical noise, often necessitating the use of a Faraday cage. This requirement for electrical shielding can negatively impact their applications in real world sensing devices. Micro- or nanoelectrodes with a band geometry, where the electrical interface is micro- or nanoscopic in one dimension and macroscopic in the other, can address this problem of sensitivity to electrical noise; a larger current output can be produced by simply having a longer band. In addition, the total current output can also be increased by using multiple single bands operated in parallel. These so-called band arrays can offer the same sensitivity as a single band electrode but with added benefits including higher total current output and less susceptibility to interference.

Micro- to nanoband electrodes and their arrays have been fabricated as chemical sensors[7] or biosensors[8]. Sensors are widely used in various fields for example in food processing, medical fields, environmental field, where some of criteria need to be taken into consideration for the sensor design and fabrication: 1) high sensitivity and selectivity; 2) low limit of detection (LOD); 3) ease of fabrication.[9] The first two requirements can be realised due to the above mentioned advantages of microbands (arrays), leading to an improved signal-to-noise ratio and hence improved sensitivity and lower detection limit. Additionally microband arrays own the advantages of easy fabrication compared to microelectrode arrays with other geometries and hence provide more possibilities in applications. Important examples of the use of band electrodes for analytical applications include the development of a chemical sensor based on screen printed carbon microband

electrodes requiring no further chemical modification to give a low detection limit for the determination of Pb^{2+}.[7c] A boron-doped diamond band electrode for use in end-column amperometric detection with enhanced sensitivity and lower noise level for several groups of important analytes (e.g. nitroaromatic explosives, phenols) on capillary electrophoresis microchips has been reported.[10] More recently, a capacitative biosensor with a high sensitivity and a wide dynamic detection range was fabricated using a commercialised gold interdigitated electrode array the surface of which was functionalised with 24-nucleotide DNA probes to detect DNA molecules.[11]

Beyond being of analytical value band electrodes are also of importance in fundamental research. The decreased resistance and capacitance of such electrode designs offer the possibility of investigating fast electrochemical reaction mechanisms and exploring electrochemical reactions in organic solvents with low permittivity such as toluene.[12] Another recent example of fundamental work is that by Zhang *et al.* who reported the use of gold nanoband electrodes to study the motion of silver nanoparticles.[13] Li *et al.* measured the resistance across individual carbon nanotubes in contact with and bridging across an interdigitated gold band electrode array.[14] These wide and varied uses of micro- or nano-band electrodes encourage the investigation of reproducible fabrication methods for making thinner band electrodes or electrodes made of different materials.

6.1.2 Fabrication methods

Generally single band electrodes are fabricated in a "sandwich" configuration, where a sheet of an electrode material is sandwiched between two insulating layers and the stack cut in a direction perpendicular to the sheet, exposing a band of the electrode material. The electrode materials are first deposited onto the insulating substrate using various methods, which, for example, include sputtering[5] or thermal vapour evaporation[5, 10, 15]. A second insulating layer is then either mechanically covered or surface printed (e.g. screen printing[7c, 7d, 16] or photolithography[17]) on top of the band layer. Metals, especially gold and platinum, are the most commonly used materials as the band layer to construct band electrodes because of their relatively wide commercial availability as thin sheets or foils of high purity.[18] Moreover, thin metal films can be obtained by sputtering or evaporation, which are usually applied during lithographic fabrication methods. Other materials such as graphite, carbon nanotubes (CNTs) and doped diamond have been used as electrode materials. In terms of the deposition method of the insulating layer, the fabrication methods can be categorised into two: "*mechanical fabrication*" and "*surface printed fabrication*".

6.1.2.1 Mechanical fabrication for single bands

This method is relatively simple and involves the mechanical sealing of a band layer between insulating layers which are normally commercially available, for example, microscope glass slides[5, 19], Mylar sheets[5] etc. The resulting electrodes are exposed by

polishing or cutting one edge of the electrode. For instance, single Pt microband electrodes with thicknesses of 5-20 μm were first constructed using the sandwich method by Wightman and co-workers where the platinum band was fabricated by sealing a thin platinum sheet in soft glass with a flame and one of the edge was exposed by polishing.[20] Electrical contact was achieved using silver epoxy with a conductive metal wire. The approximate thicknesses of Pt band electrodes were determined via the use of an optical microscope.[20] Apart from using commercially available metal sheets as the "filling" of the sandwich, metal nanoscopic band electrodes have also been fabricated using vapour deposition or sputtering on different substrates with the thickness of the metal film controlled by the deposition time. For example, gold and platinum nanoband electrodes with thicknesses of lower to 30 nm were fabricated by sputtering metal film onto a glass microscope slide, which was covered with another glass slide.[5] Carbon-based materials, such as graphite[5, 7d, 20] and CNTs[21] have also been fabricated into band electrodes. A graphite microband electrode was fabricated by sealing a thin sheet of graphite from the basal plane of a block of pressure-annealed pyrolytic graphite between two layers of heat-bondable plastic at 260 ^{o}C for 18 mins.[20] The direct measurement of the band width was attempted but the electron micrographs of graphite band electrode showed that parts of graphite surface were occluded by the plastic bonding material and hence the accurate measurement of band was considered impossible.[20]

6.1.2.2 Surface printed fabrication methods for single bands

Band electrodes fabricated using this method also have the 'sandwich' configuration but all layers are deposited using screen printing techniques. This allows scale up of the fabrication process. The fabrication of single screen-printed carbon microband electrodes has been reported by Williams and co-workers[22]. Here, a line of a suitable commercial conductive ink (Pt, Au, C etc.) was printed 2-8 mm wide and ~10 μm thick onto the surface of alumina tiles, followed by another coating layer of dielectric material.[22a] The corresponding platinum, gold and carbon band electrode was obtained by cutting perpendicularly to the direction of the line and a fresh surface could be obtained by snapping along a pre-scribed line.[22a] A more recent screen printed graphite microband electrode was reported by Banks and co-workers for the sensing of NADH and nitrite.[7d] A commercial carbon-graphite ink was screen printed onto a polyester flexible film, cured and the silver/silver chloride reference electrode was attached by screen printing Ag/AgCl paste onto the substrate.[7d] The whole surface was finally covered with a printed dielectric ink.[7d]

6.1.2.3 Fabrication of band arrays

A band electrode array which consists of multiple single bands can have different arrangements, for example, a regular band array with parallel alignments or a regular band array with an interdigitated arrangement. Band electrode arrays are mostly fabricated using surface printed method such as lithographic techniques due to the good

reproducibility. However, for "*mini-arrays*" which only consist of several single bands, sandwich-type band electrodes are made using the mechanical fabrication method. Dual or triple band electrodes are '*mini-arrays*' comprised of just two or three single bands positioned in parallel. These electrodes can be fabricated as multiple layers of sandwiches[19b, 23], of which the fabrication method is similar to the sandwich-type single band but with multiple layers. Bard and co-workers fabricated such closely spaced ultramicroband electrodes with effective thicknesses of 0.01-6 μm by sputter deposition of Pt onto both slides of 2 to 12 μm thick mica sheets that were mounted between glass slides.[23d] On the other hand, microband arrays with multiple single bands are often produced using surface printed method, in which case lithographic techniques[17a, 24] are the most frequently applied. The lithographic technology can effectively pattern and build thin film electrode materials, for example, platinum and gold on substrates with well-defined and reproducible dimensions. Dobson and co-workers fabricated a 13-microband channel flow electrode array, with electrodes ranging in size from the milimeter to the submicrometer scale using standard semiconductor processing methods.[24d, 25] This channel electrode array was used as a probe of mechanism and kinetics of complex electrode processes.[24d]

Band electrodes with a submicrometer width can be characterised using Optical Microscopy or Scanning Electron Microscopy (SEM)[7e, 8d]. However, the successful use of SEM requires a clear contrast between the materials of the band and the external insulating layers. Microdisc electrodes are routinely sized and characterised

voltammetrically where the magnitude of a steady-state diffusional current is used to calibrate the efficient electrode radius. For a microband electrode, rather than a single radius, there are two unknowns – the length and the width. An electrochemical method is described below to provide a general and easy approach for general use to calibrate the size of the unknown electrode.

Accurate electrode sizing measurements using a voltammetric method requires the appropriate choice of the electroactive redox couple to be used. Since a redox couple involving the transfer of multiple electrons would offer mechanistic complexity, fully reversible or irreversible redox couples which undergo single electron transfer are preferred. In particular well characterised standard redox couples such as $Ru(NH_3)_6^{2+/3+}$ and $Fe(CN)_6^{3-/4-}$ are often used to calibrate the size of both macroelectrodes and microelectrodes due to their well-known diffusion coefficients[8b]. The voltammetric behaviour of a band electrode has been studied using such standard redox couples[7e, 26]; however, the electrochemical characterisation of the electrode dimensions has not been attempted. The following reports a home-written simulation method developed specifically for a single microband electrode with the expectation that the dimensions of a band electrode can be characterised by comparing experimental and simulated voltammograms by analysing the kinetic information obtained from independent experiments. Note that the simulations are rigorous and do not depend on analogies being made between cylinders and bands.

Electrode processes in both the reversible and irreversible limits are considered. On the one hand, for a fully reversible one electron transfer process, knowledge of the electrode kinetics (standard rate constant and transfer coefficient) is not needed. The formal potential (E_f) can be estimated as the mid-point potential of forward and backward peak potentials ($E_{p(forward)}$ and $E_{p(backward)}$) in a conventional linear diffusional cyclic voltammogram. Conversely, using a fully irreversible redox couple requires that the kinetic parameters are known. However, the transfer coefficient can be easily calculated from Tafel analysis using a Tafel region corresponding to 1% to 30% of the peak current[9]. In both cases, the value of diffusion coefficient of the electroactive species can be found in the literature or measured using a microdisc electrode from steady-state voltammetry[7e, 26]. In the following, we develop a theoretical study showing the viability of the method and establish the requirements of the optimal redox couple for microband sizing to facilitate subsequent experiments. Thus, this theoretical study validates how simple voltammetric measurements can be used to characterise the length and width of a band electrode based on the use of a home-written programme by Dr Chuhong Lin.

6.2 Background theory

6.2.1 General theory background on band electrodes

For a molecule freely diffusing in solutions the mean squared distanced travelled $<X^2>$ in a time t can be expressed by the following equation (Equation 6.1):

$$< X^2 >= 2Dt \quad (6.1)$$

where D is the diffusion coefficient of the species. For a molecular species in aqueous solution at 25 ^{o}C the diffusion coefficient is often in the range of 0.1 - 10 × 10^{-9} m^2 s^{-1}, moreover most dynamic electrochemical experiments last between one and a few tens of seconds. Consequently, during the course of most voltammetric measurements the molecules in solution will have travelled on average between 10-1000 microns. This average distance travelled relative to the size of the electrode is important in determining the diffusion profile to an interface. When $<X^2>^{0.5}$ is small compared to the length scale of the electrode, the mass-transport to the interface is linear. Conversely when $<X^2>^{0.5}$ is large compared to the electrode length scale the mass-transport to the interface is convergent. The operative mass-transport regime controls the voltammetric response of the solution phase species at an electrode.

Chronoamperometry and cyclic voltammetry are two widely used techniques in electroanalysis. During the course of the experiment the characteristic distance travelled by a molecule varies as a function of time, as described by Equation 6.1. Hence, during the course of the chronoamperogram the diffusion profile will evolve; consequently, as with the current response at other electrode geometries, there is no simple expression for describing the variation of the mass-transport limited current as a function of time. However, the most commonly used result describing the chronoamperometric response for this band electrode geometry for a simple one electron oxidation or reduction, A ± e

→ B, under diffusion limited control is shown in Equation 6.2[27] with a reported error of up to 1.3% over the entire time range.

$$\frac{I(t)}{nFcDl} = \frac{1}{\sqrt{\pi\tau}} + 1, \quad \tau < \frac{2}{5} \qquad (6.2)$$

$$= \frac{\pi e^{-2\sqrt{\pi\tau}/5}}{4\sqrt{\pi\tau}} + \frac{\pi}{ln\left[(64e^{-\gamma}\tau)^{1/2} + e^{5/3}\right]}, \ \tau > \frac{2}{5}$$

where n is the number of electrons transferred, F is the Faraday constant, c is the bulk concentration of the reactant, D is the diffusion coefficient of the reactant, l is the length of the electrode, γ = 0.5772156 and $\tau = Dt/w^2$, w is the width of the band electrode, t is the time. At very short times ($\tau << 2/5$), the diffusion layer is small compared to the electrode dimensions and the diffusion is linear so the current follows the Cottrell equation; at very long times ($\tau >> 2/5$), it is found that the amperometric current response is equivalent to a hemicylinder electrode with a radius of w/4.[27]

In terms of cyclic voltammetry, microdisc electrodes, except at fast scan rates, exhibit a sigmoidal voltammetric waveshape response with a limiting steady-state current at high overpotentials.[28] The enhanced mass transport from radial diffusion results in higher flux densities at microelectrodes as compared to the macroscopic counterparts. In contrast, unlike microdisc or microspherical electrodes, the mass transport at a band electrode, where one of the dimensions is macrocopic, is less efficient! Voltammetrically this leads to a *quasi*-steady-state rather than a true steady-state regime. Consequently, for a band electrodes the voltammetric response still shows a vestigial peak and at high overpotentials where diffusion control operates the current varies with the inverse of log

of the experimental time.[29] In the limit where the width of the band is microscopic in dimensions, the magnitude of the voltammetric response is relatively insensitive to the width of the band. Here the voltammetric peak current is approximately proportional to the length of the electrode and the electrode width to the power of ~0.15.[30] This relative insensitivity to the electrode width is shown in Figure 6.1, where the current only increases by a factor of ~1.3 as the band width increases by a factor of 8. The inlay in Figure 6.1 shows the linear relationship between the logarithm of peak current and the logarithm of the band width with a gradient close to 0.15[30].

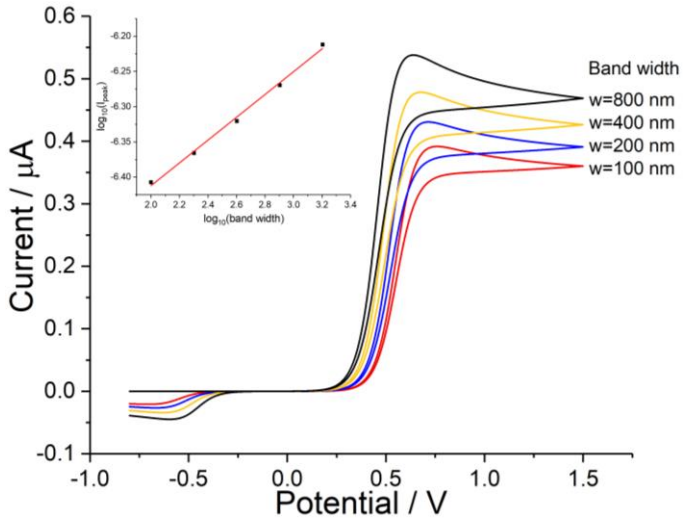
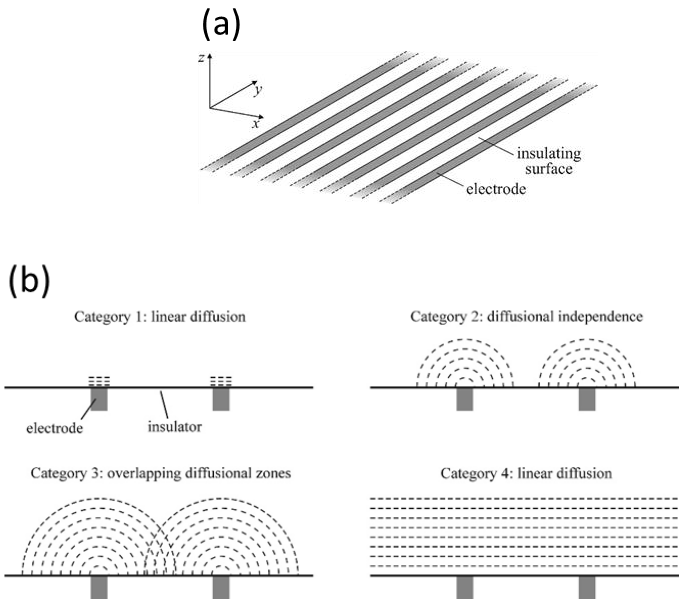


Figure 6.1 Simulated voltammograms on single band electrodes with various band widths: w = 100 nm (red), w = 200 nm (blue), w = 400 nm (yellow) and w = 800 nm (black). Parameters used in the simulations: $D = 1 \times 10^{-9}$ m^2 s^{-1}, $k^0 = 1 \times 10^{-7}$ m s^{-1}, $E_f = 0$ V, $c_{bulk} = 1$ mM, $\alpha_a = \alpha_c = 0.5$, length = 0.1 cm. The inlay shows the plot of the logarithm of the peak current as a function of the logarithm of band width. The linear relationship gives a gradient of 0.16.

A band array comprises of multiple single bands which are positioned in parallel as schematically shown in Scheme 6.1(a). The bands are microscopic in the x-direction

(band width) but macroscopic in the y-direction (length).[31] The inter-band separation is the distance between the centres of two adjacent bands in the x-direction. When multiple band electrodes are packed in parallel, unlike the diffusion profile at a single band, the diffusion fields from adjacent bands may interfere and compete with each other. The situation can be summarised into four diffusional categories as defined by Davies *et al.*[4c] which are shown in Scheme 6.1 (b)[32] and the corresponding voltammograms, at the fully irreversible limit, are shown in Figure 6.2. These voltammograms were simulated using a home-written microband programme by Dr Chuhong Lin where the diffusional regime which is operative depends on a number of factors including, the band width w, the inter-band separation $\delta_{\text{inter-band}}$, the molecular species diffusion coefficient D and the experimental time t (as often controlled by the voltammetric scan rate).[33] In category 1 which corresponds to very short times, the diffusion layer thickness is much smaller compared to the band width and band separation and the mass transport is dominated by linear diffusion. Here the magnitude of the voltammetric response is proportional to the total band area. In category 2 corresponding to longer times, the diffusion to each band is convergent and due to the large band separation, each band behaves independently. The measured total current equals to the collection of all isolated bands, where as discussed previously the magnitude of the voltammetric response is relatively insensitive to the electrode width. As is shown in Figure 6.2, the voltammetric behaviour on a band array with a band width of 100 nm and an inter-band separation $\delta_{\text{inter-band}}$ of 300 μm (black curve) is equivalent to that on a single microband electrode (gray curve) with a band width

of 100 nm at a scan rate of 0.025 V s^{-1}. However, if the inter-band separation is smaller the bands no longer remain diffusionally independent. Category 4 is the extreme of this case where the diffusion profiles overlap so significantly that the diffusional profile to the whole array becomes linear (red curve in Figure 6.3 with $\delta_{inter\text{-}band}$ of 0.3 μm) where the diffusion fields completely overlap leading to a linear concentration profile towards the entire array as a whole. The array then behaves the same as a macroelectrode with the same geometric area as the entire array. Obviously this behaviour destroys some of the benefits of using microelectrodes! Category 3 represents a transition between categories 2 and 4, where the diffusion fields overlap partially between adjacent bands, which reduces the flux at the edge of the electrodes. Examples of this case are shown as green and blue curves in Figure 6.2 where the inter-band separations $\delta_{inter\text{-}band}$ are 30 μm and 3 μm, respectively. Consequently, the highest sensitivity at a microband array (i.e. the average current measured per band) can only be obtained in category 2 due to the rapid diffusion at the band edge. The schematic shown in Scheme 6.1 focuses on regular spaced band arrays[31], whilst the voltammetric responses at *randomly* distributed microband arrays have been studied by Streeter *et al.*[32]



Scheme 6.1 (a) Schematic diagram of a section of a microband array. The theoretical array extends to infinity in both x- and z-directions.[31] (b) Schematic diagrams of diffusion categories 1-4 at a microband array.[32] Adapted with permission from refs [31] and [32]. Copyright © 2007 American Chemical Society.

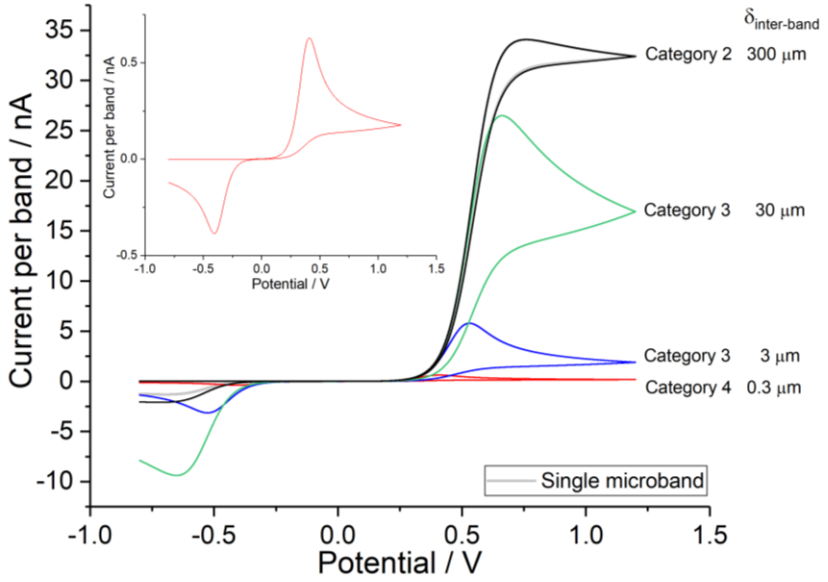


Figure 6.2 Simulated voltammograms on a single microband (gray) and microband arrays with variable inter-band separation ($\delta_{inter\text{-}band}$) at the fully irreversible limit: $\delta_{inter\text{-}band}$ = 0.3 μm (red), 3 μm (blue), 30 μm (green) and 300 μm (black). Inlay presents the zoom-in version of the voltammogram on the band electrode with the $\delta_{inter\text{-}band}$ of 0.3 μm (red). Parameters used in the simulations: band width = 100 nm, $D = 1 \times 10^{-9}$ m^2 s^{-1}, $k^0 = 1 \times 10^{-7}$ m s^{-1}, E_f = 0 V, c_{bulk} = 1 mM, $\alpha_a = \alpha_c$ = 0.5, length = 0.1 cm.

6.2.2 Numerical simulation procedures

Here we consider a heterogeneous one electron transfer oxidative process (Equation 6.3) on a microband electrode in both the fully reversible and irreversible limits:

$$A \rightleftarrows B + e^- \tag{6.3}$$

where the reactant and product are assumed to have unequal diffusion coefficients with only reactant present in the bulk solution.

A bespoke programme for single microband simulation was written by Dr Chuhong Lin so as to avoid approximating the band as a cylinder as required for example in commercial software such as DigiSim. The convergence for this programme was tested and the validation is presented in the Appendix B1. Figure 6.3(a) gives the geometry of the microband electrode. Since the length of the microband is assumed to be of a macroscale, diffusion in the y dimension can be considered constant and only the coordinates *x* and *z* are considered in the simulation. Figure 6.3(b) schematically presents the two-dimensional simulation space. The concentration distributions of the reactant as a function of time and space are found by solving the diffusion equation coupled with boundary conditions as shown in Figure 6.3(b). Dimensionless parameters are applied. The transformations between the dimensional and dimensionless parameters are listed in Table 6.1. The diffusion coefficients of the redox couples A and B are different and initially there is only the reactant in bulk solution. The boundary condition at the microband electrode is the BV equation and can be written as:

$$d_A \frac{\partial C}{\partial Z} = K^0 \exp(\alpha_a \theta)\, C_A - K^0 \exp(-\alpha_c \theta)\, C_B \tag{6.4}$$

$$d_B \frac{\partial C}{\partial Z} = -K^0 \exp(\alpha_a \theta)\, C_A + K^0 \exp(-\alpha_c \theta)\, C_B \tag{6.5}$$

where $\alpha_a + \alpha_c = 1$[24,25]. K^0 is the dimensionless form of the standard electrochemical rate constant, d_A and d_B are the dimensionless diffusion coefficients of species A and B, C_A and C_B are the dimensionless concentrations of species A and B. To simulate the cyclic voltammetry, the applied potential is defined as a function of the time as:

$$\theta = \begin{cases} \theta_i + \sigma\tau & \tau \le \frac{\theta_f - \theta_i}{\sigma} \\ \theta_f - \sigma\left(\tau - \frac{\theta_f - \theta_i}{\sigma}\right) & \tau > \frac{\theta_f - \theta_i}{\sigma} \end{cases} \tag{6.6}$$

θ_i and θ_f are the initial and final applied potentials, respectively. [θ_i, θ_f] is the voltammetric potential window. For the oxidative reaction discussed in this work, $\theta_i < \theta_f$. The dimensionless current J measured on the microband electrode is calculated from the concentration gradient at the electrode surface:

$$J = 2\int_0^1 \frac{\partial C_A}{\partial Z} dX \tag{6.7}$$

The theoretical model is numerically solved by the finite difference method and the alternating direction implicit (ADI) method[26]. The simulation program is written in Matlab R2017a and run on an Intel(R) Xeon(R) 3.60G CPU.

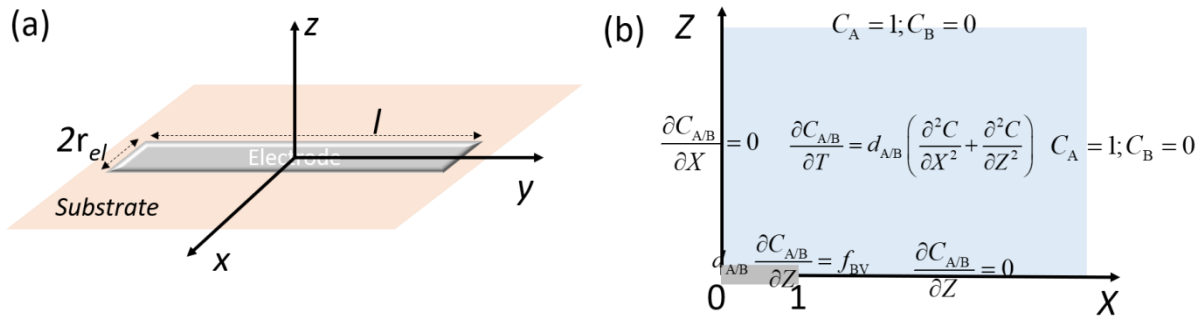


Figure 6.3 (a) A microband electrode in the Cartesian coordinate. (b) The simulation model for the redox reaction on the microband electrode. f_{BV} is the Butler-Volmer equation as written in Equations 6.4 and 6.5.

Table 6.1 Interpretation and transformation of dimensionless parameters.

SI unit parameters	**Interpretation**	**Dimensionless parameters**
r_{el} (m)	Half of the electrode width (microband);	$R_{el} = r_{el}/r_{el} = 1$
L_{el} (m)	Length of the microband	
x (m)	Space coordinate, parallel to the electrode surface	$X = x/r_{el}$
z (m)	Space coordinate, perpendicular to the electrode surface	$Z = z/r_{el}$
c_{bulk} (mM)	Concentration in the bulk solution	$C_{bulk} = c_{bulk}/c_{bulk,A}$
c (mM)	Concentration	$C = c/c_{bulk,A}$
D (m^2 s^{-1})	Diffusion coefficient	$d = D/D_A$
t (s)	Reaction time	$\tau = t*D_A/r_{el}^2$

SI unit parameters	**Interpretation**	**Dimensionless parameters**
F (C mol^{-1})	Faraday constant (96485 C mol^{-1})	
R (J · mol^{-1} · K^{-1})	Gas constant (8.3145 J · mol^{-1} · K^{-1})	
T (K)	Experiment temperature (298.2 K)	
E_f (V)	Formal potential	
E (V)	Applied electrode potential	$\theta = (E - E_f)F/(RT)$
k^0 (m s^{-1})	Standard electrochemical rate constant	$K = k^0 r_{el}/D_A$
v (V s^{-1})	Scan rate	$\sigma = vFr_{el}^2/(RTD_A)$
I (A)	Current	$J = I/(FD_A c_{bulk,A} L_{el})$

In this work, we focus on the single microband geometry, noting that although the current at a microband electrode is often approximated to that of a hemicylinder of equivalent area ($r = w/\pi$, where r is the radius of the hemicylinder and w is the width of the band), there is no true equivalence between these two geometries[4c]. In the following, we study the true, not the approximate geometry.

6.3 Results and discussion

Voltammograms on a microband electrode were simulated for the cases of both fully reversible and fully irreversible processes. We first aim to assess whether it is possible to electrochemically measure the unknown width and length of a band electrode using an

electroactive redox couple. Second, we explore how the redox couple can be used to characterise the band electrode with the minimum number of parameters known about the selected redox couple. The results presented here focus exclusively on oxidative voltammetry, but they are also equally applicable to reductive processes.

Unlike spherical or microdisc electrodes, a true steady state is impossible to obtain on band electrodes under diffusion-controlled conditions because the mass transport operates in two dimensions, one microscopic (the width) and one macroscopic (the length). This situation leads to a quasi-steady state regime[4c, 7e, 12b]; single microband electrodes exhibit quasi-steady state limiting currents at high overpotentials. The diffusional character becomes more 'linear' for a wider band electrode of a given length (l), resulting in an increasingly peaked waveshape. The magnitude of the current scales linearly with the length of the band. It is the variability of *waveshape* which gives the possibility of the measurement of width and length of a given band electrode from purely voltammetric measurements, as will be shown below.

6.3.1 Fully reversible redox couple with equal diffusion coefficients

Reaction (6.1) was first simulated as a fully reversible electron transfer process at a microband electrode where species A and B have equal diffusion coefficients. Voltammograms simulated for electrodes with variable band widths are shown in Figure 6.4(a). The voltammograms normalised to the peak current are shown in Figure 6.4(b) in order to compare the waveshapes. The diffusion coefficient used in the simulation is 7.81

$\times 10^{-10}$ m^2 s^{-1} which is the value of the diffusion coefficient of species in the ferrocenemethanol/ferrocenium methanol ($FcCH_2OH/FcCH_2OH^+$) redox couple.[34] As shown in Figure 6.4, although the waveshape becomes more peaked with wider bands, for a reversible process, the changes in the waveshape are relatively subtle. Consequently, the forward and backward peak potentials are too insensitive to the electrode dimensions to be a useful measurement technique. Hence in this work, for characterising the electrode dimensions, a reversible redox couple is not optimal for measuring the width and length of a band electrode. The following section therefore focused on simulations for fully irreversible processes where the redox couple has either equal or unequal diffusion coefficients.

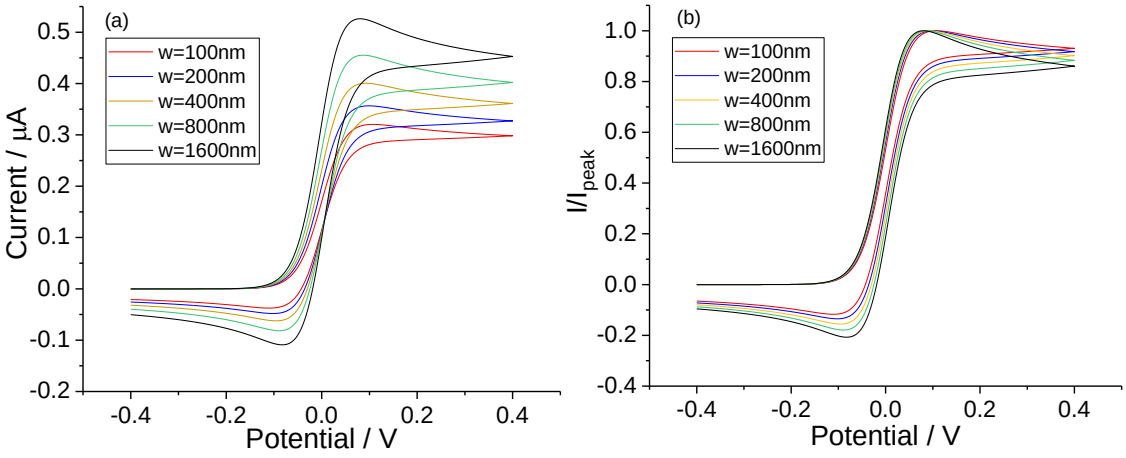


Figure 6.4 (a) Simulated voltammograms for a band electrode with variable widths for a fully reversible process. (b) Normalised voltammograms of (a). The parameters in the simulation: scan rate $\nu = 0.2$ V s^{-1}, diffusion coefficient $D = 7.81 \times 10^{-10}$ m^2 s^{-1}, formal potential $E_f = 0$ V, length of the band $l = 1 \times 10^{-2}$ m, electron transfer rate constant $k^0 = 1$ m s^{-1}, transfer coefficients $\alpha_a = \alpha_c = 0.5$.

6.3.2 Fully irreversible redox couple with equal diffusion coefficients

Voltammograms for a fully irreversible redox couple with variable electron transfer rate constant (k^0) and transfer coefficient (α_a and α_c) values on band electrodes with variable widths were simulated using the above described home-written programme. In this subsection, the reactant and product are assumed to have equal diffusion coefficients and only the reactant is taken to be present in the bulk solution. The results shown first present the cases for the anodic and cathodic transfer coefficients both equal to 0.5.

The simulated voltammograms at a given electron transfer rate constant k^0 of 1×10^{-7} m s^{-1} on a band electrode with variable widths are shown in Figure 6.5(a) as an example, with a scan rate of 0.2 V s^{-1} and anodic transfer coefficient α_a of 0.5. The low value of k^0 ensures fully irreversible electron transfer. The value of diffusion coefficient D was chosen arbitrarily as 1×10^{-9} m^2 s^{-1}. In order to compare the waveshape of electrodes with variable widths directly, the simulated voltammograms were normalised to the peak current (Figure 6.5), revealing clearly distinguishable waveshapes. The peak-to-peak separation becomes markedly smaller with increasing band width and the backward current increases for a wider band. From Figure 6.5(a) it appears that it is possible, at least in principle, to use a fully irreversible redox couple to estimate the width and length of a band electrode. Results for other k^0 values of 1×10^{-8} m s^{-1} and 1×10^{-9} m s^{-1} are shown in Figure 6.5 (b) and (c), respectively. Inspection of these data confirms the principle for other 'fully irreversible' couples albeit with different transfer coefficients, as is shown in

Figure 6.6 (α_a= 0.3), Figure 6.7 (α_a = 0.4), Figure 6.8 (α_a = 0.6) and Figure 6.9 (α_a = 0.7).

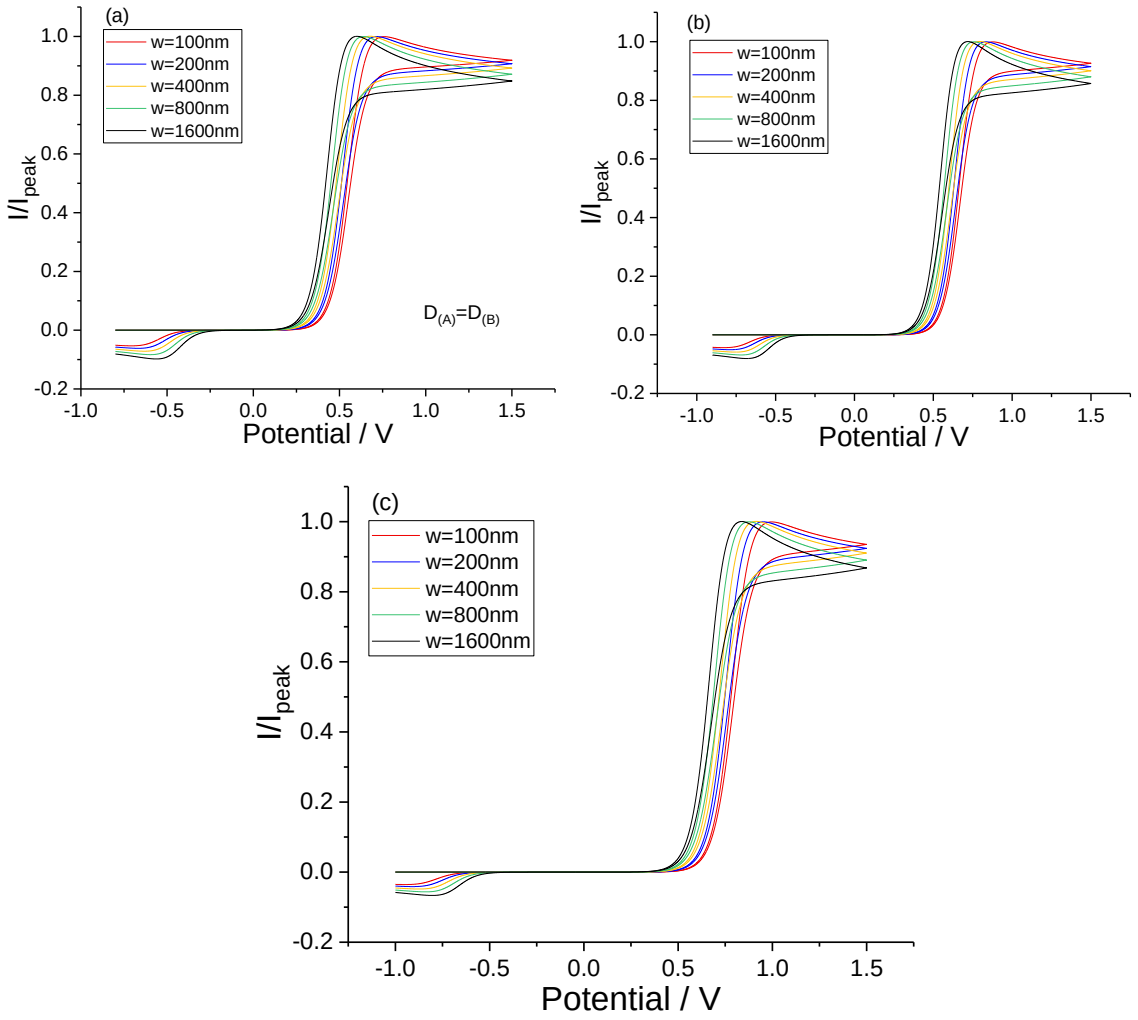


Figure 6.5 Normalised voltammograms for a band electrode with variable widths for a fully irreversible redox couple with equal diffusion coefficients with various k^0 of (a) 1×10^{-7}, (b) 1×10^{-8} and (c) 1×10^{-9} m s^{-1}. The diffusion coefficients $D_{(A)}= D_{(B)}=1\times10^{-9}$ m^2 s^{-1}. Parameters in all simulations: ν=0.2 V s^{-1}, E_f=0 V, l=1×10^{-2} m, transfer coefficients $\alpha_a = \alpha_c = 0.5$.

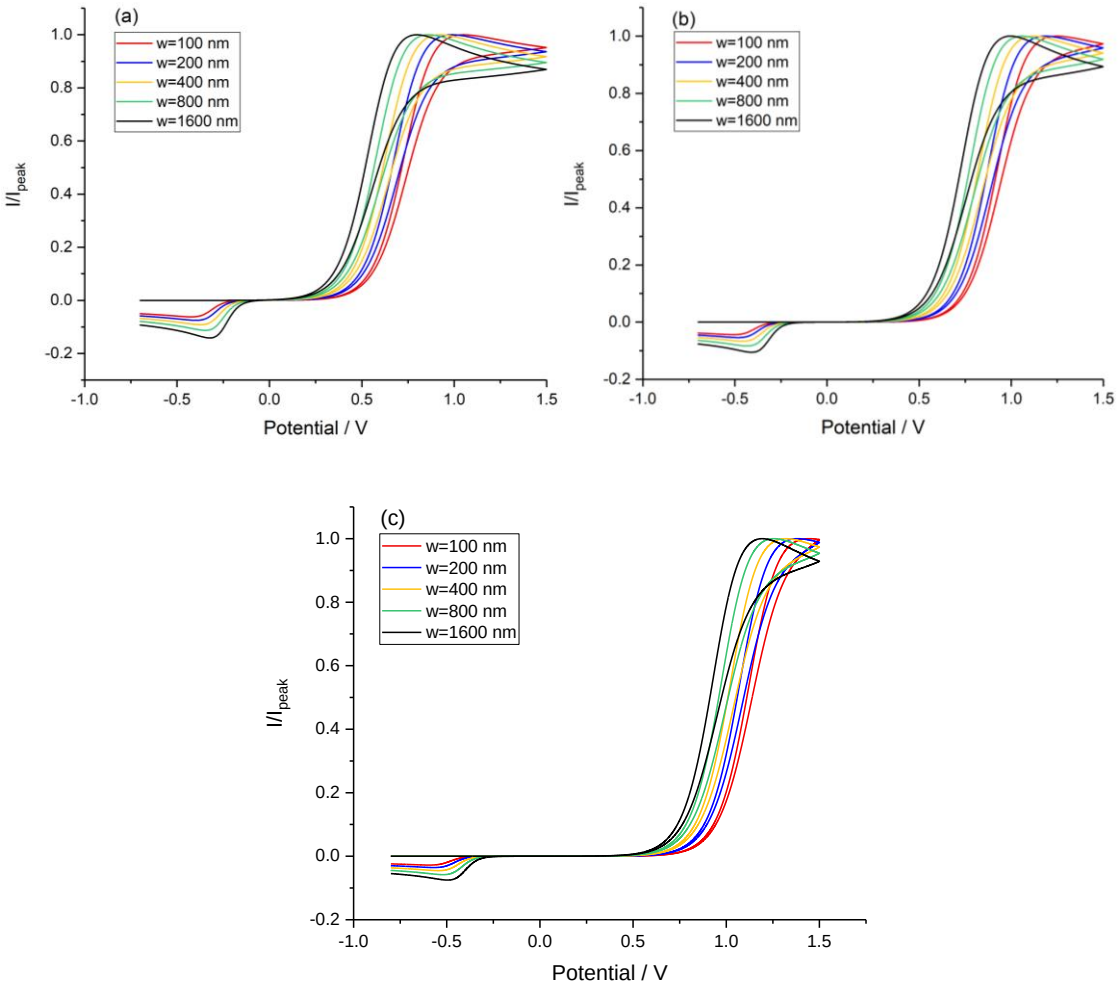


Figure 6.6 Normalised voltammograms for a band electrode with variable widths for a fully irreversible redox couple with equal diffusion coefficients with various k^0 of (a) 1×10^{-7}, (b) 1×10^{-8} and (c) 1×10^{-9} m s^{-1}. The diffusion coefficients $D_{(A)}= D_{(B)}=1\times10^{-9}$ m^2 s^{-1}. Parameters in all simulations: ν=0.2 V s^{-1}, E_f=0 V, l=1×10^{-2} m, transfer coefficients $\alpha_a = 0.3$, $\alpha_c = 0.7$.

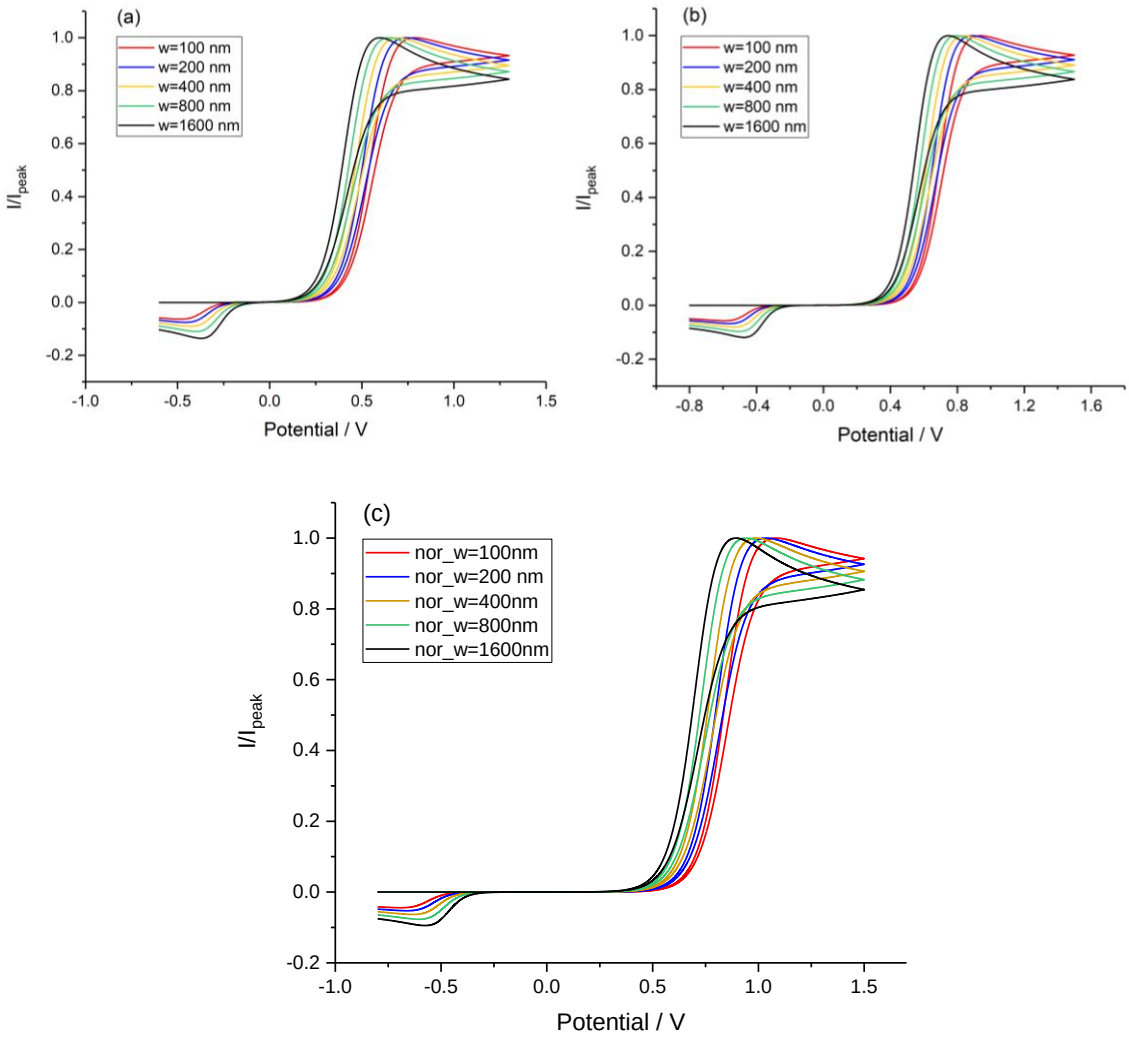


Figure 6.7 Normalised voltammograms for a band electrode with variable widths for a fully irreversible redox couple with equal diffusion coefficients with various k^0 of (a) 1×10^{-7}, (b) 1×10^{-8} and (c) 1×10^{-9} m s^{-1}. The diffusion coefficients $D_{(A)}= D_{(B)}=1\times10^{-9}$ m^2 s^{-1}. Parameters in all simulations: ν=0.2 V s^{-1}, E_f=0 V, l=1×10^{-2} m, transfer coefficients $\alpha_a = 0.4$, $\alpha_c = 0.6$.

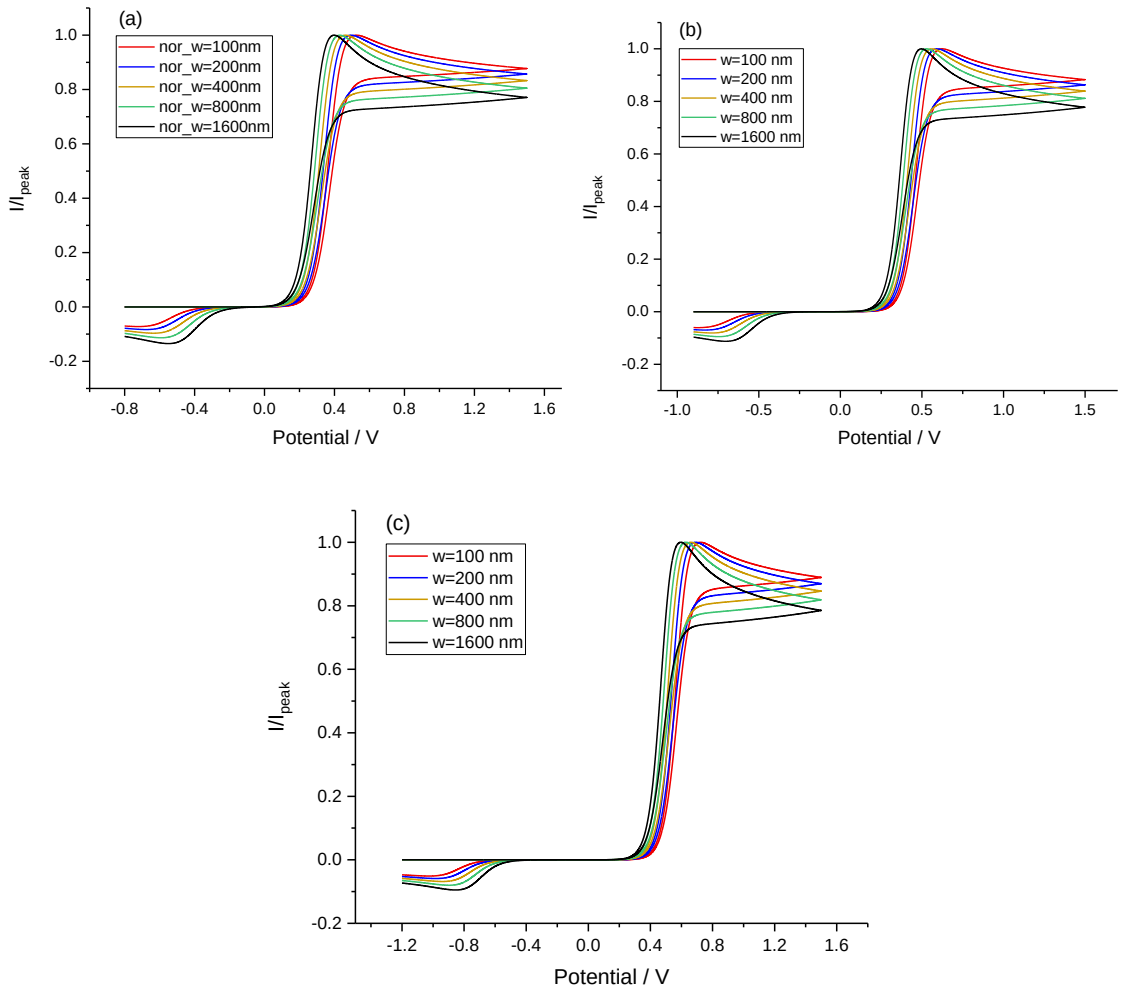


Figure 6.8 Normalised voltammograms for a band electrode with variable widths for a fully irreversible redox couple with equal diffusion coefficients with various k^0 of (a) 1×10^{-7}, (b) 1×10^{-8} and (c) 1×10^{-9} m s^{-1}. The diffusion coefficients $D_{(A)}= D_{(B)}=1\times10^{-9}$ m^2 s^{-1}. Parameters in all simulations: ν=0.2 V s^{-1}, E_f=0 V, l=1×10^{-2} m, transfer coefficients $\alpha_a = 0.6$, $\alpha_c = 0.4$.

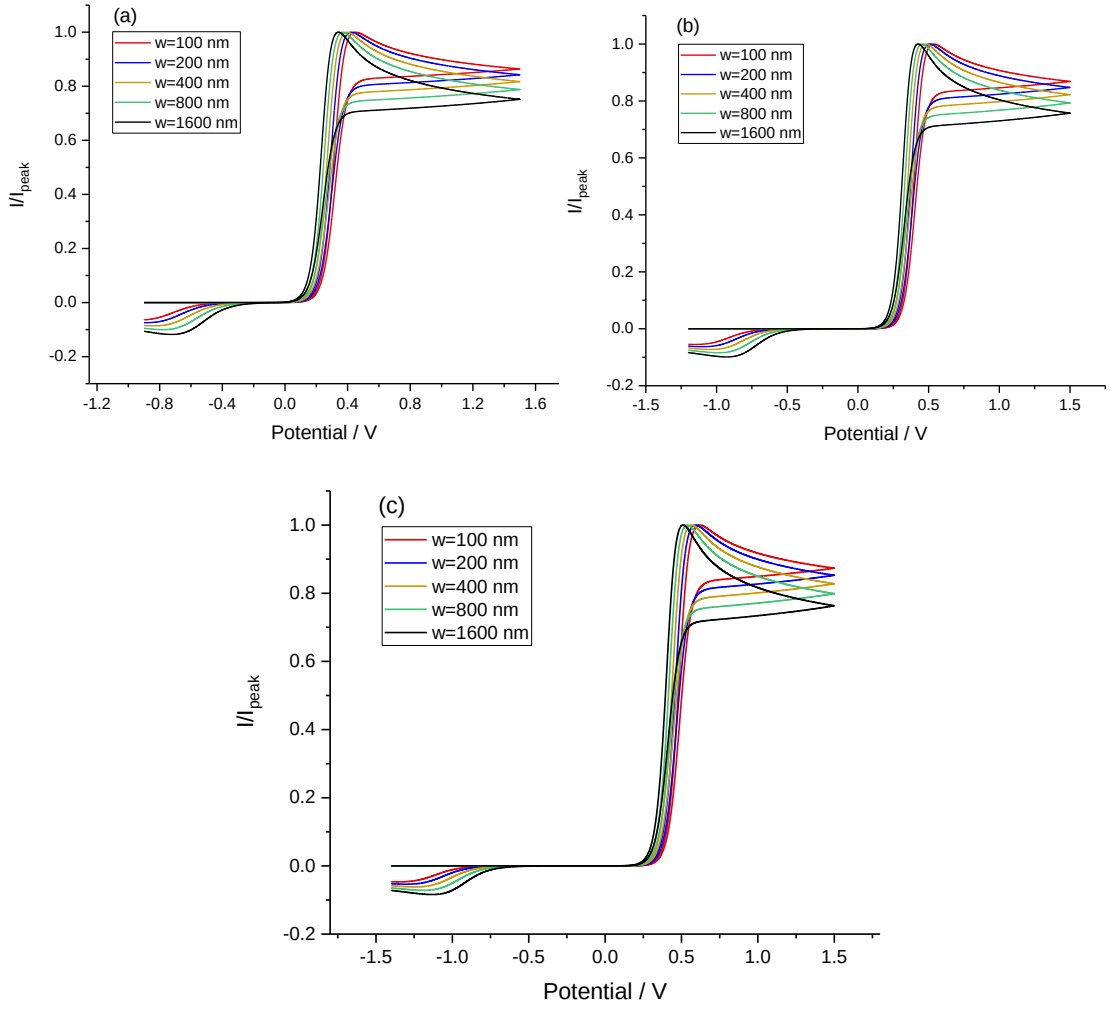


Figure 6.9 Normalised voltammograms for a band electrode with variable widths for a fully irreversible redox couple with equal diffusion coefficients with various k^0 of (a) 1×10^{-7}, (b) 1×10^{-8} and (c) 1×10^{-9} m s^{-1}. The diffusion coefficients $D_{(A)}= D_{(B)}=1\times10^{-9}$ m^2 s^{-1}. Parameters in all simulations: ν=0.2 V s^{-1}, E_f=0 V, l=1×10^{-2} m, transfer coefficients $\alpha_a = 0.7$, $\alpha_c = 0.3$.

As the length of the electrode only serves to scale the current associated with the electrode, measuring the band *width* accurately is the major task associated with characterising the electrode geometry.

The values of the forward or backward peak potentials ($E_{p(forward)}$ / $E_{p(backward)}$), the peak-to-peak separation (E_{p-p}) and the ratio of the magnitude of the backward peak current to

the forward peak current ($|I_b/I_f|$) are easily measured from an experimental voltammogram and can be used to characterise and quantify the waveshape. Consequently, plots describing $E_{p(forward)}$ or $E_{p(backward)}$, E_{p-p} and $|I_b/I_f|$ as a function of band width were considered as the diagnostic parameters via which the measurement of band width and length may be made. Since the transfer coefficient α_a and diffusion coefficient D can be relatively easily measured from experiments, the remaining unknown parameters are the formal potential E_f and electron transfer rate constant k^0. The next step in this work is to reduce the number of parameters needed for the characterisation of the geometry of band electrodes.

Considering that the use of peak potential as a diagnostic would require knowledge of the formal potential, the peak-to-peak separation was used instead. Voltammograms on a band electrode with variable k^0 were simulated, at a scan rate of 0.2 V s^{-1}, anodic transfer coefficient α_a of 0.5 and diffusion coefficient D of 1×10^{-9} m^2 s^{-1}. The corresponding plots of the two different diagnostic parameters, E_{p-p} and $|I_b/I_f|$, as a function of band width are shown in Figure 6.10. According to Figure 6.10, with a known peak to peak separation (E_{p-p}) or ratio of the magnitude of backward peak current to forward peak current ($|I_b/I_f|$), an accurate measurement of k^0 is needed to avoid a large error in the estimation of width. Consequently, the *combination* of plots of both E_{p-p} and $|I_b/I_f|$ with variable band widths were chosen as the basis for the sought discrimination. For any given band electrode, the band width estimated from the plot of E_{p-p} versus band width must be consistent with that from the plot of $|I_b/I_f|$ versus band width. In this way, by combining the measurements of

E_{p-p} and $|I_b/I_f|$, the band width can be estimated without the knowledge of formal potential E_f and electron transfer rate constant k^0. This facilitates the measurement of the band width without any prior knowledge of k^0. The parameters required for the measurement of band width using different analysing indicators are tabulated in Table 6.2.

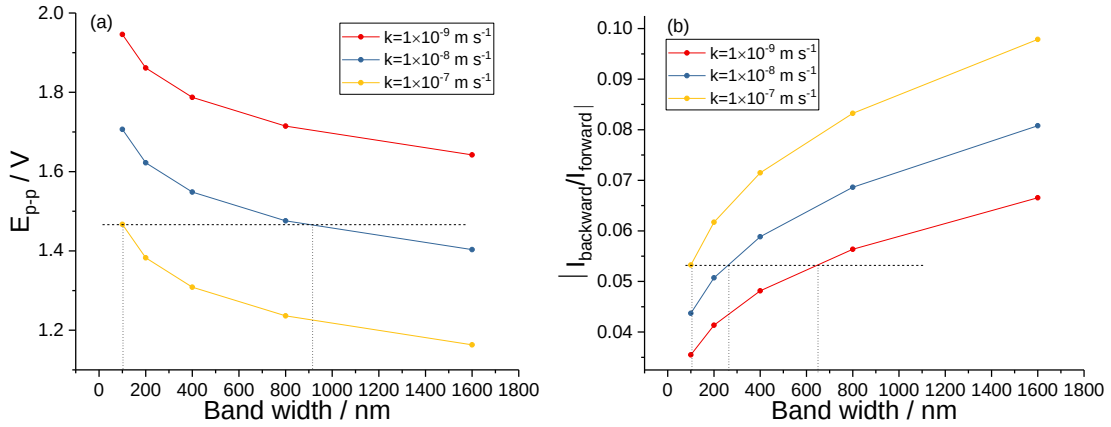


Figure 6.10 (a) Plot of E_{p-p} as a function of band widths with variable k^0. (b) Plot of $|I_{backward}/I_{forward}|$ as a function of band widths with variable k^0. Parameters in the simulations: $\alpha_a = \alpha_c = 0.5$, $D_{(A)} = D_{(B)} = 1\times10^{-9}$ m^2 s^{-1}. The dotted line shows the corresponding band width at different k^0.

Table 6.2 Parameters required for the measurement of band width and length using different indicators.

Indications	**$E_{p(forward)}$ vs E_f**	**E_{p-p}**	**$\|I_{backward}/I_{forward}\|$**	**E_{p-p} and $\|I_{backward}/I_{forward}\|$**
Parameters required	α_a	α_a	α_a	α_a
	D	D	D	D
	k^0	k^0	k^0	
	E_f			

6.3.3 Fully irreversible redox couple with unequal diffusion coefficients

Considering that the electroactive redox species might have different diffusion coefficients for the oxidised and reduced species, reaction (6.1) was also simulated on a band electrode for the case where species A and B have unequal diffusion coefficients but again only, with the reactant (A) initially present in bulk solution. Again the results shown first assume that the anodic and cathodic transfer coefficients equal 0.5. Results for other transfer coefficients are shown in Figure 6.12 (α_a= 0.3), Figure 6.13 (α_a = 0.4), Figure 6.14 (α_a = 0.6) and Figure 6.15 (α_a = 0.7), with similar conclusions drawn as to those below.

The simulated and normalised voltammograms at the various given electron transfer rate constants ($k^0 = 1\times10^{-7}$, 1×10^{-8} and 1×10^{-9} m s^{-1}) on a band electrode with variable band widths are shown in Figure 6.11(a), (b) and (c), respectively, with a scan rate of 0.2 V s^{-1}, anodic transfer coefficient α_a of 0.5, diffusion coefficient $D_{(A)}$ of 1×10^{-9} m^2 s^{-1} and diffusion coefficient $D_{(B)}$ of 5×10^{-10} m^2 s^{-1}. The comparison of waveshape was achieved through the normalisation of the voltammogram relative to the peak current.

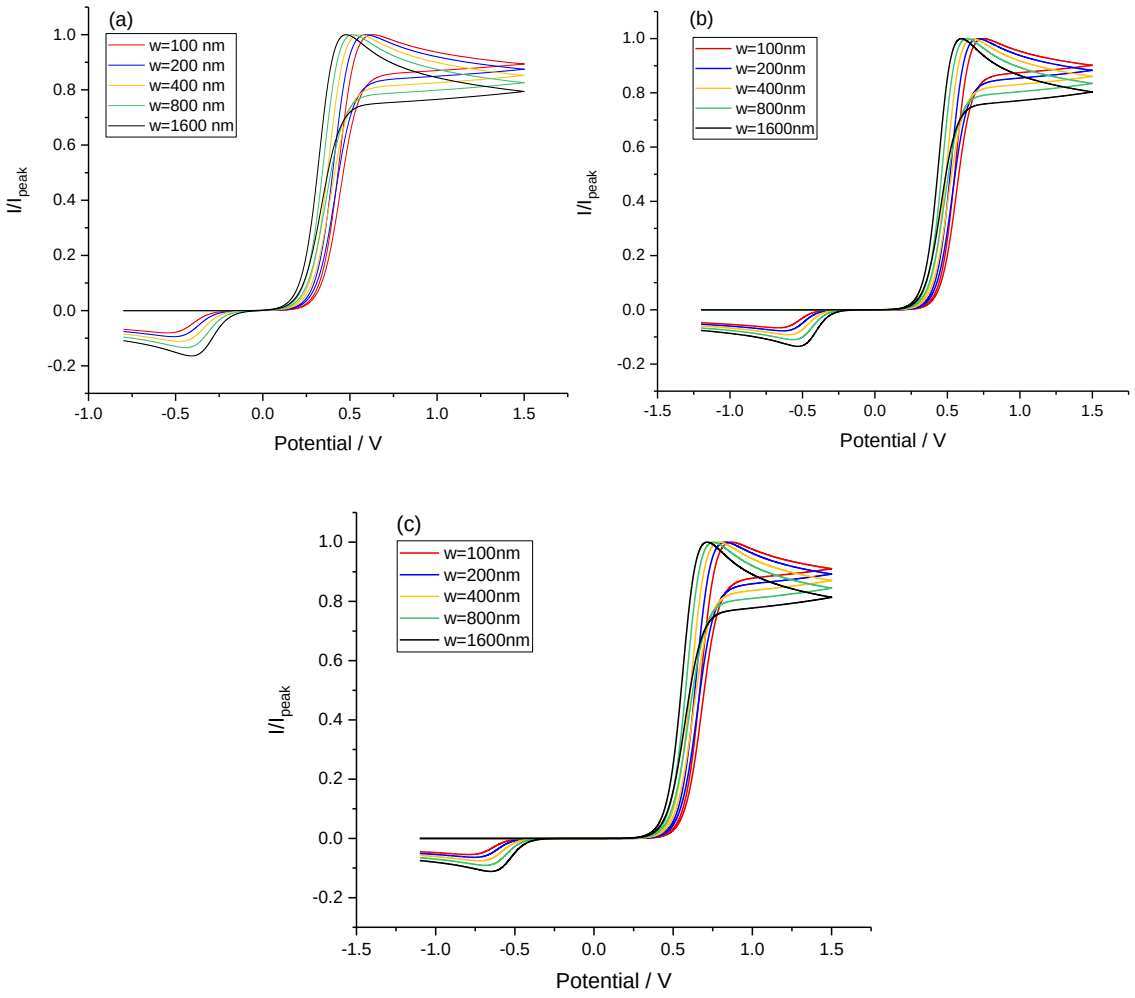


Figure 6.11 Normalised voltammograms for a band electrode with variable widths for a fully irreversible redox couple with unequal diffusion coefficients with various k^0 of (a) 1×10^{-7}, (b) 1×10^{-8} and (c) 1×10^{-9} m s^{-1}. The diffusion coefficients of A and B: $D_{(A)}=1\times10^{-9}$ m^2 s^{-1}, $D_{(B)}=5\times10^{-10}$ m^2 s^{-1}. Parameters in all simulations: $\nu=0.2$ V s^{-1}, $E_f=0$ V, $l=1\times10^{-2}$ m, transfer coefficients $\alpha_a = 0.5$, $\alpha_c = 0.5$.

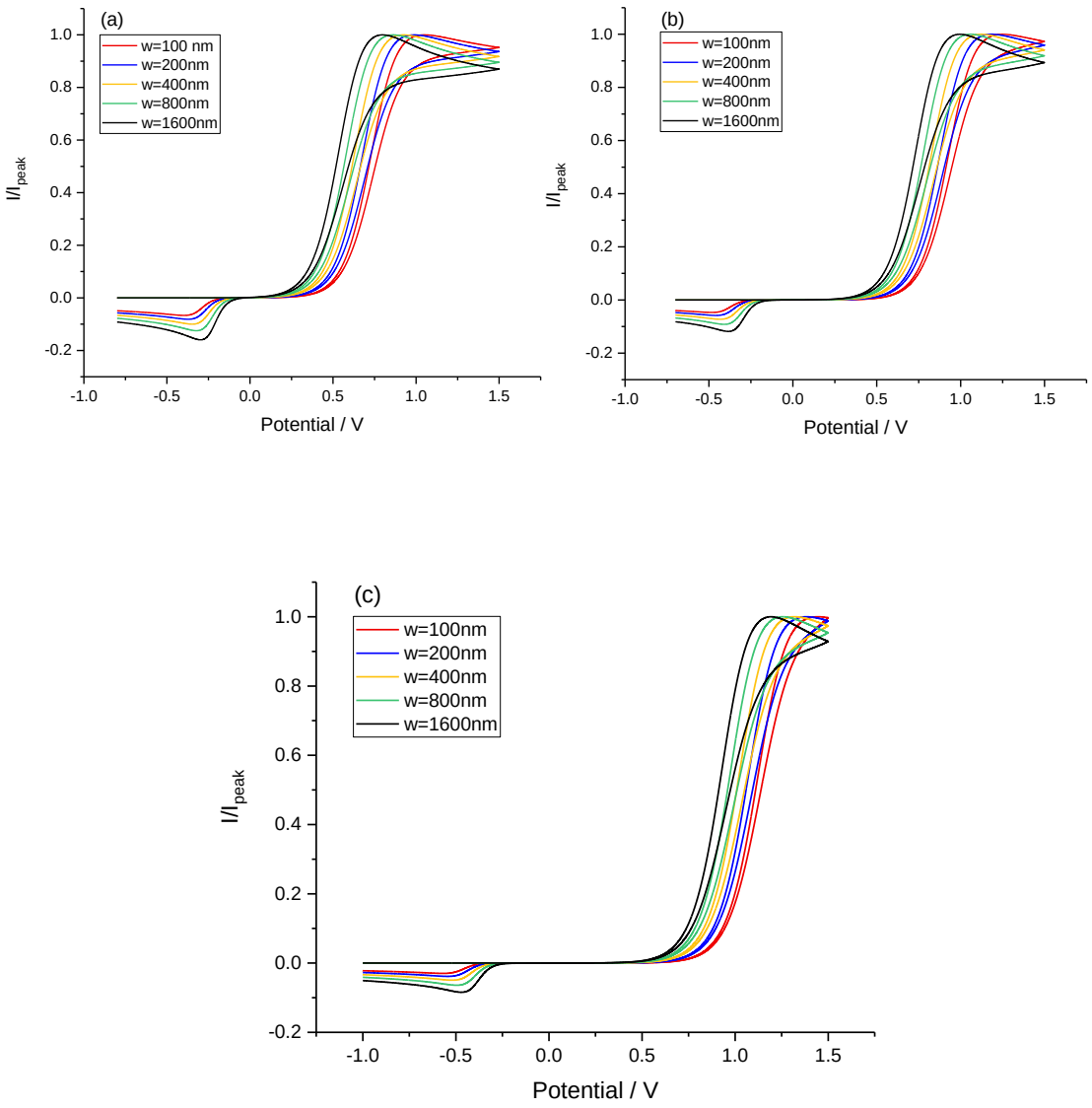


Figure 6.12 Normalised voltammograms for a band electrode with variable widths for a fully irreversible redox couple with unequal diffusion coefficients with various k^0 of (a) 1×10^{-7}, (b) 1×10^{-8} and (c) 1×10^{-9} m s^{-1}. The diffusion coefficients of A and B: $D_{(A)}=1\times10^{-9}$ m^2 s^{-1}, $D_{(B)}=5\times10^{-10}$ m^2 s^{-1}. Parameters in all simulations: ν=0.2 V s^{-1}, E_f=0 V, l=1×10^{-2} m, transfer coefficients α_a = 0.3, α_c = 0.7.

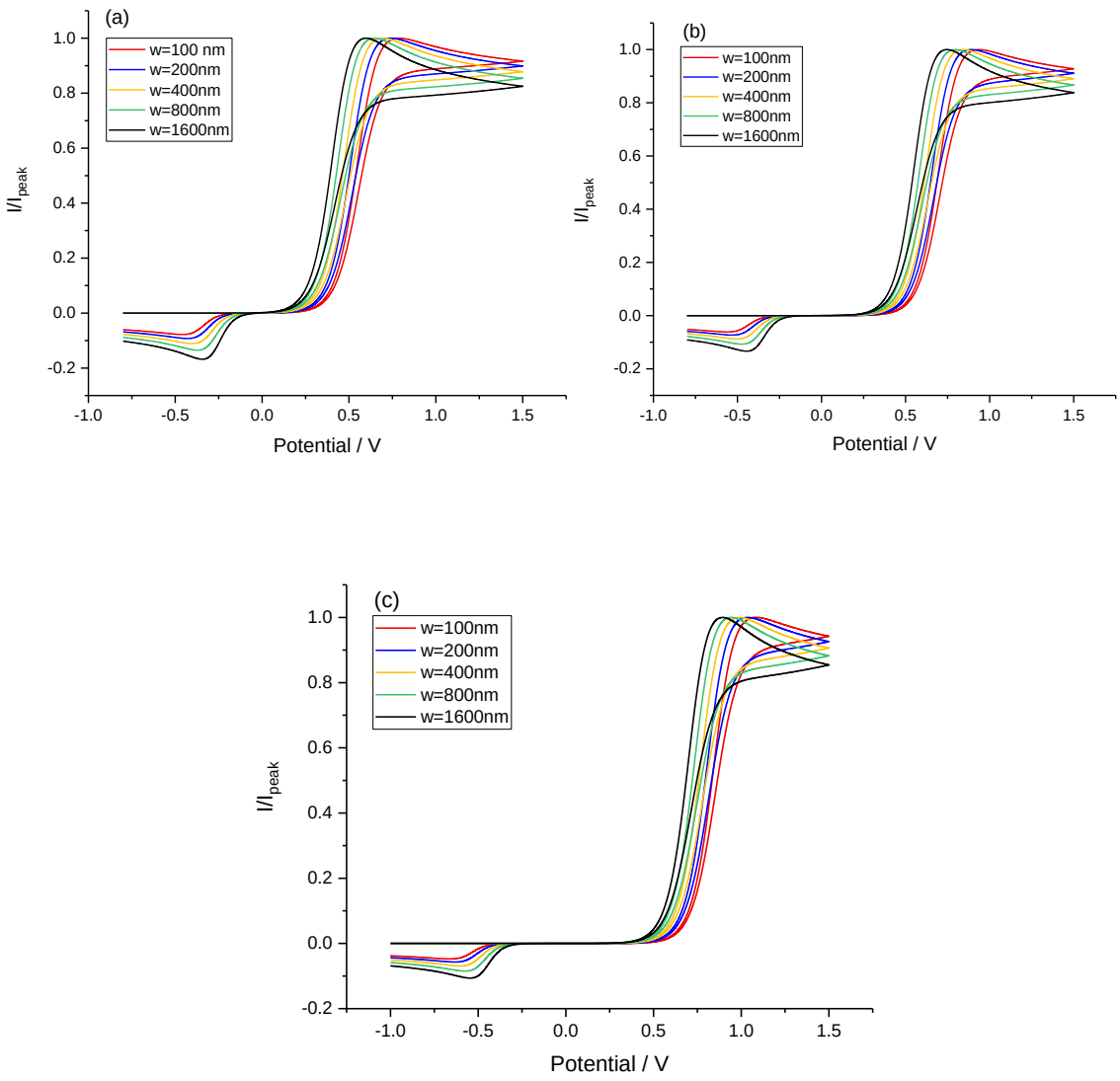


Figure 6.13 Normalised voltammograms for a band electrode with variable widths for a fully irreversible redox couple with unequal diffusion coefficients with various k^0 of (a) 1×10^{-7}, (b) 1×10^{-8} and (c) 1×10^{-9} m s^{-1}. The diffusion coefficients of A and B: $D_{(A)}=1\times10^{-9}$ m^2 s^{-1}, $D_{(B)}=5\times10^{-10}$ m^2 s^{-1}. Parameters in all simulations: $\nu=0.2$ V s^{-1}, $E_f=0$ V, $l=1\times10^{-2}$ m, transfer coefficients $\alpha_a = 0.4$, $\alpha_c = 0.6$.

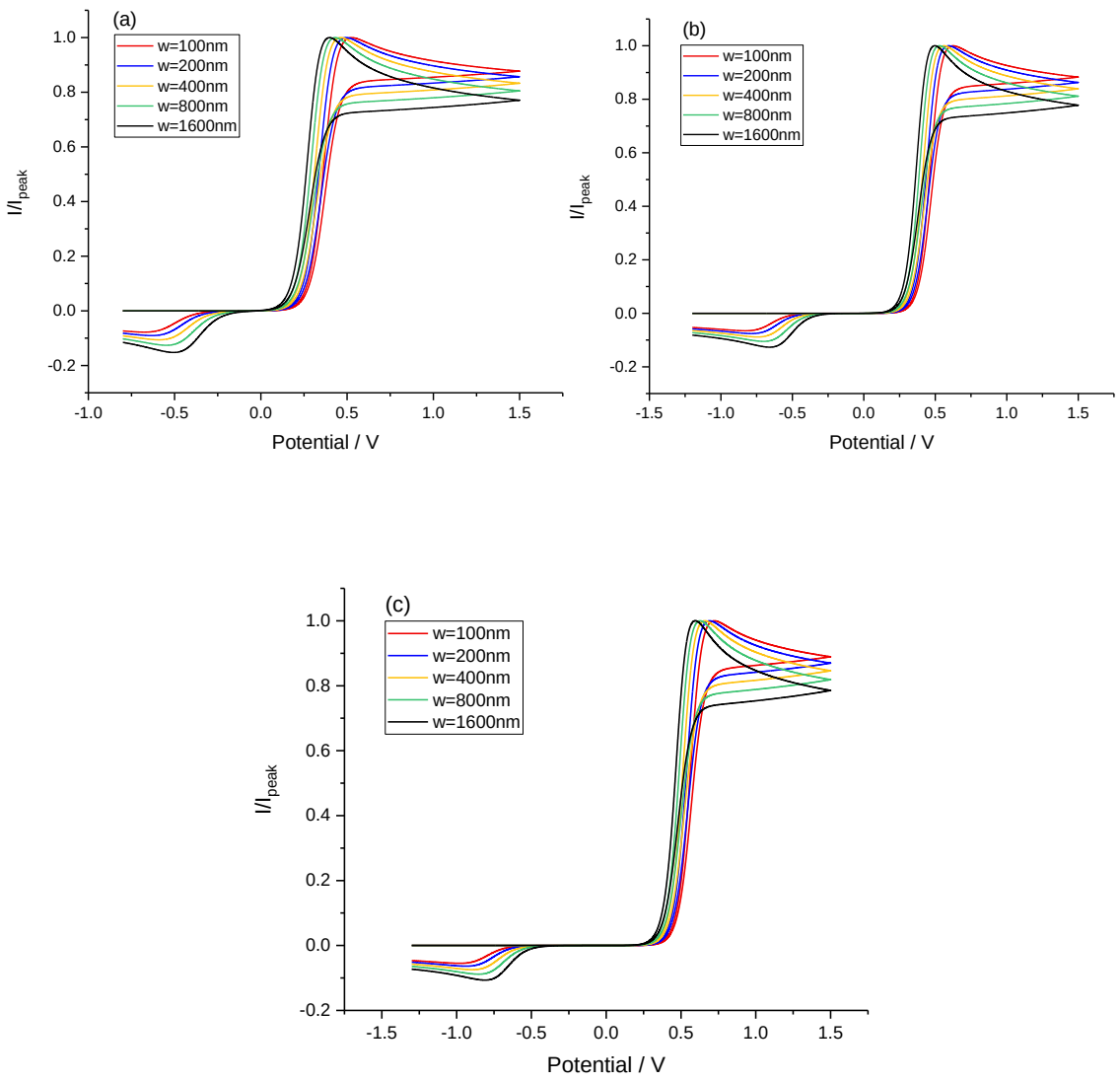


Figure 6.14 Normalised voltammograms for a band electrode with variable widths for a fully irreversible redox couple with unequal diffusion coefficients with various k^0 of (a) 1×10^{-7}, (b) 1×10^{-8} and (c) 1×10^{-9} m s^{-1}. The diffusion coefficients of A and B: $D_{(A)}=1\times10^{-9}$ m^2 s^{-1}, $D_{(B)}=5\times10^{-10}$ m^2 s^{-1}. Parameters in all simulations: $\nu=0.2$ V s^{-1}, $E_f=0$ V, $l=1\times10^{-2}$ m, transfer coefficients $\alpha_a = 0.6$, $\alpha_c = 0.4$.

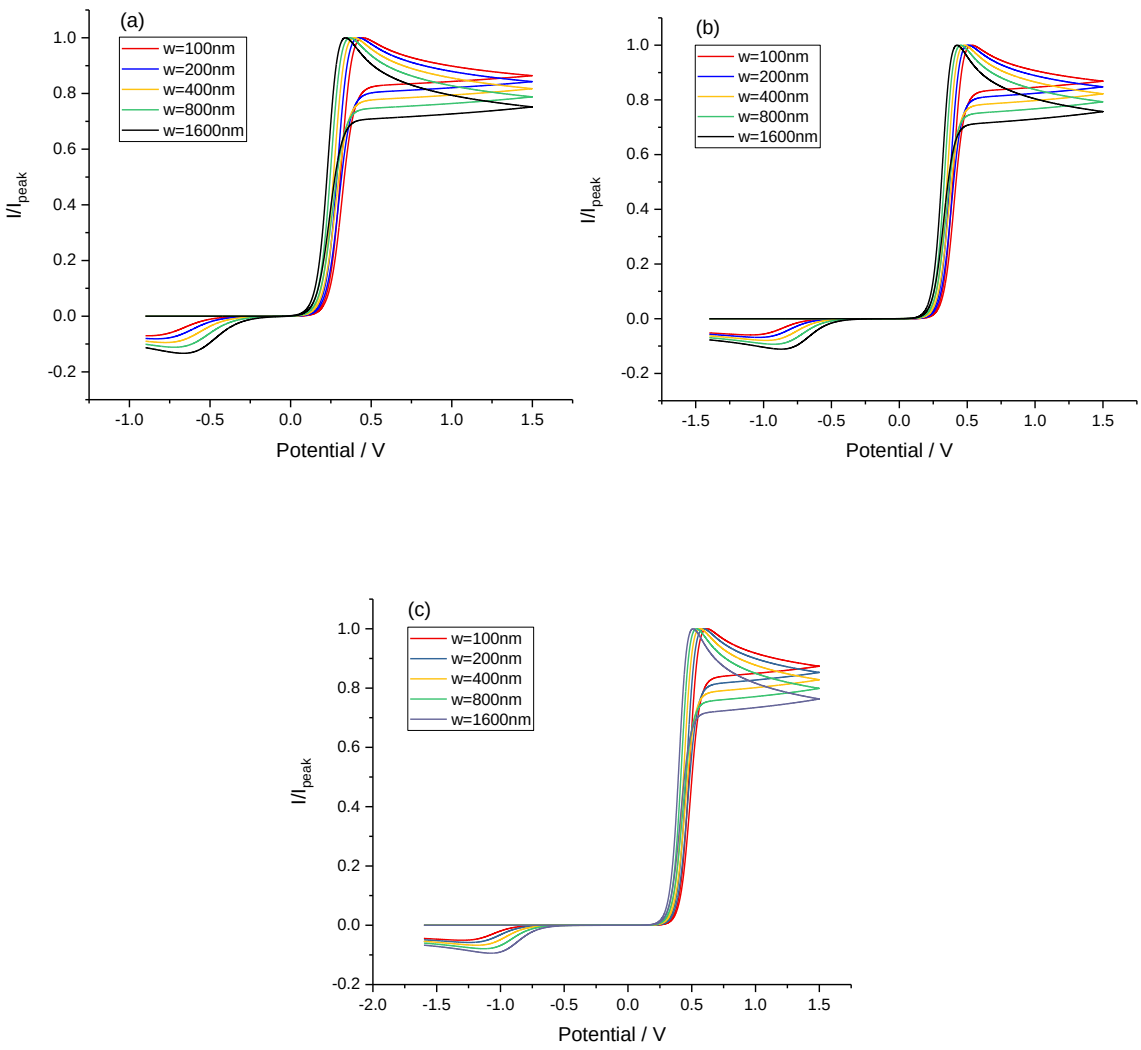


Figure 6.15 Normalised voltammograms for a band electrode with variable widths for a fully irreversible redox couple with unequal diffusion coefficients with various k^0 of (a) 1×10^{-7}, (b) 1×10^{-8} and (c) 1×10^{-9} m s^{-1}. The diffusion coefficients of A and B: $D_{(A)}=1\times10^{-9}$ m^2 s^{-1}, $D_{(B)}=5\times10^{-10}$ m^2 s^{-1}. Parameters in all simulations: $\nu=0.2$ V s^{-1}, $E_f=0$ V, $l=1\times10^{-2}$ m, transfer coefficients $\alpha_a = 0.7$, $\alpha_c = 0.3$.

Similar to case where the components of the redox couple have equal diffusion coefficients, the waveshape are distinguishable with variable band widths in the case where the redox species have unequal diffusion coefficients. The results suggest that for a given unknown band electrode, it is possible to measure the width and length of a band electrode using the combination of $E_{p\text{-}p}$ and $|I_{backward}/I_{forward}|$ with the following steps:

1. *Determination of D_A, D_B, α_a and α_c*: experimentally measure the diffusion coefficients (D_A and D_B) of the redox species from the steady-state current obtained on a microdisc electrode using double potential step chronoamperometry if necessary to give both diffusion coefficients[35]. Calculate the transfer coefficient (α_a) using Tafel analysis from the experimental voltammogram for a one-electron transfer oxidative process[33]. The cathodic transfer coefficient α_c equals (1- α_a) with a common assumption that the transfer coefficients equal to unity; a more in-depth discussion is presented in Chapter 5.
2. *Determination of k^0 and w*: calculate the values of E_{p-p} and $|I_{backward}/I_{forward}|$ from the experimental voltammogram. Using the simulations with a set of k^0 and band widths and the corresponding plots of E_{p-p} versus band width and $|I_{backward}/I_{forward}|$ versus band width. By comparing the experimental and theoretical values of E_{p-p} and $|I_{backward}/I_{forward}|$, k^0 and band width can be estimated (the values of k^0 and w are unique for a given experimental voltammogram on a band electrode).
3. *Determination of band length:* by modelling a simulation with the measured transfer coefficient and diffusion coefficients along with the estimated k^0 and w, the length of the band can be calculated using Equation 6.8.

$$length = \frac{Experimental\ I_{peak}\ (\mu A)}{Simulated\ \frac{I_{peak}}{length}\ (\mu A\ m^{-1})} \qquad (6.8)$$

6.3.4 Blind tests

In order to prove the applicability of this method, blind tests with systems each of unknown transfer coefficient, electron transfer rate constant, width and length of the band electrodes were made on simulated voltammograms.

Test 1 An example is shown in this section for a fully irreversible redox couple with unequal diffusion coefficients ($D_{(A)} = 2D_{(B)} = 1\times10^{-9}$ m^2 s^{-1}) following the procedures mentioned above. The voltammogram used for the blind test is shown in Figure 6.16. This was simulated using the data in the figure caption in Figure 6.16.

First, the measured diffusion coefficients of reactant A and product B are inferred to be 1×10^{-9} m^2 s^{-1} and 5×10^{-10} m^2 s^{-1}, respectively. The anodic transfer coefficient α_a is 0.5. These data, in experimental reality, would be found from steady-state microdisc voltammetry on scope of pure A and of pure B, and use Tafel analysis of experimental voltammograms.

Second, from the voltammogram, the measured $E_{p\text{-}p}$ is 1.2080 V and the $|I_{backward}/I_{forward}|$ is 0.0939. Voltammograms with a set of k^0 with variable band widths were simulated. With the known diffusion coefficients and transfer coefficient, the theoretical plots were obtained as shown in Figure 6.17. The experimental data is the dashed line. The corresponding band widths at each k^0 are shown as dotted line. From the plots, it shows that the corresponding band widths are relatively consistent in both plots with an electron

transfer rate constant k^0 of 7.5×10^{-8} m s^{-1}. The band width was therefore estimated as 1056 nm.

Third, further simulation was done with the known transfer coefficient of 0.5, diffusion coefficients of reactant and product of 1×10^{-9} m^2 s^{-1} and 5×10^{-10} m^2 s^{-1}, estimated rate constant of 7.5×10^{-8} m s^{-1} and band width of 1056 nm. The corresponding voltammogram was normalised to its length as shown in Figure 6.18. The length of the band in the blind test was then calculated using Equation 6.8 and was 0.0180 m. Therefore, the band width was estimated as 1056 nm with a length of 0.0180 m (the true width is 1058 nm and the true length is 0.018 m). The errors are 0.19% and 0.034% in width and length, respectively as shown in Table 6.3 'Test 1'.

$$length = \frac{Experimental\ I_{peak}\ (\mu A)}{Simulated\ \frac{I_{peak}}{length}\ (\mu A\ m^{-1})} = \frac{1.0192\ \mu A}{56.6030\ \mu A\ m^{-1}} = 0.0180\ m$$

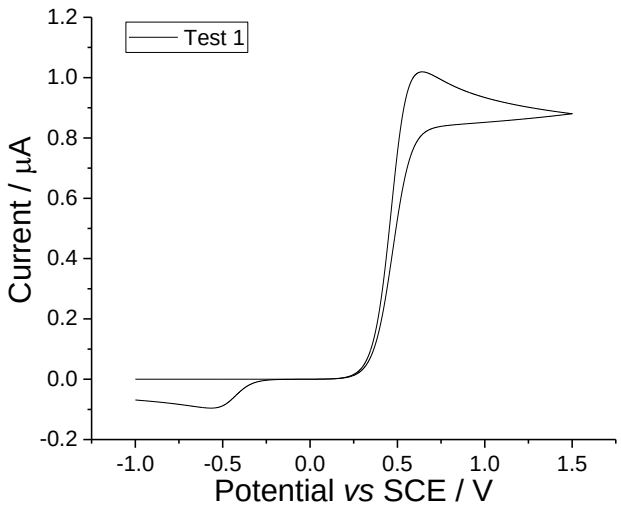


Figure 6.16 Blind test on a band electrode with unknown band length and width. Known parameters in the simulation: c = 1 mM, ν = 0.2 V s^{-1}, $\alpha_a = \alpha_c = 0.5$, $D_{(A)} = 1\times10^{-9}$ m^2 s^{-1}, $D_{(B)} = 5\times10^{-10}$ m^2 s^{-1}.

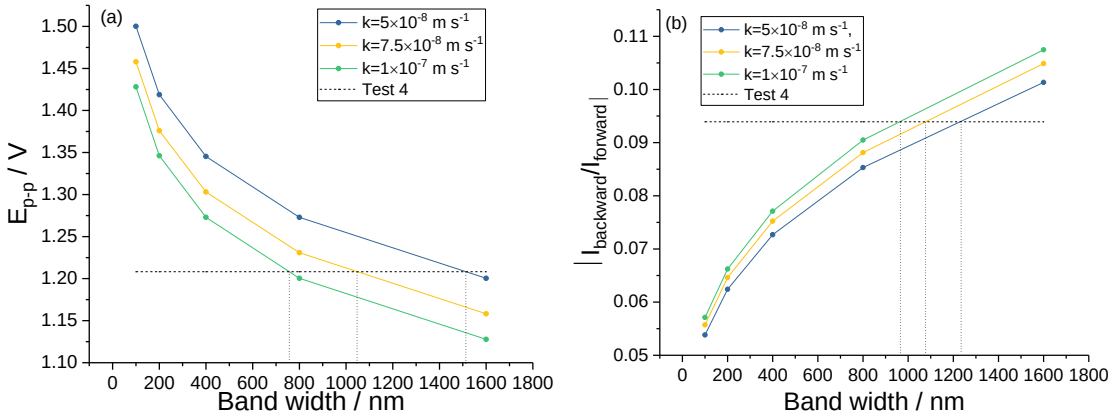


Figure 6.17 (a) Plot of $E_{p\text{-}p}$ as a function of band widths with variable k^0. (b) Plot of $|I_{backward}/I_{forward}|$as a function of band widths with variable k^0. Parameters in the simulations: $\alpha_a = \alpha_c = 0.5$, $D_{(A)} = 1\times10^{-9}$ m^2 s^{-1}, $D_{(B)} = 5\times10^{-10}$ m^2 s^{-1}. The dashed line is the measured value of $E_{p\text{-}p}$ and $|I_{backward}/I_{forward}|$ from Figure 6.16. The dotted line shows the corresponding band width at different k^0.

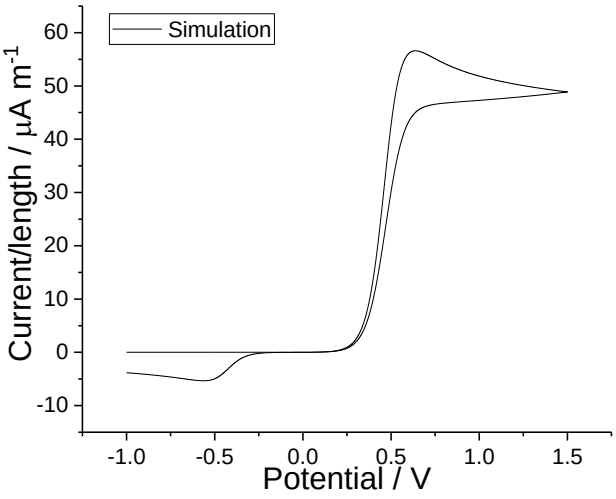


Figure 6.18 Normalised voltammogram on a band electrode with known transfer coefficient and diffusion coefficients, estimated rate constant and band width. Parameters in the simulation: $\alpha_a = 0.5$, $\alpha_c = 0.5$, $D_{(A)} = 1 \times 10^{-9}$ m^2 s^{-1}, $D_{(B)} = 5 \times 10^{-10}$ m^2 s^{-1}. $\nu = 0.2$ V s^{-1}, $E_f = 0$ V, $l = 1 \times 10^{-2}$ m, $k^0 = 7.5 \times 10^{-8}$ m s^{-1}, band width = 1056 nm.

Test 2 In order to prove the applicability to the cases where the redox species have lower diffusion coefficients ($D_{(A)} = 2D_{(B)} = 1\times10^{-10}$ m^2 s^{-1}), a blind test (test 2) where the anodic transfer coefficient equals 0.5 was tried.

The voltammogram simulated for use as the basis of the blind test is shown in Figure 6.19, along with the known parameters of concentration (1 mM), scan rate (0.2 V s^{-1}), anodic transfer coefficients ($\alpha_a = \alpha_c = 0.5$) and diffusion coefficients ($D_{(A)} = 2D_{(B)} = 1\times10^{-10}$ m^2 s^{-1}). The reactant and product have unequal diffusion coefficients. The procedures of deducing the band width and length are as follows.

First, the measured diffusion coefficients of reactant A and product B are 1×10^{-10} m^2 s^{-1} and 0.5×10^{-10} m^2 s^{-1}, respectively. The anodic transfer coefficient is 0.5. Experimentally,

these parameters would be measured from steady-state microdisc voltammetry and Tafel analysis.

Second, from the voltammogram, the measured E_{p-p} is 1.1410 V and the $|I_{backward}/I_{forward}|$ is 0.0985. Voltammograms with a set of k^0 with variable band widths were simulated. With the known diffusion coefficients and transfer coefficient, the theoretical plots were obtained as shown in Figure 6.20. The experimental data is the dashed line. The corresponding band widths at each k^0 are shown as dotted line. From the plots, it shows that the corresponding band widths are relatively consistent in both plots with an electron transfer rate constant k^0 of 5×10^{-8} m s^{-1}. The band width was therefore estimated as 306 nm.

Third, further simulation was done with the known transfer coefficient of 0.5, diffusion coefficients of reactant and product of 1×10^{-10} m^2 s^{-1} and 0.5×10^{-10} m^2 s^{-1}, estimated electrochemical rate constant of 5×10^{-8} m s^{-1} and band width of 306 nm. The corresponding voltammogram was normalised to its length as shown in Figure 6.21. The length of the band in the blind test was then calculated using Equation 6.8 and was 0.0157 m. Therefore, the band width was estimated as 306 nm with a length of 0.0157 m. The errors are 3.7% and 0.64% in width and length, respectively as shown in Table 6.3 (true width=312 nm and true length=0.0156 m in the blind test).

$$length = \frac{Experimental\ I_{peak}\ (\mu A)}{Simulated\ \frac{I_{peak}}{length}\ (\mu A\ m^{-1})} = \frac{0.0875\ \mu A}{5.5685\ \mu A\ m^{-1}} = 0.0157\ m$$

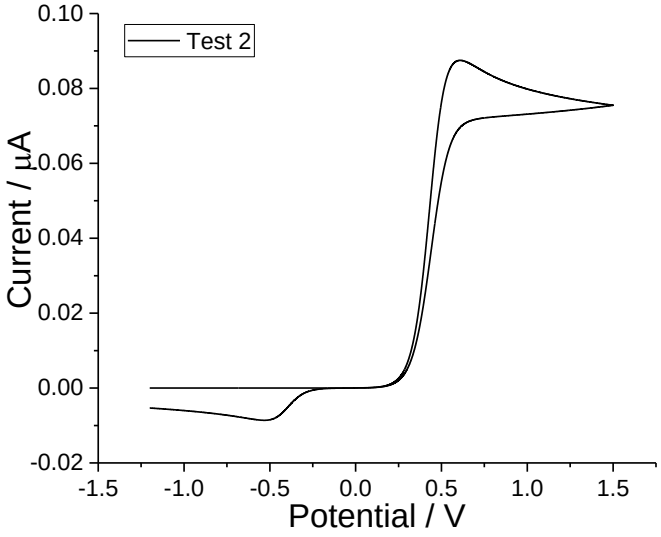


Figure 6.19 Blind test on a band electrode with unknown band length and width. Known parameters in the simulation: c = 1 mM, ν = 0.2 V s^{-1}, $\alpha_a = \alpha_c = 0.5$, $D_{(A)} = 1\times10^{-10}$ m^2 s^{-1}, $D_{(B)} = 0.5\times10^{-10}$ m^2 s^{-1}.

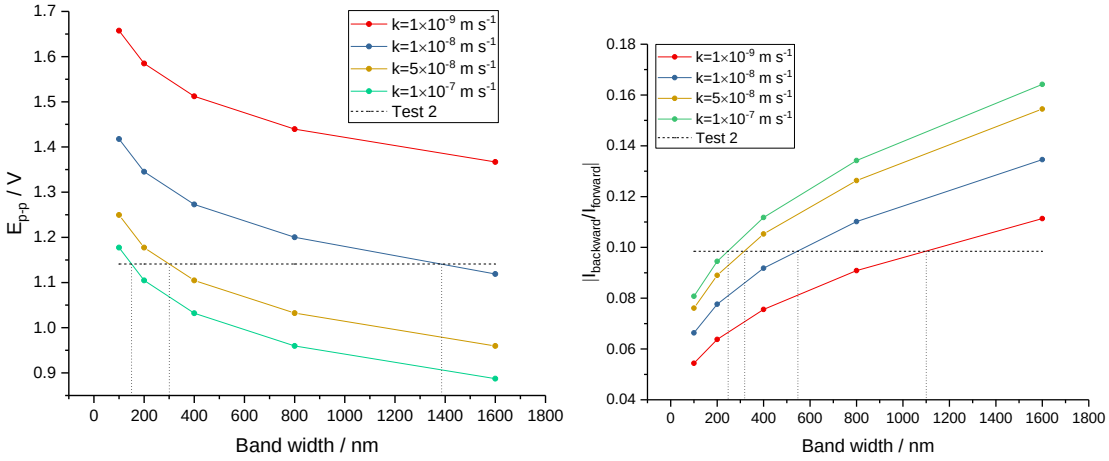


Figure 6.20 (a) Plot of $E_{p\text{-}p}$ as a function of band widths with variable k^0. (b) Plot of $|I_{backward}/I_{forward}|$as a function of band widths with variable k^0. Parameters in the simulations: $\alpha_a = \alpha_c = 0.5$, $D_{(A)} = 1\times10^{-10}$ m^2 s^{-1}, $D_{(B)} = 0.5\times10^{-10}$ m^2 s^{-1}. The dashed line is the measured value of $E_{p\text{-}p}$ and $|I_{backward}/I_{forward}|$ from Figure 6.19. The dotted line shows the corresponding band width at different k^0.

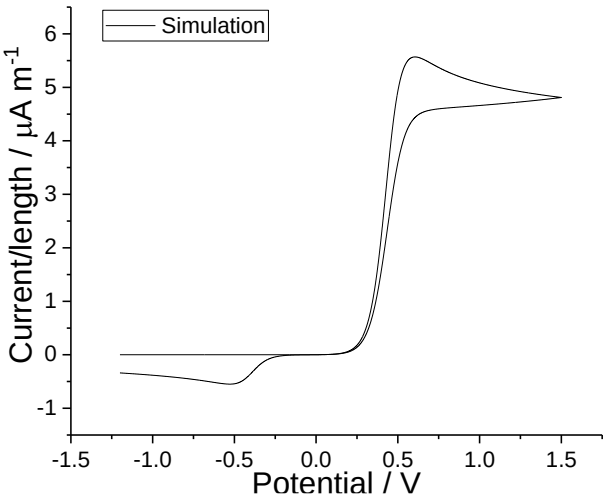


Figure 6.21 Normalised voltammogram for a band electrode with known transfer coefficient and diffusion coefficients, estimated rate constant and band width. Parameters in the simulation: $\alpha_a = \alpha_c = 0.5$, $D_{(A)} = 1\times10^{-10}$ m^2 s^{-1}, $D_{(B)} = 0.5\times10^{-10}$ m^2 s^{-1}. ν=0.2 V s^{-1}, E_f=0 V, l=1×10^{-2} m, $k^0=5\times10^{-8}$ m s^{-1}, band width=306 nm.

Table 6.3 Estimated and true band widths and lengths for blind tests 1-4. ν = 0.2 V s^{-1}, $\alpha_a = \alpha_c = 0.5$. $D_{(A)} = 1 \times 10^{-9}$ m^2 s^{-1}, $D_{(B)} = 5 \times 10^{-10}$ m^2 s^{-1}. In Test 2-4[b], $D_{(A)} = 1 \times 10^{-10}$ m^2 s^{-1}, $D_{(B)} = 0.5 \times 10^{-10}$ m^2 s^{-1}.

		Estimated	True	Error
Test 1[a]	Width (w) / nm	1056	1058	0.19%
($\alpha_a = 0.5$, $\alpha_c = 0.5$)	Length (l) / m	0.015801	0.018	0.034%
Test 2 [b]	Width (w) / nm	312	306	3.7%
($\alpha_a = 0.5$, $\alpha_c = 0.5$)	Length (l) / m	0.0157	0.0156	0.64%
Test 3[b]	Width (w) / nm	1176	1148	2.4%
($\alpha_a = 0.3$, $\alpha_c = 0.7$)	Length (l) / m	0.0328	0.033	0.6%

Test 4 [b] (α_a = 0.4, α_c = 0.6)	Width (w) / nm	1424	1350	5.5%
	Length (l) / m	0.0444	0.045	1.3%

The analysing details for other transfer coefficients are presented in the Appendix C2. The estimated dimensions of the band electrodes are tabulated in Table 6.3. According to the results in Table 6.3, it is shown that by using this method, in all cases the error in width is 3.9% ± 1.6% and the error in length is 0.85% ± 0.40%.

6.4 Conclusions

This work validates an entirely voltammetric method to characterise the dimensions of a band electrode. With a given unknown band electrode, the band width and length can be estimated electrochemically by using a fully irreversible redox couple without any prior knowledge of electron transfer rate constant k^0 and/or the formal potential E_f. Considering that the diffusion coefficient of the electroactive species and the transfer coefficient can be measured from experiments, the peak-to-peak separation $E_{p\text{-}p}$ and the ratio of the magnitude of backward peak current to forward peak current $|I_{backward}/I_{forward}|$ are combined together as the indicators to estimate the electron transfer rate constant and the band width. From the blind test, the estimated band width and length gave errors of ~4% and ~1%, respectively.

References:

[1] D. Li, C. Lin, C. Batchelor-McAuley, L. Chen, R. G. Compton, *Journal of Electroanalytical Chemistry* **2019**, *840*, 279-284.

[2] D. Li, C. Batchelor-McAuley, L. Chen, R. G. Compton, *ACS Sens* **2019**, *4*, 2250-2266.

[3] S. Karel, A. Christian, H. Karel, M. Vladimír, K. Wlodzimierz, *Pure and Applied Chemistry* **2000**, *72*, 1483-1492.

[4] aJ. Heinze, *Angewandte Chemie International Edition in English* **1993**, *32*, 1268-1288; bR. J. Forster, *Chemical Society Reviews* **1994**, *23*, 289-297; cR. G. A. B. Compton, Craig E, *Understanding Voltammetry*, third ed., World Scientific, **2018**.

[5] K. R. Wehmeyer, M. R. Deakin, R. M. Wightman, *Analytical Chemistry* **1985**, *57*, 1913-1916.

[6] aI. A. Silver, I. Bergman, M. Akhtar, C. R. Lowe, I. J. Higgins, *Philosophical Transactions of the Royal Society of London. B, Biological Sciences* **1987**, *316*, 161-167; bE. Llaudet, S. Hatz, M. Droniou, N. Dale, *Analytical Chemistry* **2005**, *77*, 3267-3273.

[7] aJ. Fraden, *Handbook of Modern Sensors: Physics, Designs, and Applications*, Springer New York, **2010**; bW. Qiu, M. Xu, R. Li, X. Liu, M. Zhang, *Analytical Chemistry* **2016**, *88*, 1117-1122; cK. C. Honeychurch, S. Al-Berezanchi, J. P. Hart, *Talanta* **2011**, *84*, 717-723; dJ. P. Metters, R. O. Kadara, C. E. Banks, *Sensors and Actuators B: Chemical* **2012**, *169*, 136-143; eC. Sapsanis, H. Omran, V. Chernikova, O. Shekhah, Y. Belmabkhout, U. Buttner, M. Eddaoudi, K. N. Salama, *Sensors* **2015**, *15*, 18153-18166.

[8] aR. M. Pemberton, J. Xu, R. Pittson, G. A. Drago, J. Griffiths, S. K. Jackson, J. P. Hart, *Biosensors and Bioelectronics* **2011**, *26*, 2448-2453; bD. Sharma, Y. Lim, Y. Lee, H. Shin, *Analytica Chimica Acta* **2015**, *889*, 194-202; cM. Falk, R. Sultana, M. J. Swann, A. R. Mount, N. J. Freeman, *Bioelectrochemistry* **2016**, *112*, 100-105; dK. Dawson, M. Baudequin, A. O'Riordan, *Analyst* **2011**, *136*, 4507-4513.

[9] P. Mehrotra, *Journal of Oral Biology and Craniofacial Research* **2016**, *6*, 153-159.

[10] J. Wang, G. Chen, M. P. Chatrathi, A. Fujishima, D. A. Tryk, D. Shin, *Analytical Chemistry* **2003**, *75*, 935-939.

[11] L. Wang, M. Veselinovic, L. Yang, B. J. Geiss, D. S. Dandy, T. Chen, *Biosensors and Bioelectronics* **2017**, *87*, 646-653.

[12] aA. M. Bond, M. Fleischmann, J. Robinson, *Journal of Electroanalytical Chemistry and Interfacial Electrochemistry* **1984**, *168*, 299-312; bM. A. Hernández-Olmos, L. Agüí, P. Yáñez-Sedeño, J. M. Pingarrón, *Electrochimica Acta* **2000**, *46*, 289-296.

[13] F. Zhang, M. A. Edwards, R. Hao, H. S. White, B. Zhang, *The Journal of Physical Chemistry C* **2017**, *121*, 23564-23573.

[14] X. Li, C. Batchelor-McAuley, L. Shao, S. V. Sokolov, N. P. Young, R. G. Compton, *The Journal of Physical Chemistry Letters* **2017**, *8*, 507-511.

[15] R. B. Morris, D. J. Franta, H. S. White, *The Journal of Physical Chemistry* **1987**, *91*, 3559-3564.

[16] J.-L. Chang, J.-M. Zen, *Electrochemistry Communications* **2006**, *8*, 571-576.

[17] aY. H. Lanyon, D. W. M. Arrigan, *Sensors and Actuators B: Chemical* **2007**, *121*, 341-347; bC. S. Henry, *Journal of The Electrochemical Society* **1999**, *146*, 3367.

[18] L. Angnes, E. M. Richter, M. A. Augelli, G. H. Kume, *Analytical Chemistry* **2000**, *72*, 5503-5506.

[19] aT. A. Postlethwaite, J. E. Hutchison, R. Murray, B. Fosset, C. Amatore, *Analytical Chemistry* **1996**, *68*, 2951-2958; bD. M. Odell, W. J. Bowyer, *Analytical Chemistry* **1990**, *62*, 1619-1623.

[20] P. M. Kovach, W. L. Caudill, D. G. Peters, R. M. Wightman, *Journal of Electroanalytical Chemistry and Interfacial Electrochemistry* **1985**, *185*, 285-295.

[21] R. Lin, T. M. Lim, T. Tran, *Electrochemistry Communications* **2018**, *86*, 135-139.

[22] aD. H. Craston, C. P. Jones, D. E. Williams, N. El Murr, *Talanta* **1991**, *38*, 17-26; bD. E. Williams, K. Ellis, A. Colville, S. J. Dennison, G. Laguillo, J. Larsen, *Journal of Electroanalytical Chemistry* **1997**, *432*, 159-169.

[23] aT. R. L. C. Paixão, R. C. Matos, M. Bertotti, *Electroanalysis* **2003**, *15*, 1884-1889; bH. A. O. Hill, N. A. Klein, I. S. M. Psalti, N. J. Walton, *Analytical Chemistry* **1989**, *61*, 2200-2206; cJ. E. Bartelt, M. R. Deakin, C. Amatore, R. M. Wightman, *Analytical Chemistry* **1988**, *60*, 2167-2169; dT. V. Shea, A. J. Bard, *Analytical Chemistry* **1987**, *59*, 2101-2111.

[24] aN. Creedon, R. Sayers, B. O'Sullivan, e. kennedy, P. Lovera, A. O'Riordan, *Label-Free Impedimetric Nanoband Sensor for Detection of Both Bovine Viral Diarrhoea Virus (BVDV) and Antibody (BVDAb) in Serum*, **2018**; bM. P. Nagale, I. Fritsch, *Analytical Chemistry* **1998**, *70*, 2902-2907; cM. P. Nagale, I. Fritsch, *Analytical Chemistry* **1998**, *70*, 2908-2913; dJ. A. Alden, M. A. Feldman, E. Hill, F. Prieto, M. Oyama, B. A. Coles, R. G. Compton, P. J. Dobson, P. A. Leigh, *Analytical Chemistry* **1998**, *70*, 1707-1720; eM. E. Hyde, T. J. Davies, R. G. Compton, *Angewandte Chemie International Edition* **2005**, *44*, 6491-6496.

[25] F. Prieto, M. Oyama, B. A. Coles, J. A. Alden, R. G. Compton, S. Okazaki, *Electroanalysis* **1998**, *10*, 685-690.

[26] A. Qureshi, J. H. Niazi, S. Kallempudi, Y. Gurbuz, *Biosensors and Bioelectronics* **2010**, *25*, 2318-2323.

[27] A. Szabo, D. K. Cope, D. E. Tallman, P. M. Kovach, R. M. Wightman, *Journal of Electroanalytical Chemistry and Interfacial Electrochemistry* **1987**, *217*, 417-423.

[28] R. M. Wightman, *Science* **1988**, *240*, 415.

[29] A. J. Bard, L. R. Faulkner, *Electrochemical Methods: Fundamentals and Applications, 2nd Edition*, Wiley Textbooks, **2000**.

[30] K. Aoki, K. Honda, K. Tokuda, H. Matsuda, *Journal of Electroanalytical Chemistry and Interfacial Electrochemistry* **1985**, *182*, 267-279.

[31] I. Streeter, N. Fietkau, J. del Campo, R. Mas, F. X. Mũnoz, R. G. Compton, *The Journal of Physical Chemistry C* **2007**, *111*, 12058-12066.

[32] I. Streeter, R. G. Compton, *The Journal of Physical Chemistry C* **2007**, *111*, 15053-15058.

[33] D. Li, C. Lin, C. Batchelor-McAuley, L. Chen, R. G. Compton, *Journal of Electroanalytical Chemistry* **2018**, *826*, 117-124.

[34] K. Ngamchuea, C. Lin, C. Batchelor-McAuley, R. G. Compton, *Analytical Chemistry* **2017**, *89*, 3780-3786.

[35] O. V. Klymenko, R. G. Evans, C. Hardacre, I. B. Svir, R. G. Compton, *Journal of Electroanalytical Chemistry* **2004**, *571*, 211-221.

Chapter 7

Electrocatalysis via Intrinsic Surface Quinones Mediating Electron Transfer to and from Carbon Electrodes

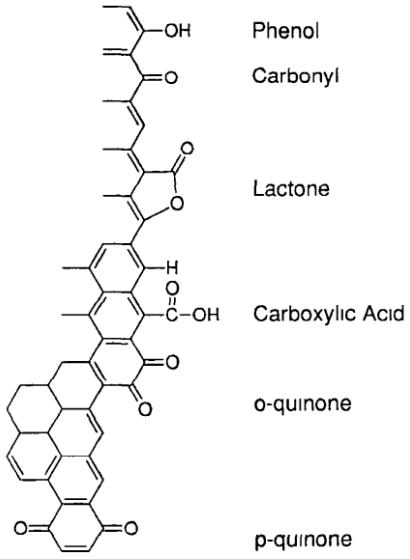
Carbon electrodes have long been employed in both fundamental studies and industrial applications such as batteries. The variety of functional groups on the carbon surface provide possibilities in electrocatalysis. The work in this chapter shows how the $Fe^{2+/3+}$ redox reaction is mediated via intrinsic surface quinones on carbon substrates. Such mediation has long been speculated in general but hitherto unproven for any specific case. This quinone-mediated process was observed voltammetrically as a quasi-steady-state like 'prewave' on a carbon microdisc electrode which becomes obvious under low mass-transport conditions. Broadly these results regarding the $Fe^{2+/3+}$ redox couple on carbon substrates have implications for the large-scale energy storage technologies such as redox flow batteries and also impacts fundamental electron transfer theory.

This work presented in this chapter has been published as a first author paper in *The Journal of Physical Chemistry Letters*[1] and was carried out in collaboration with Dr. Christopher Batchelor-McAuley and Mr. Lifu Chen.

7.1 Introduction

Low cost and abundant availability encourage carbon based electrodes to be widely used throughout electrochemical technologies including in fuel cells, batteries, sensors, etc.[2] Nevertheless understanding electron transfer at the carbon electrode-electrolyte interface is challenging over and above that at metal electrodes, such as gold or platinum, partly because carbon electrodes come in many forms – graphite, (doped) diamond, nanotubes, graphene, carbon black, glassy carbon, … - and partly because the carbon surface is particularly chemically reactive. Thus it has long been recognised, largely as a result of the pioneering work of McCreery[3], that a wide diversity of functional groups may exist on carbon surfaces as shown schematically in Scheme 7.1[4], including quinones which derive from the reaction of molecular oxygen or water with the surface[5]. Of the many groups shown, quinones have excited particular interest since as isolated molecules they are electroactive in both aqueous and non-aqueous solutions. This, in the case of intrinsic surface species, has been exploited, for example, in the development of carbon based pH sensors where voltammetric signals due to the two electron, two proton reduction of quinones are used to indicate the pH of aqueous solutions[6]. Voltammetric signals from surface quinones have been seen on a variety of carbon surfaces and their near ubiquity raises the possibility of electron transfer to solution phase redox couples at carbon electrodes being mediated via electron transfer to or from the intrinsic surface quinone groups present. Such ideas are supported by reports of carbon electrodes deliberately

modified by quinone groups, via covalent attachment, adsorption or immobilisation of polymers, which have been shown to electrocatalyse, via mediation, the reduction of, for example, peroxidase[7], oxygen[8], quinones[9] and the oxidation of several bioanalytes[10]. Further it has been suggested that electron transfer via intrinsic surface quinones is responsible for increased oxygen reduction activity[11] and for other electrochemical processes[12].



Scheme 7.1 Representation of various functional groups on Carbon surfaces. The picture was adapted from reference[8].

The aim of this chapter is to identify an electrochemical reaction in which intrinsic surface quinones unambiguously mediate and catalyse electron transfer. In particular, we focus on the Fe^{2+}/Fe^{3+} redox couple in aqueous acidic solution noting that Fe(III)/quinone mediated electron transfer is well documented in homogeneous conditions[13] for several biological systems. The $Fe^{2+/3+}$ redox couple has also been applied in large-scale energy storage technologies such as redox flow batteries due to low cost, high abundance and

low chemical toxicity[14]. Accordingly the $Fe^{2+/3+}$ system in the form of ca. milimolar concentrations of $NH_4Fe^{III}(SO_4)_2$ and $(NH_4)_2Fe^{II}(SO_4)_2$ in 0.2 M $HClO_4$ was investigated.

7.2 Experimental

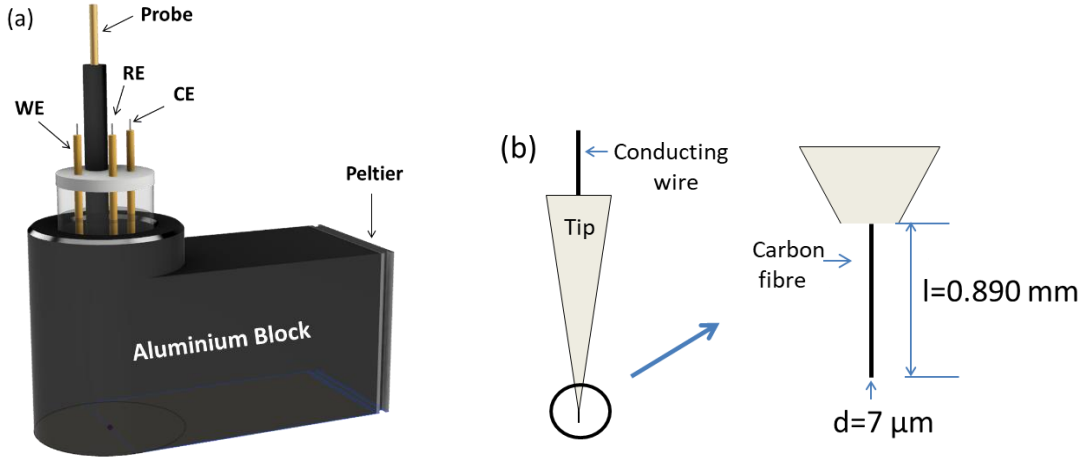
7.2.1 Chemical reagents

The ammonium iron (II) sulfate hexahydrate ($(NH_4)_2Fe^{II}(SO_4)_2$; Aldrich; 99%), ammonium iron (III) sulfate dodecahydrate ($NH_4Fe^{III}(SO_4)_2$; Aldrich; 99%), ammonium sulfate ($(NH_4)_2SO_4$; Aldrich; ≥99%), hexaammineruthenium (III) chloride ($[Ru(NH_3)_6]Cl_3$, Alfa Aesar, ≥98.3%), potassium chloride (KCl, Sigma-Aldrich, ≥99.0%) and perchloric acid (Aldrich; 70%) were used as purchased without further purification. Solutions were prepared using deionised water (Milipore) with a resistivity of 18.2 MΩ cm at 25 ^oC. Solutions containing $Fe^{2+/3+}$ species were freshly prepared prior to experiments.

7.2.2 Instrumentation

Electrochemical measurements were performed with a µAutolab Type III potentiostat using a standard three electrode setup in an optimised thermostated electrochemical cell as shown in Scheme 7.2(a). The details of this design are described in Chapter 2[4]. A carbon microdisc electrode (7 µm in diameter; BASi), a gold microdisc electrode (10 µm in diameter; BASi) and a conventional carbon fibre microcylinder electrode (7 µm in diameter; 0.890 mm in length; Scheme 7.2(b)) were used as working electrodes. The

carbon fibre microcylinder electrode was fabricated in-house using the method described in Chapter 2. A saturated calomel electrode (SCE saturated KCl; BASi, Japan) and a platinum wire were used as reference electrode and counter electrode, respectively. The working disc electrodes were polished using alumina of decreasing size (1.0, 0.3 and 0.05 µm, Buehler, IL), washed with deionised water and dried with nitrogen prior to experiments.



Scheme 7.2 (a) Schematic of the optimised thermostated electrochemical cell. The probe is used to sense the temperature of the electrochemical cell, which is controlled by a Peltier. WE, RE and CE represent the working electrode, reference electrode and counter electrode, respectively. (b) Schematic of a carbon fibre microcylinder electrode.

7.2.3 Electrochemical measurements

All electrochemical measurements were conducted at 25 (± 0.1) ^{o}C inside a Faraday cage. All the solutions were purged with nitrogen for at least 5 minutes before experiments.

Measurements of the formal potential and diffusion coefficients of the $Fe^{2+/3+}$ redox couple The formal potential was measured on a gold microdisc electrode (10 µm in

diameter; BASi) in a solution containing both Fe^{2+} and Fe^{3+} (5 mM $NH_4Fe^{III}(SO_4)_2$, 5 mM $(NH_4)_2Fe^{II}(SO_4)_2$, 2.5 mM $(NH_4)_2SO_4$ in 0.2 M $HClO_4$) at 0.05 V s^{-1}. The diffusion coefficients for Fe^{2+} and Fe^{3+} were measured on the same gold microdisc electrode at 0.01 V s^{-1} using different solutions (for Fe^{2+}: 10 mM $(NH_4)_2Fe^{II}(SO_4)_2$ in 0.2 M $HClO_4$; for Fe^{3+}: 10 mM $NH_4Fe^{III}(SO_4)_2$, 2.5 mM $(NH_4)_2SO_4$ in 0.2 M $HClO_4$).

Transfer experiments on a carbon microdisc electrode The adsorption isotherms for Fe^{2+} and Fe^{3+} were obtained by using solutions with variable concentrations of Fe^{2+} or Fe^{3+} for "transfer experiments". For each set of transfer experiment, the electrode was first scanned in blank solution (2.5 mM $(NH_4)_2SO_4$ in 0.2 M $HClO_4$), the electrode was then immersed in solutions of variable concentrations of Fe^{2+} or Fe^{3+} for 2 minutes and the voltammetry was then measured in blank solution. Voltammograms for each concentration were measured at both 0.2 V s^{-1} and 0.8 V s^{-1}.

7.2.4 Simulation programmes

The voltammetric response of a 2D diffusion microdisc electrode was simulated using a home-written programme written by Dr Oleksiy Klymenko based on the conformal mapping of the spatial coordinates and uses an exponentially expanding time grid.[15]

7.3 Tafel analysis on a microdisc electrode

Tafel analysis provides a direct route by which the transfer coefficient for a redox reaction can be determined. The transfer coefficient[16] is an experimentally measurable quantity

and is related to the fraction (and hence asymmetry) of the electrostatic potential available for the oxidation or reduction process. Importantly, in the case of inner-sphere redox reactions this fraction of the electrochemical potential available for the redox process can be influenced by the electrode double layer.[17] Tafel analysis under different electrode geometries has been discussed in Chapter 4. The anodic transfer coefficient (α_a) is defined by IUPAC as[16]:

$$\alpha_a = \left(\frac{RT}{F}\right)\left(\frac{d \ln j_a}{dE}\right) \quad (7.1)$$

where j_a is the anodic current density which has been corrected to account for changes in the concentration of the reactant at the electrode surface, R is the gas constant (8.314 J mol^{-1} K^{-1}), T is the temperature in K, F is the Faraday constant (96485 C mol^{-1}) and E is the applied potential at the working electrode.

7.3.1 Mass-transport corrected transfer coefficient plots

For a carbon microdisc electrode at low scan rates a steady-state mass-transport regime can be attained. However, the electrode surface is non-uniformly accessible which means that, in contrast to other electrode geometries such as a hemispherical electrode, there is no exact analytical expression available to correct for the influence of the mass-transport conditions on the voltammetric response as discussed in Chapter 4. Consequently, the correction made in this work to extract the transfer coefficient is strictly only approximate. Specifically this work shows the estimation of experimental transfer coefficients on a microdisc electrode via *two* different mass-transport corrections in the current range of 1%

to 95% of the steady-state current $I_{s.s}$ or limiting current I_{lim}. At high overpotentials, the voltammetric current becomes mass-transport limited, which leads to an underestimation of the transfer coefficient on a microelectrode. This first method for correcting the measured transfer coefficient uses the analytically defined mass-transport correction as derived in chapter 4, where the analytically mass-transport corrected anodic transfer coefficient α_a' was calculated using Equation 7.2[18].

$$-\frac{RT}{F}\frac{dln\left(\frac{1}{I_a}-\frac{1}{I_{lim}}\right)}{dE}=\alpha_a' \tag{7.2}$$

where I_{lim} is the mass-transport limiting current. For a microdisc electrode, the theoretical steady-state current $I_{s.s}$, calculated using Equation 7.3 was used as the mass-transport limiting current throughout the analysis.

$$I_{s.s}=4nFDcr \tag{7.3}$$

where $I_{s.s}$ is the steady-state current, n is the number of electrons transferred, c is the bulk concentration of the reactant, D is the diffusion coefficient of the reactant and r is the radius of the electrode.

7.3.2 Non-uniformly mass-transport corrected transfer coefficient plots

The second method, a correction allowing for non-uniformly mass-transport was taken into account to give a better estimation for the transfer coefficient. According to the previous theoretical study reported in chapter 4, the mass-transport corrected transfer coefficient plot on a microdisc electrode gives an improved measure of the transfer

coefficient, but shows significant fluctuation at higher fraction of the voltammetric wave due to the non-uniformly accessibility of the microdisc electrode as shown in Figure 7.1(a).[18] In Figure 7.1(a) the y-axis on the left stands for the normalised current $I/I_{s.s}$ (i.e. fraction of the wave) of the simulated voltammograms in the current range from 1% to 95% of $I_{s.s}$ while the y-axis on the right represents the normalised anodic transfer coefficient plots (α_a'/α_a) as a function of dimensionless potential ($\left(E - E_f\right)RT/F$). The simulation parameters are shown in the caption of Figure 7.1.

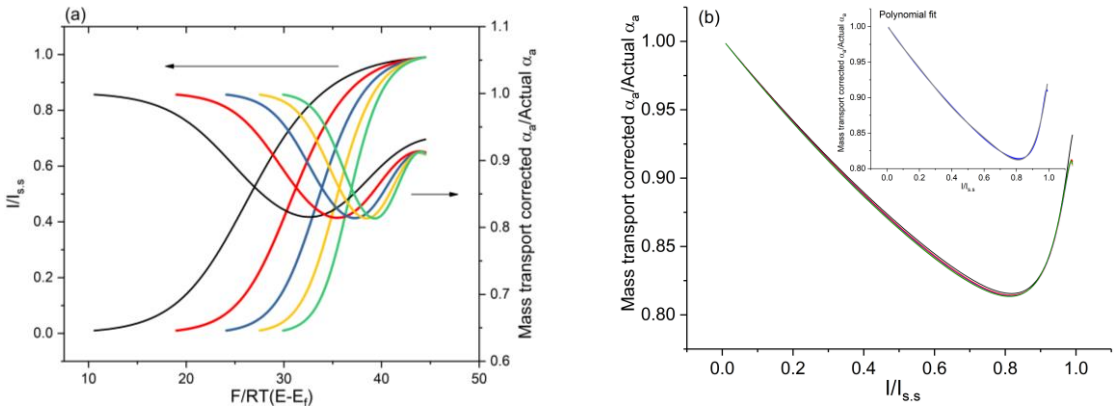


Figure 7.1 (a) Voltammograms and the normalised anodic transfer coefficient plots on a microdisc with various true transfer coefficients (Black: $\alpha_a = 0.3$, red: $\alpha_a = 0.4$, blue: $\alpha_a = 0.5$, brown: $\alpha_a = 0.6$, green: $\alpha_a = 0.7$). The current range is 1% - 99% of steady-state current. The dimensionless rate constant $K = k^0r/D = 1 \times 10^{-5}$, the dimensionless scan rate $\sigma = \nu Fr^2/(RTD) = 9.73 \times 10^{-6}$. $\alpha_c + \alpha_a = 1$. (b) The normalised anodic transfer coefficient plots as a function of the fraction of the wave ($I/I_{s.s}$). The inlay represents the polynomial fitting of the curve in the case of $\alpha_a = 0.5$.

Figure 7.1 shows that the normalised transfer coefficient has the trend as a function of the fraction of the wave shown in Figure 7.1(b), providing a relatively universal correction for the experimentally measured transfer coefficient. The inlay represents the six-order polynomial fitting of the curve when α_a=0.5, providing the value of the non-uniformly

accessibility correction factor as a function of the fraction of the wave ($I/I_{s.s}$). Therefore, the non-uniformly accessibility mass-transport corrected anodic transfer coefficient $\alpha'_{a,uni}$ can be obtained via Equation 7.4.

$$\alpha'_{a,uni} = \frac{\alpha'_a}{correction\ factor} \tag{7.4}$$

7.4 Results and discussion

7.4.1 Determination of the diffusion coefficients and the formal potential of the Fe^{2+}/Fe^{3+} redox couple

Diffusion coefficients The diffusion coefficients of Fe^{2+} and Fe^{3+} were measured using a gold microdisc electrode. The size of the electrode was first calibrated using 1.0 mM hexaammineruthenium (III) chloride solution in 0.1 M KCl with a known diffusion coefficient of 8.43 (± 0.03) × 10^{-6} cm^2 s^{-1} at 25 ^oC[19]. The corresponding voltammograms are shown in Figure 7.2 and the value of the radius at each scan was calculated using Equation 7.3, giving an average radius of 5.15 µm.

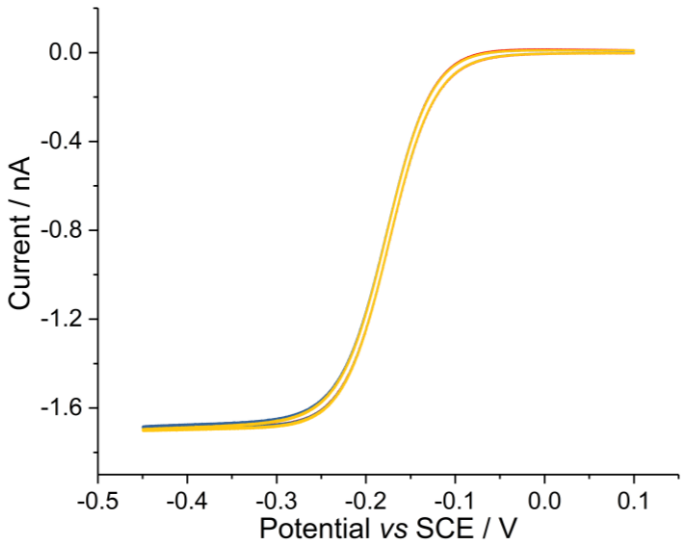


Figure 7.2 Voltammograms on a gold microdisc electrode at 25 °C at 0.01 V s^{-1} (red – 1st scan; blue – 2nd scan; yellow – 3rd scan). Solution used: 1.0 mM hexaammineruthenium (III) chloride in 0.1 M KCl.

The diffusion coefficients for Fe^{2+} and Fe^{3+} were then measured on the same gold microdisc electrode at 25 °C at 0.01 V s^{-1} using different solutions (Fe^{2+}: 10 mM $(NH_4)_2Fe^{II}(SO_4)_2$ in 0.2 M $HClO_4$; Fe^{3+}: 10 mM $NH_4Fe^{III}(SO_4)_2$, 2.5 mM $(NH_4)_2SO_4$ in 0.2 M $HClO_4$). The diffusion coefficients were calculated using Equation 7.3 with the experimentally measured steady-state current, with the known number of electrons transferred (n = 1) which is one in this case, the known bulk concentration of the reactant (c = 10 mM) and the calibrated electrode radius (r = 5.15 µm). The diffusion coefficients of Fe^{2+} and Fe^{3+} were calculated to be 6.7 (± 0.1) × 10^{-6} and 5.5 (± 0.1) × 10^{-6} cm^2 s^{-1}, respectively. The corresponding voltammograms for Fe^{2+} oxidation and Fe^{3+} reduction are shown in Figure 7.3(a) and (b), respectively.

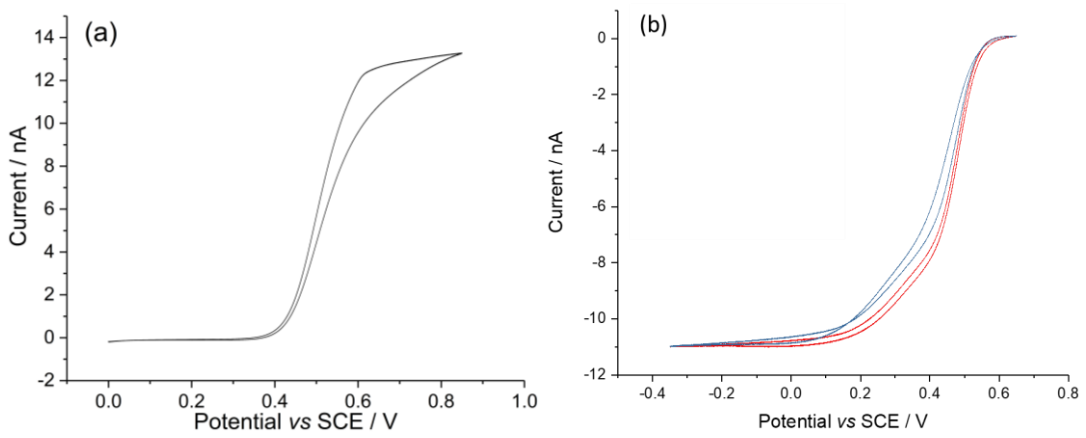


Figure 7.3 Voltammograms on a gold microdisc electrode (radius=5.15 µm) at 25 ºC towards (a) Fe^{2+} oxidation and (b) Fe^{3+} reduction at 0.01 V s^{-1}. Solutions compositions: (a) 10 mM $(NH_4)_2Fe(SO_4)_2$ with 0.2 M $HClO_4$; (b) 10 mM $NH_4Fe(SO_4)_2$, 5 mM $(NH_4)_2SO_4$ with 0.2 M $HClO_4$.

Formal potential With the known diffusion coefficients of Fe^{2+} and Fe^{3+}, the formal potential of the $Fe^{2+/3+}$ redox couple was measured on the same gold microdisc electrode (radius of 5.15 µm) using a solution containing equimolar Fe^{2+} and Fe^{3+} (5 mM $NH_4Fe^{III}(SO_4)_2$, 5 mM $(NH_4)_2Fe^{II}(SO_4)_2$, 2.5 mM $(NH_4)_2SO_4$ and 0.2 M $HClO_4$). The corresponding voltammogram is shown as Figure 7.4.

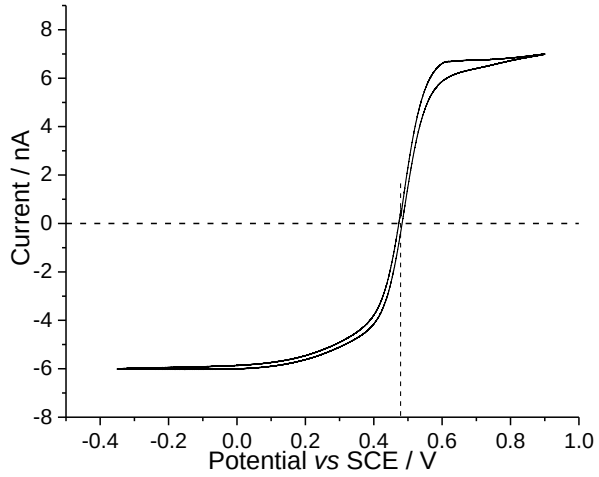


Figure 7.4 Voltammogram on a gold microdisc electrode (r=5.15 µm) at 25 ºC. Solution composition: 5 mM $(NH_4)_2Fe(SO_4)_2$, 5 mM $NH_4Fe(SO_4)_2$, 2.5 mM $(NH_4)_2SO_4$ with 0.2 M $HClO_4$. Scan rate: 0.05 V s^{-1}.

From this voltammetric response it is possible to determine the formal potential for the redox process (which is different from the standard potential[20]). The formal potential was taken as the potential when the measured current is zero ($E_{(i=0)}$), which was further corrected for the difference between diffusion coefficients of Fe^{2+} and Fe^{3+} using Equation 7.5[2], giving the formal potential value of 0.4785 (± 0.0006) V *vs.* SCE.

$$E_f^{\ominus} = E_{(i=0)} - \frac{RT}{F} \ln \left(\frac{D(Fe^{3+})}{D(Fe^{2+})}\right) \quad (7.5)$$

where $E_f^{\ominus}$ is the formal potential of $Fe^{2+/3+}$ redox couple, $E_{(i=0)}$ is the applied potential when the current is zero.

7.4.2 Comparison of voltammetric responses on gold and carbon microdisc electrodes

Figure 7.4(a) depicts the voltammetric response of a gold micro-electrode (blue-line) in a solution containing both Fe^{2+} and Fe^{3+} (5 mM). On the gold electrode the redox process is, at low potentials, fully reversible as evidenced by the continuity in the voltammogram near the equilibrium potential where significant anodic and cathodic currents flow either side of the equilibrium potential. In contrast to the gold electrode, the voltammetric response of the $Fe^{2+/3+}$ redox couple is markedly slower on a carbon substrate. Overlaid on Figure 7.4(a) is the voltammetric response of a carbon microdisc electrode under the same experimental conditions (red-line); the separation of the main waves indicates slower electron transfer. Moreover in the low anodic current region (0.5-0.7 V) the current

is appreciably above zero before the main oxidative wave appears at a half-wave potential of 0.9483 V versus SCE. The half-wave potential for the oxidation process ($\eta_{1/2}$ = +0.470 V) has been shifted to a relatively higher overpotential as compared to the reduction ($\eta_{1/2}$ = -0.258 V), evidencing a distinct asymmetry in the nature of the electron transfer kinetics. On the reductive scan of the iron redox couple a clear inflection in the voltammogram is present, however, the voltammetry does not easily allow this process to be more clearly delineated, limiting mechanistic interpretation. Hence, the focus of this work is the origin of this non-zero current at low *anodic* overpotentials; the presence of this anodic pre-wave will be both fully evidenced and a surface quinone based explanation for its origin will be provided.

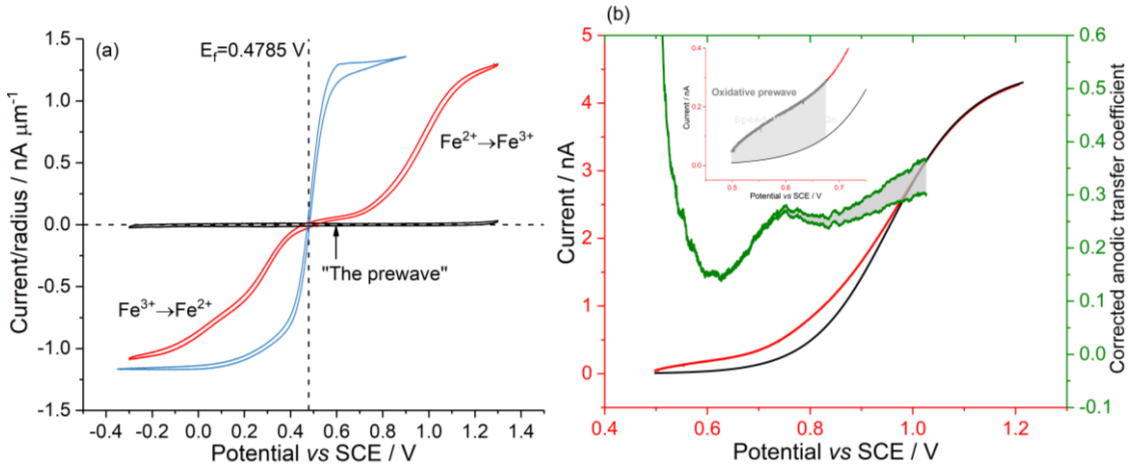


Figure 7.5 (a) Comparison of voltammograms normalised to electrode radius on a carbon microdisc electrode (radius=3.5 µm) (red) and a gold microdisc electrode (radius=5.15 µm) (blue) at 25 °C at 0.01 V s^{-1} in a solution of $Fe^{2+/3+}$ (5.0 mM $(NH_4)_2Fe(SO_4)_2$, 5.0 mM $NH_4Fe(SO_4)_2$, 2.5 mM $(NH_4)_2SO_4$ with 0.2 M $HClO_4$). The black curve represents the normalised voltammetric response without $Fe^{2+/3+}$ redox couple. The formal potential of the $Fe^{2+/3+}$ redox couple is labelled as a vertical dashed line. The horizontal dashed line labels zero current. (b) Mass transport corrected anodic transfer coefficient plots with (upper green)

and without (lower green) non-uniformly accessibility correction on the carbon microdisc electrode. The experimental oxidative voltammogram is shown as red curve and the black curve shows the simulated voltammogram on a microdisc electrode with an anodic transfer coefficient of 0.35. The current range is 1%-95% of the true steady-state current. The inlay represents the zoomed-in version of the oxidative pre-wave (highlighted in grey).

7.4.3 Transfer coefficient plots measured at carbon electrodes

7.4.3.1 Voltammetric behaviour of $Fe^{2+/3+}$ on a carbon microdisc electrode

Figure 7.5(b) depicts the anodic mass-transport corrected transfer coefficient for the oxidation of Fe^{2+} on a carbon microdisc electrode. The gray area represents the estimated uncertainty in the mass-transport correction where the upper limit in green was given using non-uniformly accessibility correction and the lower limit in green was given by the conventional mass-transport correction. Moreover, due to the limitations of the used methodology currents above 70% of the diffusion limited flux have not been considered for analysis. The measured transfer coefficient for this system is significantly below 0.5, where for a one electron process a value close to 0.5 is often observed for an outer sphere redox process. This experimental data evidences that the transfer coefficient is not constant and varies as a function of the electrode potential. At higher over potentials (>1.0 V) the transfer coefficient tends towards a value of 0.35 but at low over potentials the transfer coefficient is found to be significantly below this limit. Overlaid with the experimental voltammogram in Figure 7.4(b) is the simulated voltammetric response (black-line) for a simple one-electron transfer process with a symmetry factor of 0.35.

Here for the simulation the standard electrochemical rate constant has been used as a fitting parameter and has a value of 1×10^{-7} m s^{-1}. First, as anticipated from the measured transfer coefficient, at high overpotentials and near the mass-transport limit (>60% of $I_{s.s}$) the voltammetric response is well described by this simple single mechanistic pathway simulation model as shown in Figure 7.4(b). In addition, we further investigate the 'fitting' of this simple one-electron simulation to the experimental data. The voltammetric response on a 2D diffusion microdisc electrode is simulated using a home-written programme written by Dr Oleksiy Klymenko as described in the Experimental Section.[15b] Simulated voltammograms were made with "true" anodic transfer coefficients α_a of 0.25 (yellow), 0.35 (blue) and 0.5 (green) and overlaid with the experimental voltammetric wave (red), as is shown in Figure 7.6. Here it is shown that the voltammogram in the current range of ca. 6%-39% can be fitted well with α_a of 0.25; simulation with α_a of 0.35 gives a good fitting in the current range of over ca. 60% of $I_{s.s}$; when α_a is increased to 0.5, the oxidative wave can only be fitted when the current is above 94% of $I_{s.s}$. As the value of the anodic transfer coefficient becomes smaller, the fraction of the wave which has the best fitting becomes lower, proving the presence of an 'apparently' variable potential dependent anodic transfer coefficient. It is concluded that

no fixed single value of the transfer coefficient is able to fit the experimental current across the full range of potentials.

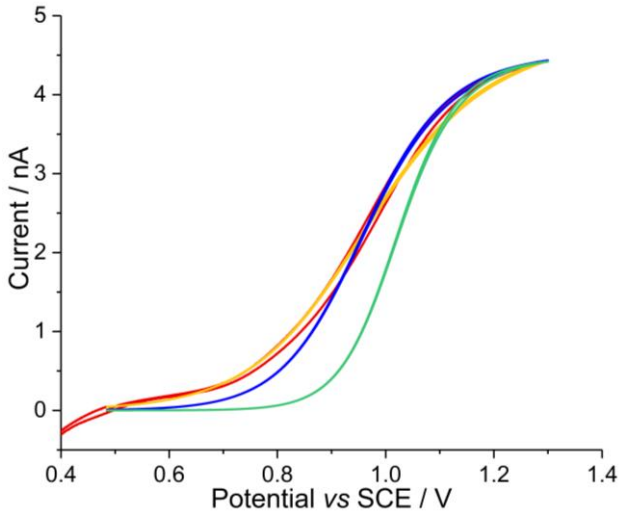


Figure 7.6 Fitting of the experimental voltammogram (red) using the simulations with different anodic transfer coefficients on a microdisc electrode (yellow: α_a =0.25; blue: α_a =0.35; green: α_a =0.5). Parameters used in the simulation: scan rate=0.01 V s^{-1}; D(Fe^{2+})=6.68×10^{-10} m^2 s^{-1}; D(Fe^{3+})=5.45×10^{-10} m^2 s^{-1}; electron transfer rate=1×10^{-7} m s^{-1}, the formal potential=0.4837 V.

7.4.3.2 Voltammetric behaviour of $Fe^{2+/3+}$ on a carbon micro-wire electrode

The measured change in the transfer coefficient as a function of the applied potential on a carbon microdisc electrode is first strongly indicative of a change in the electrochemical redox mechanism with potential. Second, as evidenced through comparison of the simulated and experimental data, at low overpotentials there is more current passed than would be expected for a simple electron transfer process. For the microdisc electrode geometry a “pre-wave” contributes approximately 0.2 nA of current and for clarity has been highlighted in the inlay of Figure 7.4(b). Moreover, for other electrode geometries where the mass-transport regime is less efficient this pre-wave becomes relatively larger.

This latter point is evidenced through the study of the voltammetric response of a carbon fibre microcylinder electrode under comparable experimental conditions; the geometry of this electrode is shown in Experimental section. Here the pre-wave is appreciably relatively larger on the microcylinder electrode. Figure 7.7(a) presents the voltammetric behaviour for $Fe^{2+/3+}$ redox process on a carbon microwire electrode in a solution containing 10 mM $(NH_4)_2Fe^{II}(SO_4)_2$, 2.5 mM $(NH_4)_2SO_4$ and 0.2 M $HClO_4$ at 25 ^oC. Figure 7.7(a) shows the corresponding voltammograms after background subtraction at variable scan rates. Figure 7.7(b) presents the overlay of the voltammogram obtained at 0.025 V s^{-1} and the voltammogram obtained in blank solution (2.5 mM $(NH_4)_2SO_4$ and 0.2 M $HClO_4$). The inlay shows the zoomed-in version of the oxidative prewave which is highlighted in yellow. The prewave observed on a carbon microwire electrode is stronger as compared to that observed on a carbon microdisc electrode. Consider if the current of the prewave is proportional to the area of the electrode (i.e. proportional to r^2) while the mass-transport limiting current is proportional to the radius. Thus when the electrode changes from a microdisc to the microwire, the area of the electrode increases and the

efficiency of the mass-transport becomes less due to the increased contribution from linear diffusion.

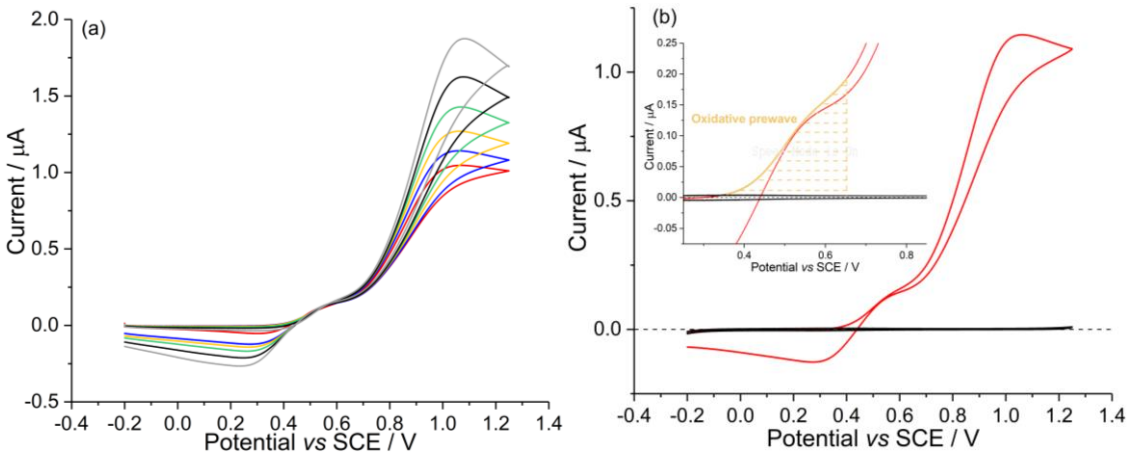


Figure 7.7 (a) Voltammograms on a carbon microwire electrode (radius of 3.5 µm; length of 0.089 cm) at 25 °C at 0.025 (red), 0.05 (blue), 0.1 (yellow), 0.2 (green), 0.4 (black) and 0.8 (gray) V s^{-1}. Solution composition: 10 mM $(NH_4)_2Fe(SO_4)_2$, 2.5 mM $(NH_4)_2SO_4$ with 0.2 M $HClO_4$. (b) Comparison of the voltammograms obtained in Fe-containing solution (red) and blank solution (black) at 0.025 V s^{-1}. The inlay represents the zoomed-in version of the prewave (highlighted in yellow). Blank solution composition: 2.5 mM $(NH_4)_2SO_4$ with 0.2 M $HClO_4$.

Consequently, the magnitude of the prewave relative to the mass-transport regime depends on the electrode geometry and it is easier to see the prewave on a microwire electrode. Moreover, in Figure 7.7(a) the current of the prewave is independent of the scan rate also proves the existence of the catalytic process which gives a steady-state current.

7.4.4 Adsorption of Fe^{2+}/Fe^{3+} on a carbon microdisc electrode

We next turn to consider the physico-chemical origins of the observed pre-wave. Although the $Fe^{2+/3+}$ redox couple is known to be sensitive to oxygen-containing

functional groups on the electrode surface[3a, 3b], it has not been proved which specific functional groups are responsible for the catalysed reaction. The origin of the interaction between Fe ions and the functional groups which results in the occurrence of pre-wave was next investigated. Transfer experiments were conducted to study possible adsorption behaviour.

7.4.4.1 Fe^{3+} reduction on a carbon microdisc electrode

A carbon microdisc was immersed into a solution containing certain concentration of $NH_4Fe^{III}(SO_4)_2$, 2.5 mM $(NH_4)_2SO_4$ in 0.2 M $HClO_4$, and the voltammetric response of this interface studied before and after exposure to the solution. The voltammetric experiments were measured in the absence of Fe(III) in the solution phase; procedures are provided in the Experimental Section. Figure 7.8(a) depicts examples of the measured voltammetric response of the electrode before (red-line) and after (black-line) immersion in the iron containing solution. For the clean carbon surface the voltammetric response of the electrode exhibits a relatively large capacitative charging current and at a pH of 0.69, a broad surface bound feature corresponding to the redox chemistry of surface quinone groups (at ca.0.38 V vs SCE)[6a]. From this voltammetric peak the surface coverage of catechol on a clean carbon electrode was calculated to be $(4.33 \pm 0.66) \times 10^{-11}$ mol cm^{-2} as ascertained from the integration of the quinone/catechol peak observed in blank solution. This value is consistent with the literature values for ortho-quinones measured on basal plane and edge plane pyrolytic graphite electrodes of 1.7×10^{-10} and 2.0×10^{-12}

mol cm^{-2}, respectively[21]. After exposure of the electrode to the Fe(II) containing solution an additional redox signal is observed at ca. 0.54 V versus SCE. The presence of this additional redox feature can be more fully resolved by background subtraction. Figure 7.8(b) shows the voltammetric response of the electrode exposed to the iron solution where variable iron concentrations have been used after removal of the capacitive and quinone responses by subtracting the voltammograms in blank solution. The voltammograms give well-defined surface-bound peaks at around 0.5 V in all cases; the peak charge increases with the increasing Fe^{3+} concentration in the range of 5 mM to 20 mM and becomes essentially constant when the Fe^{3+} concentration is larger than 20 mM. First, the charge passed oxidatively and reductively, is comparable and indicates that both the oxidised and reduced iron species remain adsorbed to the electrode surface on the voltammetric timescale. Second, integration of the peak enables the surface coverage of the adsorbed iron to be assessed as depicted in the inlay in Figure 7.8 which presents the measured Fe^{3+} adsorption isotherm on the carbon microdisc electrode in solutions containing variable concentrations of Fe^{3+}. The experimentally measured maximum surface coverage of adsorbed Fe^{3+} was calculated to be $(4.42 \pm 0.18) \times 10^{-11}$ mol cm^{-2}, which is very comparable to that expected from surface quinones. The consistency between the surface coverages of quinone/catechol and the Fe^{3+} ions strongly indicates that the occurrence of the additional peaks is attributed to $Fe^{2+/3+}$ adsorption on the electrode. In addition, the prewave was observed at lower overpotential compared to the main oxidative wave which means that such process is easier to happen, indicating a

mediated Fe^{2+} oxidation. Although it is possible that iron adsorption occurs via binding to other surface oxygen functionalities such as carboxylic acid groups, these alternate functionalities would need to have the same surface coverage as the quinone. Furthermore, the binding of iron to catechol functionalities is well documented in the literature in contexts outside of electrochemistry[22].

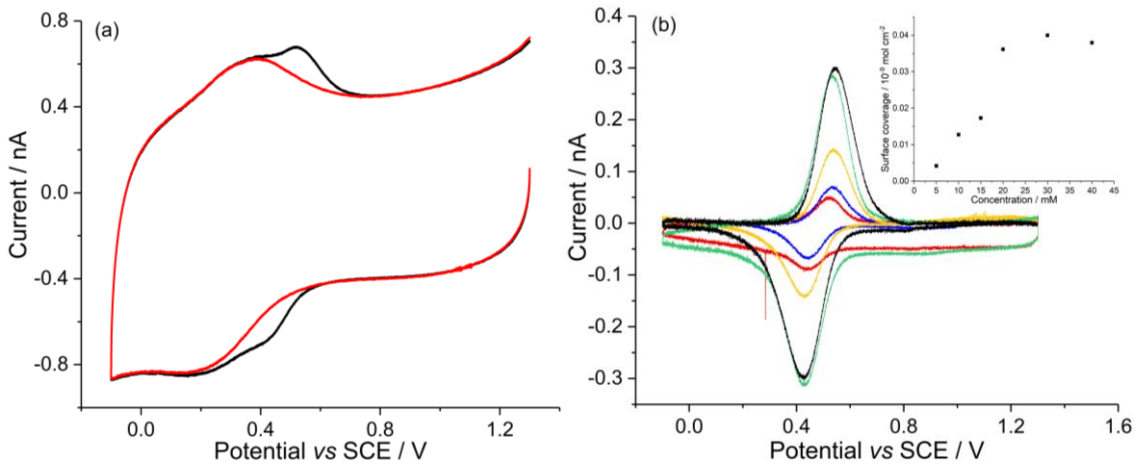


Figure 7.8 (a) Voltammograms of a carbon microdisc electrode (r=3.5 µm) in blank solution before (red) and after (black) immersion in the iron containing solution. Blank solution composition: 2.5 mM $(NH_4)_2SO_4$ with 0.2 M $HClO_4$. Iron containing solution: 15 mM $NH_4Fe(SO_4)_2$, 2.5 mM $(NH_4)_2SO_4$ with 0.2 M $HClO_4$. (b) Voltammograms with background subtraction as a function of the concentration of Fe^{3+} (5 mM – red, 10 mM – blue, 15 mM – yellow, 20 mM – green and 30 mM – black) at 25 ºC. The inlay presents Fe^{3+} adsorption isotherm at 0.2 V s^{-1}.

Voltammograms obtained in other solutions containing variable concentrations of Fe^{3+} are shown in Figure 7.9 (5 mM), Figure 7.10 (10 mM), Figure 7.11 (15 mM), Figure 7.12 (20 mM), Figure 7.13 (30 mM) and Figure 7.14 (40 mM). Figure 7.9-7.14(a) and (b) present the corresponding voltammograms obtained before adsorption (red), with adsorption (black) and after desorption (yellow) at 0.8 V s^{-1} and 0.2V s^{-1}, respectively.

Figure 7.9-7.14(c) show the voltammograms with adsorption after background subtraction at 0.8 V s^{-1} (red) and 0.2 V s^{-1} (blue). Clear adsorption peaks were observed in all cases and the voltammograms after background subtraction give nice surface-bound peaks.

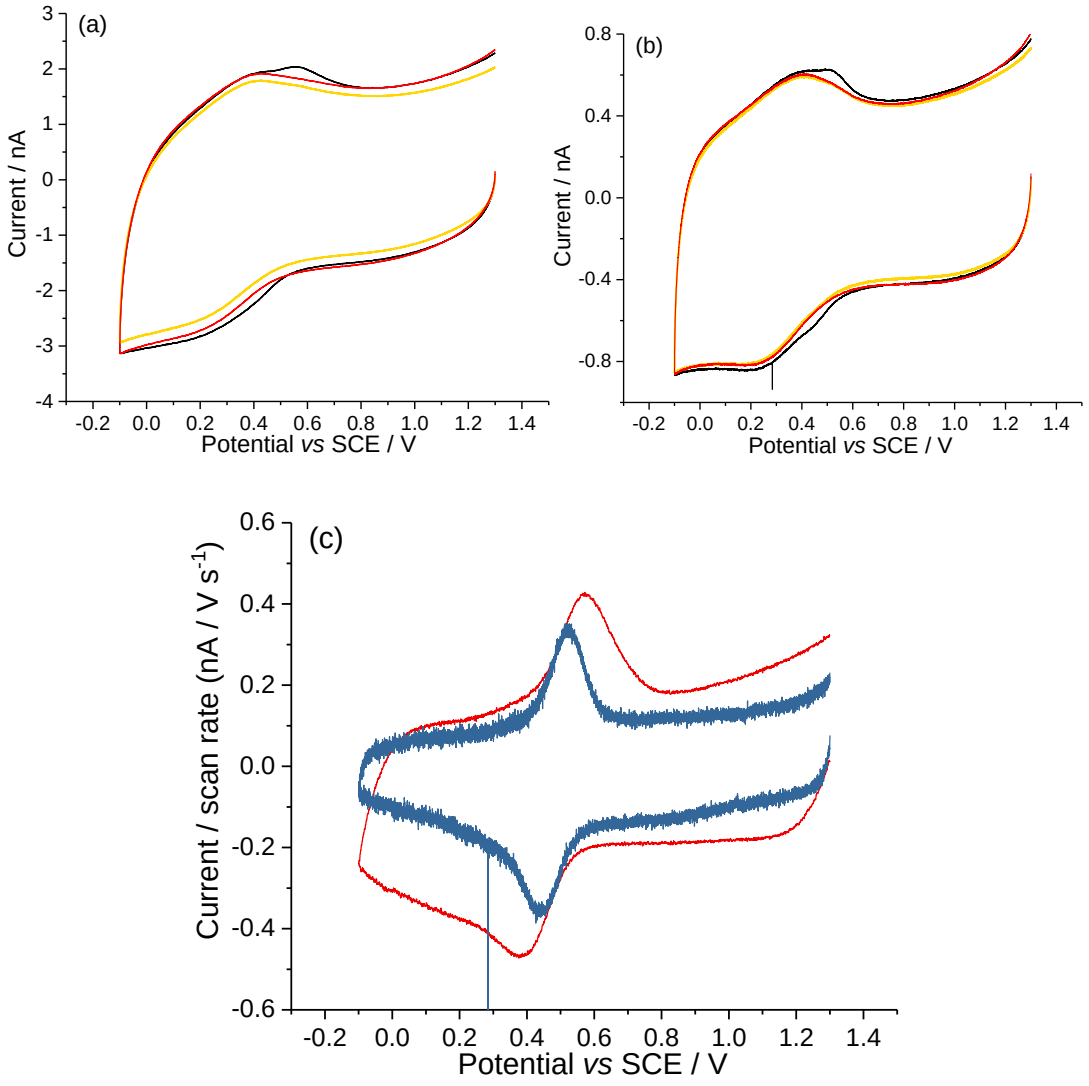


Figure 7.9 Voltammograms on a carbon microdisc electrode (r=3.5 µm) at 25 °C at (a) 0.8V s^{-1} and (b) 0.2V s^{-1}. The overlaid voltammograms in (a) and (b) were measured in blank solution 1: before adsorption (red), with adsorption (black) and after desorption (yellow). (c) presents the voltammograms after background subtraction at 0.8 V s^{-1} (red) and 0.2 V s^{-1} (blue). Solution composition: 5 mM $NH_4Fe(SO_4)_2$, 2.5 mM $(NH_4)_2SO_4$ with 0.2 M $HClO_4$.

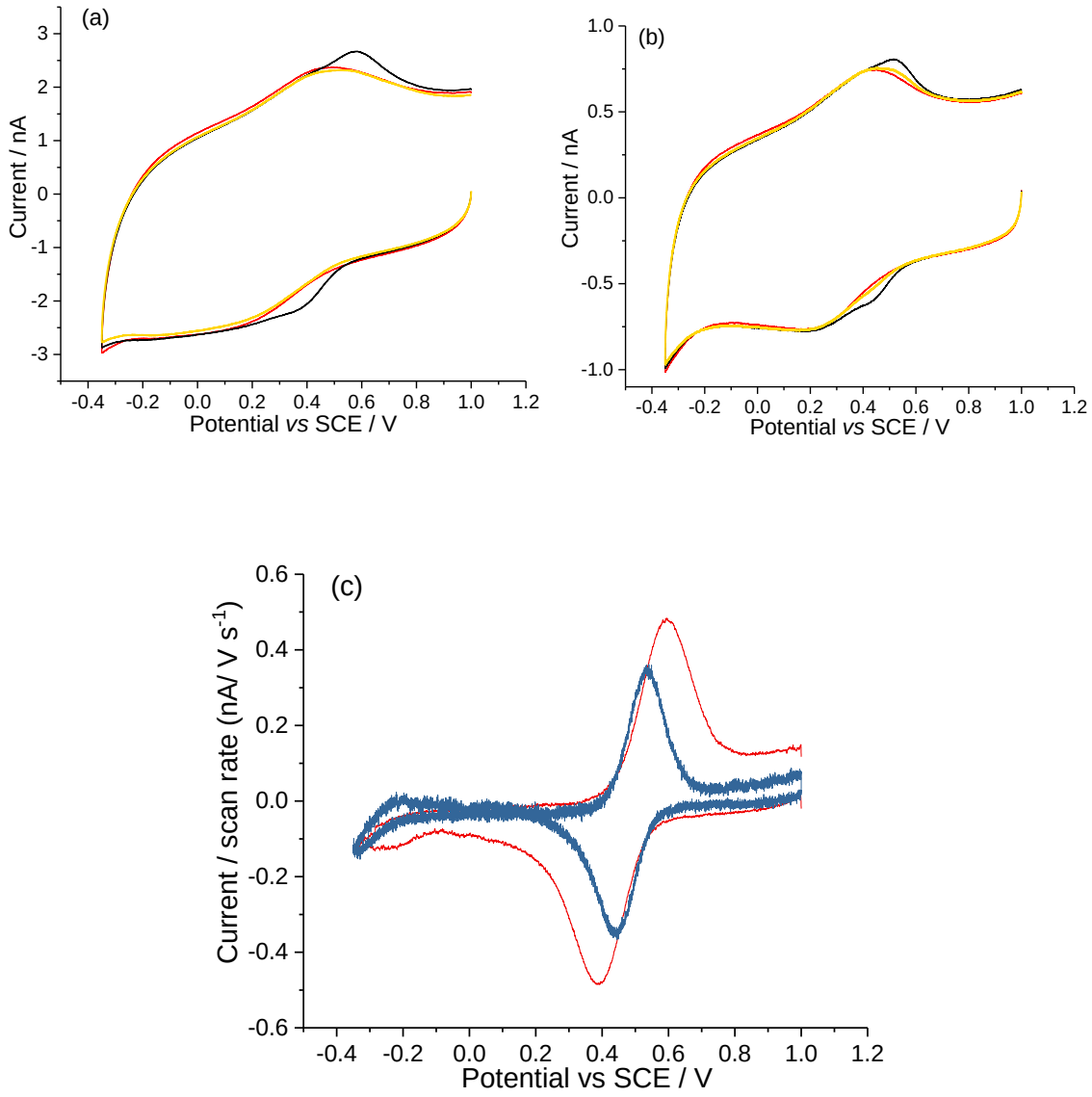


Figure 7.10 Voltammograms on a carbon microdisc electrode (r=3.5 µm) at 25 ºC at (a) 0.8V s^{-1} and (b) 0.2V s^{-1}. The overlaid voltammograms in (a) and (b) were measured in blank solution 1: before adsorption (red), with adsorption (black) and after desorption (yellow). (c) presents the voltammograms after background subtraction at 0.8 V s^{-1} (red) and 0.2 V s^{-1} (blue). Solution composition: 10 mM $NH_4Fe(SO_4)_2$, 2.5 mM $(NH_4)_2SO_4$ with 0.2 M $HClO_4$.

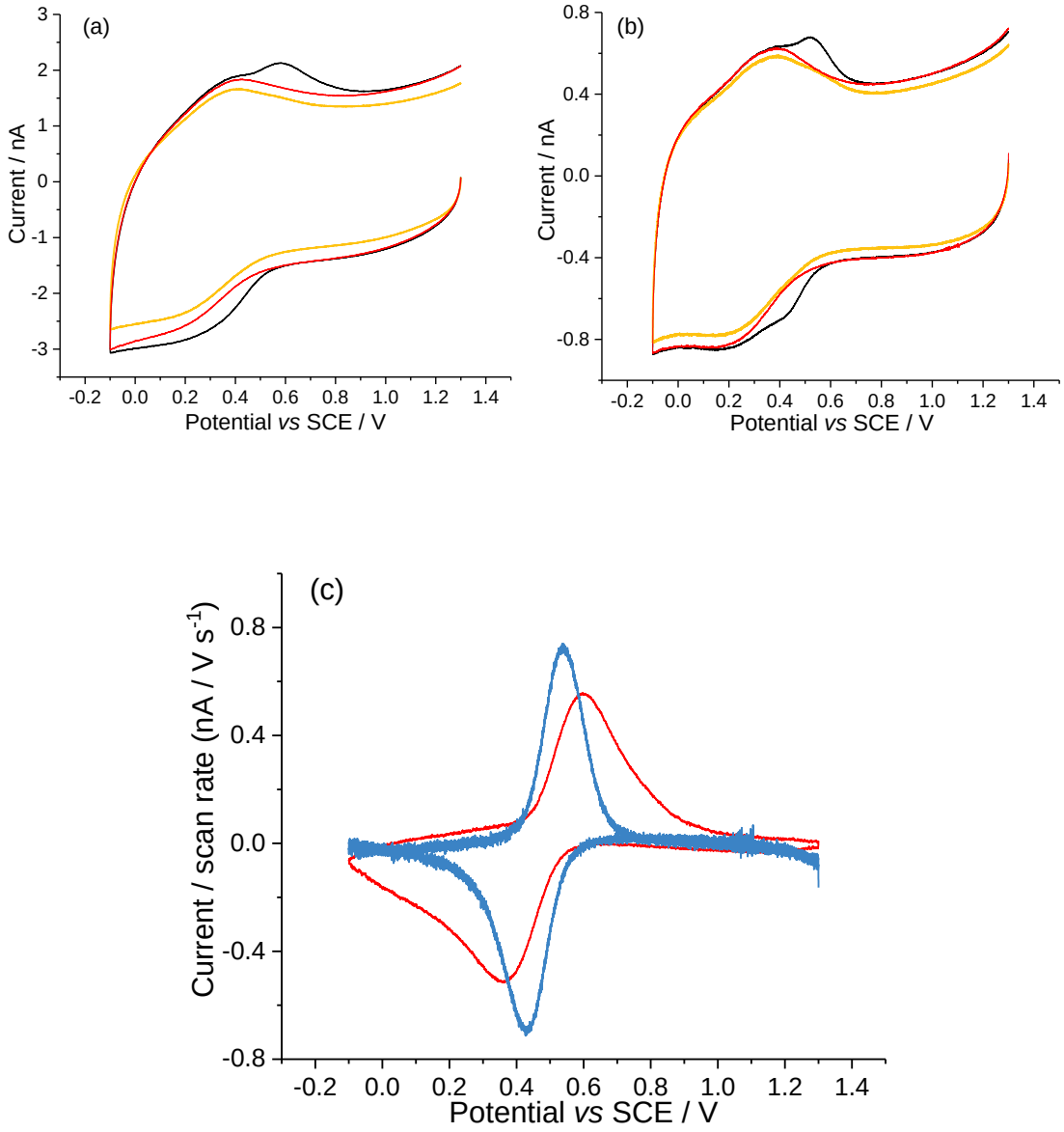


Figure 7.11 Voltammograms on a carbon microdisc electrode (r=3.5 µm) at 25 °C at (a) 0.8V s^{-1} and (b) 0.2V s^{-1}. The overlaid voltammograms in (a) and (b) were measured in blank solution 1: before adsorption (red), with adsorption (black) and after desorption (yellow). (c) presents the voltammograms after background subtraction at 0.8 V s^{-1} (red) and 0.2 V s^{-1} (blue). Solution composition: 15 mM $NH_4Fe(SO_4)_2$, 2.5 mM $(NH_4)_2SO_4$ with 0.2 M $HClO_4$.

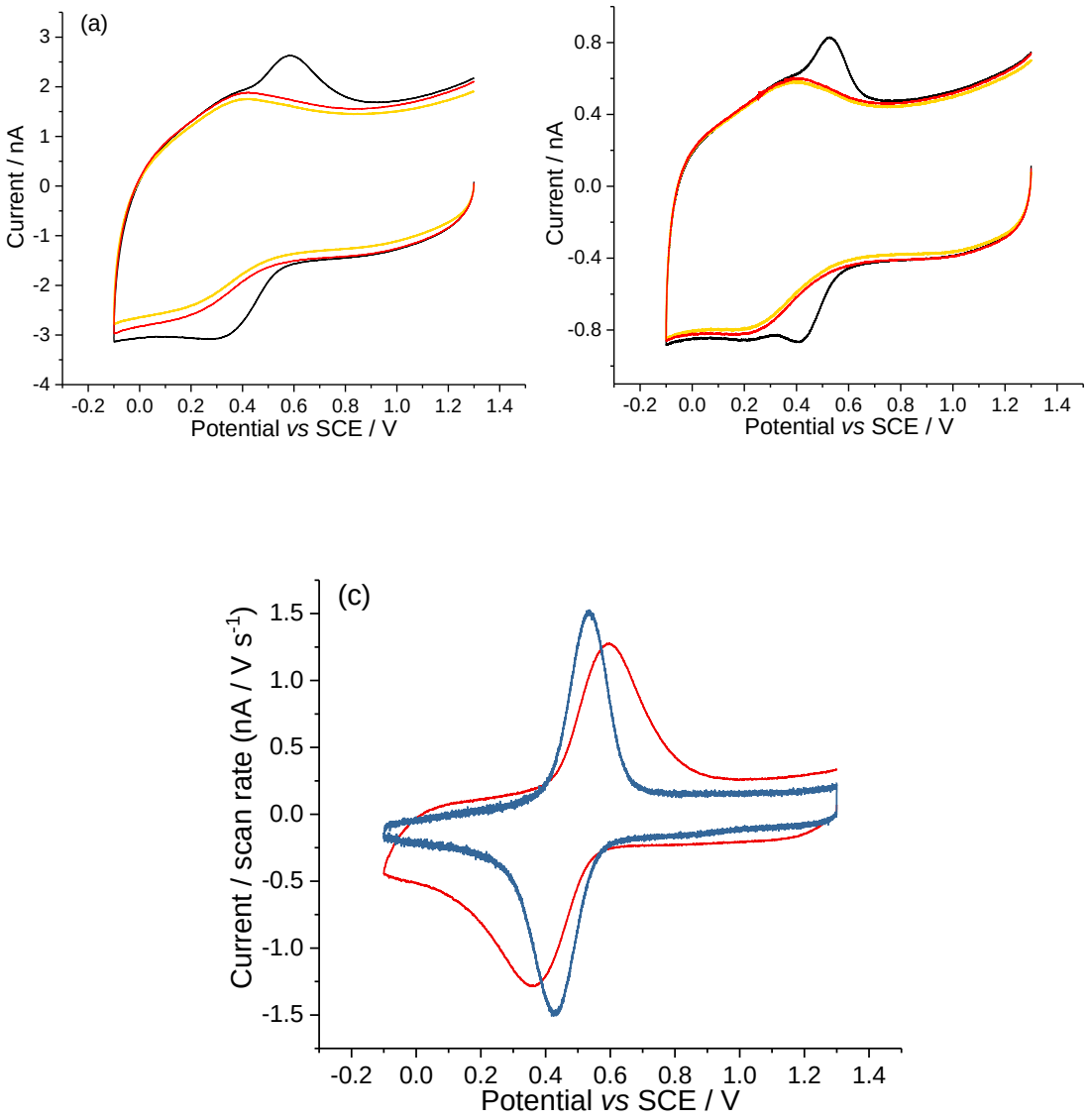


Figure 7.12 Voltammograms on a carbon microdisc electrode (r=3.5 µm) at 25 °C at (a) 0.8V s^{-1} and (b) 0.2V s^{-1}. The overlaid voltammograms in (a) and (b) were measured in blank solution 1: before adsorption (red), with adsorption (black) and after desorption (yellow). (c) presents the voltammograms after background subtraction at 0.8 V s^{-1} (red) and 0.2 V s^{-1} (blue). Solution composition: 20 mM $NH_4Fe(SO_4)_2$, 2.5 mM $(NH_4)_2SO_4$ with 0.2 M $HClO_4$.

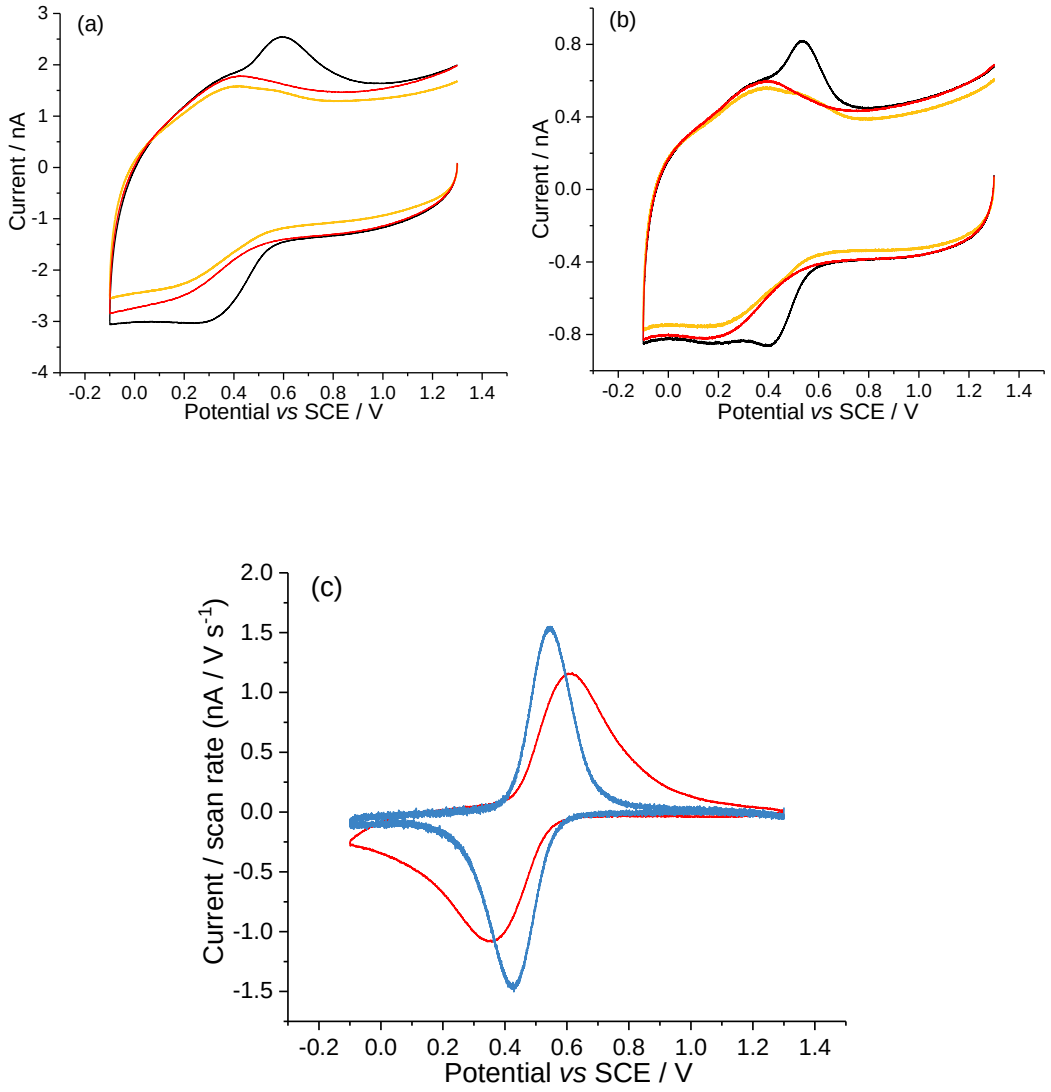


Figure 7.13 Voltammograms on a carbon microdisc electrode (r=3.5 µm) at 25 °C at (a) 0.8V s^{-1} and (b) 0.2V s^{-1}. The overlaid voltammograms in (a) and (b) were measured in blank solution 1: before adsorption (red), with adsorption (black) and after desorption (yellow). (c) presents the voltammograms after background subtraction at 0.8 V s^{-1} (red) and 0.2 V s^{-1} (blue). Solution composition: 30 mM $NH_4Fe(SO_4)_2$, 2.5 mM $(NH_4)_2SO_4$ with 0.2 M $HClO_4$.

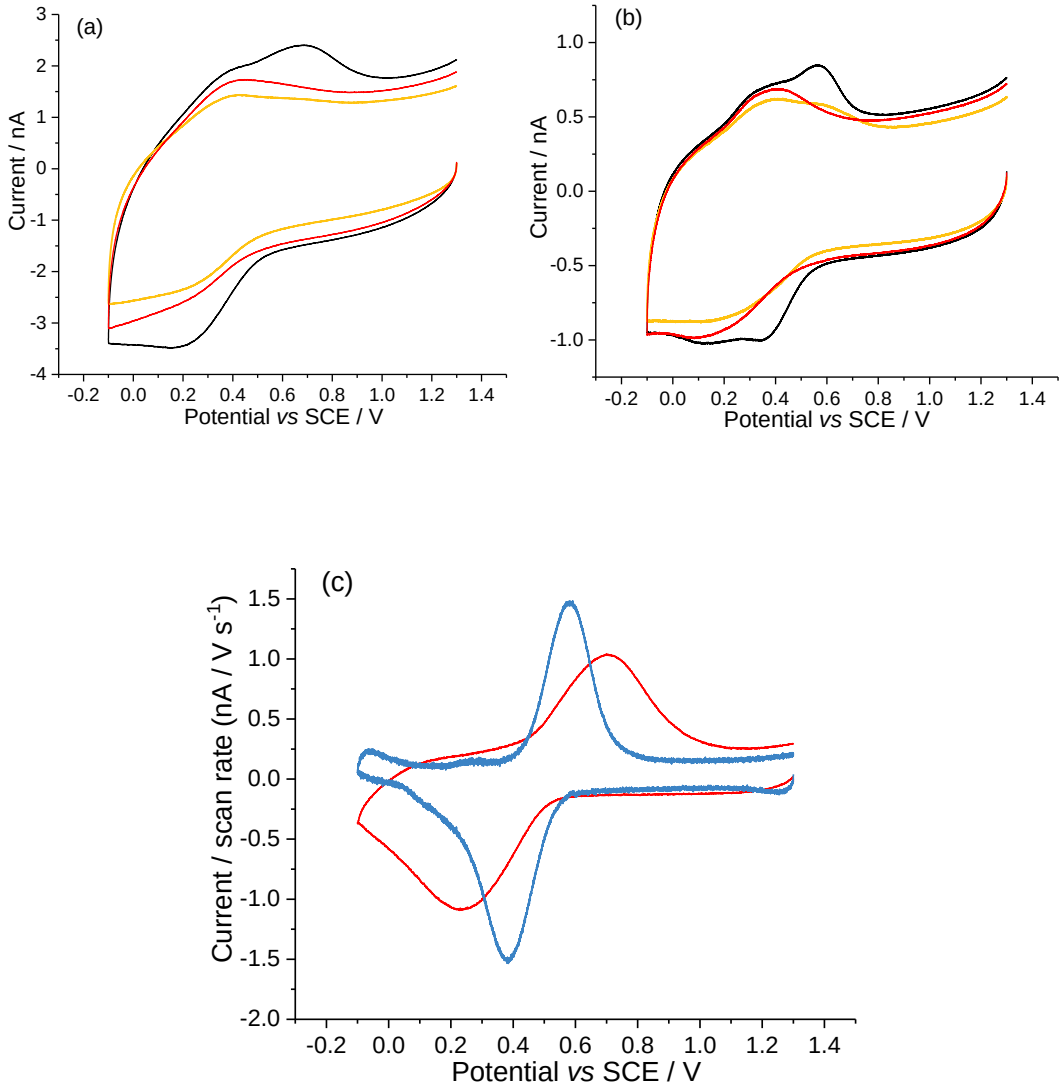


Figure 7.14 Voltammograms on a carbon microdisc electrode (r=3.5 µm) at 25 °C at (a) 0.8V s^{-1} and (b) 0.2V s^{-1}. The overlaid voltammograms in (a) and (b) were measured in blank solution 1: before adsorption (red), with adsorption (black) and after desorption (yellow). (c) presents the voltammograms after background subtraction at 0.8 V s^{-1} (red) and 0.2 V s^{-1} (blue). Solution composition: 40 mM $NH_4Fe(SO_4)_2$, 2.5 mM $(NH_4)_2SO_4$ with 0.2 M $HClO_4$.

7.4.4.2 Fe^{2+} oxidation on a carbon microdisc electrode

Similar experiments to those reported above were undertaken to investigate Fe^{2+} adsorption on carbon electrodes. The polished carbon microdisc electrode was first

measured in blank solution (2.5 mM $(NH_4)_2SO_4$ and 0.2 M $HClO_4$), the electrode was then immersed in adsorption solution with variable concentrations of Fe^{2+} and measured again in blank solution at 0.8 V s^{-1}. Figure 7.15 presents the adsorption isotherm for Fe^{2+} at different concentrations. The theoretical value for the maximum hydrated Fe^{2+} adsorption on the electrode as a monolayer was calculated to be 4.71×10^{-10} mol cm^{-2} with the assumption of a close packed Fe^{2+} with a bond length of Fe^{II}-O of 0.210 nm on a geometrically flat microdisc electrode. Note that this value is the extreme maximum value if the roughness factor of the electrode surface is assumed to unity whereas in reality this is not the case (as discussed in Chapter 5); consequently as the roughness factor increases the real electrochemical surface area of the electrode increases and therefore the corresponding surface coverage decreases. The surface coverage of catechol on the electrode was estimated from charge integration in the voltammograms, giving a value of $(4.33 \pm 0.66) \times 10^{-12}$ mol cm^{-2} as labelled as lower dotted line in Figure 7.15.

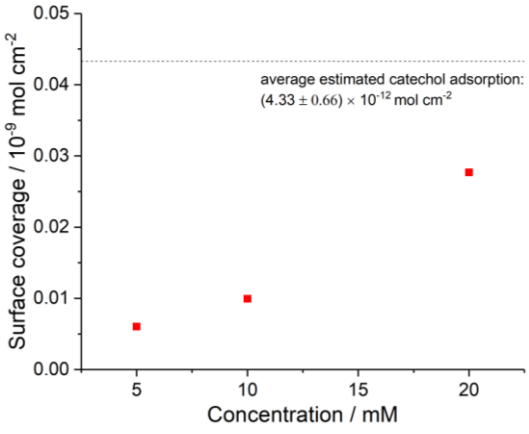


Figure 7.15 Adsorption isotherm for Fe^{2+} in adsorption solutions containing various concentrations of Fe^{2+} at 25 °C. The scan rate is 0.8 V s^{-1} (red). Solution composition: $(NH_4)_2Fe(SO_4)_2$, 2.5 mM $(NH_4)_2SO_4$ with 0.2 M $HClO_4$.

The corresponding voltammograms for Fe^{2+} transfer experiments in each concentration, 5 mM (Figure 7.16), 10 mM (Figure 7.17) and 20 mM (Figure 7.18) are shown below. Figure 7.16 - 7.18(a) present the corresponding voltammograms obtained in blank solution before adsorption (red), with adsorption (black) and after desorption (yellow) at 0.8 V s^{-1}. Figure 7.16-7.18(b) show the voltammograms with adsorption after background subtraction at 0.8 V s^{-1}. Similarly, clear adsorption peaks were observed in all cases and the voltammograms after background subtraction give nice surface-bound peaks, which further indicates that the Fe^{2+}/Fe^{3+} redox couple is sensitive to the presence of quinone/catechol groups.

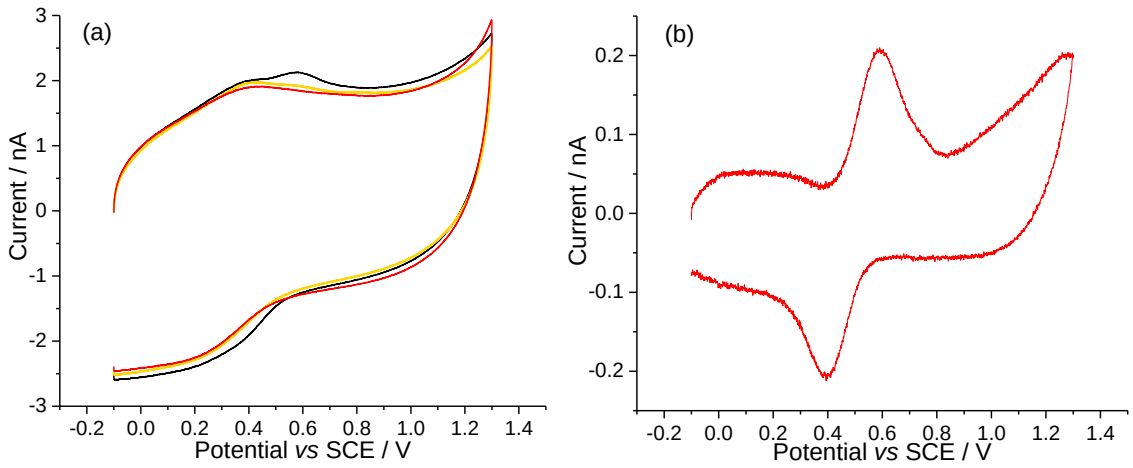


Figure 7.16 (a) Voltammograms on a carbon microdisc electrode (r=3.5 µm) at 25 °C at 0.8V s^{-1}. The overlaid voltammograms in (a) were measured in blank solution 1: before adsorption (red), with adsorption (black) and after desorption (yellow). (b) presents the voltammograms after background subtraction at 0.8 V s^{-1}. Solution composition: 5 mM $(NH_4)_2Fe(SO_4)_2$ with 0.2 M $HClO_4$.

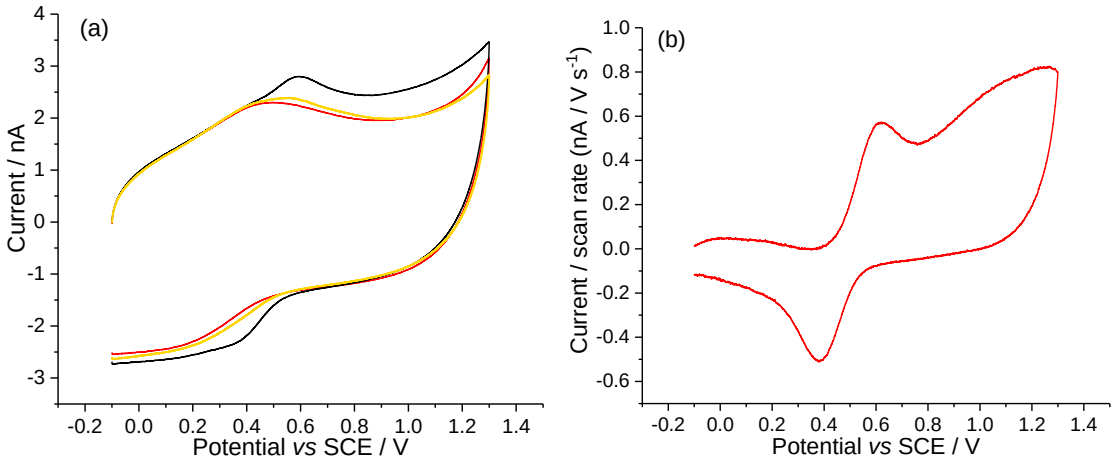


Figure 7.17 (a) Voltammograms on a carbon microdisc electrode (r=3.5 µm) at 25 ºC at 0.8V s^{-1}. The overlaid voltammograms in (a) were measured in blank solution 1: before adsorption (red), with adsorption (black) and after desorption (yellow). (b) presents the voltammograms after background subtraction at 0.8 V s^{-1}. Solution composition: 10 mM $(NH_4)_2Fe(SO_4)_2$ with 0.2 M $HClO_4$.

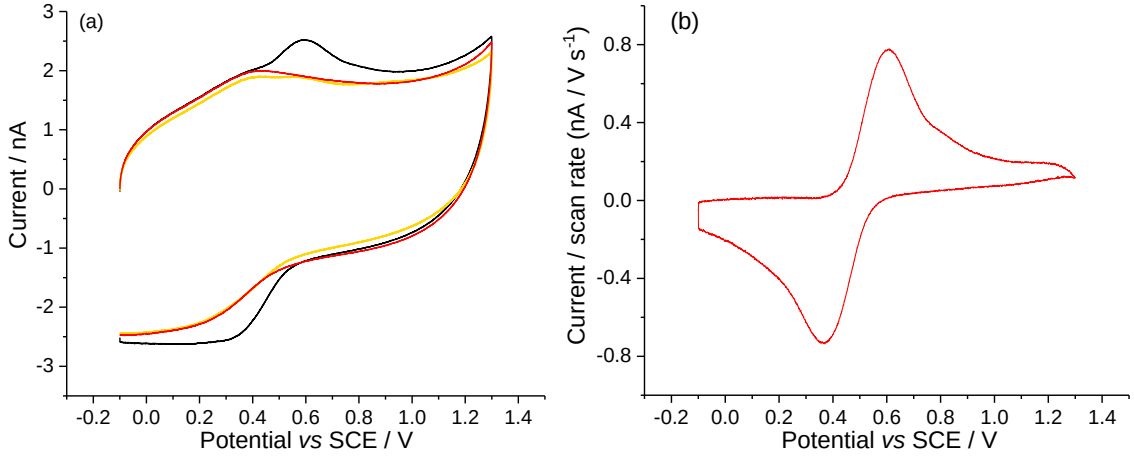
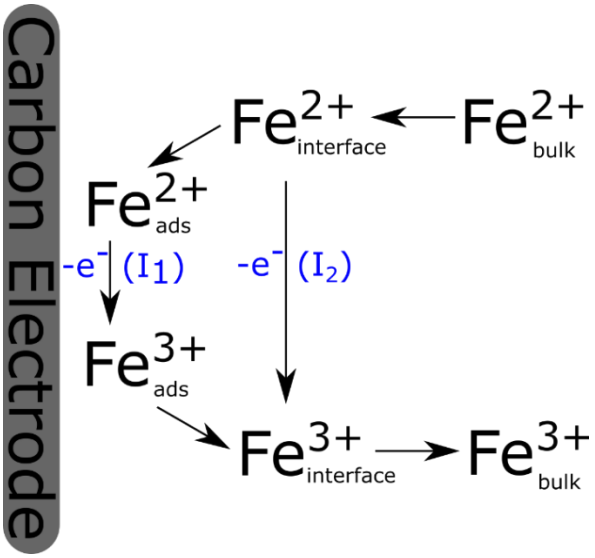


Figure 7.18 (a) Voltammograms on a carbon microdisc electrode (r=3.5 µm) at 25 ºC at 0.8V s^{-1}. The overlaid voltammograms in (a) were measured in blank solution 1: before adsorption (red), with adsorption (black) and after desorption (yellow). (b) presents the voltammograms after background subtraction at 0.8 V s^{-1}. Solution composition: 20 mM $(NH_4)_2Fe(SO_4)_2$ with 0.2 M $HClO_4$.

7.4.5 Proposed mechanistic model of the $Fe^{2+/3+}$ redox process

The pre-wave observed on the carbon electrode in Figure 7.4 gives a quasi-steady-state-like behaviour. Such steady-state behaviour was also observed by Sato *et al.* in the investigation of the catalysis of the oxidation of Fe^{2+} in aqueous solution by $[Mo(CN)_8]^{3-}$ on a rotating disk pyrolytic graphite electrode[23]. On the basis of the above experimental results we propose that the Fe^{2+} oxidation on the carbon electrode can be understood via a mechanistic model involving two parallel pathways (Scheme 7.3). First, at low overpotentials there is a surface mediated redox reaction where the results are consistent with the oxidation proceeding via a surface adsorbed iron-quinone complex (Pathway 1) and the current obtained from pathway 1 is labelled as I_1. Second, at higher overpotentials the oxidation proceeds via a direct solution phase oxidative route (Pathway 2) and the obtained current from this pathway is I_2. Here, for pathway I_1 the likely rate determining step will be desorption of the Fe^{3+} species. However, it should however be noted that an alternative reaction scheme whereby the surface adsorbed iron species serves to mediate the electron transfer in a manner comparable to that found for the self-catalysis of catechol[9] cannot be ruled out. Moreover, it is more challenging to conceive of how such a mechanism could lead to the occurrence of two parallel electron transfer pathways, as experimentally evidenced by the measured transfer coefficient. The transfer coefficient for this direct oxidative pathway (I_2) has a value of approximately 0.35, as determined from the experimental data at high overpotentials whilst the value is much smaller at low

overpotentials as presented in Figure 7.4(b). The switch in the electrode mechanism is reflected in the measured transfer coefficient which is sensitive to the applied electrode potential.



Scheme 7.3 Proposed two parallel pathways during the $Fe^{2+/3+}$ redox process in solution.

A numerical model was developed by Dr Christopher Batchelor-McAuley to demonstrate how the presence of a parallel mechanism can cause such a change in systems transfer coefficient. The voltammetric response on a 2D diffusion microdisc electrode was simulated using a home-written programme written by Dr Oleksiy Klymenko[15a]as described in the Experimental Section. The simulations were done for a simple one-electron transfer oxidative process $A - e \rightarrow B$ at a scan rate of 0.01 V s^{-1} with a formal potential of 0.4837 V, the diffusion coefficients of 6.68×10^{-10} and 5.45×10^{-10} m^2 s^{-1} for A and B, respectively. The current from pathway 2 (I_2) was simulated with an electron transfer rate of 0.08 cm s^{-1} and reaches a steady-state current of 0.2 nA which is equivalent to the current of prewave observed on the experimental voltammogram. The current

obtained under diffusion-only condition from pathway 1 (I_1) was simulated with an anodic transfer coefficient α_a of 0.35 ($\alpha_a + \alpha_c = 1$), an electron transfer rate of 1×10^{-5} cm s^{-1} and the electrode radius of 3.51 μm. The total voltammetric current was then estimated using mathematical approximation using Equation (7.4) and the corresponding voltammogram is shown in Figure 7.19(a). In the analytical approximation, $\frac{I_2}{I_{s.s}}$ stands for the amount of materials consumed by pathway 2 and $(1-\frac{I_2}{I_{s.s}})$ then represents for the amount of materials left for the pathway 1. Figure 7.19(b) shows the oxidative transfer coefficient plot in the current range of 1%-95% of $I_{s.s}$ with (green curve) and without (red curve) mass-transport correction. It shows that the non-mass-transport corrected anodic transfer coefficient significantly deviates from its true value (0.35) and approaches zero at high overpotential. The range of the transfer coefficient was given as the gray-shaded area where the upper limit was given using non-uniformly accessibility correction and the lower limit was given by the conventional mass-transport correction and the darker colour represents larger probability to its true value. As is shown in Figure 7.19(b), the corrected transfer coefficient drops down for both correction methods when the current range is larger than ca. 70% of $I_{s.s}$ due to the increased contribution from linear diffusion and therefore the larger deviation from a true steady-state condition.

$$I_{tot} = I_2 + (1-\frac{I_2}{I_{s.s}})I_1 \tag{7.6}$$

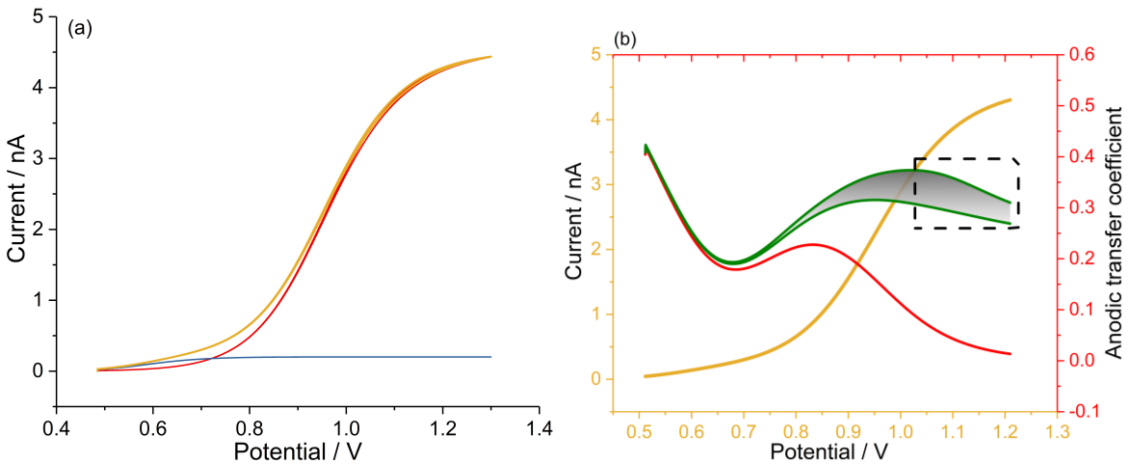


Figure 7.19 (a) Simulated voltammetric responses (I_1-red; I_2-blue; I_{tot}-yellow) on a carbon microdisc electrode for the proposed two parallel model. (b) Anodic transfer coefficient plots for the oxidative wave in the current range of 1%-95% of $I_{s.s}$. The yellow curve is the oxidative wave. The red curve is the measured anodic transfer coefficient plot without mass transport correction. The green curves are the mass-transport corrected transfer coefficient with (upper green curve) and without (lower green curve) non-uniformly accessibility correction. The estimated range of the transfer coefficient is shaded where the darker colour gives a closer to its true value.

7.5 Conclusions

To conclude, the surface quinones on carbon electrodes were found to intrinsically alter Fe^{2+} oxidation via the formation of Fe-quinone complexes under acidic conditions. Such mediation has long been suggested but not proved. This quinone mediated redox process was observed as a quasi-steady-state like '*prewave*' at lower overpotential compared to the main wave on a carbon microdisc electrode. Moreover, the presence of this electrocatalytic process (i.e. the pre-wave) is more apparent under lower mass-transport conditions and will likely be the dominant redox pathway when larger macroscale electrodes are used, as may be employed for example in a redox flow-cell battery.

References:

[1] D. Li, C. Batchelor-McAuley, L. Chen, R. G. Compton, *The Journal of Physical Chemistry Letters* **2020**, *11*, 1497-1501.

[2] aL. Yue, W. Li, F. Sun, L. Zhao, L. Xing, *Carbon* **2010**, *48*, 3079-3090; bL.-C. Jiang, W.-D. Zhang, *Biosensors and Bioelectronics* **2010**, *25*, 1402-1407; cY. Zhang, L. Liu, B. Van der Bruggen, F. Yang, *Journal of Materials Chemistry A* **2017**, *5*, 12673-12698.

[3] aP. Chen, M. A. Fryling, R. L. McCreery, *Analytical Chemistry* **1995**, *67*, 3115-3122; bP. Chen, R. L. McCreery, *Analytical Chemistry* **1996**, *68*, 3958-3965; cR. L. McCreery, *Chemical reviews* **2008**, *108*, 2646-2687.

[4] A. J. Bard, *Electroanalytical Chemistry: A Series of Advances*, Taylor & Francis, **1990**.

[5] K. Chaisiwamongkhol, C. Batchelor-McAuley, R. G. Palgrave, R. G. Compton, *Angewandte Chemie* **2018**, *130*, 6378-6381.

[6] aK. Chaisiwamongkhol, C. Batchelor-McAuley, R. G. Compton, *Analyst* **2017**, *142*, 2828-2835; bM. Lu, R. G. Compton, *Analyst* **2014**, *139*, 2397-2403.

[7] J. C. Hoogvliet, P. Van Os, E. J. Van der Mark, W. P. Van Bennekom, *Biosensors and Bioelectronics* **1991**, *6*, 413-423.

[8] aA. Sarapuu, K. Helstein, D. J. Schiffrin, K. Tammeveski, *Electrochemical and Solid State Letters* **2004**, *8*, E30; bK. Tammeveski, K. Kontturi, R. J. Nichols, R. J. Potter, D. J. Schiffrin, *Journal of Electroanalytical Chemistry* **2001**, *515*, 101-112.

[9] S. H. DuVall, R. L. McCreery, *Journal of the American Chemical Society* **2000**, *122*, 6759-6764.

[10] S. Chakraborty, C. R. Raj, *Journal of Electroanalytical Chemistry* **2007**, *609*, 155-162.

[11] T. Nagaoka, T. Sakai, K. Ogura, T. Yoshino, *Analytical Chemistry* **1986**, *58*, 1953-1955.

[12] J. Zhang, X. Wang, Q. Su, L. Zhi, A. Thomas, X. Feng, D. S. Su, R. Schlögl, K. Müllen, *Journal of the American Chemical Society* **2009**, *131*, 11296-11297.

[13] aX. Li, T. Liu, L. Liu, F. Li, *RSC Advances* **2014**, *4*, 2284-2290; bX. Li, L. Liu, T. Liu, T. Yuan, W. Zhang, F. Li, S. Zhou, Y. Li, *Chemosphere* **2013**, *92*, 218-224; cW. D. Burgos, Y. Fang, R. A. Royer, G.-T. Yeh, J. J. Stone, B.-H. Jeon, B. A. Dempsey, *Geochimica et cosmochimica acta* **2003**, *67*, 2735-2748; dY. Wu, F. Li, T. Liu, R. Han, X. Luo, *Electrochimica Acta* **2016**, *213*, 408-415.

[14] aT. J. Petek, N. C. Hoyt, R. F. Savinell, J. S. Wainright, *Journal of Power Sources* **2015**, *294*, 620-626; bL. Wei, M. C. Wu, T. S. Zhao, Y. K. Zeng, Y. X. Ren, *Applied Energy* **2018**, *215*, 98-105.

[15] aO. V. Klymenko, R. G. Evans, C. Hardacre, I. B. Svir, R. G. Compton, *Journal of Electroanalytical Chemistry* **2004**, *571*, 211-221; bO. Klymenko, R. G. Compton, Thesis (D.Phil.)--University of Oxford, 2004. **2004**.

[16] aR. Guidelli, R. G. Compton, J. M. Feliu, E. Gileadi, J. Lipkowski, W. Schmickler, S. Trasatti, *Pure and Applied Chemistry* **2014**, *86*, 259-262; bR. Guidelli, R. G. Compton, J. M. Feliu, E. Gileadi, J. Lipkowski, W. Schmickler, S. Trasatti, *Pure and Applied Chemistry* **2014**, *86*, 245-258.

[17] E. Gileadi, *Journal of Solid State Electrochemistry* **2011**, *15*, 1359.

[18] D. Li, C. Lin, C. Batchelor-McAuley, L. Chen, R. G. Compton, *Journal of Electroanalytical Chemistry* **2018**, *826*, 117-124.

[19] K. Ngamchuea, C. Lin, C. Batchelor-McAuley, R. G. Compton, *Analytical Chemistry* **2017**, *89*, 3780-3786.

[20] D. Li, C. Batchelor-McAuley, R. G. Compton, *Applied Materials Today* **2019**.

[21] C. A. Thorogood, G. G. Wildgoose, A. Crossley, R. M. J. Jacobs, J. H. Jones, R. G. Compton, *Chemistry of Materials* **2007**, *19*, 4964-4974.

[22] aM. J. Harrington, A. Masic, N. Holten-Andersen, J. H. Waite, P. Fratzl, *Science* **2010**, *328*, 216-220; bN. Holten-Andersen, M. J. Harrington, H. Birkedal, B. P. Lee, P. B. Messersmith, K. Y. C. Lee, J. H. Waite, *Proceedings of the National Academy of Sciences* **2011**, *108*, 2651-2655.

[23] K. Sato, T. Ohsaka, H. Matsuda, N. Oyama, *Bulletin of the Chemical Society of Japan* **1983**, *56*, 1863-1864.

Chapter 8

Mass Transport Corrected Transfer Coefficients from Microdisc Cyclic Voltammetry: 2D Simulation and Experiment

The transfer coefficient (or equivalently the Tafel slope) is an experimentally measurable parameter defined as the change in the logarithm of the current density as a function of the applied potential, where the current density has been corrected for changes in the concentration of the reagent at the interface. For some electrode geometries (such as the rotating disc or a micro hemispherical electrode) where the electroactive interface is uniformly accessible under a steady-state regime, these changes in concentration can be corrected for analytically which significantly increases the potential range over which Tafel analysis can be used to accurately yield information regarding the electron transfer process as discussed in Chapters 4 and 5. The important question arises therefore, for non-uniformly accessible electrodes, such as a microdisc, where the current density varies across the electrode surface, how can the experimentally measured electrochemical flux be corrected for to account for the changes in the surface concentration of the reagent? This work presents a simple simulation technique that allows the voltammetry of a microdisc to be ‘mass-transport’ corrected without recourse to the use of analytical approximations.

This work presented in this chapter has been published in *ChemElectroChem* and was carried out in collaboration with Dr. Christopher Batchelor-McAuley.

8.1 Introduction

Tafel analysis allows the experimental determination of the sensitivity of an interfacial redox reaction to the applied electrode potential.[1] This sensitivity is often expressed as a Tafel slope (b = dE/dlog|i|) with units of mV dec^{-1} or equivalently as a transfer coefficient (α = RTln10/Fb). However, as the overpotential for a redox reaction increases, the interfacial electron transfer rapidly becomes limited by the mass-transport of the reactant to the interface and not the kinetics of the electrochemical reaction. This issue of the mass-transport limitation of the reaction rate significantly constrains the range over which Tafel analysis can be performed on a voltammogram so as to allow the extraction of physically meaningful insight regarding the electron transfer kinetics. Reflecting this issue of the mass-transport limitation, the International Union of Pure and Applied Chemistry (IUPAC) have more rigorously defined the transfer coefficient (α_c) for a reductive (cathodic) process as:[2]

$$\alpha_c = -\frac{RT}{F}\left(\frac{dln|j_{c,corr}|}{dE}\right) \tag{8.1}$$

where R is the gas constant (8.314 J K mol^{-1}), T is the temperature (298.15 K), F is the Faraday Constant (96485 C mol^{-1}) and E is the applied potential at the working electrode (V) and the cathodic flux ($j_{c,corr}$) has been corrected for any changes in the reactant

concentration at the electrode surface with respect to its bulk value. Similarly, the anodic transfer coefficient is defined simply as above in Equation (8.1) but where the minus sign is removed and $j_{c,corr}$ is replaced by the anodic flux ($j_{a,corr}$).

This definition of transfer coefficient is independent of any mechanistic considerations; consequently, having experimentally determined the transfer coefficient, so as to gain insight into the interfacial process, it is for the researcher to interpret the physical meaning of the measured value. In the case where only one electron is being transferred, then the transfer coefficient can in this case be viewed as the fraction of the electrostatic potential difference 'driving' the reaction which is available to affect the interfacial reaction rate, such that the transfer coefficient serves to give a measure of the 'position' - reactant- or product-like - of the transition state.[3] In this one-electron case it is generally assumed that the transfer coefficient will have a value close to 0.5; however, for electrochemical reactions involving adsorbed species the transfer coefficient can deviate significantly away from this value.[4] Further in accordance with the Butler-Volmer equation it is commonly assumed that the transfer coefficient is a constant, independent of the applied electrode potential. As outlined by Marcus-Hush theory, which provides a microscopic model for an outer-sphere electron transfer process, the transfer coefficient is anticipated to tend to zero at high overpotentials[5]. Marcus-Hush theory rationalises the electron transfer rate in terms of the reaction Gibbs energy and a 'reorganisation energy'. So-called 'Symmetric' Marcus-Hush theory, as originally employed by Chidsey and others, assumes the force constants for the reduced and oxidised species are equal. Consequently,

this symmetric formulation is equivalent to assuming that at low overpotentials the transfer coefficient is equal to 0.5.[6] However, in reality even for outer-sphere redox processes, and as mentioned above, the transfer coefficient often deviates from 0.5.[7] Correspondence between Marcus-Hush Theory and the Butler-Volmer equation can be found by allowing the force constants for the reduced and oxidised species to differ.[8] This 'asymmetric' formulation of the Marcus-Hush theory provides a more realistic microscopic model of the outer-sphere interfacial redox process, such that the Butler-Volmer equation can be viewed as providing (in the low overpotential limit) an accurate but approximate description of the sensitivity of the electron transfer rate to the applied electrode potential. Further for outer sphere redox processes the transfer coefficient may thus be interpreted as reflecting the asymmetry in the force constants of the reduced and oxidised species. For the situation in which either multiple electrons are transferred and or the interfacial electron transfer reaction is coupled to a homogeneous chemical process then the interpretation of the transfer coefficient becomes appreciably more complex[9]. However, broadly in this case the transfer coefficient can be viewed as being a measure of the number of electrons transferred prior to transition state of the rate determining step.[10] Experimentally, the kinetics of interfacial charge transfer reactions have been demonstrated to deviate significantly from this Butler-Volmer relation, evidencing the potential dependence of the transfer coefficient as a function of the applied potential.[11] Early work by Savéant and his co-workers demonstrated that for a series of outer-sphere elementary electron transfer processes involving the redox of organic molecules in aprotic

media at a mercury electrode, the experimentally determined variation in the transfer coefficient was comparable in magnitude to that predicted by Marcus theory.[11b, 11c] Other work involving potential dependent transfer coefficient have been observed in coupled electron-proton transfer with surface attached redox couples.[12] Hence, although commonly employed the assumption that the transfer coefficient is a constant is not physically correct. However, the largest discrepancies between Butler-Volmer kinetics and Marcus-Hush theory is anticipated to occur at high overpotentials but it is precisely this region of interest that is commonly under mass-transport control, thus limiting the ability of Tafel analysis to successfully differentiate between these electron transfer models.

For a fully irreversible reductive process, when the applied potential is sufficiently far from the equilibrium potential E_{eq}, the flux contribution from the oxidation can be neglected. In this case and at low current densities the transfer coefficient can be experimentally measured[13] without considering the concentration changes of the electro-active species at the interface:

$$-\frac{RT}{F}\frac{dln|I_c|}{dE} = \alpha_{c,nc} \tag{8.2}$$

where I_c is the experimentally measured cathodic current, $\alpha_{c,nc}$ is the *non*-mass-transport corrected transfer coefficients. Hence, the measured transfer coefficient $\alpha_{c,nc}$ will, at higher potentials, deviate from its true value α_c (given by equation 8.1) due to the local depletion of reagents at the electrochemical interface. At low current densities

(relative to the mass-transport limit) this issue of reactant depletion is not significant and in this case $\alpha_{c,nc} \rightarrow \alpha_c$ and a plot of $ln|I|$ vs E should have a slope equal to $-\alpha_c F/RT$. However, at higher overpotentials such a plot of $ln|I|$ vs E will rapidly deviate away from linearity reflecting the decrease in the reagent at the interface. For voltammetry at a macrodisc (radius in ca. millimetre) electrode, if we wish to obtain the transfer coefficient within 10% error of the actual value then in the absence of correction only the current at the foot of the wave - below 19% of the peak current - can be used in the analysis.[13] Even more challengingly for a microdisc electrode (radius in ca. micrometre) only currents less than 7.9% of the steady-state flux are suitable for use in such analysis.[13] Furthermore, the current range that is suitable for use in non-mass-transport correct Tafel analysis is further constrained by the presence of background or capacitative currents which provide a practical limit on how small a current can be analysed.[14] Background subtraction of a voltammogram to, as far as possible, remove any capacitative contributions to the voltammetric signal is imperative in all cases.

Clearly when the electrode reaction is under mass-transport limited conditions no information regarding the electron transfer kinetics are contained in the voltammetric profile. However, the voltammetric waveshape still contains information regarding the electron transfer rate even in the region where the current is under *mixed* mass-transport electron transfer control (i.e. on the voltammetric wave). The question arises, how may the experimentally recorded flux be corrected for to account for changes in the surface concentration of the reactant and therefore allow accurate extraction of the interfacial

kinetics? For cases in which the electrode is uniformly accessible and under a steady-state mass-transport regime, such as is the case for a rotating disc electrode or for a micro-hemisphere electrode the problem can be solved analytically and use of this procedure has long been advocated.[15] In this case a plot of $\ln\left|\frac{1}{I}-\frac{1}{I_{lim}}\right|$ against potential yields a slope of $\alpha_a F/RT$ or $-\alpha_c F/RT$ which has been corrected to account for the change in the reactants at the interface. As will be explored in more detail later in this chapter, this mass-transport correction is very comparable to the Koutecký-Levich (K-L) analysis method[16]. Even with the use of such a mass-transport corrected Tafel plot on a rotating disc electrode voltammogram, due to the uncertainties in the magnitude of I_{lim} previous work has advised that only the lower 80% of the steady-state voltammetric wave be used for analysis.[15b] Although such analytical correction is possible for these uniformly accessible and steady-state mass-transport conditions, for other electrode geometries this is not feasible and the application to the above correction leads to errors in the measurement of the transfer coefficient even before considering uncertainties in the magnitude of the mass-transport limited current.[13]

Most notably in the case of transient voltammetry at a macro-disc electrode under a linear diffusion regime attempting to correct for the change in the surface concentration using the above analytical mass-transport correction is no better (in fact it is worse!) than simply analysing the transfer coefficient from a plot of $\ln|I|$ vs. E.[13] Conversely for a microdisc electrode, although a steady-state mass-transport regime is obtained the waveshape differs from that of a micro-hemisphere electrode as the electrochemical interface is not

uniformly accessible.[17] Hence, application of the above analytical correction ($\ln\left|\frac{1}{I}-\frac{1}{I_{lim}}\right|$) in the analysis of microdisc voltammetry improves the analysis. However it is not exact, leading to errors at higher current densities. For a microdisc electrode at true steady-state and with the use of this analytical correction, the foot of the voltammetric wave up to 71% of the steady-state current can be analysed and the resulting transfer coefficient will be within 10% of its true value.[13] As a note of caution however, this analysis, concluding that 71% of the wave can be used, assumes that the limiting current is known with perfect accuracy; in reality, as will be in-part broached in this work, this is not the case. Furthermore, we comment that a similar issue regarding the application of the analytical mass-transport correction arises with voltammetry at both cylindrical and band electrode geometries where the mass-transport regime is inherently quasi-steady-state.

The K-L analysis method was originally developed for use with rotating disc electrode voltammetry; however, it has been more recently adapted for application to the analysis of microelectrodes.[16, 18] First and foremost, this standard K-L analysis implicitly assumes that the transfer coefficient is a constant. Disregarding this issue the use of the K-L analysis on a microdisc electrode suffers the same issue as the analytical mass-transport correction ($\ln\left|\frac{1}{I}-\frac{1}{I_{lim}}\right|$) presented above; both analyses assume the electrode to be uniformly accessible and the errors incurred through application of this assumption are extremely comparable (see section 8.2 more detail). Given that the K-L method uses the current at discrete potentials the analytical mass-transport correction of the voltammetric

data is arguably a better method for analysing the transfer coefficient of a system due to its use of more of the voltammetric data and its none reliance on the assumption of a potential independent transfer coefficient.

As neither of these analytical procedures for correcting for the depletion of the reagent can be applied to many common electrode geometries – such as static disc, band or cylinder electrodes – the conventional way forward is to use numerical simulation to facilitate analysis of the electrochemical response. Here the approach often taken is for a model of the electrochemical reaction and the interfacial electron transfer kinetics to be proposed and the resulting voltammetric response predicted via numerical simulation.[3] In this approach unknown parameters in the model are varied so as to find a best fit for the simulated to the experimental data. A primary issue here is that the validity of the results is requisite on the accuracy of the applied model. As an alternative approach and as will be explored in this work it is possible to directly numerically extract the kinetics for an electrochemical reaction from an experimental voltammogram, without any *a priori* assumption regarding the underlying dependences between the electrochemical reaction rate and the applied potential.

Previous work has demonstrated how in the case of quasi-reversible voltammetry at a large (50 μm, scan rate = 1 V s^{-1}) hemi-spherical electrode (i.e. not under steady-state mass-transport conditions and at a uniformly accessible electrode), it is possible to use simulation to directly extract kinetic information regarding both the forward and back

reactions directly from experimental data.[19] In this earlier work the experimental voltammetry was used as an input and the one-dimensional diffusion equation solved for the known geometry of the system, thus allowing the electron transfer kinetics to be directly assessed without any prior assumption regarding how the rate of reaction will vary with the applied potential. Other literature examples using convolution methods have also been restricted to considering systems that are one-dimensional with respect to the mass-transport.[20] [21]

In this chapter we focus on the numerical extraction of electrochemical reaction kinetics from the voltammetric response of a disc electrode, the proposed method considers a fully irreversible reaction and can be applied to both macro and micro disc experiments and the common situation in which the mass-transport is mixed and is in neither limit. Having demonstrated how this information may be directly obtained from the voltammogram, the sensitivity of the extracted results to uncertainties in the input parameters is considered. It is demonstrated that for a micro and macro-disc electrodes up to 78% and 99% of the voltammetric wave may be used respectively, yielding a measure of the systems transfer coefficient that is within 10% of the true value (this analysis assumes that the physical parameters determining the system are known to a combined accuracy of 2.5% or greater).

8.2 Applications of the Koutecký-Levich method and the normal mass transport corrected method on a microdisc electrode

In the following we first investigate the accuracy of applying the Koutecký-Levich (K-L) method and the normal mass transport corrected method to the analysis of steady-state voltammograms on a microdisc electrode for an irreversible one electron transfer process $A + e^- \rightleftarrows B$. We then turn to investigate how the accuracy changes if the electrodes are under a 'near' but not perfect steady-state regime.

We first calculate the expected steady-state voltammograms for microdisc electrodes with various radii (a=1, 5, 25 and 125 μm) using a previously reported analytical approximate equation for the steady-state flux to a microsdic electrode as developed by Oldham *et al.*[17, 22]. This current-voltage theoretical profile is then analysed using both the K-L method and the normal mass transport corrected method so as to assess the 'best case scenario' for the error incurred by using these more approximate analysis methods. Note the expression for the current presented by Oldham accounts to a high degree of accuracy for the non-uniform accessibility of the microdisc electrode.

8.2.1 The Koutecký-Levich method on a microdisc electrode

For a fully irreversible one electrode transfer process, the total current density is expressed as Equation (8.3)[16]:

$$\frac{1}{j} = \frac{1}{j_{lim}} + \frac{1}{j_{et}} = \frac{1}{Fm_0C} + \frac{e^{\alpha_c\theta}}{Fk^0C} \tag{8.3}$$

where j_{lim} is the mass-transport limiting current, j_{et} is the limiting current for heterogeneous kinetics at the electrode surface calculated using Butler-Vomer model with the assumption of a uniformly accessible electrode, m_0 is the mass transfer coefficient ($m_0 = 4Da/\pi$ for a microdisc electrode), D is the diffusion coefficient of species A, θ is the dimensionless potential where $\theta = F(E - E_0)/(RT)$, C is the bulk concentration of A in solution and k^0 is the electrochemical rate constant.

By using such an'analogous' K-L equation, the information on reaction kinetics can be obtained by plotting $\frac{1}{j}$ versus $\frac{1}{m_0 C}$ at different potentials, giving an intercept of $\frac{e^{\alpha_c \theta}}{Fk^0 C}$ from which the cathodic transfer coefficient and electrochemical rate constant can be calculated. The parameters used in the simulation is shown in the caption of Figure 8.1. Figure 8.1(a) shows the normalised voltammograms at microelectrodes with various radii. The set of plots of $\frac{1}{j}$ versus $\frac{1}{m_0 C}$ at different potentials is given in Figure 8.1 (b), where the linear relationship is obtained as expected with a gradient of 1/F and intercept of $\frac{e^{\alpha_c \theta}}{Fk^0 C}$. The value of the intercept represents the two competing processes of mass transfer and electron transfer. At higher cathodic potentials, the overall process becomes mass transport controlled and hence the intercept will close to zero. As is shown in Figure 8.1(b), the intercept tends to across origin as the potential becomes more negative. The calculated cathodic transfer coefficient and electrochemical rate constant using K-L method are tabulated in Table 8.1 where no prior knowledge of cathodic transfer coefficient and electrochemical rate constant is given. The corresponding plot is shown in Figure 8.2. Here it is shown that the value of k^0 determined from the K-L method varies

over 50% and consequently the accuracy in the estimated cathodic transfer coefficient decreases. The accuracy of the 'K-L' analysis method can be improved is either the transfer coefficient or electron transfer rate is known, however, in most (all?) experimental cases both values are unknown variables.

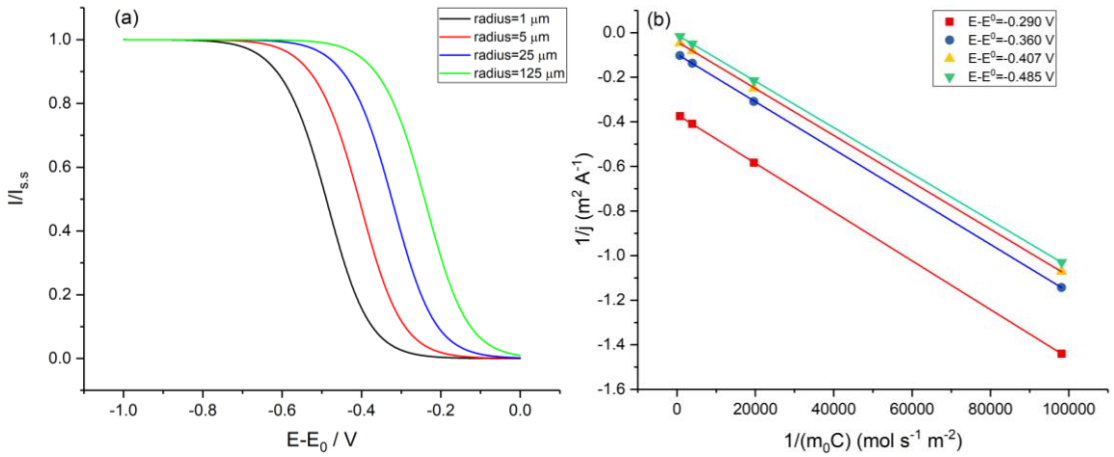


Figure 8.1 (a) Voltammograms at microdisc electrodes with various radii of 1 μm (black), 5 μm (red), 25 μm (blue) and 125 μm (green). All the currents are normalised to their respective steady-state current calculated using Oldham equation. The parameters used in the equation: E_0=0 V; C=1 mM; k^0=1×10^{-7} m s^{-1}; D=1×10^{-9} m^2 s^{-1}; α_a=α_c=0.5. (b) Plots of 1/j vs. 1/(m_0C) obtained from voltammograms in (a) at different potentials E-E_0=-0.0290, -0.360, -0.407, -0.485 V.

Table 8.1 Calculated α_c and k^0 from plots in Figure 8.1(b) where α_c and k^0 are unknown.

Sets of data	**E-E₀ / V**	**Intercept**	**Sets of data used in the calculation**	**α_c and k^0 are unknown actual α_c = 0.5, k^0= 1x10^{-7} m s^{-1}**	
				$\alpha_{c,\ K\text{-}L}$	**k^0 / m s^{-1}**
1)	-0.29	-0.367	1) and 2)	0.4915	1.096×10^{-7}
2)	-0.36	-0.0961	1) and 3)	0.4854	1.176×10^{-7}
3)	-0.407	-0.0402	1) and 4)	0.4759	1.309×10^{-7}
4)	-0.485	-0.00989	2) and 3)	0.4761	1.360×10^{-7}
\	\	\	2) and 4)	0.4671	1.544×10^{-7}
\	\	\	3) and 4)	0.4617	1.712×10^{-7}

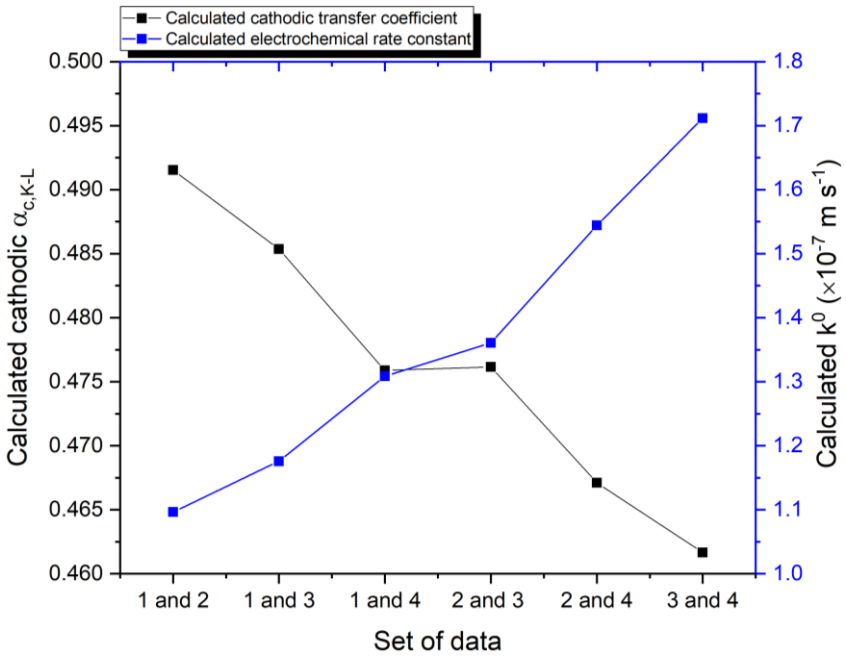


Figure 8.2 Plot of calculated cathodic transfer coefficient and electrochemical rate constant calculated using different set of data from K-L method where α_a and k^o are unknown.

8.2.2 The mass transport corrected method applied to a microdisc electrode

The conventional mass transport correction was applied to the analysis of the steady-state voltammogram obtained on a microdisc electrode with radius of 5 μm (red curve in Figure 8.1a). The corresponding cathodic transfer coefficient plot is obtained using Equation (8.4)[13]:

$$\frac{dln\left|\frac{1}{I_c}-\frac{1}{I_{lim}}\right|}{d\theta} = \alpha_c{}' \tag{8.4}$$

where I_c is the cathodic current, I_{lim} is the mass-transport limiting current, $\alpha_c{}'$ is the mass transport corrected cathodic transfer coefficient. This equation is based on the assumption that the current is uniform across the whole electrode surface.

Figure 8.3 presents the mass transport corrected cathodic transfer coefficient plot where the $\alpha_c{}'$ deviates from its true value 0.5 at high overpotentials and undergoes a fluctuation due to the non-uniform accessibility of microdisc electrodes. The errors estimated in transfer coefficient at different fraction of the wave are tabulated in Table 8.2. It is shown that if the transfer coefficient is estimated by using the Tafel region of 10%-30% of steady-state current, the averaged $\alpha_c{}'$ is calculated to be 0.492 with only 1.6% error compared to its true value.

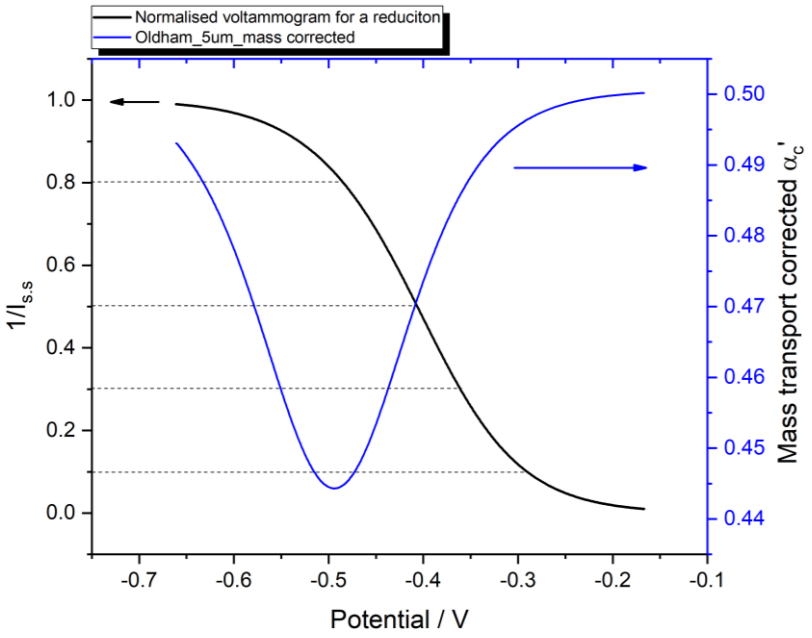


Figure 8.3 Mass transport corrected cathodic transfer coefficient on a microdisc electrode with radius of 5 μm. The black solid curve is the normalised voltammogram simulated using Oldham equation where E_0=0 V; C=1 mM; $k^0=1\times10^{-7}$ m s^{-1}; $D=1\times10^{-9}$ m^2 s^{-1}; $\alpha_a=\alpha_c=0.5$. The dotted line stands for different fractions of the wave (10%, 30%, 50% and 80% of $I_{s.s}$). The blue solid curve is the mass transport corrected cathodic transfer coefficient plot as a function of potential. The current range analysed is 1-99% of $I_{s.s}$.

Table 8.2 Error in α_c at different fraction of the voltammetric wave.

Fraction of the wave	10% of $I_{s.s}$	30%	50%	80%
Error in α_c	<1 %	2.8%	6.0%	12%

Due to the non-uniform accessibility of microdisc electrodes, the voltammograms obtained are often under a very 'near' steady state regime. Here we further investigated how the accuracy of applying the K-L method and normal transfer coefficient changes on microdisc electrodes under a very 'near' steady-state regime where the deviation from true steady state behaviour reflects the application of a finite scan rate as opposed to an infinitesimally slow one. The voltammograms on microdisc electrodes with various radii

(a=5, 10 and 20 μm) were simulated using a home-written programme by Dr Oleksiy Klymenko based on the conformal mapping of the spatial coordinates and uses an exponentially expanding time grid.[23] The results of using the K-L method are shown in Figure 8.4 and Table 8.3. Figure 8.4(a) shows the normalised voltammograms at microelectrodes with various radii. The set of plots of $\frac{1}{j}$ versus $\frac{1}{m_0 C}$ at different potentials is given in Figure 8.4 (b). It is shown that for a 'near' steady state voltammogram, the calculated value of $\alpha_{c,\,K\text{-}L}$ varies by 13% and the calculated value of k^0 varies by over 50% as shown in Table 8.3. The results analysed using normal mass transport corrected method are shown in Figure 8.5 and Table 8.4. Figure 8.5 gives the mass transport corrected cathodic transfer coefficient on a microdisc electrode with radius of 20 μm, where the α_c' deviates from its true value at higher overpotentials. Moreover, the behaviour of transfer coefficient as a function of potential tend to be more like the behaviour under linear regime[13] as the radius of electrode increases. Therefore, the results show that the accuracy in analysing a 'near' steady-state voltammogram decreases for both K-L and normal mass transport corrected methods.

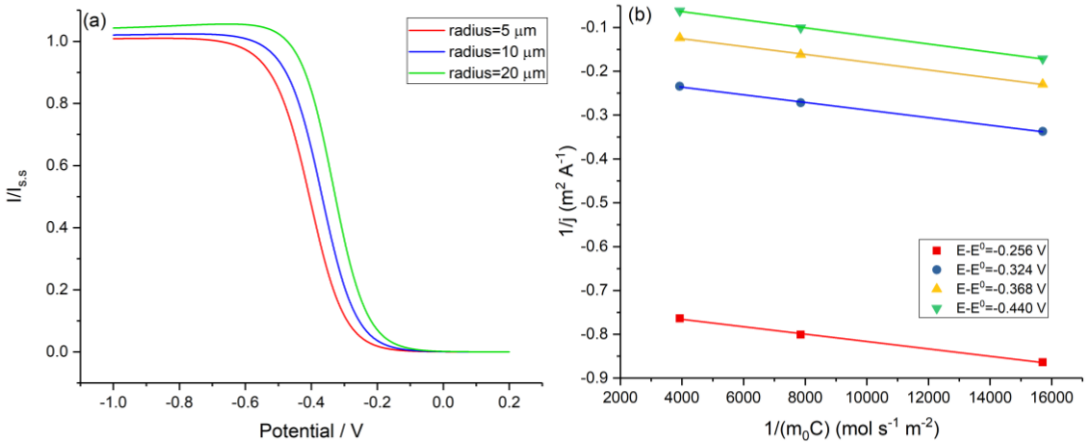


Figure 8.4 (a) Reductive voltammograms at microdisc electrodes with various radii of 5 μm (red), 10 μm (blue) and 20 μm (green). All the currents are normalised to their respective steady state current calculated using $I_{s.s}$=4FDCa. The parameters used in the equation: E^0=0.0 V; C=1 mM; k^0=1×10$_{-7}$ m s_{-1}; D=1×10$_{-9}$ m_2 s_{-1}; $\alpha_a=\alpha_c$=0.5, scan rate=0.025 V s^{-1}. (b) Plots of 1/j vs. 1/(m_0C) obtained from voltammograms in (a) at different potentials E-E^0=-0.256, -0.324, -0.368, -0.440 V.

Table 8.3 Calculated α_c and k^0 from plots in Figure 8.4(b) when α_c and k^0 are unknown.

Sets of data	E-E_0 / V	Intercept	Sets of data used in the calculation	α_c and k^0 are unknown	
				$\alpha_{c,\ K\text{-}L}$	k^0 / m s^{-1}
1)	-0.256	-0.7321	1) and 2)	0.4872	1.101×10^{-7}
2)	-0.324	-0.2015	1) and 3)	0.4806	1.176×10^{-7}
3)	-0.368	-0.09001	1) and 4)	0.4607	1.433×10^{-7}
4)	-0.44	-0.02697	2) and 3)	0.4703	1.362×10^{-7}
\	\	\	2) and 4)	0.4452	1.870×10^{-7}
\	\	\	3) and 4)	0.4298	2.432×10^{-7}

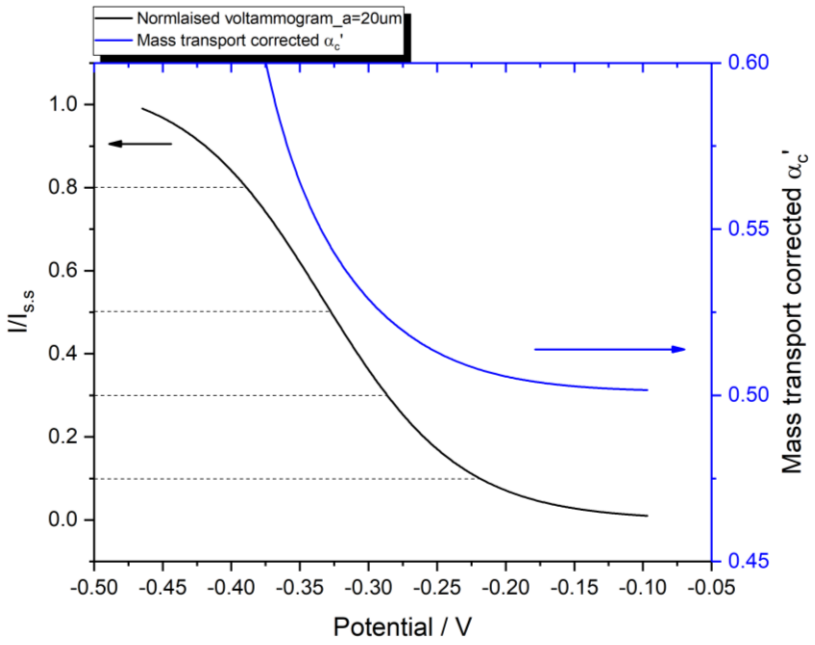


Figure 8.5 Mass transport corrected cathodic transfer coefficient on a microdisc electrode with radius of 20 μm. The black solid curve is the reductive voltammetric wave simulated normalised to its steady state current ($I_{s.s}$=4FDCa) where E_0=0 V; C=1 mM; k^0=1×10^{-7} m s^{-1}; D=1×10^{-9} m^2 s^{-1}; α_a=α_c=0.5; scan rate=0.025 V s^{-1}. The dotted line stands for different fractions of the wave (10%, 30%, 50% and 80% of $I_{s.s}$). The blue solid curve is the mass transport corrected cathodic transfer coefficient plot as a function of potential.

Table 8.4 Error in α_c at different fraction of the voltammetric wave in Figure 8.5.

Fraction of the wave	10% of $I_{s.s}$	30%	50%	80%
Error in α_c	1.4%	4.6%	9.0%	26.5%

Although the K-L method and the normal mass transport corrected method have high accuracy in the analysis of microdisc electrode under certain circumstances, neither of them can be used as a universal analysis methodology on microdisc electrodes. Compared to the normal mass transport corrected method and K-L method, one of the big advantages of the extraction method in this work is that it works equally well for linear and radial mass-transport regimes and the transition between these two limits.

8.3 Experimental

8.3.1 Chemical reagents

The ammonium iron (II) sulfate hexahydrate ($(NH_4)_2Fe^{II}(SO_4)_2$; Aldrich; 99%) and perchloric acid (Aldrich; 70%) were used as purchased without further purification. Solutions were freshly prepared using deionised water (Milipore) with a resistivity of 18.2 MΩ cm at a temperature of 25 ^oC.

8.3.2 Instrumentation

Electrochemical measurements were performed with a μAutolab Type III potentiostat using a standard three electrode setup in an optimised thermostated electrochemical system as described in the literature[24]. A carbon microdisc electrode (7 μm in diameter; BASi), a saturated calomel electrode (SCE; BASi, Japan) and a platinum wire were used as working electrode, reference electrode and counter electrode, respectively. The working electrode was polished using alumina of decreasing size (1.0, 0.3 and 0.05 μm, Buehler, IL), washed with deionised water and dried with nitrogen. All electrochemical measurements were conducted at 25 ^oC inside a Faraday cage.

8.4 Theory

The aim of this work is to extract the electron transfer kinetics for an irreversible electrochemical process directly from a voltammogram experimentally recorded at a

planar disc electrode of any size. The following theory is outlined for a reduction reaction; however, it is equally applicable to the study of oxidative processes, as is undertaken later in this text. The programme for this extraction was written by Dr Christopher Batchelor-McAuley. Here we consider the one electron transfer process as given by:

$$A + e^{-} \rightleftarrows B \tag{8.5}$$

where A and B are solution phase species, and initially only the reactant A is present in solution. Furthermore, we assume that the reaction is first order with respect to the concentration of the reactant such that the electrochemical flux at the electrode ($j_{A,0}$)is given by:

$$j_{A,0} = k_{red} c_{A,0} \tag{8.6}$$

k_c is the potential dependent electrochemical rate constant for the reduction of A to B and $c_{A,0}$ is the concentration of species A at the electrode surface (mol m^{-3}). From this rate constant, k_{red}, and from the definition provide in Equation 8.1, it is possible to assess the systems cathodic transfer coefficient (α_c) as given by:

$$\alpha_c = -\frac{RT}{F}\frac{d \ln k_{red}}{dE} \tag{8.7}$$

In the course of the simulations we assume that the mass-transport of species in the solution phase occurs only by diffusion and so that the system is therefore well described by Fick's second law. In this work we consider a planar disc electrode embedded into a

flat plane; consequently, for numerical efficiency[24] oblate spheroidal co-ordinates are used.

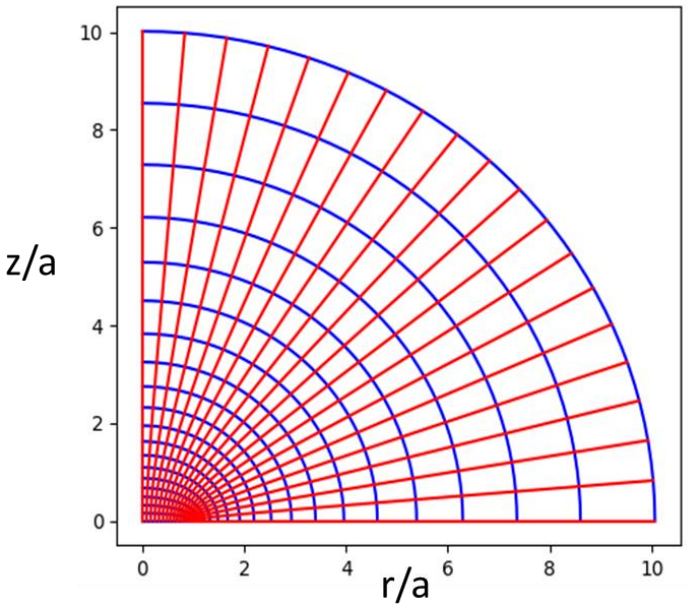


Figure 8.6 Cross-section of the coordinate system. r and z in the figure are dimensionless where a is the electrode radius. Y-axis is the coordinate perpendicular to the electrode surface and x-axis is the coordinate parallel to the electrode. The vertical line at the extreme left represents the axis normal to the disc electrode through its centre. The red and blue curves represent the uniform grid spacing in μ and ν respectively. Equations (8.9) and (8.10) give the conversion between the spherical oblate (μ and ν) and cylindrical coordinates (r and z).

Figure 8.6 provides a cross-section of this coordinate system. As the system is axially symmetric then the problem can be reduced to two-dimensions and Fick's second law expressed as [25]:

$$\frac{\partial c_A}{\partial t} = \frac{D_A}{a^2(\sinh^2\mu + sin^2\nu)}\left(\tanh\mu\frac{\partial c_A}{\partial \mu} + \frac{\partial^2 c_A}{\partial \mu^2} - \tan\nu\frac{\partial c_A}{\partial \nu} + \frac{\partial^2 c_A}{\partial \nu^2}\right) \quad (8.8)$$

where D_A is the diffusion coefficient of species A ($m^2\ s^{-1}$), a is the electrode radius (m), t is the experimental time (s). Both μ and ν are coordinates in the oblate spheroidal

coordinate system and are related to the more familiar cylindrical coordinates in the 2D-plane by:

$$z = a \sinh\mu \sin \nu \tag{8.9}$$

$$r = a \cosh\mu \cos \nu \tag{8.10}$$

where z is the coordinate perpendicular to the electrode surface and r is parallel to the electrode surface. μ is a nonnegative real number and for the present case ν varies between 0 and π/2. In the simulation space the electrode surface is set as where μ = 0.

Boundary conditions

To solve Equation 8.8 we need suitable boundary conditions. At the onset of the experiment we assume the species A has a uniform concentration profile and that no B is present in solution. The outer boundary of the simulation space is set to be sufficiently far from the electrode to ensure that at this distance the concentrations of the electroactive species are not altered from those of the bulk:

$$\mu_{max} = cosh^{-1}(1 + \frac{6}{a}\sqrt{D_A t_{max}}) \tag{8.11}$$

where t_{max} is the duration of the experiment. The inert substrate surrounding the electrode is defined as where $\nu = 0$ and the central axis is at $\nu = \pi/2$. For both of these boundaries we set a condition of zero flux. All that remains is to determine a suitable boundary condition for the electrode surface. Usually one would assume a model for the electron transfer kinetics and therefore simulate how the current varies as a function of

potential; however, here we do not assume any prior knowledge of the electrochemical rate constant, k_{red}. In the simulation we take a given measured current at a given potential and on the basis of the known electrode geometry infer the reaction rate while accounting fully for the local depletion of the reagent in the vicinity of the electrode surface. First, taking Equation 8.6 and Fick's first law then at the electrode interface the concentration of the species A is described by the following:

$$k_{red} c_{A,0} = D \nabla c_A \tag{8.12}$$

where k_c is an additional unknown and needs to be related to the electrochemical current of the system. The total flux of the system is found by integration across the electrode surface in oblate spheroidal co-ordinates this integral is:

$$I = \pi F D a^2 k_{red} \int_0^{\pi/2} c_{A,0} \sin(2\nu)\, d\nu \tag{8.13}$$

After discretisation the above equation provides an additional simultaneous equation to be solved for given a knowledge of I. This set of simultaneous equations do not lead to a simple banded matrix. To solve the problem and find k_{red} as a function of potential it is necessary that all of the surface concentrations which vary over the electrode surface are considered and solved for simultaneously; consequently, the ADI method[26] is not applicable to this problem and the equation set needs to be solved fully implicitly. Second, the boundary condition Equations 8.12 and 8.13 are weakly non-linear. Due to this non-linearity the system of equations were solved iteratively via the Newton-Raphson

method.[27] The convergence tolerance criterion required that the average absolute magnitude of the correction term in the concentrations must be less than $1x10^{-8}$.

8.5 Numerical methods

The equation set was solved using a central finite difference method. Although the use of a uniform grid spacing allows rapid convergence in the limit of a small (micro) electrode simulation, for larger (macro) electrode dimension the simulation became computationally expensive; consequently, a patching scheme was used for the grid spacing in the μ coordinate as given by;

$$\mu[i] = \mu[i-1] + \gamma_\mu \mu_s \qquad \mu < \mu_s \tag{8.14}$$

$$\mu[i] = \mu[i-1] + \gamma_\mu \mu[i-1] \qquad \mu_{max} > \mu > \mu_s \tag{8.15}$$

where i relates to the grid indexing. Suitable grid parameters were found to be $\gamma_\mu = 5 \times 10^{-2}$ and μ_s = $\sinh^{-1}(2\times10^{-6}/a)$. Allowing efficient simulation of the concentration profiles in both the macro and microscopic electrode limits. The grid was uniformly spaced in the ν coordinate with 400 points. As the problem is solved fully implicitly there are no restrictions on the size of the time step used. Simulation and extraction of the electrochemical rate constant was undertaken using a script written and run using Python 3.7, solving the sparse Jacobian matrix was achieved using spsolve function provided as part of the SciPy package. Simulation time varies but extraction of the electrochemical rate constant for a total of 500 time steps require 8-10 minutes of computing time on an

Intel Xeon E5-1620. This simulation programme is credited to Dr Christopher Batchelor-McAuley.

8.6 Results and discussion

In the following, first a series of theoretical results are considered where the electrochemical rate constant is 'extracted' from a series of numerically simulated results predicting current-voltage curves for fully irreversible voltammograms at a microdisc electrode. These "voltammograms" were created by a previously reported simulation program[23] that has been extensively tested. Using these model results it is possible to investigate the uncertainties associated with the extracted electrochemical kinetics. Second, we use the experimental example of the oxidation of Fe^{2+} in aqueous solution at a carbon micro-electrode and demonstrate how the electrochemical rate constant and hence transfer coefficient can be directly obtained from the experimentally recorded voltammetric response.

8.6.1 Data extraction process

Figure 8.7 depicts three simulated voltammetric profiles for a fully irreversible one electron reduction process where the electron transfer kinetics have been simulated using the Butler-Volmer formalism with transfer coefficients of 0.4, 0.5 and 0.6 on both microdisc (a = 5 μm) and macroelectrode (a = 500 μm). These simulated voltammetric profiles were then used as input for the "extraction program" and used to infer the

electrochemical rate constant as a function of potential from the voltammetric response. The extraction program requires along with the (previously simulated) current voltage profile, knowledge of the electrode radius, scan rate, analyte diffusion coefficient and analyte concentration. From these inputs the diffusion equation (Equation 8.6) is numerically solved to yield the concentration profile and the electrochemical rate constant at each time step. The extraction program makes no a *priori* assumption regarding the variation of the electron transfer kinetics as a function of the electrode potential. For the three simulated voltammograms used as an input the inlay of Figure 8.7(a) depicts the extracted electrochemical rate constant as a function of the applied potential, where the electron transfer kinetics have been analysed up to 90% of the wave relative to the steady-state current noting that the y axis of the inlay is on a logarithm scale. From the extracted electrode kinetics and through the use of equation 8.5 the electrochemical transfer coefficient can be determined. The resulting 'extracted' transfer coefficients are overlaid with the original simulated voltammetry in Figure 8.7(a) and seen to be nearly constant. The extraction simulation is able to quantitatively determine the system's transfer coefficient across the near entirety of the electrochemical wave. Figure 8.7(b) depicts comparable data for a macroelectrode simulation (a = 500 μm) where the 'extracted' transfer coefficient only shows a small deviation from its true value in the analysed current range up to 100% of the peak current.

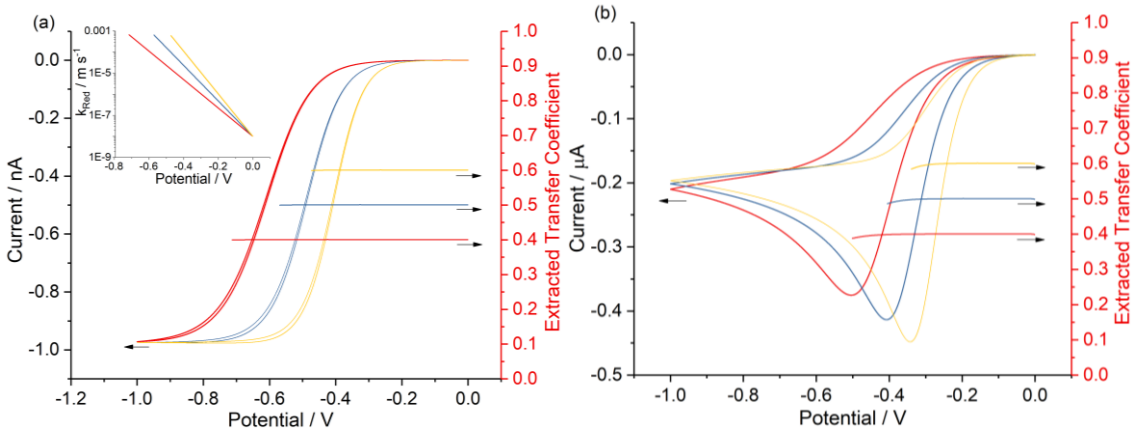


Figure 8.7: Simulated voltammograms for a one-electron reduction process at (a) microdisc electrode (radius of $5x10^{-6}$ m) and (b) macroelectrode (radius of $5x10^{-4}$ m). E_f= 0.0 V, $k^0 = 1x10^{-8}$ m s^{-1}, $D_A = 5x10^{-10}$ m^2 s^{-1} and scan rate = 10 mV s^{-1}. The transfer coefficient (α) has values of 0.4 (red), 0.5 (blue) and 0.6 (yellow). Right-hand y-axis depicts the extracted transfer coefficients as determined up to 90% of the steady-state current for the microelectrode (a) and until the peak current for the macroelectrode (b). Inlay in Figure 8.7(a) depicts the extracted electrochemical rate constant as a function of the applied potential from which the extracted coefficient is obtained.

8.6.2 Accuracy of the data extraction method

Precise extraction of the electron transfer kinetics from the mixed mass-transport/electron transfer control region requires accurate knowledge of the input parameters. Specifically we need to know the electrode radius, analyte concentration and analyte diffusion coefficient. For normal experimental cases there is a limit to the accuracy with which these parameters are known. Consequently, having demonstrated how under ideal conditions the transfer coefficient can be successfully extracted from a voltammetric wave, we now consider how reliable this value might be for real experimental cases. Under near-steady-state conditions (such as those employed in Figure 8.7) the current is proportional to magnitude of the mathematical product DCa (the diffusion coefficient

multiplied by both the analyte concentration and the radius of the electrode). Under these conditions it is important to consider to what accuracy this combined parameter is known and how this may affect the extracted electron transfer kinetics. Figure 8.8 shows the same simulated irreversible one-electron reduction process with a transfer coefficient of 0.5 on both microdisc and macroelectrode, as used in Figure 8.7. However, in Figure 8.8 the value of the combined parameter used to extract the electron transfer kinetics has been varied (±2.5%, ±5% and ±10% accuracy). As can be seen, in the case where the combined parameter is *not* known with *perfect* accuracy, as the electrochemical current increases the extracted transfer coefficient deviates significantly away from the expected value of 0.5. This behaviour is as expected; the sensitivity of the extraction simulation to the input parameters increases as the electrochemical response becomes controlled by the mass-transport of the material to the electrode surface. Similar results were found for the macro-electrode limit; however, in this mass-transport regime the relevant parameter is $D^{0.5}Ca^2$ (the square-root of the diffusion coefficient multiplied by the analyte concentration and the square of the electrode radius). Table 8.5 summarises for the steady-state and macro-electrode regimes what fraction (relative to either the steady-state or peak current) of the irreversible one-electron voltammetric wave can be used to extract the transfer coefficient with less than a 10% error when the combined parameter (DCa or $D^{0.5}Ca^2$) is only known with ±2.5%, ±5% and ±10% accuracy. Between these two regimes no clear combined parameter will exist and the error associated with each term should be considered separately.

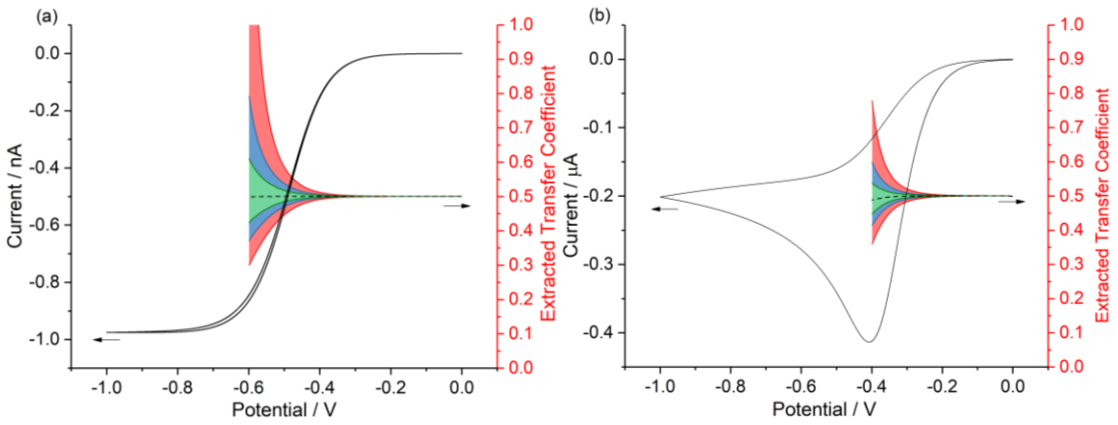


Figure 8.8 Variation and uncertainty in the extract transfer coefficient for (a) a steady-state voltammetric response from a microdisc electrode and (b) a peak-shaped voltammetric response from a macroelectrode with a constant transfer coefficient of 0.5. For the extraction of the electron transfer coefficient the combined parameter DCa (microelectrode) and $D^{0.5}Ca^2$ (macroelectrode, see text) has been varied by ±2.5% (green), ±5% (blue) and ±10% (red). At higher current densities and as the voltammetric reaction rate becomes controlled by the mass-transport of material to the electrode surface the extracted transfer coefficient deviates significantly away from the actual value of 0.5.

Table 8.5: Fraction of the voltammetric wave (relative to the steady-state or peak current) that can be analysed to extract the transfer coefficient with less than 10% error when the combined parameter DCa (microelectrode) or $D^{0.5}Ca^2$ (macroelectrode) is only known to an accuracy of ±2.5%, ±5% and ±10%.

	±2.5%	±5%	±10%
Microelectrode DCa	0.78	0.61	0.44
Macroelectrode $D^{0.5}Ca^2$	0.99	0.93	0.73

8.6.3 Experimental example using the extraction method

Having evidenced the ability of the procedure to extract the transfer coefficient and assess the accuracy with which this can be done we next experimentally turn to consider the case of the oxidation of Fe^{2+} in aqueous solution at a carbon microdisc electrode. In this section, we first prove that the measured anodic transfer coefficient and the mass transport corrected transfer coefficient on a microdisc electrode are independent on either the concentration of Fe^{2+} (Figure 8.9) or the scan rate (Figure 8.10); we then next turn to apply this extraction method to evaluate the transfer coefficient on a microdisc electrode.

8.6.3.1 Independence of transfer coefficient plots on the concentration of Fe^{2+} and the scan rate at a carbon microdisc electrode

Figure 8.9 presents the anodic transfer coefficient plots at a carbon microdisc electrode in solutions containing various concentration of $(NH_4)_2Fe(SO_4)_2$ (red – 5 mM; black – 10 mM; blue – 20 mM). Figure 8.9 (a) and (b) represents the transfer coefficient plot with (Figure 8.9 b) and without (Figure 8.9 a) mass transport correction, respectively. It is shown that the transfer coefficient is independent of the Fe^{2+} concentration. The voltammograms on a carbon microdisc electrode at 0.05 (red curve), 0.1 (black curve) and 0.2 (blue curve) V s^{-1} in a solution containing 5 mM $(NH_4)_2Fe(SO_4)_2$, 2.5 mM $(NH_4)_2SO_4$ in 0.2 M $HClO_4$ are shown in Figure 8.10, proving that the charge transfer coefficient is relatively insensitive to the scan rate considering the possible error induced from capacitative current at higher scan rates.

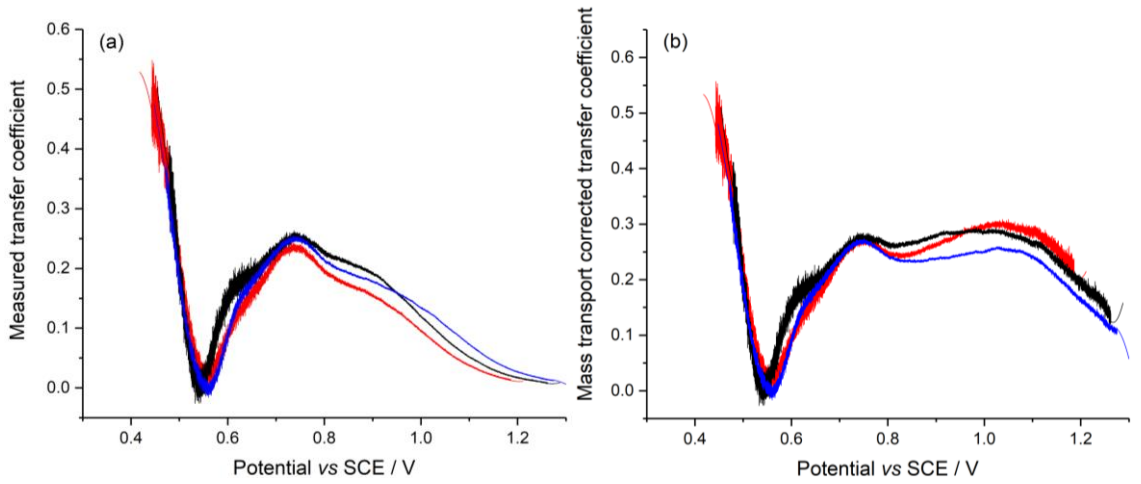


Figure 8.9 Anodic transfer coefficient plot as a function of concentration of Fe^{2+} (red – 5mM; black – 10 mM; blue – 20 mM) without (a) and with (b) mass transport correction. Solution composition: $(NH_4)_2Fe(SO_4)_2$, 2.5 mM $(NH_4)_2SO_4$ in 0.2 M $HClO_4$. Analysis was done with background subtraction.

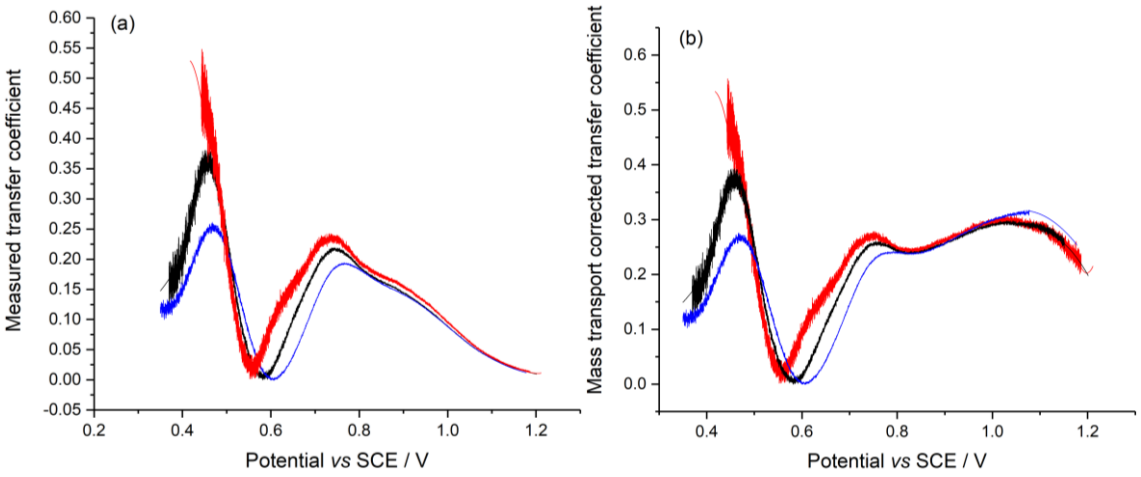


Figure 8.10 Anodic transfer coefficient plot as a function of scan rate (red – 0.05 V s^{-1}; black – 0.1 V s^{-1}; blue – 0.2 V s^{-1}) without (a) and with (b) mass transport correction. Solution composition: $(NH_4)_2Fe(SO_4)_2$, 2.5 mM $(NH_4)_2SO_4$ in 0.2 M $HClO_4$. Analysis was done with background subtraction.

8.6.3.2 Experimental example of the extraction applied to a microdisc electrode

In Figure 8.11 the background current associated with the capacitative charging which was measured in blank solution without $Fe^{2+/3+}$ redox couple in the same potential window has been subtracted and removed. There are two notable features regarding this

voltammetric response, first as the formal potential for this redox couple is 0.4785 (± 0.0006) V vs. SCE then the main oxidation process occurs at a high overpotential.[28] Second, at low over potentials a significant pre-wave is observable. The origin of this pre-wave has recently been extensively investigated and shown to be due to a surface specific catalytic mechanism.[28] Overlaid on the experimental voltammetric response is the extracted transfer coefficient for the system where the uncertainty of this extracted value has been accounted for by considering the accuracy to which the input parameters are known. The diffusion coefficient for Fe^{2+} under these conditions has been determined to be 6.68 (± 0.14) × 10^{-10} m^2 s^{-1}. Further the electrode has been previously calibrated and found to have a radius of 3.64 µm.[28] We consider that this radius is accurate within 2% and that the uncertainty in the bulk concentration of Fe^{2+} is essentially negligible. From Figure 8.11 it can be seen that across the full potential range the transfer coefficient is significantly below 0.5. At low overpotentials (around + 0.55 V vs SCE) the transfer coefficient goes through a minimum, this is due to the oxidative pre-wave where the rate of electron transfer becomes relatively insensitive to changes in the applied potential. Again at higher potentials the transfer coefficient increases but to a value in the region of ~0.3. In this case the variable transfer coefficient directly reflects the change in the electrochemical mechanism of the oxidation of solution phase Fe(II) as a function of the applied potential. Due to the presence of the pre-wave at potentials that would commonly be used for Tafel analysis determination of the electrochemical transfer coefficient for the

oxidation mechanism at higher overpotentials can only be achieved if the mass-transport of the system is accounted for.

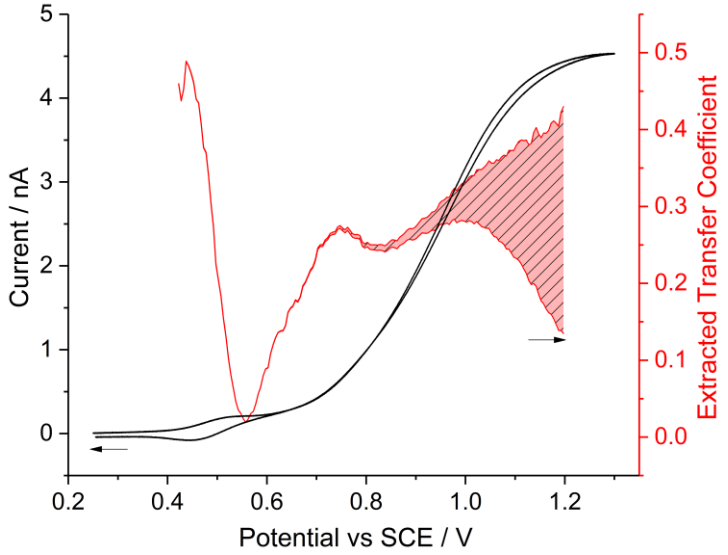


Figure 8.11: Oxidation of Fe^{2+} at a carbon microdisc electrode and the associated extracted transfer coefficient of the system where the red hatched area represented the uncertainty in the extracted transfer coefficient on the basis of the uncertainty in the diffusion coefficient of the analyte and the electrode radius. Solution composition: 5 mM $(NH_4)_2Fe(SO_4)_2$ in 0.2 M $HClO_4$. Scan rate=0.05 V s^{-1}.

8.7 Conclusions

A numerical fully implicit 2D numerical procedure for analysing a voltammogram measured at a disc electrode and extracting the underlying electron transfer kinetics is presented. Compared to the conventional mass transport corrected method and K-L method, a big advantage of this extraction method is that it works equally well for linear and radial mass-transport regimes and the transition between these two limits. This numerical extraction procedure requires knowledge of the reagent concentration, scan rate, diffusion coefficient and electrode size but does not make any *a priori* assumption

regarding the sensitivity of the electrode kinetics to the applied electrode potential. Changes in the surface concentration of the reagent is accounted for by solving the 2D diffusion equation and numerically simulating to find the concentration profile in the vicinity of the electrode and therefore inferring the surface concentrations during the course of the voltammetric experiment, where the concentrations vary across the electrode surface. The accuracy of this extraction process is predicated on precise knowledge of the physical parameters defining the system, most importantly the diffusion coefficient, analyte concentration and electrode radius need to be known as accurately as possible. Assuming that the combination of these physical parameters is known to with ±2.5% accuracy then for a microdisc electrode 78% of the voltammetric wave can be analysed and the resulting transfer coefficient will be within 10% of the actual value. Similarly, for a macro-disc system up to 99% of the peak current can be used to determine the electrochemical systems transfer coefficient. Hypothetically, with the diffusion coefficient, electrode dimensions and analyte concentration known to arbitrary accuracy then in principle the proposed numerical extraction procedure could allow in all case > 99% of the voltammetric wave to be analysed to yield an accurate measure of the transfer coefficient.

References:

[1] R. Guidelli, R. G. Compton, J. M. Feliu, E. Gileadi, J. Lipkowski, W. Schmickler, S. Trasatti, *Pure and Applied Chemistry* **2014**, *86*, 245-258.

[2] R. Guidelli, R. G. Compton, J. M. Feliu, E. Gileadi, J. Lipkowski, W. Schmickler, S. Trasatti, *Pure and Applied Chemistry* **2014**, *86*, 259-262.

[3] R. G. Compton, E. L. Laborda, K. R. Ward, *Understanding Voltammetry: Simulation Of Electrode Processes*, World Scientific Publishing Company, **2013**.

[4] E. Gileadi, *Journal of Solid State Electrochemistry* **2011**, *15*, 1359.

[5] C. E. D. Chidsey, *Science* **1991**, *251*, 919-922.

[6] S. W. Feldberg, *Analytical Chemistry* **2010**, *82*, 5176-5183.

[7] V. Mirceski, E. Laborda, D. Guziejewski, R. G. Compton, *Analytical Chemistry* **2013**, *85*, 5586-5594.

[8] E. Laborda, M. C. Henstridge, C. Batchelor-McAuley, R. G. Compton, *Chemical Society Reviews* **2013**, *42*, 4894-4905.

[9] C. Batchelor-McAuley, R. G. Compton, *Journal of Electroanalytical Chemistry* **2012**, *669*, 73-81.

[10] S. Fletcher, *Journal of Solid State Electrochemistry* **2009**, *13*, 537-549.

[11] aJ. M. Savéant, D. Tessier, *Journal of Electroanalytical Chemistry and Interfacial Electrochemistry* **1975**, *65*, 57-66; bJ.-M. Savéant, D. Tessier, *Faraday Discussions of the Chemical Society* **1982**, *74*, 57-72; cJ. M. Saveant, D. Tessier, *The Journal of Physical Chemistry* **1977**, *81*, 2192-2197.

[12] aH. O. Finklea, *The Journal of Physical Chemistry B* **2001**, *105*, 8685-8693; bH. O. Finklea, *Journal of Electroanalytical Chemistry* **2001**, *495*, 79-86.

[13] D. Li, C. Lin, C. Batchelor-McAuley, L. Chen, R. G. Compton, *Journal of Electroanalytical Chemistry* **2018**, *826*, 117-124.

[14] D. Li, C. Batchelor-McAuley, R. G. Compton, *Applied Materials Today* **2019**.

[15] aW. J. Albery, *Electrode kinetics, Vol. 14*, Oxford University Press, **1975**; bK. J. J. Mayrhofer, D. Strmcnik, B. B. Blizanac, V. Stamenkovic, M. Arenz, N. M. Markovic, *Electrochimica Acta* **2008**, *53*, 3181-3188.

[16] J. Kim, A. J. Bard, *Analytical Chemistry* **2016**, *88*, 1742-1747.

[17] A. Molina, J. Gonzalez, E. O. Barnes, R. G. Compton, *The Journal of Physical Chemistry C* **2014**, *118*, 346-356.

[18] Q. Chen, L. Luo, *Langmuir* **2018**, *34*, 4554-4559.

[19] M. C. Henstridge, R. G. Compton, *Journal of Electroanalytical Chemistry* **2012**, *681*, 109-112.

[20] C. G. Zoski, K. B. Oldham, P. J. Mahon, T. L. E. Henderson, A. M. Bond, *Journal of electroanalytical chemistry and interfacial electrochemistry* **1991**, *297*, 1-17.

[21] P. J. Mahon, K. B. Oldham, *Electrochimica acta* **2001**, *46*, 953-965.

[22] K. B. Oldham, C. G. Zoski, *Journal of Electroanalytical Chemistry and Interfacial Electrochemistry* **1991**, *313*, 17-28.

[23] O. V. Klymenko, R. G. Evans, C. Hardacre, I. B. Svir, R. G. Compton, *Journal of Electroanalytical Chemistry* **2004**, *571*, 211-221.

[24] aA. C. Michael, R. M. Wightman, C. A. Amatore, *Journal of Electroanalytical Chemistry and Interfacial Electrochemistry* **1989**, *267*, 33-45; bA. Oleinick, C. Amatore, I. Svir, *Electrochemistry Communications* **2004**, *6*, 588-594.

[25] aJ. C. Myland, K. B. Oldham, *Journal of Electroanalytical Chemistry* **2005**, *576*, 353-362; bP. Moon, D. E. Spencer, *Field Theory Handbook: Including Coordinate Systems, Differential Equations and Their Solutions*, Springer Berlin Heidelberg, **2012**.

[26] J. Heinze, *Journal of Electroanalytical Chemistry and Interfacial Electrochemistry* **1981**, *124*, 73-86.

[27] aE. Ziegel, Taylor & Francis Group, **1987**; bE. J. F. Dickinson, J. G. Limon-Petersen, N. V. Rees, R. G. Compton, *The Journal of Physical Chemistry C* **2009**, *113*, 11157-11171.

[28] D. Li, C. Batchelor-McAuley, L. Chen, R. G. Compton, *The Journal of Physical Chemistry Letters* **2020**, *11*, 1497-1501.

Chapter 9

Overall Conclusions

Tafel analysis is a key component of the electrochemists' tool box for the study of electrode kinetics. This thesis has investigated how Tafel analysis can be employed to improve the insights gleaned in interpreting kinetic information from heterogeneous electron transfer processes.

In voltammetric measurements where the voltammograms are generally analysed on the basis of diffusion-controlled processes, the control of temperature of the system is therefore vital to eliminate the change in mass transport due to natural convection induced by the changes in solution temperature. The work presented in this thesis first proves that imperfect thermostating system can lead to the presence of bulk convective flow the velocity of which is experimentally shown to be of the order of 100 $\mu m\ s^{-1}$ and therefore significantly influences the voltammetric response. It is suggested that an electrochemical cell which is closed to the environment should be employed to minimise convective flows induced by evaporative loss of the solution. Importantly it is also shown that for microelectrodes where the electrode material is inlaid into a large macroscopic insulating surface the observed voltammetry is less sensitive to the solution phase convection. Such studies provide the basis for the further kinetics study based on the voltammograms

obtained in electrochemical systems in which the effect of natural convection is minimised.

Tafel analysis of a voltammogram yields a measure of the electrochemical system's transfer coefficient which provides information on electrochemical mechanisms. The appropriate Tafel region used in Tafel analysis under different electrode geometries and if and how the measurement of transfer coefficient can be improved by mass transport correction were investigated theoretically. It is proved that the analytical mass transport correction using a plot of $\ln\left|\frac{1}{I}-\frac{1}{I_{lim}}\right|$ against potential is only applicable to microelectrodes under a true steady-state regime (i.e. micro-(hemi)spherical electrodes). For electrodes under quasi-steady state regimes, the fraction of the voltammetric wave used in Tafel analysis can be improved to 48.3% (micro-hemicylinder) and 77.6% (single microband) with less than 10% error in the measured transfer coefficient after this analytical mass transport correction. For macroelectrodes under a linear diffusion regime, a new empirical mass-transport correction is suggested to improve the estimation of the transfer coefficient.

Furthermore, such analytical mass transport correction is found to give significant error in the transfer coefficient on a microdisc electrode due to its non-uniform accessibility. A simple simulation method is developed to extract the electrochemcial kinetics based on the knowledge of the values of the diffusion coefficient, analyte concentration and electrode radius which need to be known as accurately as possible. Most importantly this

extraction process is applicable for both linear and radial mass-transport regimes. Assuming that the diffusion coefficient, electrode dimensions and analyte concentration are known to arbitrary accuracy then in principle the proposed numerical extraction procedure could allow in all cases > 99% of the voltammetric wave to be analysed to yield an accurate measure of the transfer coefficient.

Tafel analysis has been widely employed to evaluate the activity of electrocatalysts. In this thesis, we discuss how Tafel analysis can be applied and interpretated to accurately report the electrocatalytic performance of nanomaterials. We suggest that it is preferable to define a current range relative to the limiting steady state value as opposed to defining a suitable potential range for meaningful Tafel analysis giving either a transfer coefficient or, equivalently, a 'Tafel slope'. In addition, a suitable background subtraction of the voltammogram needs to be first applied to eliminate the error in kinetic analysis caused by the existence of capacitative current of the electrode.

Such theoretical results on Tafel anlysis are further employed in characterising band electrodes with unknown dimensions using a fully irreversible redox couple without prior knowledge of the electron transfer rate constant or the formal potential. By using the peak-to-peak separation (E_{p-p}) and the magnitude of the ratio of backward peak current to forward peak current ($|I_{backward}/I_{forward}|$) as diagnostic parameters, the band width can be estimated within 4% of its true value and with an error in length of less than 1%.

Finally, based on the results of Tafel analysis, the $Fe^{2+/3+}$ redox reaction is proved to be mediated via intrinsic surface quinones on carbon substrates with the evidence of a potential dependent transfer coefficient from experimentally obtaiend voltammograms.

To summarise, this thesis has presented the investigations on how Tafel analysis can be employed under different electrode geometries to accurately interpretate the kinetic information of electrode processes. The capacitative current should be removed from the experimental voltammogram using a suitable background subtraction prior to further analysis. Proper mass-transport corrected Tafel analysis is then suggested to improve the accuracy of the estimation of the transfer coefficient.

Appendix A

Section A1: Derivation of the analytical expression for the mass-transport corrected transfer coefficient α' in Chapter 4

The detail of deviation for oxidative process is given below.

Under Butler-Volmer theory, the anodic flux is given by:

$$j_a = k_a[A]_0 = k^0 exp\left[\frac{\alpha_a F(E-E_f)}{RT}\right][A]_0 \quad \text{(A1-1)}$$

$$j_a = k_a[A]_0 = k^0 exp[\alpha_a \theta][A]_0 \quad \text{(A1-2)}$$

where j_a is the experimentally measured anodic flux density, $[A]_0$ is the concentration of the reactant at the electrode surface and θ is the dimensionless potential.

The flux using the Nernst diffusion layer can be given as:

$$j_a = D\left(\frac{[A]_0 - [A]_{bulk}}{\delta}\right) \quad \text{(A2)}$$

where $[A]_{bulk}$ is the bulk concentration and δ is the Nernst diffusion layer thickness.

Equation A1-2 can be rearranged to:

$$[A]_0 = \frac{j_a}{k^0 exp[\alpha_a \theta]} \quad \text{(A3)}$$

Equation A2 can be rearranged to:

$$[A]_0 = [A]_{bulk} + \frac{j_a \delta}{D} \quad \text{(A4)}$$

By combing Equations (A3) and (A4), the unknown $[A]_0$ can be eliminated:

$$\frac{j_a}{k^0 exp[\alpha'_a \theta]} = [A]_{bulk} + \frac{j_a \delta}{D} \quad \text{(A5-1)}$$

$$\frac{1}{k^0 exp[\alpha'_a \theta]} = \frac{[A]_{bulk}}{j_a} + \frac{\delta}{D} \quad \text{(A5-2)}$$

$$\frac{1}{k^0 exp[\alpha'_a \theta][A]_{bulk}} = \frac{1}{j_a} + \frac{\delta}{D[A]_{bulk}} \quad \text{(A5-3)}$$

The flux can be expressed as:

$$\frac{1}{j_a} = \frac{1}{k^0 e^{\alpha'_a \theta}[A]_{bulk}} - \frac{\delta}{D[A]_{bulk}} \quad \text{(A5-4)}$$

where α'_a is the mass-transport corrected anodic transfer coefficient.

For an oxidative process, a mass-transport limiting flux j_{lim} can be approached at sufficiently positive potential under steady state condition:

$$\frac{1}{j_{lim}} = -\frac{\delta}{D[A]_{bulk}} \quad \text{(A6)}$$

By combining Equation (A5-4) and (A6), δ term can be eliminated:

$$\frac{1}{j_a} = \frac{1}{k^0 e^{\alpha'_a \theta}[A]_{bulk}} - \frac{1}{j_{lim}} \quad \text{(A7-1)}$$

$$\frac{1}{j_a} - \frac{1}{j_{lim}} = \frac{1}{k^0 e^{\alpha'_a \theta}[A]_{bulk}} \quad \text{(A7-2)}$$

The electrochemical flux can be directly related to the measured current by:

$$I = FjA \quad \text{(A8-1)}$$

$$\frac{1}{j} = \frac{FA}{I} \quad \text{(A8-2)}$$

where A is the area of the electrode.

Hence, Equation (A7-2) can be re-written as below by the substitution using Equation (A8-2):

$$\frac{FA}{I_a} - \frac{FA}{I_{lim}} = \frac{1}{k^0 e^{\alpha_a' \theta} [A]_{bulk}} \tag{A9-1}$$

$$\frac{1}{I_a} - \frac{1}{I_{lim}} = \frac{1}{FAk^0[A]_{bulk}} e^{-\alpha_a' \theta} \tag{A9-2}$$

$$ln\left(\frac{1}{I_a} - \frac{1}{I_{lim}}\right) = ln\left(\frac{1}{FAk^0[A]_{bulk}} e^{-\alpha_a' \theta}\right) \tag{A9-3}$$

$$ln\left(\frac{1}{I_a} - \frac{1}{I_{lim}}\right) = ln\left(e^{-\alpha_a' \theta}\right) + ln\left(\frac{1}{FAk^0[A]_{bulk}}\right) \tag{A9-4}$$

$$ln\left(\frac{1}{I_a} - \frac{1}{I_{lim}}\right) = -\alpha_a' \theta + ln\left(\frac{1}{FAk^0[A]_{bulk}}\right) \tag{A9-5}$$

Therefore, the mass-transport corrected Tafel plot ($ln\left(\frac{1}{I_a} - \frac{1}{I_{lim}}\right)$ versus θ) is given by Equation (A9-5).

From the first derivation of Equation (A9-5), the plot describing mass-transport corrected anodic transfer coefficient $\alpha_a{}'$ value is given by:

$$-\frac{dln\left(\frac{1}{I_a} - \frac{1}{I_{lim}}\right)}{d\theta} = \alpha_a{}' \tag{A10}$$

Similarly, the mass-transport corrected cathodic transfer coefficient $\alpha_c{}'$ is given by:

$$\frac{dln\left|\frac{1}{I_c} - \frac{1}{I_{lim}}\right|}{d\theta} = \alpha_c{}' \tag{A11}$$

Section A2: Establishing the lower current limit on different electrodes in Chapter 4

The charge transfer in a reaction is either faradaic or capacitive. The total current is therefore assumed to be composed of the faradaic current I_f and a capacitive current I_c (i.e. $I_{tot} = I_f + I_c$). The current region chosen in the Tafel analysis should avoid the influence from background current, where the ratio of I_f to I_c should be larger than 10. For both macroelectrodes and microelectrodes, the I_c is proportional to the electroactive area of the electrode. However, $I_{f,mac}$ varies linearly with the area of the macroelectrode, whereas $I_{f,mic}$ varies linearly with the radius of the microelectrode[1]. Therefore, the lower limit should be different for different electrodes. Examples of a microelectrode and macroelectrode are given below.

We consider an irreversible one-electron transfer process on a macroelectrode and assume the radius of the electrode r_{el} is 1 mm, the bulk concentration of reactant $[A]_{bulk}$ is 1 mM, the diffusion coefficient of reactant D is 1×10^{-9} m^2 s^{-1}, the anodic transfer coefficient α_a is 0.5 and the scan rate ν is 0.025 V s^{-1}. At the electrode-solution interface, the double-layer capacitance C is typically in the range of 10 to 40 μF cm^{-2} at a given potential[2]. A specific apparent capacitance (Farads per unit geometric area) of 20 μF cm^{-2} is assumed in the calculation.

The peak current on a macroelectrode is:

$$I_{peak} = 2.99 \times 10^5 A D^{1/2} \nu^{1/2} {\alpha_a}^{1/2} [A]_{bulk} = 3.32 \times 10^{-6}\ A$$

The capacitive current[3] is:

$$I_{c,mac} = C \times A \times \nu = 1.57 \times 10^{-8}\ A$$

If the lower limit is chosen when the ratio of I_f to I_c is larger than 10, the lower percentage of the current is given by:

$$Lower\ percentage\ of\ the\ current \geq \frac{10 \times I_{c,mac}}{I_{peak}} = 4.7\%$$

In the case of a microdisc electrode with a radius r_{el} of 10 μm, which is 100 times smaller than that of the macroelectrode, the steady-state current is then calculated as:

$$I_{s.s} = 4FD[A]_{bulk}r_{el} = 3.86 \times 10^{-9}\ A$$

The capacitive current is: $I_{c,mic} = C \times A \times \nu = 1.57 \times 10^{-12}\ A$

Hence, $Lower\ percentage\ of\ the\ current \geq \frac{10 \times I_{c,mic}}{I_{s.s}} = 0.41\%$

From the calculation, theoretically a lower current limit in Tafel analysis can be chosen on a microelectrode that on a macroelectrode. In reality, the capacitance is normally much larger, which may be due to the larger electroactive area of the electrode compared to its geometric area, poor sealing and the stray capacitance at the electrode etc[4]. This leads to an increase in the background current, and the lower percentage limit can become hundreds of times larger than the theoretical value. Therefore, the lower limit of 1% for Tafel analysis is used in this paper to analyse the whole current region. However, care must be taken for the lower current limit in real situations.

Section A3: Determination for diffusion limit in Chapter 4

Both linear and radial diffusion can contribute to the total flux. The transition from mainly linear diffusion to radial diffusion can be expressed by the dimensionless scan rate σ.

$$\sigma = \frac{r^2 F}{DRT}\nu$$

It is shown in the literature that when σ > 3350, the simulated peak current is no more than 3% greater compared to the theoretical value from Randles–Ševčík equation. Hence, the diffusion to the electrode can be assumed to be linear[5].

In this section, the conditions when the diffusion can be considered to be mainly convergent on micro-hemispherical and microdisc electrode are investigated. Voltammograms were simulated using DigiSim and the home written programme (described in the main Chapter 4 Section 4.3), respectively. In the simulation, the radii of both electrodes were set to be 10 μm, the electron rate constant was 1×10^{-7} m s^{-1}, the diffusion coefficient D was 1×10^{-9} m^2 s^{-1} and the bulk concentration of the reactant was 1 mM. Therefore, the value of σ changes by varying the scan rate ν in the simulation.

For a hemispherical electrode, the theoretical steady state current is:

$$I_{s.s,sphere} = 2\pi FD[A]_{bulk} r_{el} = 6.06 \times 10^{-9}\ A$$

When ν=0.011 V s^{-1}, the simulated peak current is 6.24×10^{-9} A, which is 2.9% larger than the theoretical value. The dimensionless scan rate σ is now:

$$\sigma_{hemispherical} = \frac{r^2 F}{DRT}\nu = 4.30 \times 10^{-2}$$

Therefore, for a hemispherical electrode, the diffusion can be considered as mainly convergent when $\sigma<4.30\times10^{-2}$.

For a microdisc electrode, the theoretical steady state current is:

$$I_{s.s,disc} = 4FD[A]_{bulk}r_{el} = 3.86 \times 10^{-9}\ A$$

When ν=0.035 V s^{-1}, the simulated peak current is 3.98×10^{-9} A, which is 3.1% larger than the theoretical value. The dimensionless scan rate σ is now:

$$\sigma_{disc} = \frac{r^2 F}{DRT}\nu = 0.316$$

Therefore, for a hemispherical electrode, the diffusion can be considered as mainly convergent when $\sigma < 0.316$.

The values of σ for the simulation on micro-hemispherical and microdisc electrodes presented in this paper were far less than 4.30×10^{-2}, leading to a true steady-state current.

References:

[1] R. G. A. B. Compton, Craig E, *Understanding Voltammetry*, third ed., World Scientific, **2018**.

[2] A. J. Bard, L. R. Faulkner, *Electrochemical Methods: Fundamentals and Applications, 2nd Edition*, Wiley Textbooks, **2000**.

[3] D. O. Wipf, A. C. Michael, R. M. Wightman, *Journal of electroanalytical chemistry and interfacial electrochemistry* **1989**, *269*, 15-25.

[4] K. Cinková, M. Clark, S. V. Sokolov, C. Batchelor-McAuley, Ľ. Švorc, R. G. Compton, *Electroanalysis* **2017**, *29*, 1006-1013.

[5] C. Batchelor-McAuley, M. Yang, E. M. Hall, R. G. Compton, *Journal of Electroanalytical Chemistry* **2015**, *758*, 1-6.

Appendix B

Section B1: Convergence test for the home-written microband programme

The convergence of the microband programme was tested in terms of the grid interval and the step size. For the potential step size as shown in Figure B1(a), the current difference in the oxidative peak current is negligible (only 0.28%) as the potential step changes from 0.00005 to 0.0001 V. Likewise, the voltammograms superimpose perfectly as the grid interval changes from 0.003 to 0.001. Therefore, the programme was confirmed to be fully converged, and the potential step size and the grid interval for use in simulations were chosen as 0.0001 V and 0.003, respectively.

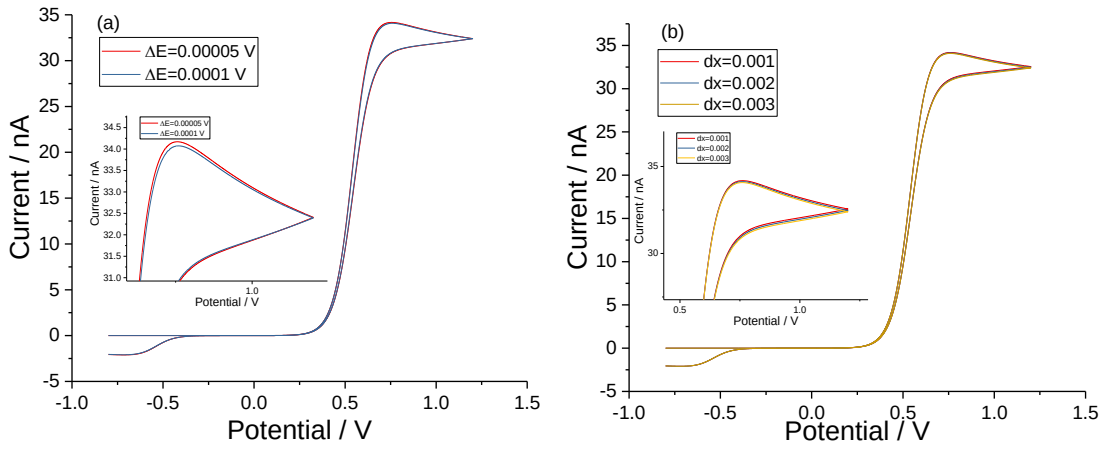


Figure B1 Convergence test on microband programme as a function of (a) potential step size (b) grid interval. The inlayer is the zoom-in version of the voltammogram. Fixed parameters used in the simulation: scan rate ν = 25 mV s^{-1}, formal potential E^0 = 0 V, width w = 2 r_{el} = 100 nm, concentration c = 1 mM, diffusion coefficient D = 1 × 10^{-10} m^2 s^{-1}, electron transfer rate constant k^0 = 1 × 10^{-7} m s^{-1}, transfer coefficient $\alpha_a = \alpha_c = 0.5$.

Section B2: Blind tests

This section shows examples of the electrochemical measurement of width and length of unknown band electrodes. The blind tests were run using 'synthetic' voltammograms generated with known diffusion coefficients of reactant and product ($D_{(A)}=2D_{(B)}= 1\times10^{-10}$ m^2 s^{-1}) as well as two different anodic transfer coefficients ($\alpha_a=0.3$, $\alpha_a=0.4$). The case where $\alpha_a=0.3$ and $\alpha_a=0.4$ are shown in Section B2.1 and Section B2.2, respectively.

Section B2.1: Test 3 - Redox couple with low unequal diffusion coefficients ($\alpha_a = 0.3$, $\alpha_c = 0.7$)

The voltammogram of the blind test is shown in Figure B2 for a band electrode width unknown band width and length. The reactant and product have unequal diffusion coefficients. The procedures of measuring the band width and length are shown below.

First, the known diffusion coefficients of reactant A and product B are 1×10^{-10} m^2 s^{-1} and 0.5×10^{-10} m^2 s^{-1}, respectively. The anodic transfer coefficient is 0.3. Experimentally, these parameters would be measured from steady-state micodisc voltammetry and Tafel analysis.

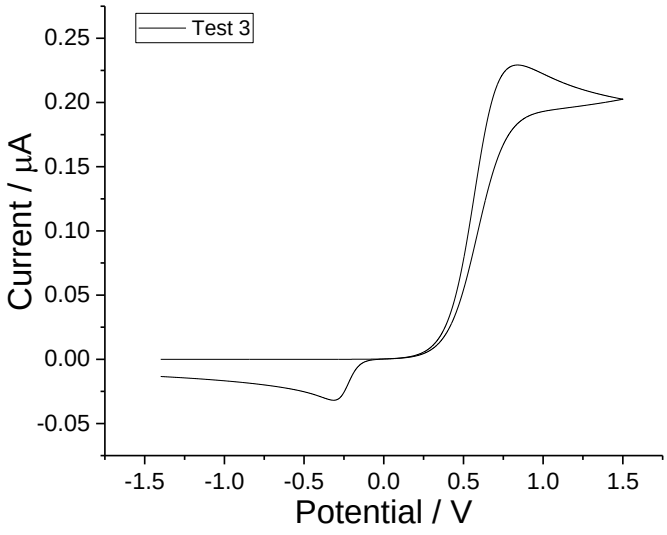


Figure B2 Blind test on a band electrode. Known parameters in the simulation: c = 1 mM, ν = 0.2 V s^{-1}, α_a = 0.3, α_c = 0.7, $D_{(A)} = 1\times10^{-10}$ m^2 s^{-1}, $D_{(B)} = 0.5\times10^{-10}$ m^2 s^{-1}.

Second, from the voltammogram, the measured $E_{p\text{-}p}$ is 1.1542 V and the $|I_{backward}/I_{forward}|$ is 0.1391. Voltammograms with a set of k^0 with variable band widths were then simulated and the corresponding plots of Ep-p versus band width and $|I_{backward}/I_{forward}|$ versus band width are shown in Figure B3(a) and (b). The experimental data is shown as a dashed line. The corresponding band widths at each k^0 are shown as dotted line. From the plots, it shows that the corresponding band widths are relatively consistent in both plots with an electron transfer rate constant k^0 of 9×10^{-8} m s^{-1}. The band width was therefore estimated as 1176 nm.

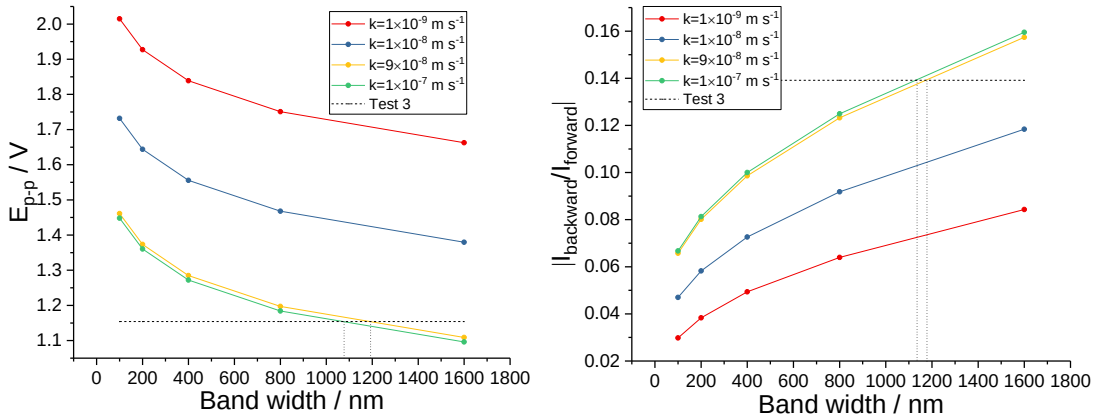


Figure B3 (a) Plot of $E_{p\text{-}p}$ as a function of band widths with variable k^0. (b) Plot of $|I_{backward}/I_{forward}|$as a function of band widths with variable k^0. Parameters in the simulations: $\alpha_a = 0.3$, $\alpha_c = 0.7$, $D_{(A)} = 1\times10^{-10}$ m^2 s^{-1}, $D_{(B)} = 0.5\times10^{-10}$ m^2 s^{-1}. The dashed line is the measured value of $E_{p\text{-}p}$ and $|I_{backward}/I_{forward}|$ from Figure B2. The dotted line shows the corresponding band width at different k^0.

Third, further simulation was done with the known transfer coefficient of 0.3, diffusion coefficients of reactant and product of 1×10^{-10} m^2 s^{-1} and 0.5×10^{-10} m^2 s^{-1}, estimated rate constant of 9×10^{-8} m s^{-1} and band width of 1176 nm. The corresponding voltammogram was normalised to its length as shown in Figure B4. The length of the band in the blind test was then calculated using Equation 6.8 (main text) and was 0.0328 m. Therefore, the band width was estimated as 1176 nm with a length of 0.0328 m. The errors are 2.4% and 0.6% in width and length, respectively as shown in the Main text Table 6.3 (true width=1148 nm and true length=0.033 m in the blind test).

$$length = \frac{Experimental\ I_{peak}\ (\mu A)}{Simulated\ \frac{I_{peak}}{length}\ (\mu A\ m^{-1})} = \frac{0.2292\ \mu A}{6.9850\ \mu A\ m^{-1}} = 0.0328\ m$$

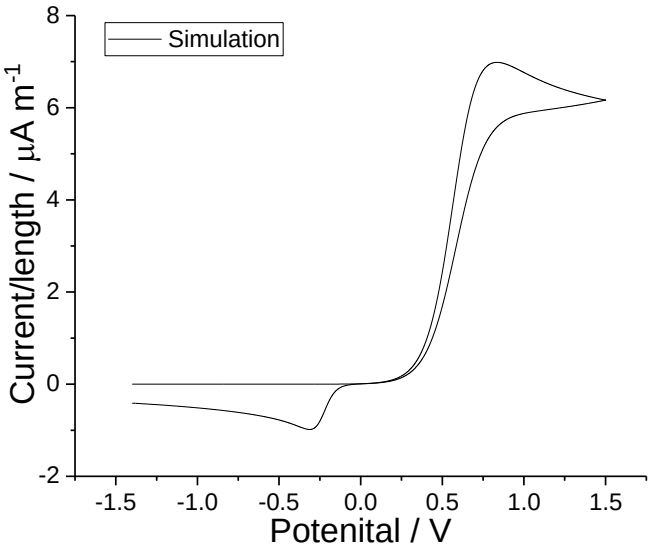


Figure B4 Normalised voltammogram on a band electrode with known transfer coefficient and diffusion coefficients, estimated rate constant and band width. Parameters in the simulation: $\alpha_a = 0.3$, $\alpha_c = 0.7$, $D_{(A)} = 1\times10^{-10}$ m^2 s^{-1}, $D_{(B)} = 0.5\times10^{-10}$ m^2 s^{-1}. ν=0.2 V s^{-1}, E_f=0 V, l=1×10^{-2} m, $k^0=9\times10^{-8}$ m s^{-1}, band width=1176 nm.

Section B2.2: Test 4 - Redox couple with low unequal diffusion coefficients ($\alpha_a = 0.4$, $\alpha_c = 0.6$)

The voltammogram of the blind test is shown in Figure B5 for a band electrode width unknown band width and length. The reactant and product have unequal diffusion coefficients. The procedures of measuring the band width and length are shown below.

First, the known diffusion coefficients of reactant A and product B are 1×10^{-10} m^2 s^{-1} and 0.5×10^{-10} m^2 s^{-1}, respectively. The anodic transfer coefficient is 0.4. Experimentally, these parameters would be measured from steady-state micodisc voltammetry and Tafel analysis.

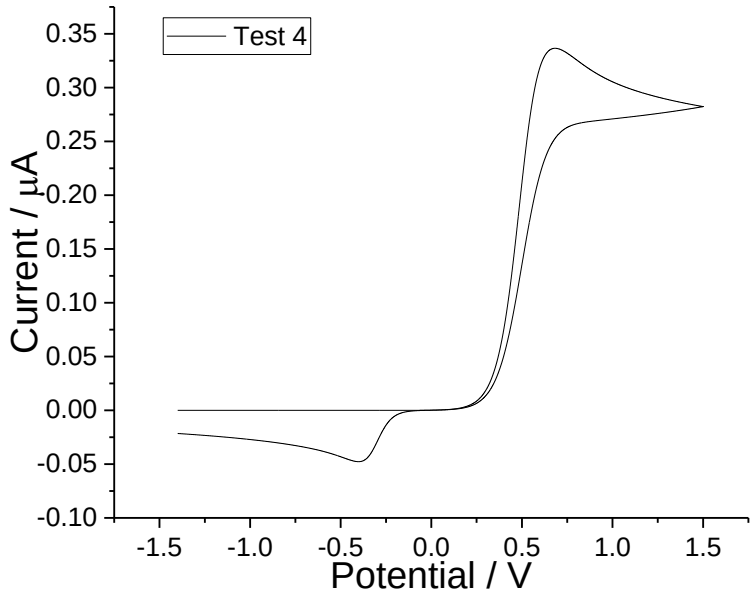


Figure B5 Blind test on a band electrode. Known parameters in the simulation: c = 1 mM, ν = 0.2 V s^{-1}, α_a = 0.4, α_c = 0.6, $D_{(A)} = 1\times10^{-10}$ m^2 s^{-1}, $D_{(B)} = 0.5\times10^{-10}$ m^2 s^{-1}.

Second, from the voltammogram, the measured $E_{p\text{-}p}$ is 1.0846 V and the $|I_{backward}/I_{forward}|$ is 0.14178. Voltammograms with a set of k^0 with variable band widths were then simulated and the corresponding plots of Ep-p versus band width and $|I_{backward}/I_{forward}|$ versus band width are shown in Figure B6(a) and (b). The experimental data is the dashed line. The corresponding band widths at each k^0 are shown as dotted line. From the plots, it shows that the corresponding band widths are relatively consistent in both plots with an electron transfer rate constant k^0 of 3×10^{-8} m s^{-1}. The band width was therefore estimated as 1424 nm.

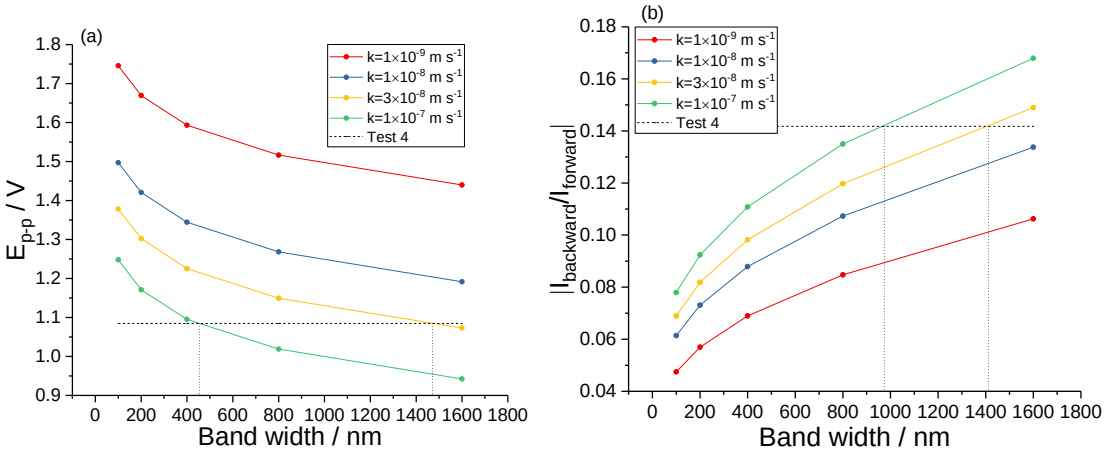


Figure B6 (a) Plot of $E_{p\text{-}p}$ as a function of band widths with variable k^0. (b) Plot of $|I_{backward}/I_{forward}|$as a function of band widths with variable k^0. Parameters in the simulations: $\alpha_a = 0.4$, $\alpha_c = 0.6$, $D_{(A)} = 1\times10^{-10}$ m^2 s^{-1}, $D_{(B)} = 0.5\times10^{-10}$ m^2 s^{-1}. The dashed line is the measured value of $E_{p\text{-}p}$ and $|I_{backward}/I_{forward}|$ from Figure B5. The dotted line shows the corresponding band width at different k^0.

Third, further simulation was done with the known transfer coefficient of 0.4, diffusion coefficients of reactant and product of 1×10^{-10} m^2 s^{-1} and 0.5×10^{-10} m^2 s^{-1}, estimated rate constant of 4×10^{-8} m s^{-1} and band width of 1424 nm. The corresponding voltammogram was normalised to its length as shown in Figure B7. The length of the band in the blind test was then calculated using Equation 6.8 (main text) and was 0.0444 m. Therefore, the band width was estimated as 1424 nm with a length of 0.0444 m. The errors are 5.5% and 1.3% in width and length, respectively as shown in the Main text Table 6.3 (true width=1350 nm and true length=0.045 m in the blind test).

$$length = \frac{Experimental\ I_{peak}\ (\mu A)}{Simulated\ \frac{I_{peak}}{length}\ (\mu A\ m^{-1})} = \frac{0.3366\ \mu A}{7.5808\ \mu A\ m^{-1}} = 0.0444\ m$$

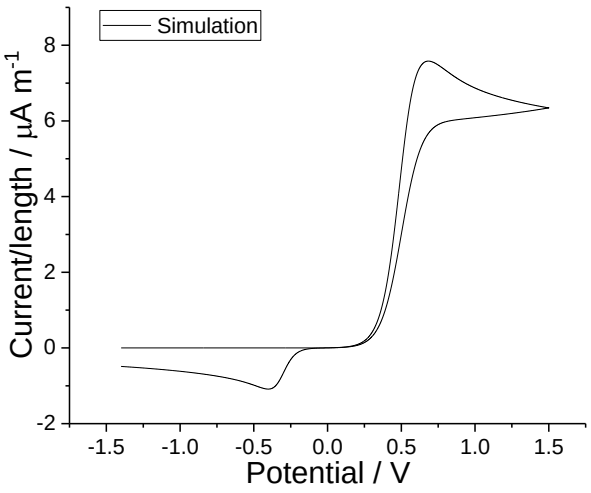


Figure B7 Normalised voltammogram on a band electrode with known transfer coefficient and diffusion coefficients, estimated rate constant and band width. Parameters in the simulation: $\alpha_a = 0.4$, $\alpha_c = 0.6$, $D_{(A)} = 1\times10^{-10}$ m^2 s^{-1}, $D_{(B)} = 0.5\times10^{-10}$ m^2 s^{-1}. ν=0.2 V s^{-1}, E_f=0 V, l=1×10^{-2} m, $k^0=9\times10^{-8}$ m s^{-1}, band width=1424 nm.